Nonlinear Finite Element Analysis of Punching Shear of Reinforced Concrete Slab-Column Connections

by

Aikaterini Genikomsou

A thesis

presented to the University of Waterloo

in fulfillment of the

thesis requirement for the degree of

Doctor of Philosophy

in

Civil Engineering

Waterloo, Ontario, Canada, 2015

Author’s declaration

I hereby declare that I am the sole author of this thesis. This is a true copy of the thesis, including any required final revisions, as accepted by my examiners.

I understand that my thesis may be made electronically available to the public.

Abstract

The code provisions for the design of reinforced concrete slabs are based on empirical and mostly statistical formulations derived from the tests. The available testing database consists of different types of slabs and in some cases it is limited due to the extensive cost and time that a punching shear test requires. Thus, there is a need for verification of the actual code provisions and this can be done in part by using finite element (FE) simulations. The finite element analyses (FEA) can supplement the existing testing background and can be used for parametric investigation, since they can indicate different aspects on punching shear failure, leading to possible recommendations for the design codes and models.

In this thesis, 3D FEA of reinforced concrete slabs with the FE software ABAQUS using the concrete damaged plasticity model are presented. The appropriate calibration of the concrete model, is done in this study based on an interior slab-column connection without shear reinforcement (SB1), considered as the control specimen, which was tested under vertical loading in a previous study. The predictive capability of the calibrated model was demonstrated by simulating and analyzing different types of slabs without shear reinforcement. Interior specimens under static and reversed cyclic loadings and edge slabs under static and horizontal loadings are examined. The predicted capability of the calibrated model is then examined by simulating slab-column connections with shear reinforcement. Four different modelling approaches for the shear bolts are presented. Discussion and comparison between the design codes are also presented. A parametric study based on the different shear reinforcement patterns that ACI code (rectangular) and EC2 (radial) propose is conducted. This study also involves the investigation of the effect of openings on the punching shear behaviour of the reinforced

concrete slabs without shear reinforcement. The effect of the location, the distance from the column and the size of the opening on the punching shear resistance, are investigated. The results, confirm that the punching shear resistance is decreased with an increase in the opening size and with a decrease in the opening distance from the column. Finally, the compressive membrane action effect on reinforced concrete slabs is examined. FEA are performed considering an isolated interior flat slab (SB1) as continuous. The predictive capability of the FEA models enhance their effectiveness for further investigation on the effect of membrane action by supplementing the limited testing background in this area.

Acknowledgements

At this point, I would like to acknowledge all the people who helped me to pursue my Ph.D. I will start expressing my special thanks to my wonderful advisor and mentor, Professor Marianna Polak, for sharing with me her extensive knowledge and for guiding me through her valuable advices. I would like to thank her for being there for me all these four years with her continuous support.

I gratefully acknowledge the funding for the research that was provided by the Natural Sciences and Engineering Research Council (NSERC) of Canada.

I would also like to acknowledge my dissertation committee members, Professors Jeffrey West, Mahesh Pandey, Hamid Jahedmotlagh and Stavroula Pantazopoulou for their time and helpful remarks. I am deeply grateful to Professor Stavroula Pantazopoulou as teacher and mentor. She patiently and kindly advised me to pursue my Ph.D. in Canada, being my inspiration to continue studying for my doctoral degree.

I wish to express my appreciation to all the extraordinary professors at the University of Waterloo for their help and support and especially, I thank Professor Scott Walbridge for guiding me through my teaching assistantship experience. My sincere thanks also go to all the staff at the University of Waterloo for being always helpful and kind with me.

My thanks are extended to my friends and colleagues, Paulina Arczewska, María José Rodríguez Roblero, Adam Wosatko, Olivier Daigle, Martin Krall, Joe Stoner, Shayan Sepiani,

Izabela Murzyn. I would also like to thank my Greek Electrical Engineers friends, Nikolaos Papadopoulos and Anastasios Livogiannis.

Then, I would like to thank from the bottom of my heart, Georgios Balomenos, for his continuous support and help all these four years. He was offering me his valuable advices, ideas, insights and thoughts during my research, being a source of encouragement and strength that helped me to complete successfully my graduate studies.

Last but not least, there are no words to express my thanks to my wonderful parents, Sophia and Stefanos, and my loving brother, Alexis. They were always supporting and encouraging my choices by providing to me their love, knowledge, advices, wishes and thoughts. This journey would not have been possible without their support. Thank you!

Table of Contents

List of Figures

Chapter 2

Chapter 3

Chapter 4

Chapter 5

Chapter 6

Chapter 7

Chapter 8

List of Tables

Chapter 5

Chapter 6

Chapter 7

Chapter 8

Chapter 1

Introduction

1.1 Research significance and objectives

Reinforced concrete flat slabs supported on columns are used as a construction system worldwide due to the advantages that they offer; such as reduction of floor height, easy construction and formwork and reduction of the construction cost. However, high stresses in the slab-column connection area can be developed resulting in a punching shear failure. This failure mostly happens without warning and may lead to a progressive collapse of the structure. In order to avoid the punching shear failure, the punching shear capacity of the reinforced concrete flat slab should be enhanced. This can be done in many ways; such as, creating larger columns, increasing the effective depth of the slab, increasing the flexural reinforcement ratio, increasing the compressive strength of concrete and finally installing shear reinforcement around the slab-column connection area. Among these methods, the most effective way to increase the strength of a slab-column connection is to use shear reinforcement in the punching shear zone, around the column. Various forms of punching shear reinforcement are used such as stirrups, bent up bars and shear studs.

Many tests have been conducted in order to investigate the punching shear failure of the reinforced concrete flat slabs and their experimental results were used as the basis of the current punching shear design codes. Therefore, the actual code provisions for the design and

construction of reinforced concrete slabs are based on empirically and statistically developed formulations. However, the existing testing background does not satisfy geometrical similarity or similarity in the material properties. The reason for not having the required repeatability in the testing background is the extensive cost and required time of performing experiments. Thus, the properly calibrated finite element analysis (FEA) can be used in order to supplement the test results and to overcome these testing shortcomings. Nonlinear finite element analysis can be a powerful and useful source of information on slabs behaviour; such as, the ultimate punching shear loads, the activation of the flexural reinforcement and the formation of the flexural and shear cracks. These FE models must be calibrated based on selected experimental results, and then can be used for parametric investigations addressing different aspects of the punching shear failure of flat slabs.

A literature survey on punching shear tests and researchers who contributed in this field is presented in Chapter 2, however, at this point it is important to trace and write about the pioneers in finite element methods. Who first developed the idea that led to the finite element analysis method and who first used the term “finite element method”? Finite element method was first invented by M.J.J. Turner at Boeing in the 1950s using the direct stiffness method. Pioneers in developing and transferring the practice from the aerospace industry to general applications were: J.H. Argyris, R.W. Clough, H.C. Martin and O.C. Zienkiewicz. The first published “pioneering” paper using FEM belongs to Turner, Clough, Martin and Topp (1956) entitled: Stiffness and deflection analysis of complex structures. They developed the triangular element stiffness matrix and they studied the displacement convergence characteristics of planar elements. Clough was the first that used the term “finite element” in 1960, trying to show the difference between the continuum analysis and the structural analysis using the matrix method.

The first published paper using the term “finite element” belongs to Clough (1960) and its title is: The finite element method in plane stress analysis. During the following years the finite element method (FEM) started to be used and its validity was recognized. Fully developed FEA software started during the 1970s and 1980s. Nowadays, many researchers conduct research using finite element methods and FEA software packages. *However, all researchers must apply,* as Clough stated, *good engineering judgment in interpreting the results of the analysis, based on a thorough knowledge of the finite element stiffness formulation.*

In this thesis, FEA of selected previously tested reinforced concrete slabs are analyzed using the finite element software ABAQUS. The concrete damaged plasticity model that ABAQUS offers is studied and considered for the constitutive modelling of concrete. The complexity of this model necessitates proper investigation on its parameters, starting with FEA of simple problems and finally moving to the punching shear examples. The simulated punching shear examples are chosen from tests that have been done at the University of Waterloo. El-Salakawy et al. (1998) tested edge slab-column connections subjected to unbalanced moments and it was found that the shear stresses increase with the higher moment to the shear ratio. In 1999, El-Salakawy et al. presented the experimental results of reinforced concrete edge slab-column connections examining the effect of openings. The effect of the shear studs in the reinforced concrete slabs was studied in 2000 by El-Salakawy, Polak and Soliman and it was found that the shear studs increase the stiffness of the edge slabs and enhance the shear strength and ductility of the slabs. Shear studs are the reinforcement that can be installed into the slabs before casting. Another type of shear reinforcement, the shear bolts, can be installed in existing slab-column connections as a retrofit method. El-Salakawy et al. (2003) presented test results of slab-column connections strengthened with shear bolts. They found that the shear bolts increase

the capacity and ductility of the edge slab-column connections, and also can change the failure mode from punching shear to flexural. Adetifa and Polak in 2005, tested interior slab-column connections with shear bolts subjected to vertical loading. They observed that shear bolts prevent the propagation of the shear cracks in strengthened slabs and improve the performance of the slabs with openings. Bu and Polak (2009) investigated the behaviour of slab-column connections subjected to cyclic lateral drift and constant gravity loading. The specimens were retrofitted using shear bolts and the results indicated that the shear bolts increased the punching shear capacity and ductility of the connections. Thus, in this work, selected specimens from the above mentioned tests are considered in the FEA for examining the punching shear failure of the reinforced concrete flat slabs. The general objective of this thesis is the development of the FEA predictive tool for punching shear in concrete slabs that can be used to investigate slab behaviour, supplement the existing test database and help in the development of future code provisions.

The specific objectives of this research are the following:

1. The efficient calibration of the concrete damaged plasticity model in ABAQUS;
2. The predictive capability of the proposed and calibrated model in ABAQUS in punching shear simulations;
3. The applicability of the calibrated model in reinforced concrete slabs without shear reinforcement and then the use of the model in slabs with punching shear reinforcement;
4. The investigation of the opening effect in the concrete slabs and the critical review on the design provisions addressing this issue and;

5. The investigation of the compressive membrane action effect of the continuous slabs.

By achieving the above specific objectives of this research, the use of the calibrated concrete damaged plasticity model in punching shear FEA is proposed; where testing background can be supplemented by giving more information regarding the crack formation and propagation, where the test measurements are not known. Finally, parametric analyses can be conducted in order to identify different aspects in punching shear with final goal all the parametric studies to be used for future code modifications.

1.2 Outline

The outline of the thesis is presented with the following order:

After the introduction (Chapter 1), where the research objectives and the outline of the thesis are presented, Chapter 2 starts discussing the critical phenomenon of punching shear failure in reinforced concrete flat slabs. Then, a review on the existing testing database of slabs without and with punching shear reinforcement is presented. Additionally, a brief description on the code provisions and the mechanical models in punching shear is shown. Chapter 3 presents an overview on the material behaviour of concrete, the non-linear modelling of concrete with respect to cracking models, plasticity theory, continuum damage mechanics and damage mechanics coupled with plasticity. In Chapter 4, the description of the constitutive concrete material model in ABAQUS can be found. The concrete damaged plasticity model is discussed in detail and its calibration is presented. FEA examples are presented in order to verify the accuracy of the constitutive concrete material model. Based on the calibrated material modelling, Chapter 5 presents the development of a nonlinear finite element approach in ABAQUS in order

to investigate the punching shear failure of reinforced concrete slabs without shear reinforcement. Chapter 6 shows the adoption of the calibrated concrete damaged plasticity model in modelling and analyzing reinforced concrete slabs with punching shear reinforcement. Different modelling approaches for the shear bolts are presented and finally the most appropriate is chosen. The comparison between the numerical and test results indicates that the concrete damaged plasticity model works in a proper way for simulating the shear-reinforced specimens. Chapter 7 discusses the critical issue of the effect of openings in flat concrete slabs where a comparison between the tests, numerical results and the code predictions is provided. Then, Chapter 8 discusses the membrane action effect on the reinforced concrete slabs. The isolated test specimens do not consider the increased punching shear strength compared to the continuous real slabs that are influenced by the membrane action. Continuous slabs are analyzed with the calibrated concrete damaged plasticity model and compared to the isolated specimens. Compressive membrane action effect increases the ultimate capacity of the slabs while the design codes do not consider that increase as they are based on test results coming from isolated specimens. Finally, Chapter 9 presents the summary and the conclusions of the research with the future considerations and suggestions.

Chapter 2

Punching shear in reinforced concrete slabs

2.1 Introduction

Reinforced concrete flat slabs are often used for monolithic concrete construction. Their construction started in the beginning of the 20th century in the North America and Europe. Such type of construction is efficient, economical and provides many advantages, such as, no beams are needed, no overhead obstacles, more ceiling height, easy construction. The first slabs that were built supported on columns included large column capitals in order to avoid shear problems when the loads were transferred from the slab to the column. Slabs without column capitals and/or drop panels appeared in the 1950s. These slabs developed high shear stresses near the column and thus they were considered as vulnerable to the punching shear failure. The first flat slabs were designed by George M. Hill in 1901, however, the most famous contributors were C.A.P. Turner (1869-1955) in USA and R. Maillart (1872-1940) in Switzerland. Shear, in the design, was taken into account through larger column capitals creating a system that functioned like "mushroom plates". Figure 2.1 shows one of the first mushroom flat slab floor systems constructed in Minneapolis by Turner (1906). In this chapter, the punching shear failure as a phenomenon that occurs in flat slabs is presented first and then, a review on the punching shear testing background is given. Then, some of the most important developed punching shear models are presented and finally, the design code provisions against punching shear are discussed.

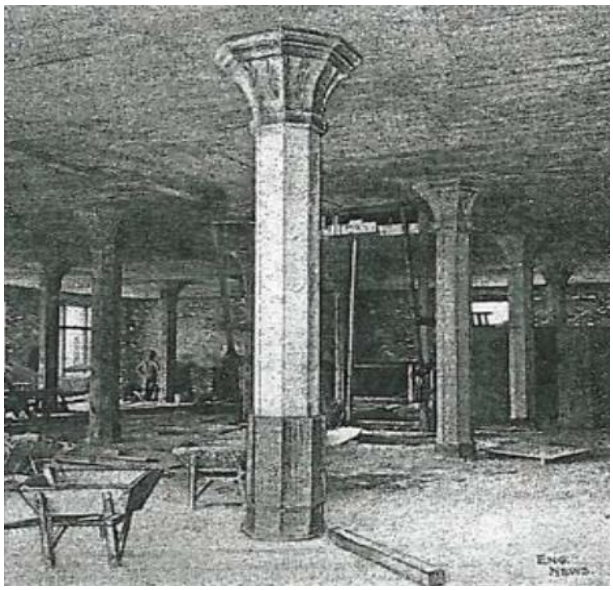

Figure 2.1 Johnson Bovey Building in Minneapolis, 1906 (http://www.mbjeng.com/wp-content/uploads/2011/03/NL13_Oct2010-Meghans-article.pdf).

2.2 Punching shear failure

Two-way reinforced concrete slabs are a unique type of floor construction. It is an efficient, economical, and widely used structural floor system. In practice, two-way slabs take various forms, as shown in Figure 2.2 and Figure 2.3.

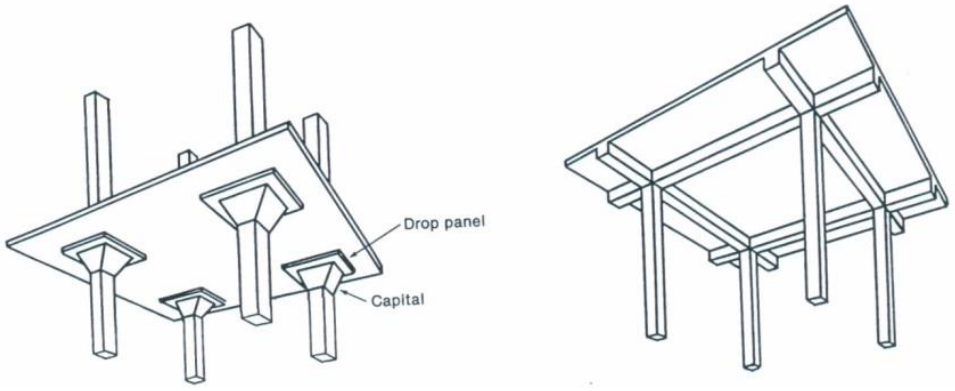

Figure 2.2 Flat-slab and two-way slab with beams (McGregor and Bartlett, 2000).

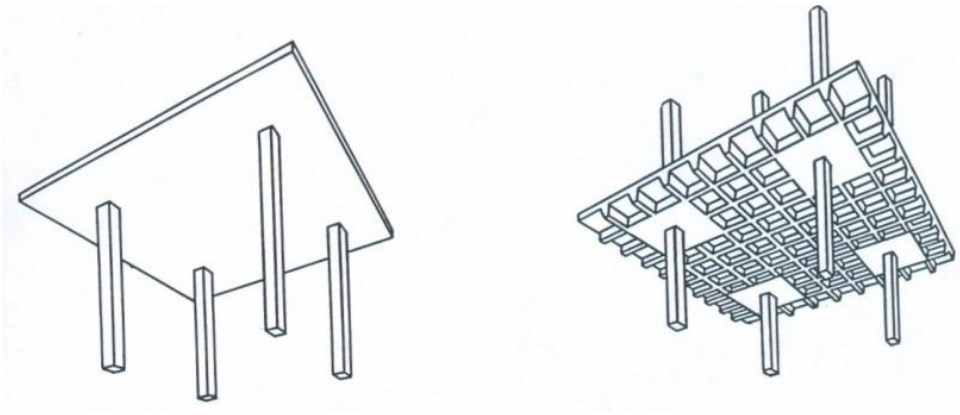

Figure 2.3 Flat plate and waffle slab (McGregor and Bartlett, 2000).

Concrete flat-slabs are one of the most common floor system employed in the construction of many multi-story buildings; such as parking garages, offices, hotels, and apartments. They are used in multistory building constructions because of such advantages as flat ceilings, simplified formwork and reduced story height. Reinforced concrete flat-slabs are considered in structures because their advantages result in reduction in material and construction cost. However, flat-slabs, depending on their design layout (i.e., concrete strength, reinforcement layout, slab depth, etc.), are susceptible to punching shear failure around the columns (Figure 2.4 and Figure 2.5). Punching shear failure is caused by the transfer mechanism of shear forces from the slab to the slab-column connection and occurs within the discontinuity D-region, where the 3D state of stress is complex. These shear stresses are developed from gravity loads and from unbalanced moments (combination of gravity loading and lateral deflections) and movement during events; such as earthquakes and high winds. Once these shear stresses exceed the slab's shear capacity, punching occurs, and depending on the severity and intensity of the event, this can happen with little or no warning. Punching shear failures are generally brittle phenomena. Cracks occur inside the slab into the vicinity of the column and then they propagate through the slab's thickness at an angle of 20°- 45° to the

bottom of the slab. This can lead to punching shear failure of the slab along the cracks. An inclined crack forms around the column and at the end the punching shear cone appears, where the column separates from the slab (Figure 2.6).

Figure 2.2.4 Cracks after punching shear failure of flat slabs (MacGregor and Bartlett, 2000).

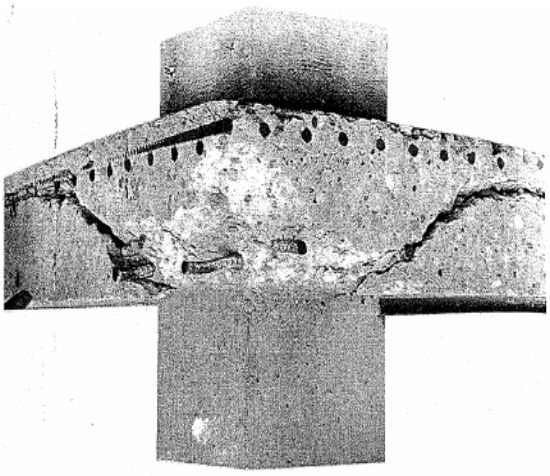

Figure 2.2.5 Inclined cracks in a slab after a shear failure (MacGregor and Bartlett, 2000).

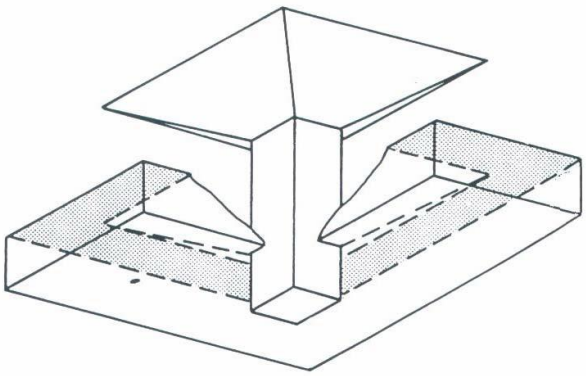

Figure 2.2.6 Failure surface of punching shear (MacGregor and Bartlett, 2000).

2.3 Review on punching shear tests

Punching shear testing started at the beginning of the 20th century and continued in 1950s. Mostly, in all tests, the slab is considered as isolated specimen representing the slab around the column extending to the line of contra-flexure. According to Moe (1961), significant early contribution to punching shear testing was done by Talbot (1913), Bach and Graf (1915) and Graf (1933, 1938). Talbot (1913) tested reinforced concrete footings and proposed a formula for the assessment of concrete's strength at the column. His formula is still used, after modifications, in many design codes. He introduced the concept of the critical perimeter (located at distance d from the loaded area) and he came up with the observation that the shear strength is increased with an increase in the amount of the flexural reinforcement. The test observations offered by Talbot (1913) led to the first recommendations for punching shear published in 1925 in ACI-American Code.

The footings tested by Talbot (1913) were very thick and the results found to be not adequate for describing the punching shear strength of slabs. Thus, experimental investigation on concrete flat slabs started to be considered. Due to the fact that the test specimens in punching

shear use variety of test configurations, a review of selected experimental setups is presented. Isolated specimens subjected to gravity loading at the center of the slab were tested among others by Elstner and Hognestad (1956), Kinnunnen and Nylander (1960) and Moe (1961). Elstner and Hognestad (1956), Hanson and Hanson (1968) and Corley and Hawkins (1968) tested specimens with distributed uniform load. Most of the slabs, tested under gravity load, were supported at the edges (Elstner and Hognestad (1956), Moe (1961), Sieble et al. (1980), Swamy and Alo (1982), Harajli et al. (1995), Adetifa and Polak (2005), Naaman et al. (2007)). However, Broms (2007) and Brikle and Dilger (2008) tested specimens supported at discrete points and not around the edges in order to simulate the points of contra-flexure. Specimens subjected to gravity load and unbalanced moments were tested by Hawkins et al. (1974), Robertson et al. (2002), Pan and Moehle (1989), Elgabry and Ghali (1987) and El-Salakawy and Polak (1999). Pan and Moehle (1989) tested slab-column connections subjected to lateral displacement cycles and gravity load. They found that the lateral drift capacity of the connections is dependent on the gravity to shear ratio. An increase in the gravity shear ratio with the lateral cyclic loading led to a reduction of strength, stiffness and displacement. It was recommended that the 0.4 gravity to shear ratio as the upper limit in order to have a drift capacity in the range of 1.5%. Many important contributions regarding the lateral cyclic loading applied to the slab-column connections have been offered also by Robertson and Durrani (1992), Megally and Ghali (2000) and Bu and Polak (2009).

First attempt to include shear reinforcement in the tested slabs was done by Graf (1933) and Wheeler (1936). The researchers tested flat slabs with different types of shear reinforcements. Graf (1933), Elstner and Hognestad (1956), Andersson (1963), Hawkins (1974), Islam and Park (1976) and Dilger and Ghali (1981) tested specimens with bent-up bars. Bent-up bars increase the punching shear resistance, however it is better to combine them with other

types of shear reinforcement, because punching shear failure can happen behind the bent-up bars. Hawkins (1974) reported tests performed with different punching shear reinforcements and he found that the shear reinforcement increases the punching shear capacity of the slabs. Broms (2000) combined the bent-up bars in the first two perimeters with closed stirrups and such arrangement was able to avoid any punching shear failure. Closed stirrups were also used by many researchers, as another type of shear reinforcement; among others Islam and Park (1976), Hanna et al. (1975), Pillai et al. (1982) and Robertson et al. (2002). Slabs with shear heads were tested by Corley and Hawkins (1968) and by Dilger and Ghali (1981). The shear studs that consist of individual vertical bars were used in slabs tested by Seible et al. (1980), Dilger and Ghali (1981), Elgabry and Ghali (1987), Megally and Ghali (2000), Robertson et al. (2002), Kang and Wallace et al. (2005) and Tan and Teng (2005). Shear heads are an expensive type of shear reinforcement, however, it is essential to be used in cases where large openings close to the connection area are needed and thus this demands large adjustments to the flexural reinforcement. The shear studs have been widely used due to the advantages that they provide such as mechanical anchorage and highly quality. Shear studs are difficult in installation, however they are the most popular punching shear reinforcement. Adetifa and Polak (2005) used a new type of shear reinforcement post-installed in flat slabs, called shear bolts.

Important early contributions in understanding the punching failure came from Elstner and Hognestad (1956) who tested 39 slabs in order to estimate the influence of the flexural reinforcement ratio, concrete strength, compression reinforcement, size of the column, support conditions and amount of shear reinforcement in the punching shear capacity of the flat slabs. The outcomes from their tests were that all of these factors have an important influence on the shear strength, except the compressive reinforcement that was found to have the smallest

influence on the punching shear capacity of the slabs. Moe (1961) reported, after analyzing many tests that he conducted, the influence of the unbalanced moments in the slab-column connections. His work remains until now the basis for the ACI 318 code.

The opening effect in flat slabs started to be examined only recently by researchers, such as, El-Salakawy et al. (1999), Teng et al. (2004), Bu and Polak (2009), Borges et al. (2013), and Anil et al. (2014). Unfortunately, this testing background is limited due to the time and cost demands on testing.

Chana and Desai (1992) tested conventional slabs and continuous slabs in order to investigate the compressive membrane action effect. During their research, they concluded that the punching shear strength of a real slab is much higher compared to the strength of the isolated slab. Their research reported also the performance of a special punching shear reinforcement system, known as shear-hoop and compared it to the shear links.

Figures 2.7, 2.8 and 2.9 show some from the discussed types of punching shear reinforcement used in many experiments.

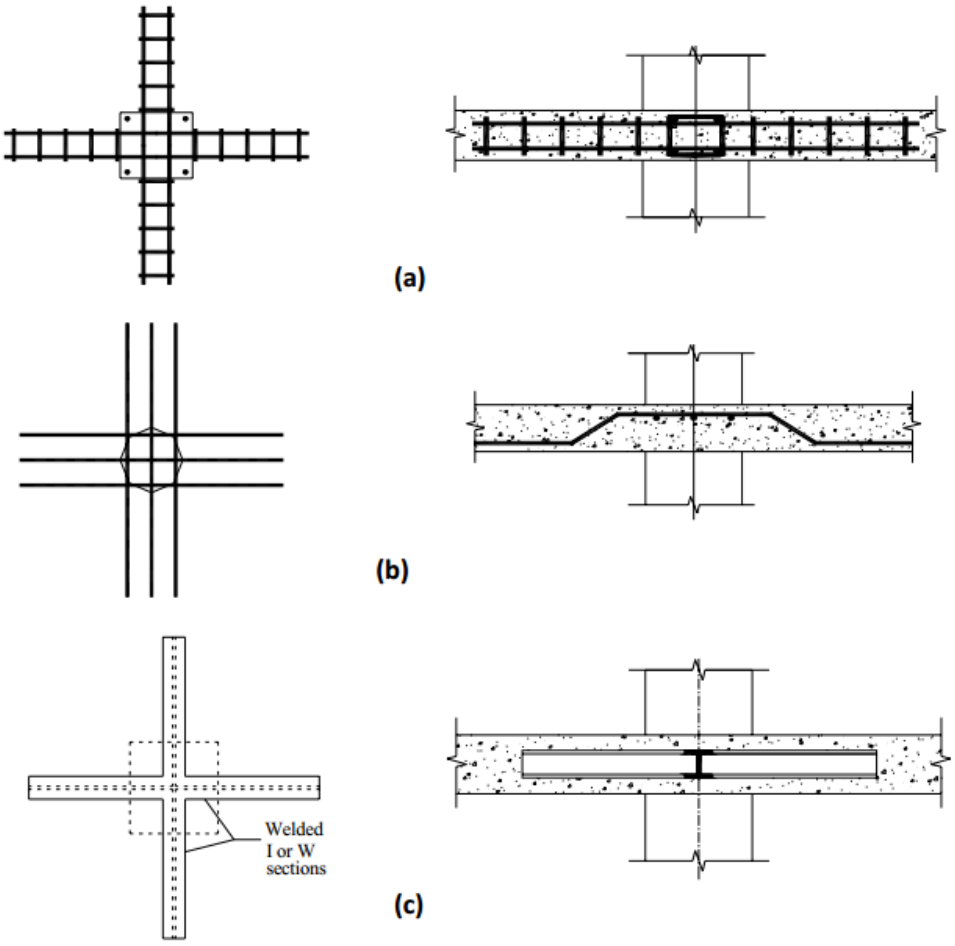

Figure 2.7 Different types of shear reinforcement in plan and section view: a) stirrups; b)bent bars and c) shear heads (taken from Polak et al., 2005).

Figure 2.8 Shear studs (taken from Polak et al., 2005).

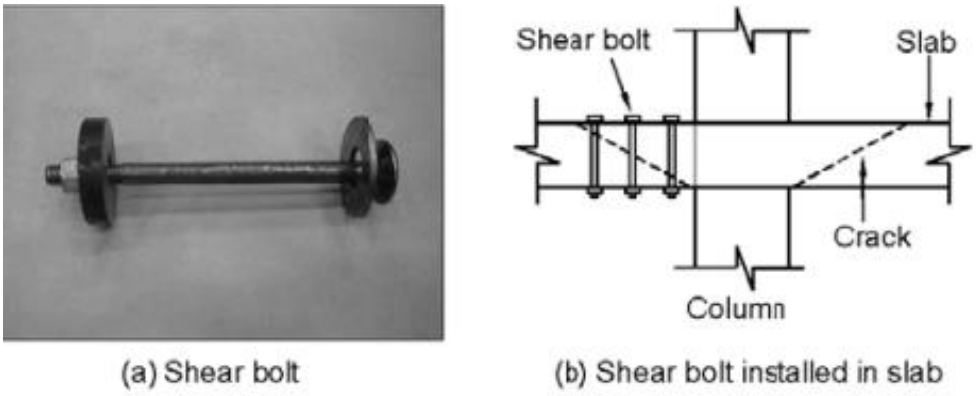

Figure 2.9 a) Shear bolt and b) its installation (Polak and Adetifa, 2005).

2.4 Review of punching shear mechanical models

Due to the extensive research on punching shear, several analytical mechanical models have been proposed. Some of them formed the basis of the design formulae employed in code provisions. Below only few of some important models for punching shear are presented.

Kinnunen and Nylander (1963) suggested their model based on 61 tests of circular columns and slabs with radial reinforcements done in the 1960's. Significant findings of their research had to deal with the formation of the shear cracks, the deformation of the sector elements and the expansion of the concrete and the steel. In their model, the internal forces are dependent on the angle of the section α (see Figure 2.10) and the material properties. The failure criterion according to Kinnunen is: "The tangential compressive concrete strain on the bottom surface of the slab under the root of the shear crack reaches a characteristic value at which favorable embedment of the conical shell is impaired". The ultimate load was determined from the equilibrium of flexure and shear. This theory was derived for slabs with ring reinforcement, however, then it was expanded to slabs with two-way reinforcements.

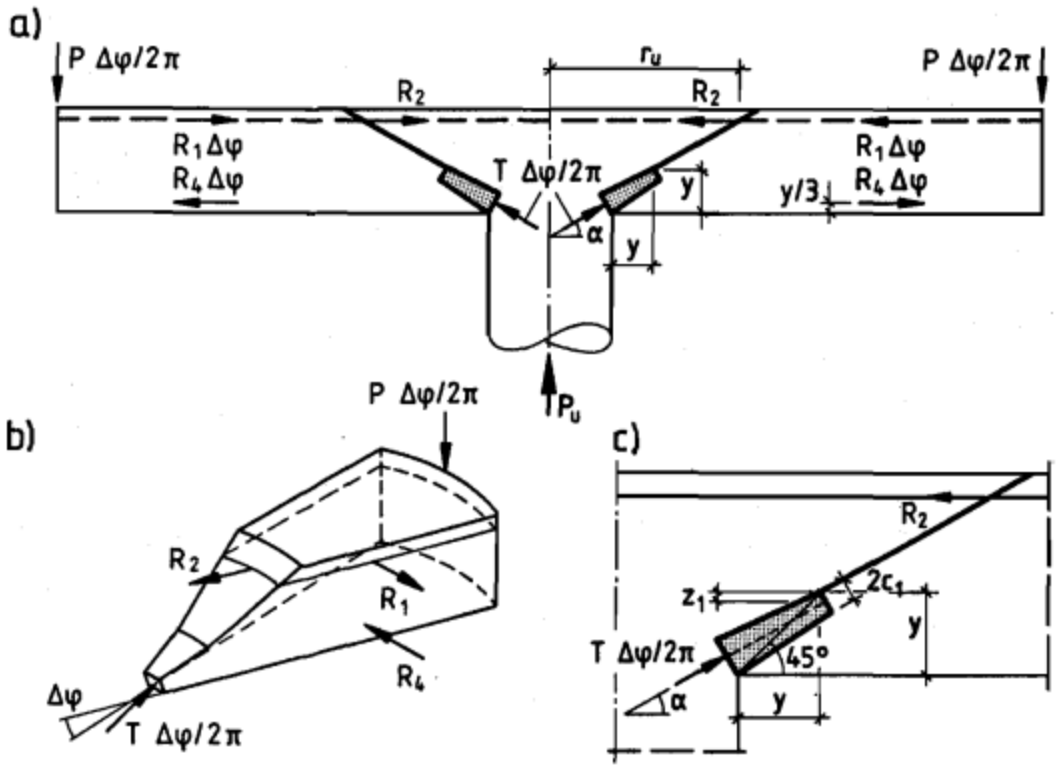

Figure 2.10 Kinnunen and Nylander punching shear model (1963).

In 1976, Braestrup et al. proposed an upper bound plasticity model on an axisymmetric slab supported by a circle ring (Figure 2.11). The basic assumptions of their model were: a) concrete is a perfect plastic material, b) the failure criterion is based on the Coulomb's law and c) the tensile strength of concrete is assumed to be low. P_u denotes the ultimate load that is found by comparing the fracture energy of the conical shaped shell with the work carried out by the applied loads. As it is shown in Figure 2.10, the shape of the conical shell is added by the straight line and the catenary curve. This model is mostly able to give an upper bound solution for the ultimate loads. However, the model does not account for the flexural reinforcement ratio and also the first assumption of the model that the concrete behaves as a perfectly plastic material leads to many simplifications.

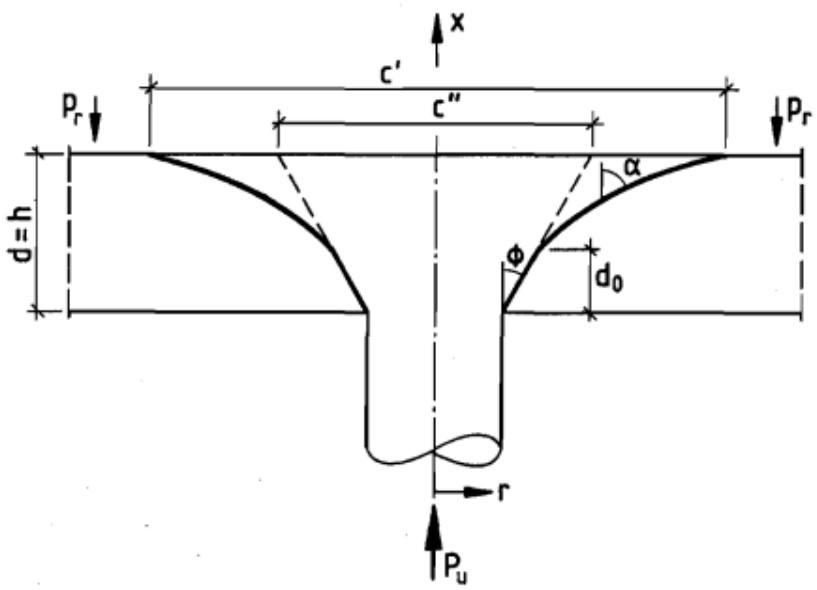

Figure 2.11 Predicted failure surface by Braestrup et al. (1976).

Alexander and Simmonds (1986) (see Figure 2.12) suggested a truss model that considers the top reinforcement as a horizontal tie and the concrete as inclined strut. The punching shear resistance is dependent on the area of the flexural reinforcement near the column, considered as shear strut, the strength of the flexural reinforcement and the angle of the strut. Alexander and Simmonds in 1992 proposed the curved compression strut model, the so-called bond model (Figure 2.13). According to this model, the shear is transferred to the column by the curved compression strut. In the truss model, the compression struts are straight and inclined while in the bond model the compression struts are considered curved. These curved arches are located in four radial strips and these strips separate the column from the slab in order for the load to be carried out by the radial strips. The reinforcement forces are limited by the bond failure or by yielding. That model combines the radial arch action associated with the critical shear stress (beam action shear). Also, the bond strength of the reinforcements seems to be a significant factor that reduces the beam action shear, especially for brittle punching shear failures.

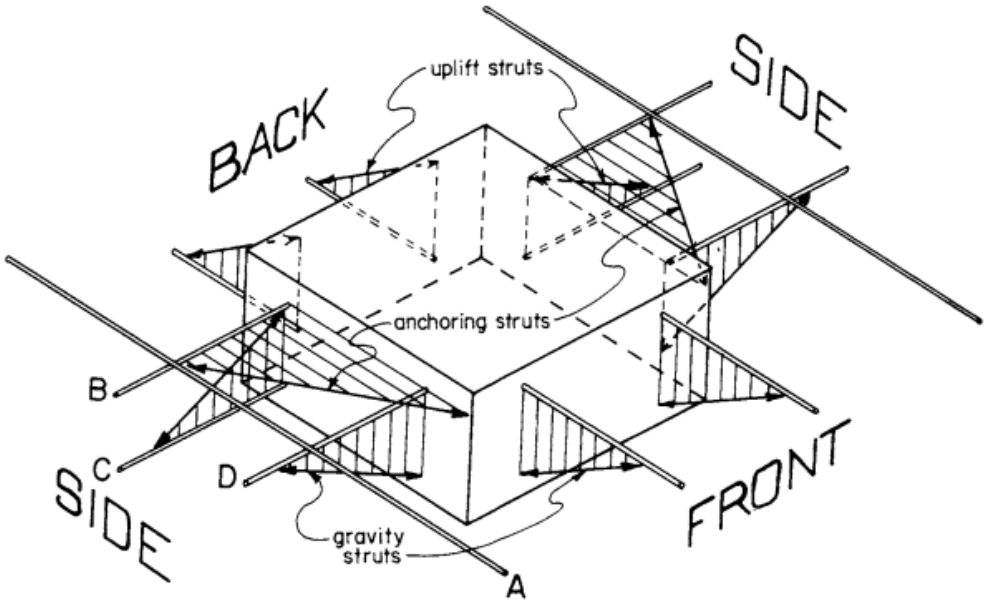

Figure 2.12 Alexander and Simmonds – Truss model (1987).

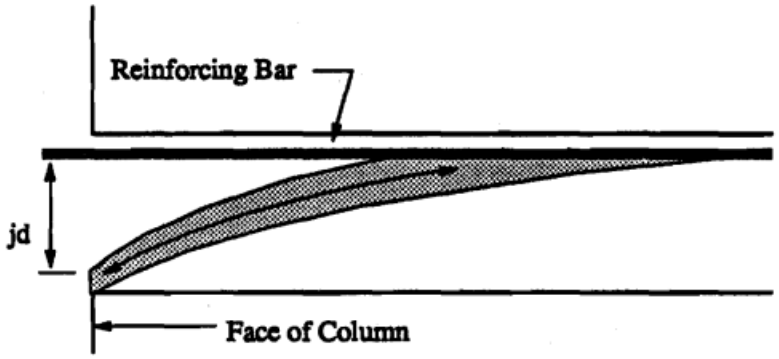

Figure 2.13 Alexander and Simmonds – Curved compression strut (1992).

Rankin and Long (1987) proposed the yield line model. They indicated that as the flexural reinforcement yields, the slab can be divided into several elastic plates connected with plastic hinges. The equilibrium of all of these plates gives the ultimate load for the whole slab.

Figure 2.14 shows the yield line pattern that Rankin and Long proposed. The ultimate vertical load P_{flex} can be calculated according to Eq. 2.1.

$$P_{flex} = 8 \cdot (\frac{s}{a - c} - 0.172) \cdot M_b \tag{2.1}$$

where, s denotes the length of the slab, a is the support length of the slab, c is the dimension of the column and M_b denotes the nominal capacity of the slab using tension reinforcement. Rankin and Long also proposed a formula for calculating the punching shear strength P_{vs} according to Eq. 2.2.

$$P_{vs} = 1.66 \cdot \sqrt{f_c'} \cdot (c + d) \cdot d \cdot (100 \cdot \rho)^{0.25} \tag{2.2}$$

where, d denotes effective depth of the slab and ρ is the flexural reinforcement ratio.

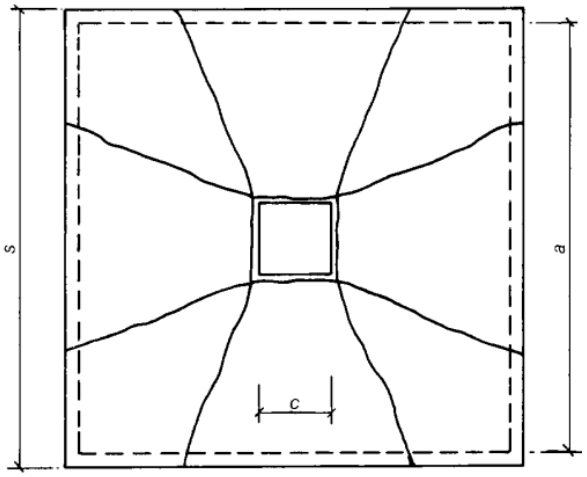

Figure 2.14 Rankin and Long–Yield line pattern for conventional slab-column specimen (1987).

Dilger (2000) and Dechka (2001) presented a shear friction model for calculating the punching shear resistance of a slab. This model can be used in reinforced concrete slabs under concentric loading and for slabs without or/and with shear reinforcement. In this model, there are

two forms; the general and the simplified. The general form can be used only for computer programming calculations and the simplified for hand calculations.

The most recent mechanical punching shear model proposed by Muttoni (2008). The Critical Shear Crack Theory (CSCT) assumes that the punching shear resistance decreases as the rotation of the slab increases. The shear strength of a slab is reduced if a critical shear crack is present and propagates through the slab into the inclined compression strut that carries the shear force to the column. This reduction of the shear strength leads to punching shear failure. The width of the crack is assumed to depend on the product ψd (see Figure 2.15) leading to a failure criterion proposed by Muttoni and Schwartz (1991). After, Muttoni (2003) modified this failure criterion considering that the capacity of the critical shear crack to carry shear forces can be accounted by dividing the nominal crack width ψd by the quantity $(d_{go} + d_g)$, where d_{go} is a reference aggregate size equal to 16 mm and d_g denotes the maximum aggregate size. The modified failure criterion was compared with 99 punching shear tests form the literature and was found to be in good agreement with the test results. The rotation ψ is multiplied with $d/(d_{go} + d_g)$ in order to cancel the effect coming from the slab thickness and aggregate size. Comparison with the ACI punching prediction was also given. ACI seems to be conservative for small values of $\psi d/(d_{go} + d_g)$, while for larger values of $\psi d/(d_{go} + d_g)$ predicts larger punching shear strength compared to the tests and seems to be unsafe. According to Muttoni (2008) that happens because the ACI code is based on tests with small effective depths where the influence of the size effect was not known. Muttoni (2008) derived the load-rotation relation for an isolated slab assuming that the deflected shape of the slab is conical after the critical shear crack. All expressions are given in Subsection 2.5.4. Then, in 2009 Fernandez Ruiz and Muttoni proposed a

model based on the Critical Shear Crack Theory that can be used for slabs with shear reinforcement. All equations are also given in the Subsection 2.5.4.

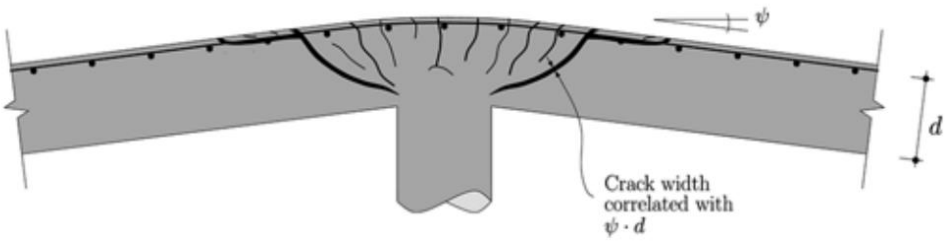

Figure 2.15 Correlation between the critical shear crack opening, thickness and rotation of the slab (taken from Muttoni (2008)).

2.5 Review of punching shear code provisions

The first design provisions for punching shear (1916-1917) were based on the equation presented by Talbot (1913) in order to calculate the shear stresses using the critical perimeter at distance varying from d to d/2 from the column or in general the loaded area. These calculated stresses in order to satisfy the punching shear resistance of the slab should be smaller than the shear strength calculated based on the compressive strength of concrete. It was observed that the shear strength was related to the diagonal tension; however, the first time that the punching shear strength was compared to the percentage of the square root of the compressive strength of concrete was in ACI code in 1963.

The research on punching shear failure in the United States of America started in the 1950s. by Richart (1948), Elstner and Hognestad (1956) and Whitney (1957). In 1961, Moe suggested that the shear strength is proportional to the $\sqrt{f_c'}$ and not to the f_c', showing that the shear failures are influenced primarily by the tensile strength of concrete. The research done by

Moe led to the ACI design provisions. In 1962, the ACI-ASCE Committee 326 specified the critical section to be at distance d/2 from the column's face, based on the Moe's work. In Europe, Kinnunnen and Nylander (1960), Regan (1981) and Regan and Braestrup (1985) proposed empirical equations that were used as the basis of the European punching shear codes. Regan considered that the punching shear strength is influenced by the reinforcement ratio and a size effect factor.

Nowadays, the majority of the current code provisions for punching shear are based on the work done in 1970s and 1980s; with significant influence and contribution in USA by Hawkins (1974), Corley and Hawkins (1974), Langhor et al. (1976) and Dilger and Ghali (1981) and in Europe by Regan (1981) and Regan and Braestrup (1985).

The current design code provisions (ACI 318 11 and EC2 2004) for punching shear are presented In addition, Model Code 2010 and the Critical Shear Crack Theory proposed by Muttoni (2008, 2009) are also presented. The CSA Standard A23.3-04 is not presented in this dissertation because it is based on the ACI code and it shows similar results.

The design codes (ACI 318-11 and EC2), the Model Code (MC 2010) and the Critical shear crack theory (CSCT) adopt an approach involving a critical section, which is at a certain distance from the column perimeter. On the critical perimeter the shear stress should be less than the shear capacity. The critical section in EC2 is located at a distance 2d from the column faces (see Figure 2.16), while in ACI318-1, MC 2010 and CSCT is at 0.5d (see Figure 2.17). The main difference between them is that the ACI318-11 does not account for the flexural reinforcement ratio and size effects for the calculation of shear resistance directly, while the EC2, MC 2010 and CSCT consider the effects. The ACI318 is based on Moe's research (1961), EC2 is based on

Regan's research (1985), CSCT is a theory proposed by Muttoni (2008, 2009) and MC 2010 is based on the CSCT model. Below, the basic equations used by each code and model for calculating the punching shear resistance for slabs without and with shear reinforcement are described in detail.

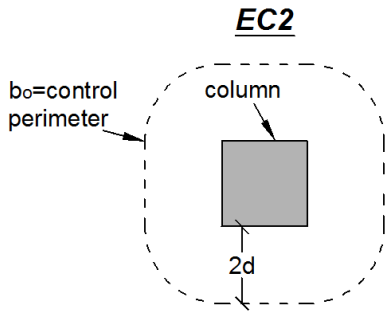

Figure 2.16 Control section according to EC2.

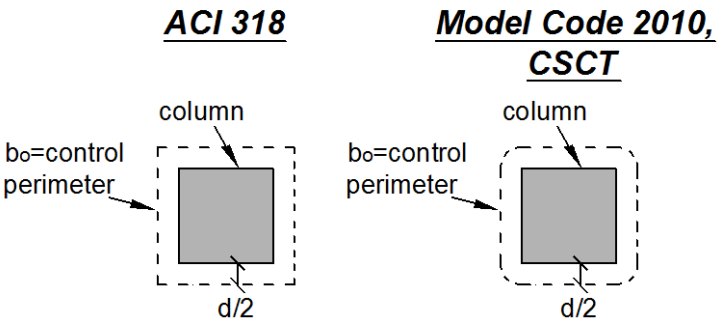

Figure 2.17 Critical section according to ACI, Model Code and CSCT.

2.5.1 ACI 318-11

The factored shear force V_f on the critical section should be more than the factored shear resistance V_n times a shear strength reduction factor $\varphi = 0.75$. Thus, $V_f \leq \varphi V_n = \varphi(V_c + V_R)$,

where V_c is the shear resistance provided by concrete and $V_R$is the shear resistance provided by shear reinforcement.

According to ACI 318-11 code the punching shear resistance of concrete for slabs without shear reinforcement is:

$$V_c = min\begin{cases} 0.33\lambda b_o d\sqrt{f'_c} \\ 0.17\lambda b_o d\sqrt{f'_c}\left(1+\frac{2}{\beta_c}\right) \\ 0.083\lambda b_o d\sqrt{f'_c}\left(2+\frac{\alpha_s d}{b_o}\right) \end{cases} \quad (f'_c\ in\ MPa) \tag{2.3}$$

where, λ is the concrete density factor equal with 1 for a normal-weight concrete, b_o is the critical shear perimeter, d is the effective depth of the slab, f'_c is the compressive strength of concrete, β_c is the ratio of the long to short side of the column and α_s is 40 for interior columns, 30 for edge columns and 20 for corner columns.

The punching shear resistance of slabs with shear reinforcement (shear studs) is calculated according to Eq. (2.4), while the punching shear resistance of slabs with shear reinforcement (stirrups) is calculated according to Eq. (2.5):

$$V_R = 0.5V_c + \frac{A_{vs} f_{yv} d}{s} \leq 0.66 b_o d\sqrt{f'_c}\ (MPa) \tag{2.4}$$

$$V_R = 0.75V_c + \frac{A_{vs} f_{yv} d}{s} \leq 0.5 b_o d\sqrt{f'_c}\ (MPa) \tag{2.5}$$

where, b_o is the critical shear perimeter, d is the effective depth of the slab, f'_c is the compressive strength of concrete, A_{vs} is the cross-sectional area of all legs of shear reinforcement on one peripheral line, f_{yv} is the specified yield strength of the shear

reinforcement and s is the spacing between the perimeters of shear reinforcement. According to ACI Code, the punching shear strength within the shear reinforced area can be calculated by adding the contribution from the shear reinforcement, whereby the contribution of the concrete corresponds to 0.5 times the punching shear strength of the slabs without shear reinforcement for the case of stirrups, while 0.75 times the punching shear strength of the slabs without shear reinforcement for the case of double headed studs.

The calculated punching shear resistance for the shear reinforced slabs is calculated also outside the shear reinforced area according to Eq. (2.6):

$$V_R = 0.17\lambda b_{out} d\sqrt{f'_c}\ (MPa) \tag{2.6}$$

where, b_{out} is control perimeter at distance $d/2$ from the last line of the shear reinforcement.

For slabs under gravity load and unbalanced moment (M_f), the moment in ACI318-11 can be derived from the following equation:

$$v_f = \frac{V_f}{b_o d} + \left[\frac{\gamma_v M_f c}{J_c}\right]_x + \left[\frac{\gamma_v M_f c}{J_c}\right]_y \tag{2.7}$$

where, v_f is the factored shear stress, V_f is the vertical factored shear force, b_o is the control perimeter, d is the effective depth of the slab, J_c is the property of assumed critical section analogous to the polar moment of inertia, $\gamma_v = 1 - \frac{1}{1+\frac{2}{3}\sqrt{\frac{b_1}{b_2}}}$ is the fraction unbalanced moment

transferred by shear eccentricity, where b_1 is the width of the critical section perpendicular to the moment vector and b_2 is the other side length and c is the centroid of the shear perimeter.

2.5.2 EC2 (2004)

According to EC2 (2004) the following checks should be carried out:

a) At the perimeter of the column (or loaded area), where the punching shear stress (v_{Ed}) should less than the maximum punching shear stress $(v_{Rd,max})$.

b) Punching shear reinforcement is not needed if $v_{Ed} < v_{Rd,c}$.

c) If $v_{Ed} > v_{Rd,c}$, punching shear reinforcement is required.

The maximum punching shear stress along the control section is calculated as:

$$v_{Rd,max} = 0.5 v f_{cd} \tag{2.8}$$

where, v is the strength reduction factor for concrete cracked in shear (Eq. 2.9) and f_{cd} is the design compressive strength of concrete (Eq. 2.10).

$$v = 0.6\left(1 - \frac{f_{ck}}{250}\right) \ (MPa) \tag{2.9}$$

$$f_{cd} = \alpha_{cc}\frac{f_{ck}}{\gamma_c} \tag{2.10}$$

where, α_{cc} is a coefficient taking account for long term effects and recommended value is 1. γ_c is the partial safety factor for concrete equal to 1.5.

If the support reaction is eccentric with regard to the control perimeter, the maximum shear stress is taken as:

$$v_{Ed} = \beta \frac{V_{Ed}}{u_i d} \tag{2.11}$$

where, d is the effective depth of the slab, u_i is the length of the considered control perimeter and β is given by:

$$\beta = 1 + k \frac{M_{Ed}}{V_{Ed}} \frac{u_1}{W_1} \tag{2.12}$$

where, u_1 is the length of the basic control perimeter, k is a coefficient based on the ratio between the column's dimensions (for a square column $k = 0.6$) and W_1 corresponds to a distribution of shear and is a function of the basic control perimeter.

For a rectangular column W_1 is given as:

$$W_1 = \frac{c_1^2}{2} + c_1 c_2 + 4 c_2 d + 16 d^2 + 2\pi d c_1 \tag{2.13}$$

where, c_1 is the column dimension parallel to the eccentricity of the load and c_2 is the dimension of the column that is perpendicular to the eccentricity of the load.

For an internal rectangular column where the loading is eccentric to both axes β is taken as:

$$\beta = 1 + 1.8\sqrt{\left(\frac{e_y}{b_z}\right)^2 + \left(\frac{e_z}{b_y}\right)^2} \tag{2.14}$$

where, e_y and e_z are the eccentricities $\frac{M_{Ed}}{V_{Ed}}$ along y and z axes, respectively and b_y and b_z are the dimensions of the control perimeter.

For edge slab-column connections the control perimeter can be considered according to Figure 2.18 as u_{1*}.

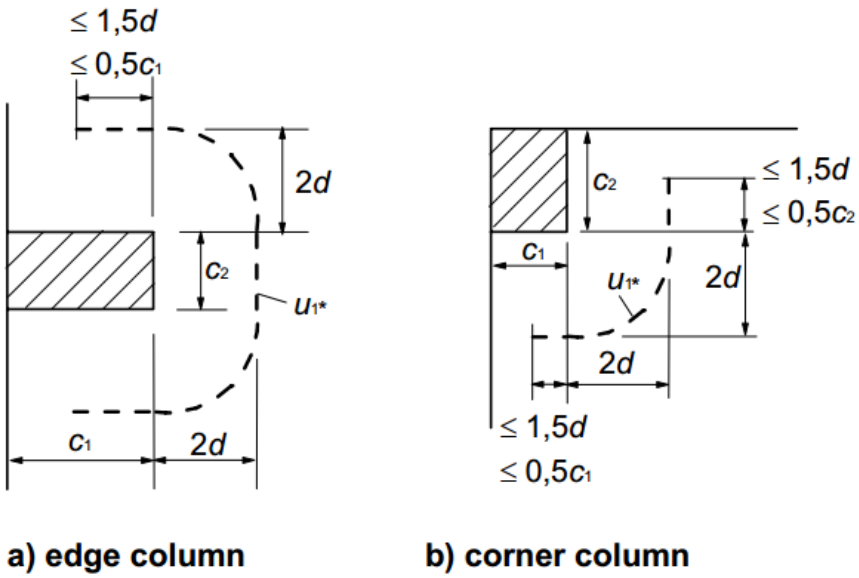

Figure 2.18 Reduced basic control perimeter for edge and corner columns.

If eccentricities exist in both orthogonal directions, β can be determined using the following equation:

$$\beta = \frac{u_1}{u_{1*}} + k\frac{u_1}{W_1}e_{par} \tag{2.15}$$

where, e_{par} is the eccentricity parallel to the slab edge resulting from a moment about an axis perpendicular to the slab edge.

For a rectangular column W_1 is calculating using the following equation:

$$W_1 = \frac{c_2^2}{4} + c_1 c_2 + 4 c_1 d + 8 d^2 + \pi d c_2 \tag{2.16}$$

According to EC2 the punching shear resistance of concrete for slabs without shear reinforcement is defined as:

$$V_{Rd,c} = C_{Rd,c} k b_o d (100 \rho_l f_{ck})^{1/3} \geq V_{min} = 0.035 (k)^{3/2} (f_{ck})^{1/2} \, b_o d \tag{2.17}$$

where, $C_{Rd,c} = 0.18/\gamma_c$, γ_c is the partial safety factor for concrete equal to 1.5, b_o is the control perimeter at distance $2d$ from the column, d is the effective depth of the slab, ρ_l is the flexural reinforcement ratio limited to the maximum value of 0.02, f_{ck} is the characteristic compressive strength of concrete and k is the size effect factor that is defined as:

$$k = 1 + \sqrt{\frac{200}{d}} \leq 2 \quad (d \; in \; mm) \tag{2.18}$$

The punching shear resistance for slabs with vertical shear reinforcement is defined as:

$$V_{Rd} = 0.75 V_{Rd,c} + 1.5 (d/s) A_{vs} f_{ywd,ef} \tag{2.19}$$

where, A_{vs} is the area of one row of the vertical shear reinforcement, s is the spacing between the perimeters of shear reinforcement and $f_{ywd,ef}$ is the effective design strength of the shear reinforcement that is defined according to Eq. (2.20). The concrete resistance in Eq. (2.17) is taken as 75% of the design strength of a slab without shear reinforcement. That reduction

accounts for the activation of the shear reinforcement and also shows that the strength of concrete reduces due to the vertical movement of the punching cone after the yielding of the shear reinforcement.

$$f_{ywd,ef} = (250 + 0.25d) \leq f_{ywd} \quad (MPa) \tag{2.20}$$

where, f_{ywd} is the yield strength of the shear reinforcement.

Next to the column the punching shear resistance is limited to a maximum of:

$$v_{Ed} = \frac{\beta V_{Ed}}{u_o d} \leq v_{Rd,max} \tag{2.21}$$

where, u_o is length of the column periphery for interior column. For edge column $u_o = c_2 + 3d \leq c_2 + 2c_1$ and for corner column $u_o = 3d \leq c_1 + c_2$.

The control perimeter at which shear reinforcement is not required u_{out} is calculated as:

$$u_{out,ef} = \frac{\beta V_{Ed}}{v_{Rd,c} d} \tag{2.22}$$

The outermost perimeter of shear reinforcement should be placed at a distance not greater than kd within the $u_{out,ef}$. Recommended value for k is 1.5.

2.5.3 Model Code (MC 2010)

The Model Code (MC 2010) is based on the Critical Shear Crack Theory that is described later in Subsection 2.5.4, where the punching shear strength depends on the rotation of the slab. Model Code 2010 adopts different levels of approximation. Level I can be used for the

conception. Level II is recommended for the design of a new structure. Level III may be used for special cases or in general for an analysis of an existing structure and finally, Level IV is recommended for special cases and for an accurate assessment of an existing structure. Herein, the Level III of approximation is described because that is used for the calculation of the punching shear strength of the tested slabs in the next chapters.

For slabs without shear reinforcement the punching shear resistance is equal to Eq. (2.23):

$$V_{R,c} = k_{\psi}\sqrt{f_{ck}}b_o d \tag{2.23}$$

where, b_o is the control perimeter at distance $0.5d$ from column's face, d is the effective depth of the slab, f_{ck} is the characteristic compressive strength of concrete and k_{ψ} is a parameter that is defined as:

$$k_{\psi} = \frac{1}{1.5 + 0.9\,\psi\,d\,k_{dg}} \leq 0.6 \tag{2.24}$$

where, ψ is the rotation of the slab and k_{dg} is a factor depending on the aggregate size (d_g) as:

$$k_{dg} = \frac{32}{16 + d_g} \geq 0.75 \tag{2.25}$$

For the Level of approximation III, the rotation of the slab is calculated according to Eq. (2.26) as:

$$\psi = 1.2\frac{r_s}{d}\frac{f_{ys}}{E_s}\left(\frac{m_S}{m_R}\right)^{3/2} if\ \ m_S \leq m_R \tag{2.26}$$

where, r_s is the distance between the axis of the column and the contraflexure, f_{ys} is the yield strength of the tensile flexural reinforcement, E_s is the modulus of elasticity of the tensile flexural reinforcement, m_S is the average moment per unit length in the support strip and m_R is the flexural strength.

The punching shear strength of slabs with shear reinforcement is defined according to Eq. (2.27) as:

$$V_R = V_{R,c} + V_s \tag{2.27}$$

The punching shear resistance provided by the shear reinforcement (V_s) in Eq. (2.27) can be expressed according to Eq. (2.28) as:

$$V_s = \frac{E_s \psi}{6} A_{sw} \leq f_{ywd}\ A_{sw} \tag{2.28}$$

where, A_{sw} is the amount of one row of shear reinforcement and f_{ywd} is the yield strength of the shear reinforcement.

The punching shear resistance outside the shear reinforced area is defined as:

$$V_{R,out} = k_\psi \sqrt{f_{ck}} b_{out} d \tag{2.29}$$

where, b_{out} is the control perimeter at distance $d/2$ from the outermost perimeter of the shear reinforcement.

Model Code (MC 2010) calculates the punching shear resistance due to failure of the concrete strut by increasing the punching shear strength of slabs without shear reinforcement by a factor, (k_{sys}).

$$V_R = k_{sys} k_\psi \sqrt{f_{ck}} b_o d \leq \sqrt{f_{ck}} b_o d \tag{2.30}$$

The factor k_{sys} corresponds to 2.4 for slabs with stirrups and to 2.8 for slabs with double-headed studs.

2.5.4 Critical Shear Crack Theory (CSCT 2008, 2009)

The punching shear strength of a slab without shear reinforcement is defined according to Eq. (2.31) as:

$$V_{R,c} = \frac{3}{4} \frac{b_o d \sqrt{f'_c}}{1 + 15 \frac{\psi d}{d_{g0} + d_g}} \tag{2.31}$$

where, b_o is the critical shear perimeter, d is the effective depth of the slab, f'_c is the compressive strength of concrete, d_{g0} is a reference aggregate size equal to 16mm, d_g is the maximum aggregate size and ψ is the rotation of the slab expressed according to Eq. (2.32).

$$\psi = 1.5 \frac{r_s}{d} \frac{f_{ys}}{E_s} \left(\frac{V_E}{V_{flex}} \right)^{3/2} \quad if\ V_E \leq V_{flex} \tag{2.32}$$

where, r_s is the distance between the axis of the column and the contra flexure, f_{ys} is the yield strength of the tensile flexural reinforcement, E_s is the modulus of elasticity of the tensile flexural reinforcement, V_E is the applied shear force and V_{flex} is the resistance to flexure that can be defined according to yield line theory by Rankin and Long (1987).

The punching shear strength of a slab with shear reinforcement is defined according to Eq. (2.33) as:

$$V_R = V_{R,c} + V_s \tag{2.33}$$

The punching shear resistance provided by the shear reinforcement (V_s) in Eq. (2.33) can be expressed according to Eq. (2.34) as:

$$V_s = \frac{E_s \psi}{6} A_{sw} \leq f_{ywd}\ A_{sw} \tag{2.34}$$

where, A_{sw} is the amount of one row of shear reinforcement and f_{ywd} is the yield strength of shear reinforcement.

The punching shear resistance outside the shear reinforced area is defined as:

$$V_{R,out} = \frac{3}{4} \frac{b_{out} d \sqrt{f'_c}}{1 + 15 \frac{\psi d}{d_{g0} + d_g}} \tag{2.35}$$

where, b_{out} is the control perimeter at distance $d/2$ from the outermost perimeter of the shear reinforcement.

CSCT calculates the punching shear resistance when the concrete strut crushes. According to this failure criterion, the compressive strength of the concrete depends on the transverse strains, and these strains depend on the rotation of the slab. Therefore, the failure criterion of crushing of concrete strut is a function that multiplies the punching shear strength of the slabs without shear reinforcement by a factor λ that depends on the different punching shear reinforcement systems that can be used. For studs or in general for systems with perfect anchorage conditions the factor λ can be assumed equal to 3. For other systems, such as stirrups where the reinforcement is developed by bond, the factor λ can be assumed equal to 2.5.

$$V_R = \lambda \frac{3}{4} \frac{b_o d \sqrt{f'_c}}{1 + 15 \frac{\psi d}{d_{g0} + d_g}} \tag{2.36}$$

2.6 Review on finite element methods/analyses of punching shear

Nonlinear finite element analyses of reinforced concrete slabs can provide an insight into the slabs behaviour; predict the possible modes of failure; support the experimental conclusions; and extend these conclusions in cases where the test measurements are not known. FEA of reinforced concrete slabs have been performed by many researchers (Menétrey (1994), Hallgren (1996), Ožbolt et al. (2000), Polak (2005), Guan and Polak (2007), Negele at al. (2007), Eder et al. (2010), Mamede et al. (2013)); with the recent publication by Genikomsou and Polak (2015). Menétrey (1994) and Hallgren (1996) studied reinforced concrete slabs with two dimensional models using rotationally symmetric elements. The results obtained from Menétrey (1994) and Hallgren (1996) show that the rotational symmetric continuum elements can simulate the punching shear failure. However, the 2D elements cannot be considered for applications where orthogonal reinforcement or unsymmetrical punching should be modelled. Therefore, 3D elements became the state-of-the-art for recent research. Ožbolt et al. (2000) examined and analyzed concrete slabs using three-dimensional systems based on the micro-plane material model and a smeared crack approach. The mesh sensitivity was avoided with the improved crack band approach or the nonlocal integral approach. Nevertheless, the analysis of larger structures using three-dimensional elements is difficult. Shell elements according to Polak (2005) can be reasonable for large structures. However, FEA of shear reinforced concrete slabs are limited due to the complexity in modelling the punching shear reinforcement. Polak (2005) used shell elements with layered integration where the reinforcement was modeled as property of the concrete by modifying the stiffness in the reinforcement's direction. Also, Guan and Polak (2007) used layered finite element methods to investigate the influence of shear stud reinforcement of flat slabs. Negele et al. (2007) used 3D nonlinear finite element analyses with a

micro-plane material model using the smeared crack approach together with the crack band method. The simulations were able to predict the ultimate load for the slabs tested by Adetifa and Polak (2005), but in terms of the ultimate deflection the predictions were not able to illustrate the influence of the amount of the shear bolts. Eder et al. (2010) used 3D finite elements for the simulation of the concrete and shell elements embedded into the solid elements for the simulation of the shear heads.

2.7 Summary and Conclusions

Chapter 2 presents a brief literature review that starts by discussing the development of the flat slabs in construction. Going back to the beginning of the 20th century, flat slabs started to be used in many multistory buildings due to their benefits. However, flat slabs are vulnerable in punching shear and thus the appropriate testing started by examining the punching shear failure. Many researchers tested and studied reinforced concrete flat slabs without shear reinforcement and then continued their research on shear reinforced specimens. Different types of shear reinforcement were used and all observations led to the code design provisions for punching shear. However, the code provisions were also influenced from many developed mechanical models.

From the short discussion on the testing background presented herein, comes out that even though the experiments are many, sometimes they cannot easily be grouped and analyzed. The design formulas differ as they are based on different research. The finite element formulations can be used in order to supplement the punching shear tests and provide more information regarding the punching shear failure mechanism. With that way, the existing testing database can be used as a tool to calibrate the finite element models. Then, based on the

calibrated models many and different analyses and parametric investigation can be performed. Chapter 3 that follows presents the constitutive modelling and behaviour of concrete.

Chapter 3

Constitutive modelling of concrete

3.1 Introduction

Concrete is an isotropic heterogeneous composite material made by cement, water and aggregates, however, macroscopically, it is considered as homogeneous. The compressive strength of concrete is much higher than its tensile strength and its complex behaviour requires the development of appropriate constitutive models for its simulation and analysis. All of the proposed constitutive models, e.g. (Willam and Warnke 1975, Simo and Ju 1987, Mazars and Pijaudier-Cabot 1989, Yazdani and Schreyer 1990, Feenstra and de Borst 1995, Lee and Fenves 1998, Imran and Pantazopoulou 2001, Grassl et al. 2002, Addessi et al. 2002, Jirasek et al. 2004, Salari et al. 2004); may show limitations and they are not suitable for all types of analysis. In continuum mechanics, the macroscopic response of concrete can be characterized through its evolution law of the failure envelope in multi-axial loading. A brief description on the mechanical behaviour of concrete and then an overview on its non-linear modelling with respect on cracking models, plasticity theory, continuum damage mechanics and damage coupled with plasticity, are presented in this chapter.

3.2 Mechanical behaviour of concrete

The mechanical behaviour of concrete is nonlinear in both tension and compression. In uniaxial compression, concrete shows a linear elastic behaviour up to 30% of the maximum

compressive stress f_c' and beyond that bond cracks start to be formed. Then, from $0.3f_c'$ to $0.75f_c'$, micro-cracks open and join the bond cracks creating continuous cracks. After the stress level of $0.75f_c'$, strain softening occurs depending on the size of the tested specimen and the strength of concrete. The stress-strain curve of long specimens compared to short specimens is sharper, because of the localized deformation in some regions during the unloading. During the strain softening, mortar cracks join the bond cracks and form a fracture zone creating internal damage. At the end, major cracks appear parallel to the direction of loading.

The initial modulus of elasticity of concrete depends on its compressive strength and actually it is related to the square root of the compressive stress. According to Park and Paulay (1975), the modulus of elasticity of concrete can be taken as: $E_c = w^{1.5}33\sqrt{f_c'}$. w is the density of concrete in pounds per cubic foot and f_c' is the compressive cylinder strength in psi. For normal weight concrete, the modulus of elasticity can be considered as: $E_c = 57000\sqrt{f_c'}\ (psi)$ or $E_c = 4730\sqrt{f_c'}\ (N/mm^2)$.

Poisson's ratio, ν, for concrete denotes the ratio of the transverse strain to the strain in the loading direction. That ratio for concrete ranges between 0.15 to 0.20. However, according Park and Paulay (1975) values between 0.10 to 0.30 have been defined. According to Chen (1982), during uniaxial loading the Poisson's ratio is constant until around 80 percent of the f_c' and then it starts to increase. During the crushing phase of concrete, the Poisson's ratio becomes larger than 0.5. There is no information regarding the dependence of the Poisson's ratio with the properties of concrete, however, the Poisson's ratio is considered lower for high strength concrete.

In uniaxial tension, concrete shows a linear response up to a stress about 60% to 80% of its tensile stress (f_t'), where micro-cracks appear making the concrete to be softer and highly non-linear. After the tensile stress of f_t', the strength, due to the quasi-brittle nature of concrete, does suddenly drop to zero. Under tensile applied loading, the direction of the crack propagation is transverse to the stress direction. In the weakest regions of the concrete member, damage initiates during unloading of the other parts. Due to the aggregate interlock, stress is transferred in the fracture zone across the crack zone of the crack opening direction, until a complete crack is formed which cannot transfer any stress and finally tensile failure happens. The concrete during this process undergoes tension softening. The strain of the specimen increases because of the effect of the fracture zone and decreases in the rest of the specimen that is under elastic unloading.

The ratio between the uniaxial tensile and compressive strength ranges from 0.05 to 0.1. Under uniaxial tension the modulus of elasticity becomes higher, however, the Poisson's ratio is lower. The direct tensile strength of concrete, f_t', is difficult to be obtained from tests, however, it is normally considered as: $f_t' = 4\sqrt{f_c'}\ \left({}^{lb}/_{in^2}\right)$. The modulus of rupture f_r' and/or the splitting tensile strength are often used to estimate the tensile strength of concrete. The modulus of rupture is taken as: $f_r' = 7.5\sqrt{f_c'}\ \left({}^{lb}/_{in^2}\right)$. The split-cylinder tensile strength is around 50 to 75 % lower than the modulus of rupture.

Biaxial stresses appear when the principal stresses act only in two in-plane directions and the third principal stress is zero. The biaxial behaviour of concrete was studied, among others, by Kupfer et al. (1969). They observed that the biaxial strength envelope can be found through three different loading conditions; biaxial tension, biaxial compression and tension-compression (see

Figure 3.1). They concluded that when the concrete is subjected to biaxial compression its strength may be around 27% higher than its uniaxial strength. When equal-biaxial compressive stresses are applied, its strength increases around 16%. Biaxial tension shows almost the same strength to the uniaxial tensile strength. When the concrete is subjected to combined tension and compression, both tensile and compressive strength at failure are reduced. Under biaxial stresses the ductility of concrete has different values depending on the loading conditions (compressive or tensile). For uniaxial and biaxial compression based on the tests done by Kupfer et al. (1969) it was found that the average maximum compressive strain is about 0.003 and the average maximum tensile strain ranges between 0.002 to 0.004. The tensile ductility was observed greater in biaxial compression compared to this one under uniaxial compression. During compression-tension, both compressive and tensile strains are decreased as the tensile stress increases.

During the loading and as the failure is approached, the volume of concrete increases as the compressive loading increases (Figure 3.2). That inelastic increase of the volume is called dilatancy and it is a characteristic of the progressive growth of the major cracks in concrete. Figure 3.2 shows the volumetric strain under biaxial compression, where the strain decreases up to 0.75 to 0.9 of the failure stresses and after that, the stresses are increased.

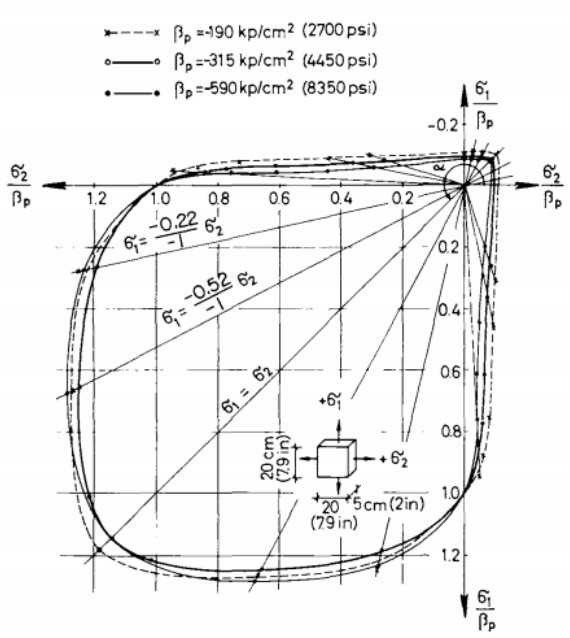

Figure 3.1 Biaxial strength envelope of concrete (Kupfer et al. 1969).

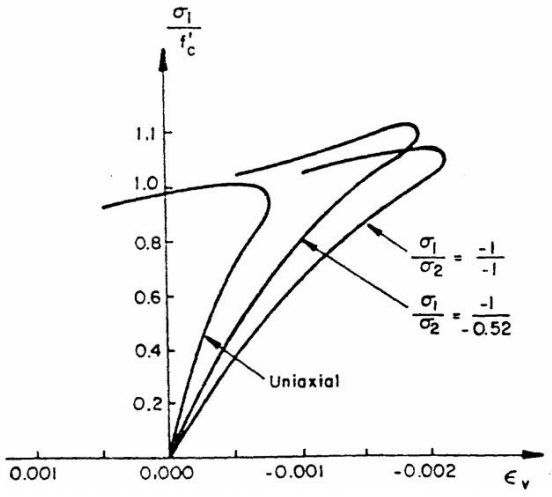

Figure 3.2 Volumetric strain under biaxial compression (Kupfer et a al., 1969) (taken from Chen and Han, 1988).

The strength of concrete is increased under tri-axial loading. Figure 3.3 shows that the lateral confining pressure has a significant effect on the deformation of the tested cylinders. As it

is obvious in Figure 3.3, an increase in the lateral pressure increases significant the ductility and the strength. That effect is due to the confinement of the concrete that comes from the lateral pressure that reduces the tedency for internal cracks and volume increase before the failure.

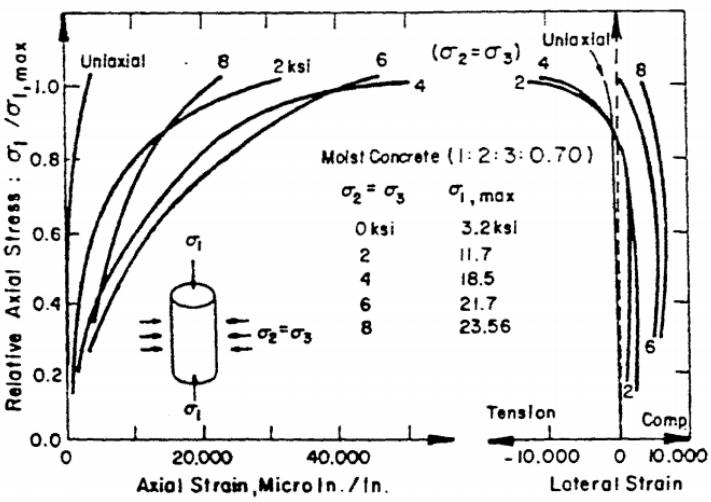

Figure 3.3 Stress-strain curves under tri-axial compression (Palaniswamy and Shah, 1974) (taken from Chen and Han, 1988).

The tri-axial behaviour of concrete is characterized by the strength envelope of the concrete and its evolution that is a function of the three principal stresses. Figure 3.4 shows the elastic limit surface and the failure surface where the last illustrates the maximum strength of the concrete. When the hydrostatic compressive stresses along the $\sigma_1 = \sigma_2 = \sigma_3$ axis (see Figure 3.4) increase, the deviatoric sections, that are perpendicular to the axis $\sigma_1 = \sigma_2 = \sigma_3$, of the failure surface are almost circular. That shows that the failure at that region is independent of the third stress invariant. When the hydrostatic pressure is smaller, the deviatoric sections become non-circular.

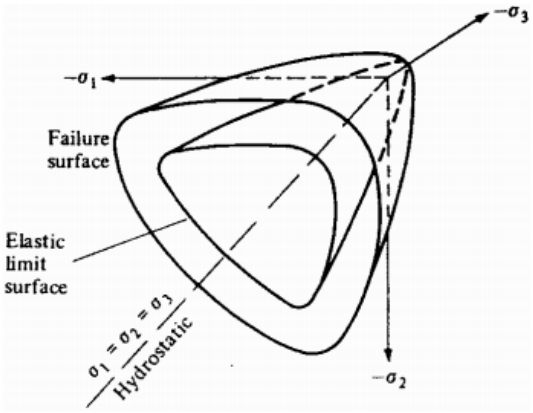

Figure 3.4 Failure surface of concrete in three-dimensional stress space (Chen, 1982).

3.3 Cracking models of concrete

When concrete fails in tension it is characterized by a progressive development of cracking. This process is considered as brittle because the tensile strength goes abruptly to zero after the cracking has been formed. However, when reinforcement exists, it bridges the cracks and the strength mechanism becomes more complex. Cracked concrete can be modelled by a linear elastic fracture approach. The commonly used fracture criteria are: the maximum principal stress criterion and the maximum principal strain criterion. When the stress or strain exceeds a specified limit, then cracking occurs normal to the direction of the principal stresses or strains, and then the cracking direction is set for all following applied load conditions. Once the cracking is formed, the stiffness in that direction is reduced due to the fact that the tensile stresses cannot be sustained across the cracks. Nevertheless, when the material is not normal to the cracking direction is still able to retain stresses. Further loading leads to more cracking that also appears perpendicular to the initial crack. While cracking can be open to the normal direction, it can be also possible that the opposite faces subjected to parallel motion will interlock. That depends on the grain of the cracked surface and the constrained force that prevent the crack surfaces to

move. In normal weight concrete the cracked surfaces are rough, however, in present of reinforcement, the surfaces are able to transfer shear forces by the significant phenomenon that is called aggregate interlock.

In order to model the cracking of concrete in finite element analysis methods, there are two different models: the discrete crack approach and the smeared crack approach.

Discrete crack approach

This approach is based on the spread of the discontinuities in concrete with two different ways: the inter-element and the intra-element. In the inter-element crack way, as it is shown in Figure 3.5a, the cracks are modeled by a separation on the element edges. However, this approach has two disadvantages; first, the crack path is restricted because it follows the predefined boundaries of inter-elements and second, separated nodes are created when the cracking opens, adding extra degrees of freedom that increase the computation time and maybe decrease the efficiency of the solution. In the intra-element crack approach (see Figure 3.5b) the cracks propagate through the elements. Two different types of the intra-element approach can be found: the embedded discontinuous model that is used for strain localization problems and the partition-of-unity concept which adds degrees of freedom in the nodes in order to show the displacement that shows up beyond the cracks. The discrete crack approach is mostly used in structures where the localization of cracking is significant but in other cases the smeared crack approach is more capable.

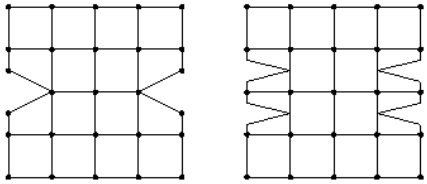

a) b)

Figure 3.5 Discrete crack model: a) Inter-element crack approach, b) Intra-element crack approach.

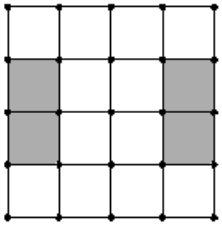

Figure 3.6 Smeared crack model.

Smeared crack approach

The smeared crack method assumes that the cracking is smeared (see Figure 3.6), by reducing the concrete stiffness in the direction of the principal stresses. The already cracked concrete, in the smeared crack approach, is assumed to remain continuum. After the cracking, the concrete becomes orthotropic or transversely isotropic (Chen, 1982). The main benefit of this approach is that when the cracks are developed and then propagated, the already meshed structure does not need a new mesh. However, the disadvantage of the smeared crack model is that localizes the cracks into a single row of elements, leading to mesh sensitive results and in some cases not proper results. In the smeared crack approach, the cracking propagates in alignment with the mesh direction and thus three approaches are used depending on the crack

planes. The fixed crack model assumes that the cracking is fixed during the loading and propagates normal to the principal stresses. In the rotating crack model the cracking propagates also normal to the principal stresses, but the direction of the cracks rotates if the principal stresses change direction during the loading. Finally, the multi-directional fixed crack model assumes again that the cracking develop fixed and normal to the principal stresses. However, new developed cracks can propagate at different directions.

3.4 Interaction between concrete and reinforcement – Tension stiffening

The stress-strain curve for steel appears a linear elastic region up to its yield. Then, a yield plateau is observed up to the strain hardening strain. Afterwards, a strain-hardening region occurs until its ultimate strain and following its fracture strain. The ultimate stress of steel is approximately 1.55 times its yield strength (Chen, 1982). The stress-strain behaviour for steel in tension and compression are assumed identical. In the design of reinforced concrete structures, the reinforcement is considered as one-dimensional and for that reason no multi-axial complexities in its constitutive behaviour are considered. Three different idealizations for the stress-strain curve of reinforcement are considered: a) the elastic perfect plastic, b) the tri-linear and c) the complete curve.

The material incompatibility between concrete and reinforcement due to their different behaviours leads to: a bond failure, sliding of the steel bars, local deformations and cracking. When large shear forces are applied in the structure (e.g. supports at a beam), sliding of the rebar occurs and the reinforcement is pulled out. This pullout effect can be modeled by using spring elements that simulate the contact between concrete and reinforcement. When both concrete and reinforcement tension forces are applied, then large cracks appear. Bond failure and opening of

the cracks happen together, and the shear forces at the contact surface create tensile stresses in concrete. This creates higher stiffness of the reinforced concrete than the steel alone and it is called tension stiffening. The tension stiffening effect was, first, introduced by Scanlon (1971) and it was considered indirectly by assuming the loss of the tension in concrete to happen gradually by a descending branch of the concrete stress-strain curve. One other way to consider the tension stiffening effect can be by increasing the stiffness and stress of the reinforcement. This additional stress in reinforcement at the same strain shows the total tensile force carried by reinforcement and concrete between the potential cracks. However, the dowel effect that takes place when the reinforcement bars act as dowels after the tensile cracking, can be considered in the same way as the aggregate interlock effect by using the shear stiffness and stresses of the cracked concrete.

3.5 Plasticity of concrete

The uniaxial stress-strain curves for concrete in tension and compression are presented in Figure 3.7.

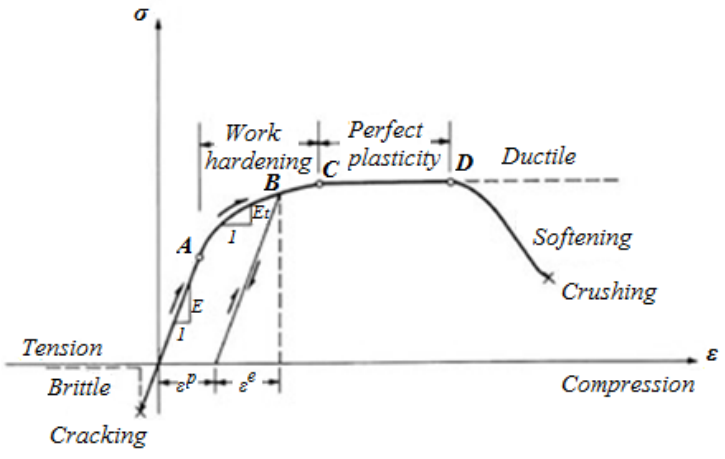

Figure 3.7 Uniaxial stress-strain curve of concrete (Chen, 1982).

The concrete in tension is linear elastic until its failure and no plastic strains appear. In compression, the concrete has linear behaviour until point A. After that point, the concrete shows internal micro-cracks until the end of the perfect plastic region CD at point D. Region AC shows the behaviour of hardening of concrete and region CD corresponds to the elastic perfect plastic concrete. The total strain ε can be considered as the summation of the elastic strain ε^e and the permanent plastic strain ε^p. When the permanent (plastic) strain under constant stress appears, the concrete can be considered as perfect plastic. After the initial yield stress is reached, the stress-strain curve rises although the slope becomes less, until it falls and failure happens. With that way the stress is further increased as the strain increases and the material is able to withstand more stress after the plastic deformation happens. This is known as strain hardening or work hardening. After the failure the slope of the stress-strain curve becomes negative, such behaviour is called strain softening. In the inelastic behaviour of reinforced concrete structures, the steel in both tension and compression can be considered as an elastic perfect plastic material and the concrete as an elastic perfect plastic material in compression and as an elastic brittle material in tension.

Over the previous years, different constitutive models for concrete have been proposed. All macro-mechanical constitutive models should represent mathematically the macroscopic stress-strain behaviour of concrete under different loading conditions; microscopic behaviour is not considered explicity in such modelling. The plasticity modelling approach belongs in this category and its origin starts with research done for the behaviour of metals. A plasticity model is based on three conditions: 1) the definition of the initial yield surface, which defines the level at which plastic deformation starts; 2) the definition of the hardening rule, which shows the changes of the loading surface; and 3) the definition of the flow rule, which together with the

plastic potential function shows the plastic stress-strain relationship of concrete. In general, a constitutive model requires a detailed description of the concrete's behaviour, including the pre-failure (hardening) and post-failure (softening).

The initial isotropic behaviour of concrete has been accepted and considered in several experiments, indicating that concrete has a consistent failure surface in the three-dimensional principal stress space (Chen, 1982). The shapes of the failure surface in the meridian and deviatoric planes are shown in Figure 3.8. The deviatoric sections of the failure surface have different shape and size, depending on the hydrostatic pressure. The meridians ρ_t, ρ_s, ρ_c correspond to the values of the angle θ of 0°, 30° and 60°, respectively (see Figure 3.8).

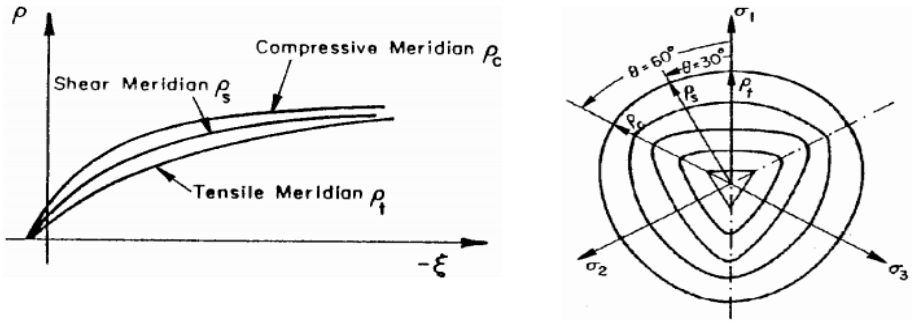

Figure 3.8 Failure surface in the meridian and deviatoric planes (Chen and Han, 1988).

The failure surface based on the three coordinates can be calculated according to Eq. 3.1. Following, Eq. 3.2 to 3.4 provide the relationship between the coordinates and the stress invariants (I_1, J_2, J_3).

$$f(\xi, \rho, \theta) = 0 \tag{3.1}$$

$$\xi = \frac{I_1}{\sqrt{3}} \text{ and } I_1 = \delta_{ij}\sigma_{ij} = \sigma_{11}+\sigma_{22} + \sigma_{33} \tag{3.2}$$

$$\rho = \sqrt{2J_2} \text{ and } J_2 = \frac{1}{2}\sigma'_{ij}\sigma'_{ij} \text{ and } \sigma'_{ij} = \sigma_{ij} - \frac{1}{3}\delta_{ij}\sigma_{kk} \tag{3.3}$$

$$\cos 3\theta = \frac{3\sqrt{3}}{2}\frac{J_3}{J_3^{3/2}} \text{ and } J_3 = \frac{1}{3}\sigma'_{ij}\sigma'_{jk}\sigma'_{ki} \tag{3.4}$$

Some of the most popular concrete models are presented in Figure 3.9. All these models are categorized with the number of the material parameters found in their expressions. The one-parameter models, among them, the von Mises, are mostly used for metals but also they were used in analyzing concrete under compressive loadings by the early attempts of using finite element methods. These models have pressure-independent yield surface and in order to account for the tensile capacity, their surface is increased by the maximum principal stress surface or by the tension cut-off surface. Among the two-parameter models (pressure dependent); the Drucker-Prager is mostly used for soils, while the Mohr-Coulomb model for concrete.

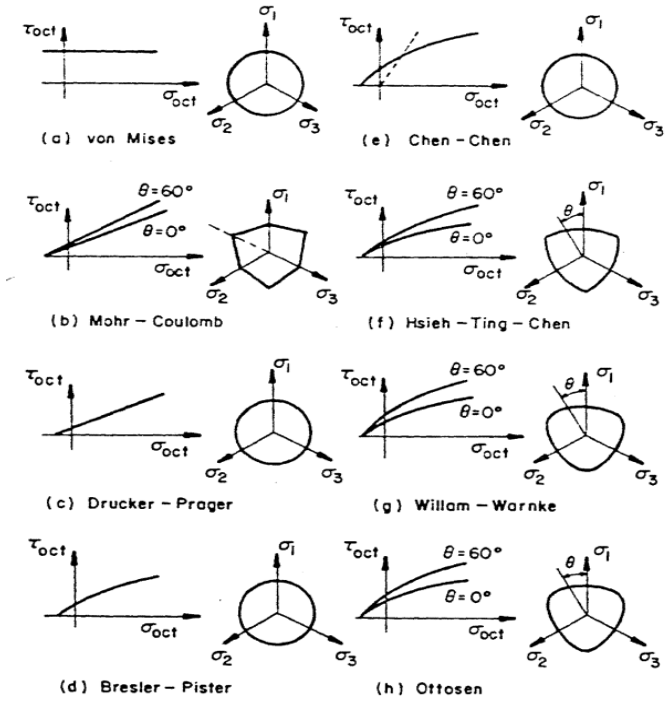

Figure 3.9 Failure models (Chen and Han, 1988).

The hardening rule, in a plasticity model, defines the motion of the yield surface during the plastic loading. If the yield function depends on the loading through the hardening variable k, and it can only expand or shrink in the stress space, without translation or rotation; it is called isotropic hardening. As previously mentioned the shape of the yield surface at any given loading condition can be determined by the hardening rule. The connection between the yield surface and the stress-strain relationship is defined by a flow rule. Concrete can exhibit a significant volume change when is subjected to inelastic loads. This change in volume, usually called as dilatancy, is caused by the plastic deformation and can be reproduced by using a proper plastic potential function, G. When the plastic potential function coincides with the yield function, the plastic flow develops normal to the yield surface and this is called associated flow rule, because the plastic flow is associated with the yield function. However, there is also the non-associated flow rule, where two separate functions are adopted for the plastic flow rule and the yield surface, and these two functions do not coincide. In such flow rule, the plastic flow develops along the normal to the plastic flow potential and not to the yield surface. Figure 3.10 illustrates the non-uniform hardening plasticity model proposed by Han and Chen (1988) in the hydrostatic plane.

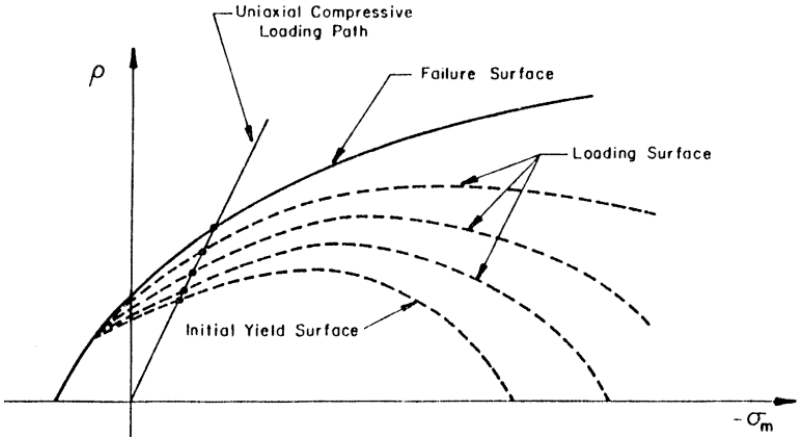

Figure 3.10 A non-uniform hardening plasticity model (Chen and Han, 1988).

The strain-softening plastic behaviour of a material according to Chen and Han, 1988, can be described with three ways as it is illustrated in Figure 3.11. The elastic-plastic behaviour happens when the slopes of the unloading and reloading do not change with the plastic deformation (Figure 3.11a). However, the elastic-plastic behaviour does not describe the behaviour of concrete. Due to cracking and fracturing the stiffness of concrete decreases as the strain increases. The progressively fractured behaviour (Figure 3.11b) describes a perfect elastic material. During the unloading the material returns to its initial stress-strain state without permanent deformation. The stiffness degradation that occurs due to the micro-cracking cannot be explained using the plasticity theory. Therefore, the fracture theory was developed further to the recent damage theory that is described in the next section. Finally, the plastic fracturing behaviour (Figure 3.11c) can describe the concrete that exhibits both plastic deformation and stiffness degradation. This behaviour, nowadays, is called coupled damage plasticity behaviour and it is also discussed later.

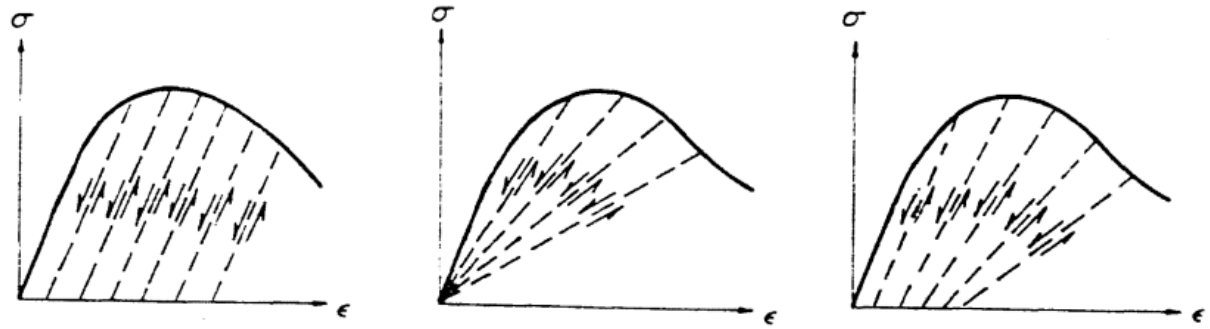

a) b) c)

Figure 3.11 Typical material behaviours for strain softening: a) elasto-plastic, b) progressively fracturing, c) plastic-fracturing (Chen and Han, 1988).

3.6 Damage mechanics in concrete

All solid materials can appear surface and volume discontinuities (micro-cracks). In engineering, this phenomenon is called damage. Continuum damage mechanics is a constitutive theory that considers the damage macroscopically as a variable that affects the stiffness degradation of the material. The pioneer in continuum damage mechanics in creep rupture was Kachanov (Lemaite, 1992).

Continuum mechanics considers the "Representative Volume Element" which represents averages of a certain volume where the stress-strain values should be determined as mean quantities over this volume element. Considering the Representative Volume Element (RVE) oriented by a plane defined by its normal $\vec{n}$, along the direction $\vec{n}$, the damage value D is defined as:

$$D = \frac{S_D}{S} \tag{3.5}$$

where, S is the area of the intersection of the plane with the RVE and S_D is the effective area of intersections of all microcracks in S (Figure 3.12). The value of the damage parameter D ranges between 0 (undamaged) to 1 (fully damaged). When anisotropic damage is considered, the damage of the RVE depends on the direction $\vec{n}$.

Damage mechanics describes the deterioration of the material microscopically by means at the macroscopic level. If the micro-cracks are uniformly distributed over the RVE, it can be assumed that the damage is isotropic and does not depend on the direction of $\vec{n}$. That is the

simplest version where the damaged stiffness is assumed as a scalar multiplied with the initial elastic stiffness.

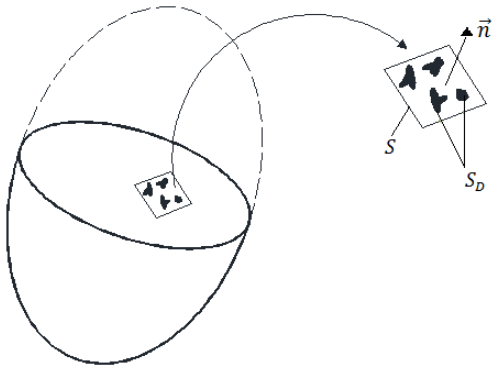

Figure 3.12 Definition of damage.

In order to introduce the damage mechanics concepts, we can consider the uniaxial stress state. In uniaxial tension with scalar damage variable, the cross sectional area is reduced $(S - S_D)$ and the nominal stress (σ) is replaced by the effective stress $(\bar{\sigma})$ according to Eq. (3.6):

$$\bar{\sigma} = \frac{F}{S - S_D} = \frac{\sigma S}{S - S_D} = \frac{\sigma}{1 - \frac{S_D}{S}} = \frac{\sigma}{1 - D} \tag{3.6}$$

During the unloading from tension to compression the effective cross sectional area becomes larger than $(S - S_D)$, because some micro-cracks close. In such a case that all micro-cracks close, the stress and the effective stress are equal. This should be considered in the constitutive modelling of concrete. Although there are many ways to show the damage, in the microscopic constitutive modelling, the physical interpretation of the damage variables sometimes becomes complicated. However, the definition of the damage variable D related to

the effective stress-strain relationship is the most widely adopted way in constitutive modelling in literature.

Continuum damage mechanics can be used in constitutive modelling for elements subjected only to monotonic loading, as it can reproduce the softening response without capturing any permanent deformation. The damage theory employed in any constitutive model is considered with a stress-strain relationship together with a damage variable in order to describe the material deterioration, with a damage criterion and sometimes with a damage evolution law. This damage progress is adopted in the damaged-based models and it can be different in each continuum damage mechanics model.

Due to the different responses of concrete in tension and compression, the damage in the constitutive modelling, can be adopted and used in two different ways where separate damage variables in tension and compression are used in order to simulate the stiffness degradation. The first approach considers different damage criteria for tension and compression (Comi 2001, Comi and Perego 2001) and the second that is based on the decomposition of the stresses and strains into positive and negative parts (Ladeveze 1983, Ortiz 1985, Simo and Ju 1987, Mazars and Pijaudier-Cabot 1989), considers two different loading surfaces. However, it is difficult by using only two scalar damage variables for tension and compression in constitutive modelling to observe different responses for concrete subjected to arbitrary loads. Therefore, the hardening and softening processes are assumed isotropic with a uniform expansion and contraction of the failure surface. Many researchers (Jirasek and Patzak 2002, Jirasek et al. 2004, Comi and Perego 2001) tried to consider this evolution of the failure surface by using the uniaxial behaviour of the material. However, concrete in continuum mechanics should be simulated under multi-axial loading and the initial stress-strain response using the damage criteria should be in good

agreement with the experiments observations. Among others, some researchers could not properly simulate the multi-axial response of concrete (Peerlings 1999, Jirasek and Patzak 2002, Addessi et al. 2002), because even if it is easy to model the stress-strain relationship by using the scalar variables, the damage criterion and the damage evolution law, it becomes difficult to model the macroscopic concrete behaviour. This drawback in modelling becomes significant when the unloading and reloading should be considered. Also, the damage model cannot capture the permanent deformation of the concrete as in the experimental results. Therefore, the coupling between damage and plasticity is essential for the macroscopic behaviour of concrete and it should be taken into consideration in constitutive modelling.

3.7 Coupled plasticity and damage

According to Lemaitre (1992), in the constitutive modelling of concrete there are two approaches for coupling damage and plasticity. The first approach is called state coupling and considers the coupling between damage and elasticity and the second approach is called kinetic or indirect coupling and examines the coupling between damage and plasticity.

The concept of the effective stresses in damage mechanics permits the coupling between damage and elasticity. However, the coupling between damage and plasticity is introduced implicitly in the yield and damage criteria with the material strength being decreased due to the damage variable D (Luccionni et al. 1996, Nguyen 2002, Nguyen and Houlsby 2004, Salari et al. 2004). With that implicit coupling, the effective stress used in the yield function replaces the nominal stress (Lemaitre and Chaboche 1990, Lemaitre 1992) and thus the constitutive modelling adopts separate forms for the yield and failure criteria and can solve problems that

need a combined yield-failure criterion. Also, there is no dependency between the damage variable and the plastic strains in the coupled model.

Other researchers (Lemaitre 1992, Lee and Fenves 1998, Faria et al. 1998, Lemaitre 2000) use a different approach for coupling the damage and the plasticity. They use only one loading function in order to examine the dissipation process. This loading function is a damage function with an evolution law for the plastic strains (Faria et al. 1998) and sometimes requires a damage criterion based on the equivalent plastic strains in terms of the internal variables that control the plastic flow (Lemaitre 1992, Lee and Fenves 1998, Lemaitre 2000). By using one loading surface it can be easier than using two separate; one for the damage and one for the yield.

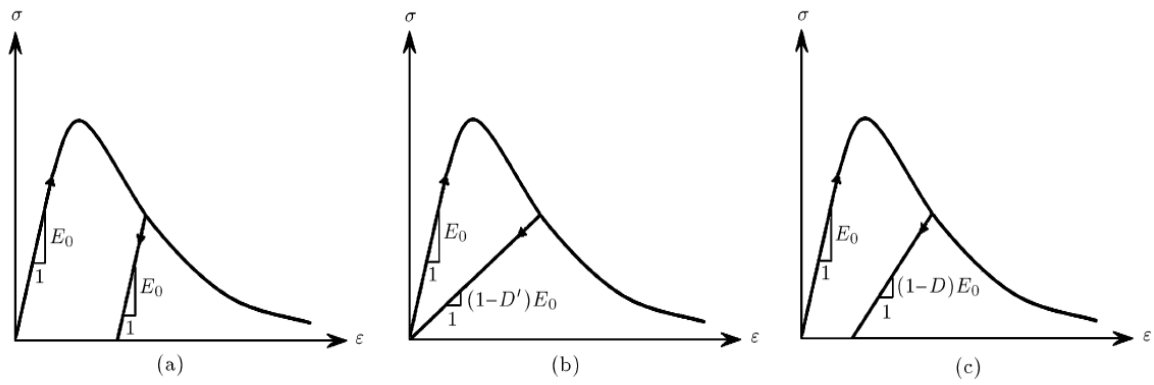

Figure 3.13 Stress-strain curves in uniaxial loading (Omidi and Lotfi, 2010).

In this coupling model, the plasticity theory describes the permanent deformation and the damage theory describes the modelling of the material deterioration (Figure 3.13). This approach in constitutive modelling of concrete combines the two theories (Plasticity theory and Damage theory) and despite its complexity; it has been widely used by many researchers (Simo and Ju 1987, Yazdani and Schreyer 1990, Luccioni et al. 1996, Lee and Fenves 1998, Hansen et al.

2001, Addessi et al. 2002, Ung-Quoc 2003, Jefferson 2003, Salari et al. 2004) over the previous years.

3.8 Summary and Conclusions

The mechanical behaviour of concrete and its non-linear modelling based on cracking models, plasticity theory, continuum damage mechanics and damage coupled with plasticity are presented in Chapter 3. All plasticity models have three major assumptions: 1) the definition of the initial yield surface; 2) the definition of the hardening rule; and 3) the definition of the flow rule. A constitutive model requires a detailed description of the concrete's behaviour, including the hardening and the softening processes. Fracture mechanics and damage mechanics theories were developed in order to explain and consider the plasticity modelling of concrete, the permanent deformation and changing in loading and unloading. In the combined approach (coupled damage-plasticity), the plasticity theory is used for the description of the permanent deformation and the damage theory for modelling the material deterioration. Chapter 4 that follows describes the coupled damaged plasticity model for concrete and its calibration in ABAQUS. That model is considered for all of the analyses done in this work.

Chapter 4

Calibration of the Concrete Damaged Plasticity model in ABAQUS

4.1 Introduction

ABAQUS is a finite element analysis software that allows to evaluate the behaviour of the structures under applied loads. ABAQUS can be used for analyzing static and/or dynamic structural problems as it offers an advanced element and material library for simulating 2D and 3D elements with different shapes and contacts. For analyzing concrete structures, ABAQUS offers three different constitutive models: 1) the concrete damaged plasticity model, that can be used in both ABAQUS/Standard and ABAQUS/Explicit; 2) the concrete smeared cracking model in ABAQUS/Standard only; and 3) the cracking model for concrete only in ABAQUS/Explicit. The cracking model for concrete is considered for applications where the concrete fails by tensile cracking considered as anisotropic and thus the compressive failure is not dominant (elastic behaviour in compression is assumed). The concrete smeared cracking model is used for monotonic loading when the concrete fails due to tensile cracking and/or compressive crushing. The cracking of concrete is considered as the most important failure in this model with a post-cracking anisotropic behaviour to be dominant. Finally, the concrete damaged plasticity model is based on the scalar isotropic damage assumption considering the stiffness degradation in both compression and tension and also it accounts for the stiffness

recovery under cyclic loading. In this work, the concrete damaged plasticity model is chosen for the punching shear simulations due to the arbitrary loading conditions that it can consider, such as cyclic loading. However, many researchers have conducted research using the concrete damaged plasticity in order to examine the behaviour of different reinforced concrete structures, e.g., prestressed concrete beams (Mercan, Schultz and Stolarski, 2010) and reinforced concrete bridge columns (Babazadeh, Burgueno and Silva, 2015).

In this chapter, the concrete damaged plasticity model is firstly presented and then some examples in order to verify its accuracy are shown and discussed. The concrete model is calibrated based on tests from literature. Selected tests by Kupfer et al. (1969) in plain concrete specimens are analyzed using the concrete damaged plasticity model. These specimens were tested under uniaxial/biaxial compression, uniaxial/biaxial tension and tension-compression. Then, a reinforced concrete shear panel tested by Vecchio (1999) is analyzed in order to verify the accuracy of the concrete damaged plasticity model simulating shear stresses-strains. A reinforced concrete beam without stirrups tested by Leonhardt (1962) and two beams, one with stirrups and the other without stirrups, tested by Aoude et al. (2012), are simulated and analyzed in order to investigate the effect of the dilation angle. Finally, the model is used for the analysis of a reinforced concrete flat slab (SB1) tested by Adetifa and Polak (2005) that failed in punching shear. SB1 is considered as the control specimen for all punching shear analyses in this thesis.

4.2 Concrete damaged plasticity model in ABAQUS

The concrete damaged plasticity model from ABAQUS is presented herein. This model is a continuum, plasticity, damaged-based model considering both tensile cracking and

compressive crushing of concrete as possible failure modes. This model was firstly called as Barcelona model and it was developed by Lubliner et al. (1989). The main components of the plasticity based models are the yield function, the flow rule and the hardening rule. Lubliner and the co-authors developed the yield function of the model (1989) and then, this yield function was modified by Lee and Fenves (1998). The form of the yield function is defined according to Eq. (4.1):

$$F = \frac{1}{1-\alpha}\left(\bar{q} - 3\alpha\bar{p} + \beta(\tilde{\epsilon}^{pl})\langle\bar{\hat{\sigma}}_{max}\rangle - \gamma\langle-\bar{\hat{\sigma}}_{max}\rangle\right) - \bar{\sigma}_c\left(\tilde{\epsilon}_c^{pl}\right) \tag{4.1}$$

Parameter α is calculated according to Eq. (4.2), where (σ_{b0}) and (σ_{c0}) denote the biaxial compressive strength and the uniaxial compressive strength, respectively. The default value of the ratio $\left({}^{\sigma_{b0}}/_{\sigma_{c0}}\right)$ is 1.16, according to ABAQUS (ABAQUS Analysis user's manual 6.12-3, 2012) . The Macauley bracket $\langle\cdot\rangle$ is found out as: $\langle x\rangle = \frac{1}{2}(|x| + x)$.

$$\alpha = \frac{\left({}^{\sigma_{b0}}/_{\sigma_{c0}}\right) - 1}{2\left({}^{\sigma_{b0}}/_{\sigma_{c0}}\right) - 1}, \qquad 0 \le \alpha \le 0.5 \tag{4.2}$$

In Eq. (4.1), $\bar{p}$ denotes the hydrostatic pressure stress and $\bar{q}$ the Mises equivalent effective stress. Function $\beta(\tilde{\epsilon}^{pl})$ appears in the yield function, when the algebraically maximum principal effective stress ($\bar{\hat{\sigma}}_{max}$) is positive. The effective stress in concrete damaged plasticity model is defined as: $\bar{\sigma} = E_o \cdot (\epsilon - \epsilon^{pl})$. Also, $\beta(\tilde{\epsilon}^{pl})$ is determined as:

$$\beta(\tilde{\epsilon}^{pl}) = \frac{\bar{\sigma}_c\left(\tilde{\epsilon}_c^{pl}\right)}{\bar{\sigma}_t\left(\tilde{\epsilon}_t^{pl}\right)}(1-\alpha) - (1+\alpha) \tag{4.3}$$

where, $\bar{\sigma}_c\left(\tilde{\epsilon}_c^{pl}\right)$ and $\bar{\sigma}_t\left(\tilde{\epsilon}_t^{pl}\right)$ are the effective compressive and tensile cohesion stresses, respectively. These effective compressive and tensile cohesion stresses, as they called in the

concrete damaged plasticity model, determine the size of the yield surface. The $\bar{\hat{\sigma}}_{max}$ in biaxial compression becomes zero and the parameter $\beta(\tilde{\epsilon}^{pl})$ becomes not active and the only remaining parameter is the α.

The shape of the yield surface is determined by the parameter γ according to Eq. (4.4). Parameter γ is active in Eq. (4.1) when the maximum effective principal stress ($\bar{\hat{\sigma}}_{max}$) becomes negative (tri-axial compression).

$$\gamma = \frac{3(1-K_c)}{2K_c - 1}, \qquad 0.5 < K_c \leq 1 \tag{4.4}$$

The parameter K_c in Eq. (4.4), denotes the ratio of the tensile to the compressive meridian and also defines the shape of the yield surface in the deviatory plane (Figure 4.1).

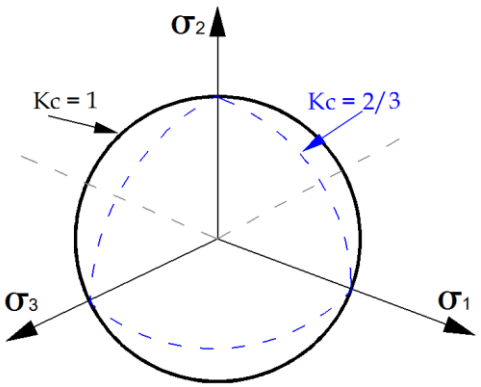

Figure 4.1 Yield surfaces in plane stress.

In the concrete damaged plasticity model the flow potential function, $G(\sigma)$, is a non-associated Drucker-Prager hyperbolic function and is defined according to Eq. (4.5)

$$G(\sigma) = \sqrt{(\varepsilon\sigma_{t0}\,tan\,\psi)^2 + \bar{q}^2} - \bar{p}\,tan\,\psi \tag{4.5}$$

where, ε is the eccentricity that gives the rate at which the plastic potential function approximates the asymptote, σ_{t0} is the uniaxial tensile stress and ψ is the dilation angle measured in the $p-q$ plane at high confining pressure. Figure 4.2 shows the plastic potential function compared to the yield surface, where the plastic strain increment is normal to the plastic potential function. In Figure 4.3 is illustrated schematic the dilation angle and the eccentricity. According to ABAQUS (ABAQUS Analysis user's manual 6.12-3, 2012) the default value for the eccentricity is equal to 0.1, showing that the concrete has the same dilation angle through a wide range of confining pressure stresses. By increasing the value of the eccentricity a more curvature potential function occurs, where the dilation angle increases rapidly as the confining pressure decreases. The dilation angle also shows the direction of the plastic strain increment vector. With the non-associated flow rule adopted in the concrete damaged plasticity model the plastic strain vector is normal to the plastic potential function, which is different from the yield surface.

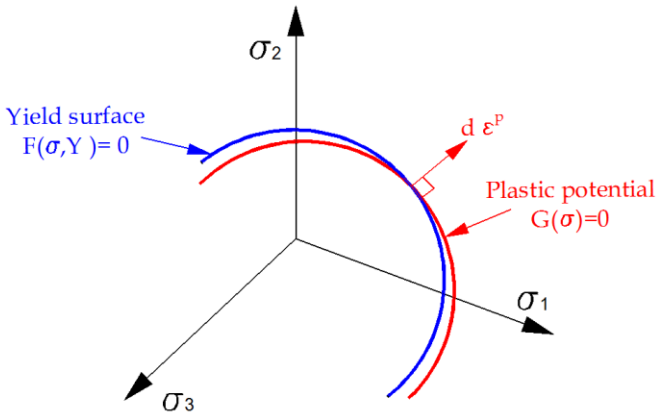

Figure 4.2 Plastic potential and yield surfaces in the deviatory plane.

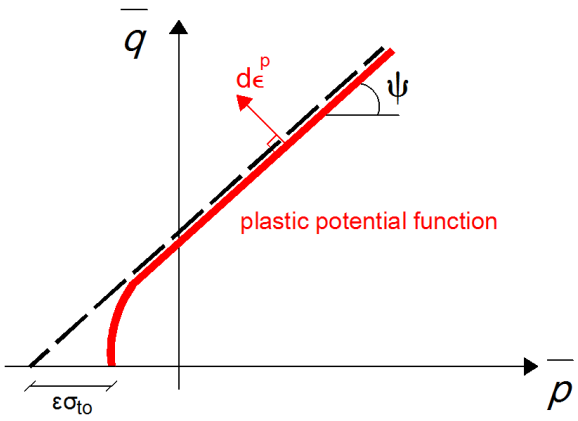

Figure 4.3 Dilation angle and eccentricity in meridian plane.

Damage is introduced in the model according to Eq. (4.6):

$$\sigma = (1-d)\bar{\sigma} = (1-d)E_0 : (\epsilon - \epsilon^{pl}) \tag{4.6}$$

where d denotes the damage parameter and is defined in terms of compression and tension, d_c and d_t, respectively, such that:

$$(1-d) = (1-s_t d_c)(1-s_c d_t) \tag{4.7}$$

where s_t and s_c describe the tensile and compressive stiffness recovery, respectively and they are defined as:

$$s_t = 1 - w_t r(\sigma) \tag{4.8}$$

$$s_c = 1 - w_c(1 - r(\sigma)) \tag{4.9}$$

where, w_t and w_c are weight factors (see Figure 4.4), and $r(\sigma)$ is a direction weight prescribed by the principal stresses. The damage variables can take values from zero (undamaged material) to one (fully damaged material).

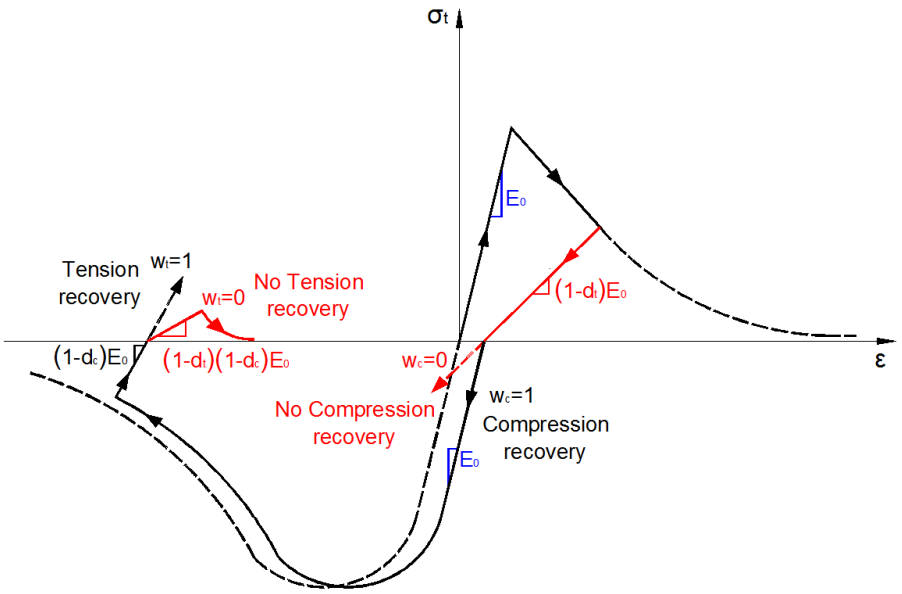

Figure 4.4 Uniaxial load cycle (tension-compression-tension) assuming default values for the stiffness recovery factors: $w_t = 0$ and $w_c = 1$.

Viscoplastic regularization according to Devaut-Lions approach can be defined in the concrete damaged plasticity model. By introducing the viscous parameter (μ) the plastic strain tensor is upgraded and the damage is deduced using additional relaxation time. Eq. (4.10) shows the relationship between the strain rates using the viscoplastic regularization.

$$\dot{\epsilon}_v^{pl} = \frac{1}{\mu}\left(\epsilon^{pl} - \epsilon_v^{pl}\right) \tag{4.10}$$

By using the viscous parameter, the viscoplastic damage increment is determined in Eq. (4.11):

$$\dot{d}_v = \frac{1}{\mu}(d - d_v) \tag{4.11}$$

where d_v is the viscous stiffness degradation variable. Finally, the relationship between stress and strain according to the viscoplastic model is given in Eq. (4.12).

$$\sigma = (1 - d_v)E_0 : \left(\epsilon - \epsilon_v^{pl}\right) \tag{4.12}$$

From the stress-strain diagram that describes the compressive curve for concrete damaged plasticity model in ABAQUS, the inelastic strain $\tilde{\varepsilon}_c^{in} = \varepsilon_c - \frac{\sigma_c}{E_0}$ is calculated first. The plastic strain is equal to: $\tilde{\varepsilon}_c^{pl} = \tilde{\varepsilon}_c^{in} - \frac{d_c}{(1-d_c)}\frac{\sigma_c}{E_0}$. Therefore, the elastic strain $\tilde{\varepsilon}_c^{el}$ is equal to $\tilde{\varepsilon}_c^{el} = \varepsilon_c - \tilde{\varepsilon}_c^{pl}$. And the damage parameter for compression is equal to $d_c = 1 - \frac{\sigma_c}{\tilde{\varepsilon}_c^{el}}/E_0$.

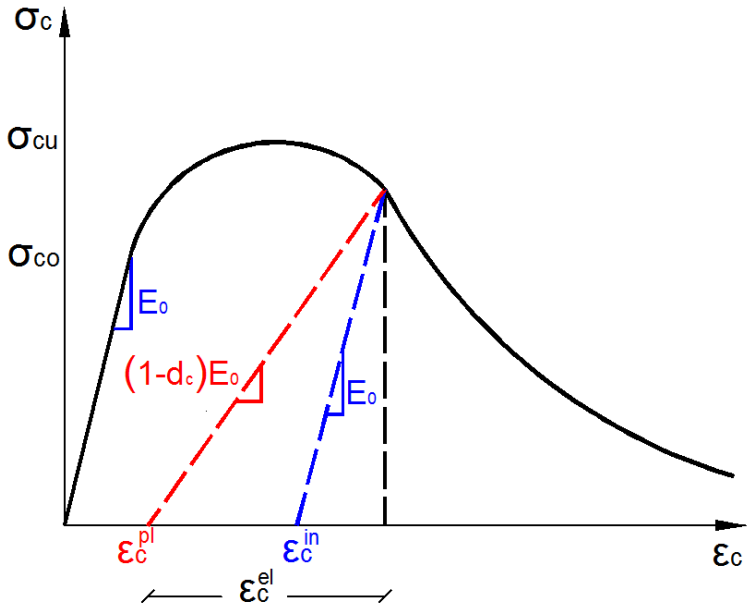

Figure 4.5 Definition of the compressive inelastic (or crushing) strain $\tilde{\varepsilon}_c^{in}$ used for the definition of compression hardening data.

From the stress-strain diagram that describes the tensile curve for concrete damage plasticity model in ABAQUS we can calculate first the cracking strain $\tilde{\varepsilon}_t^{ck} = \varepsilon_t - \frac{\sigma_t}{E_0}$. The plastic strain is equal to $\tilde{\varepsilon}_t^{pl} = \tilde{\varepsilon}_t^{ck} - \frac{d_t}{(1-d_t)}\frac{\sigma_t}{E_0}$. The elastic strain $\tilde{\varepsilon}_t^{el}$ is equal to $\tilde{\varepsilon}_t^{el} = \varepsilon_t - \tilde{\varepsilon}_t^{pl}$. After the

calculation of the elastic strain we can calculate the damage parameter for tension as, $d_t = 1 - \frac{\sigma_t}{\tilde{\varepsilon}_t^{el}}/E_0$.

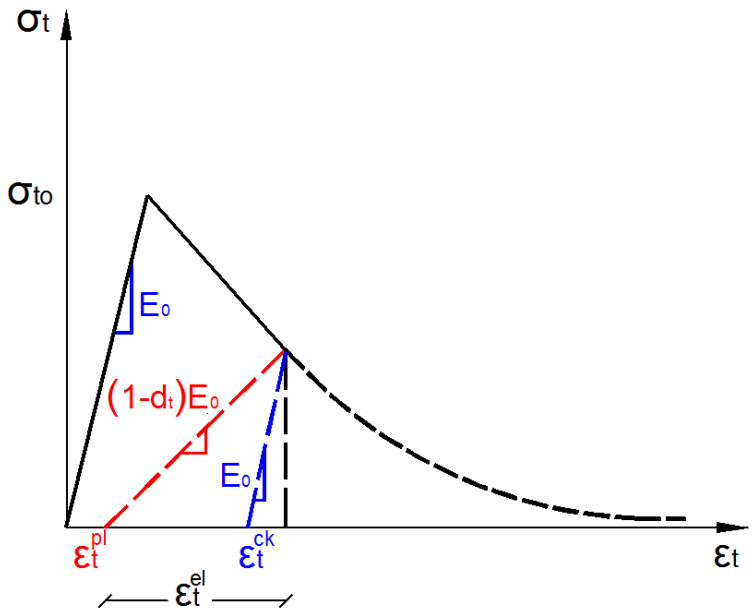

Figure 4.6 Illustration of the definition of the cracking strain $\tilde{\varepsilon}_t^{ck}$ used for the definition of tension stiffening data.

The uniaxial stress-inelastic strain curves are converted automatically in ABAQUS into stress-plastic strain curves. The hardening behaviour of concrete is considered by varying the size and shape of the yield and/or failure surface. This evolution of the yield and/or failure surface is controlled by two hardening variables ($\tilde{\varepsilon}_t^{pl}, \tilde{\varepsilon}_c^{pl}$) referred as tensile and compressive equivalent plastic strains, respectively.

For the visualization of cracking, concrete damaged plasticity model assumes that cracking starts at points where the tensile equivalent plastic strain is bigger than zero and the maximum principal plastic strain is positive. The direction of the cracking is assumed to be

parallel to the direction of the maximum principal plastic strain and it is viewed in the Visualization module of ABAQUS/CAE.

4.3 Adopted concrete modelling

The concrete material parameters in the concrete damaged plasticity model that should be used are: the modulus of elasticity E_0, the Poisson's ratio v and the compressive and tensile strengths of concrete. The uniaxial stress-strain response of concrete in tension is linear elastic up to its tensile strength, f_t'. After cracking, the descending branch is modeled by a softening process, which ends at a tensile strain ε_u, where zero residual tensile strength exists (Figure 4.9). Concrete in tension can be characterized by stress-crack displacement response instead of a stress-strain relationship due to its brittle behaviour. The stress-crack displacement relationship can be described with different options: linear, bilinear or exponential tension softening response (Figure 4.7). The exponential stiffening curve can be calculated according to Cornelissen et al. (Cornelissen et al., 1986), where the following equations should be considered:

$$\sigma/f_t = f(w) - (w/w_c)f(w_c) \tag{4.13}$$

$$f(w) = \left(1 + \left(\frac{c_1 w}{w_c}\right)^3\right) exp\left(-\frac{c_2 w}{w_c}\right) \tag{4.14}$$

$$w_c = 5.14\frac{G_f}{f_t} \tag{4.15}$$

where c_1 and c_2 are material constants and can be considered equal to 3 and 6.93 for normal concrete, respectively.

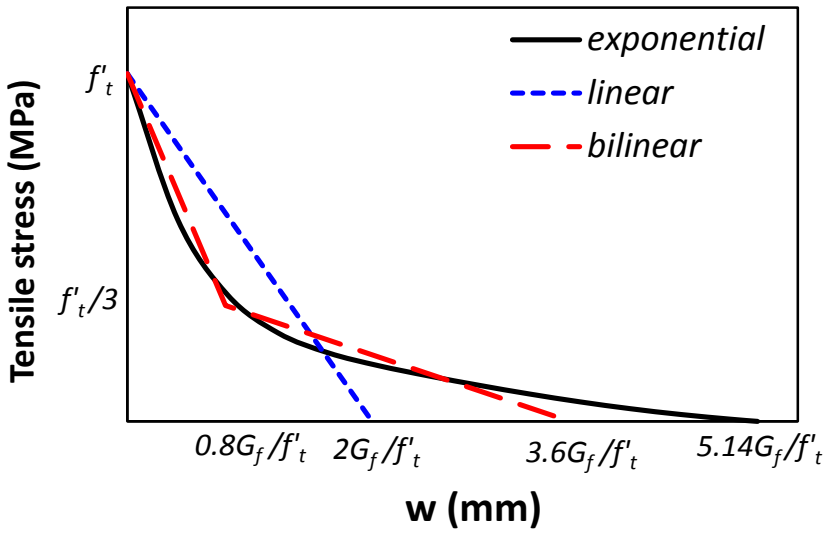

Figure 4.7 Stress-crack width curves in tension for concrete.

In this study, bilinear stiffening response is used and can be calculated according to Figure 4.8, where, f_t' is the maximum tensile strength and G_f is the fracture energy of concrete that represents the area under the tensile stress-crack displacement curve. The fracture energy G_f is related to the concrete's strength and aggregate size and can be calculated using the Eq. (4.16) (CEB-FIP Model Code 90).

$$G_f = G_{fo}(f_{cm}/f_{cmo})^{0.7} \qquad (N/mm) \tag{4.16}$$

According to CEB-FIP Model Code 90, $f_{cmo} = 10\,MPa$, f_{cm} is the mean value of the compressive strength associated with the characteristic compressive strength (f_{ck}), ($f_{cm} = f_{ck} + 8\,MPa$) and G_{fo} is the base fracture energy that depends on the maximum aggregate size, d_{max}. The value of the base fracture energy G_{fo} can be obtained from the CEB-FIP Model Code 90 and for example for an aggregate size d_{max} equal to 10 mm, G_{fo} is equal to 0.026 N/mm. According to ABAQUS (ABAQUS Analysis user's manual 6.12-3, 2012), one possible way to minimize the

localization of fracture is the adoption of the tensile stress-strain relationship. The tensile strains can be defined by dividing the cracking displacement (w) by the characteristic length of the element (l_c). For 3D first order elements the characteristic length is adopted as the cubic root of the element's volume. The tensile stress-strain graph is illustrated in Figure 4.9.

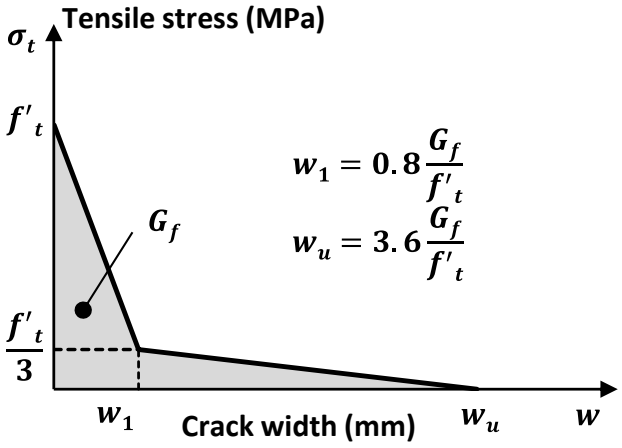

Figure 4.8 Uniaxial tensile stress-crack width relationship for concrete.

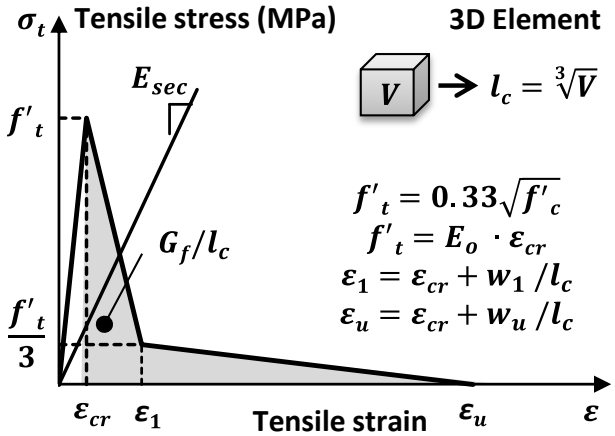

Figure 4.9 Uniaxial tensile stress-strain relationship for concrete.

Concrete in compression can be modeled with the Hognestad parabola (Figure 4.10). The stress-strain behaviour of the concrete under uniaxial compressive loading can be divided into

three domains. The first one represents the linear-elastic branch, with the initial modulus of elasticity, $E_o = 5500\sqrt{f_c'}$. The linear branch ends at the stress level of σ_{co} that here is taken as: $\sigma_{co} = 0.4\, f_c'$. The second section describes the ascending branch of the uniaxial stress-strain relationship for compression loading to the peak load at the corresponding strain level, $\varepsilon_o = 2f_c'/E_{sec}$. The secant modulus of elasticity is defined as: $E_{sec} = 5000\sqrt{f_c'}$. The third part of the stress-strain curve after the peak stress and until the ultimate strain ε_u represents the post-peak branch.

Damage can be introduced in concrete damaged plasticity model in tension and compression according to Figure 4.11 and Figure 4.12, respectively. Concrete damage occurs in the softening range in both tension and compression. In compression the damage is introduced after reaching the peak load corresponding to the strain level, ε_o.

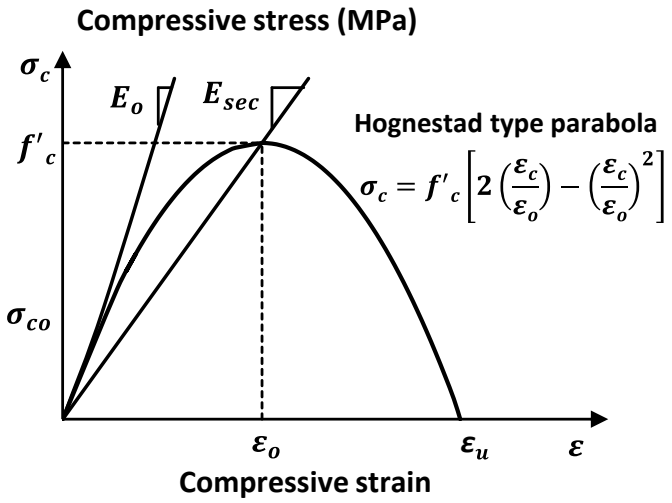

Figure 4.10 Uniaxial compressive stress-strain relationship for concrete.

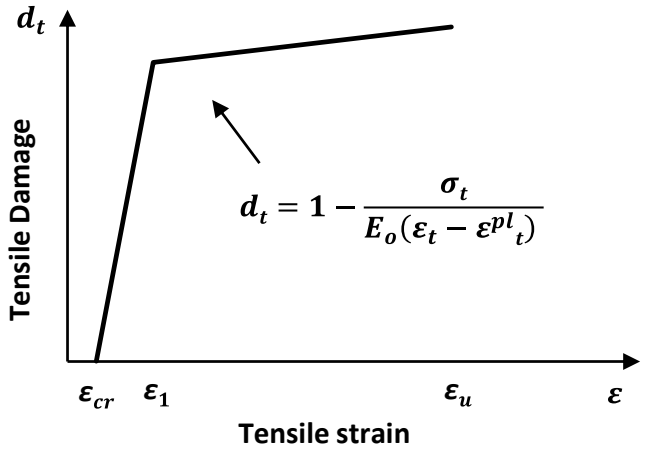

Figure 4.11 Tensile damage parameter-strain relationship for concrete.

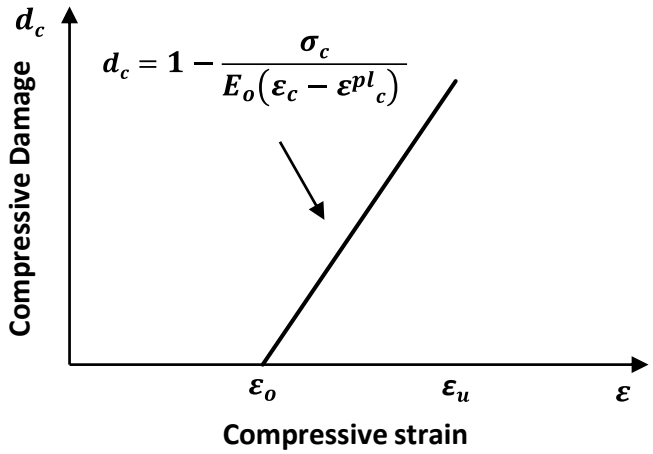

Figure 4.12 Compressive damage parameter-strain relationship for concrete (simplified in linear form).

4.4 Numerical examples – Calibration of the concrete damaged plasticity model

A few examples, taken from literature, are analyzed and presented in order to show how the model is studied and calibrated for the following punching shear examples.

4.4.1 Tests by Kupfer et al. (1969)

In order to investigate the modelling behaviour of the concrete under uniaxial/biaxial compression, uniaxial/biaxial tension and tension-compression using the concrete damaged plasticity model in ABAQUS, a finite element model is analyzed and compared with the test results by Kupfer et al. (1969). The tested plain concrete specimens with dimensions 20x20x5 cm are simulated with an eight-node brick element with reduced integration (C3D8R) by performing displacement control analysis in ABAQUS/Standard. The compressive strength of concrete is 32 MPa. All used model and material parameters are considered based on the previous given and presented information in Sections 4.2 and 4.3. The eccentricity is adopted equal to 0.1, the ratio of biaxial compressive strength to uniaxial compressive strength is considered equal to 1.16, the parameter that defines the shape to yield surface is taken equal to 0.667 and finally no viscosity is considered in the model. The effect of the dilation angle is investigated. Five different values for the dilation angle are given range from 10-50 degrees. Figure 4.13 shows the tested failure modes of the specimens under biaxial compression and tension, respectively.

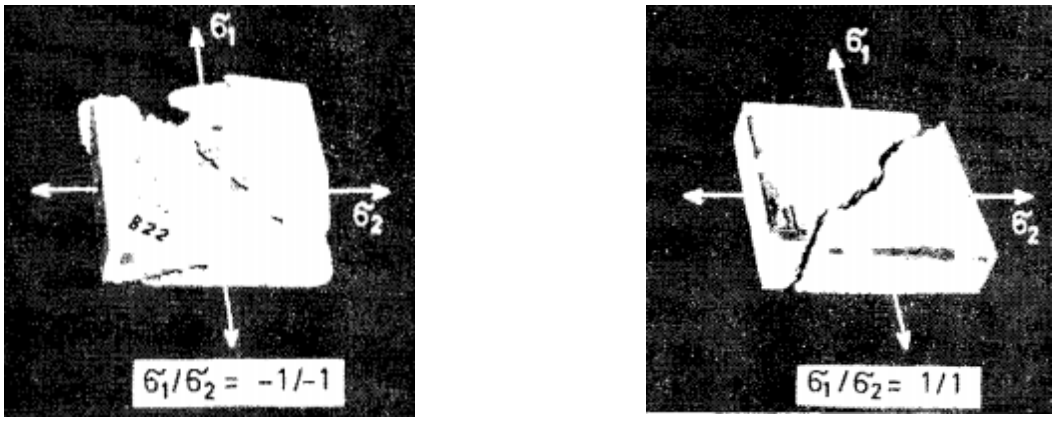

a) Biaxial compression b) Biaxial tension

Figure 4.13 Failure modes of specimen under biaxial stresses by Kupfer et al. (1969).

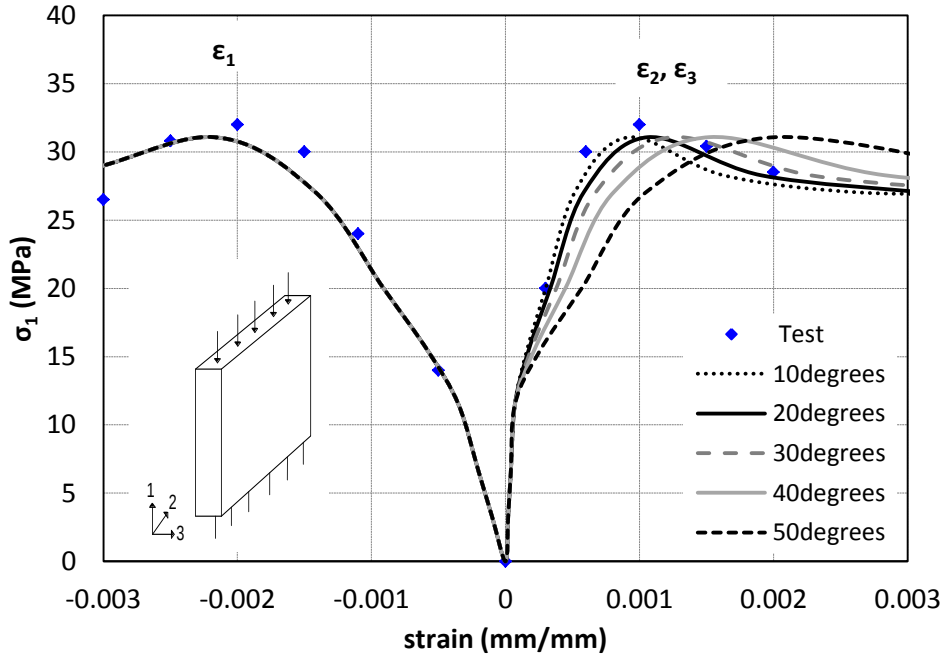

Figure 4.14 Comparison between FEA and tested uniaxial compressive stress-strain curves (dilation angle investigation).

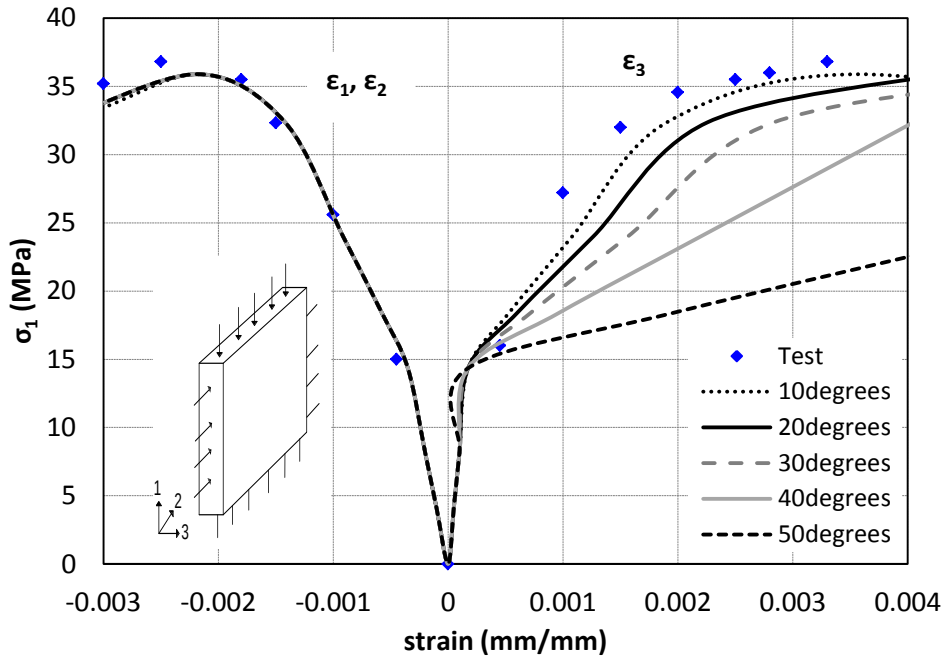

Figure 4.15 Comparison between FEA and tested biaxial compressive stress-strain curves (dilation angle investigation).

Figure 4.14 and Figure 4.15 illustrate the comparison between FEA and tested compressive stress-strain curves for uniaxial and biaxial loading, respectively. The variation of the dilation angle has no effect on the responses in the loading direction (i.e., direction 1 for the uniaxial compression and directions 1 and 2 for the biaxial compression). However, the response of the FEA model depends on the value of the dilation angle for the unloading directions. An increase in the dilation angle makes the response of the model to behave in a more ductile manner. Comparing the test and analytical results in uniaxial compression, it is shown that the dilation angle of 10, 20 and 30 degrees gives a response that is close to the tested response. In the biaxial compression the dilation angle of 10 degrees seems to capture the stress-strain response of the test in the unloading direction. The dilation angle determines the plastic strain direction based on the deviatoric stresses in the meridian plane and actually controls the volumetric expansion of concrete. According to Lubliner et al. (1989) a dilation angle of 15 degrees should

be used for a low-confined concrete. In these two presented examples a small value for the dilation angle seems to give a good prediction compared to the test results, as the specimen is unconfined concrete and in particular plain concrete.

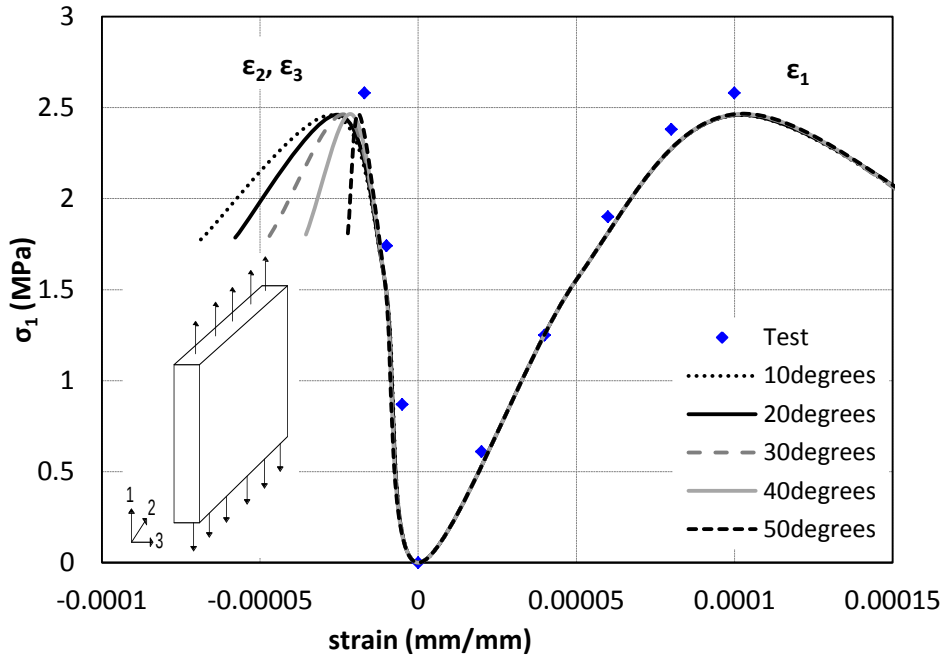

Figure 4.16 Comparison between FEA and tested uniaxial tensile stress-strain curves (dilation angle investigation).

Figure 4.16 and Figure 4.17 illustrate the comparison between FEA and test stress-strain curves for uniaxial and biaxial tensile loading, respectively. Similar to the compressive loading, the variation of the dilation angle has no effect on the responses in the loading direction (i.e., direction 1 for the uniaxial tension and directions 1 and 2 for the biaxial tension). However, the response of the model depends on the value of the dilation angle for the unloading directions. In tension, compared to the compressive loading, an increase in the dilation angle makes stiffer the response of the model. The test results in tension do not allow for any comparison in order to consider the most appropriate value for the dilation angle in the unloading directions. However,

we have to consider that in the tensile tests the concrete specimen does not expand as happens in the compressive tests. Under biaxial tension the tensile stress of concrete is the same with the tensile stress under uniaxial tension.

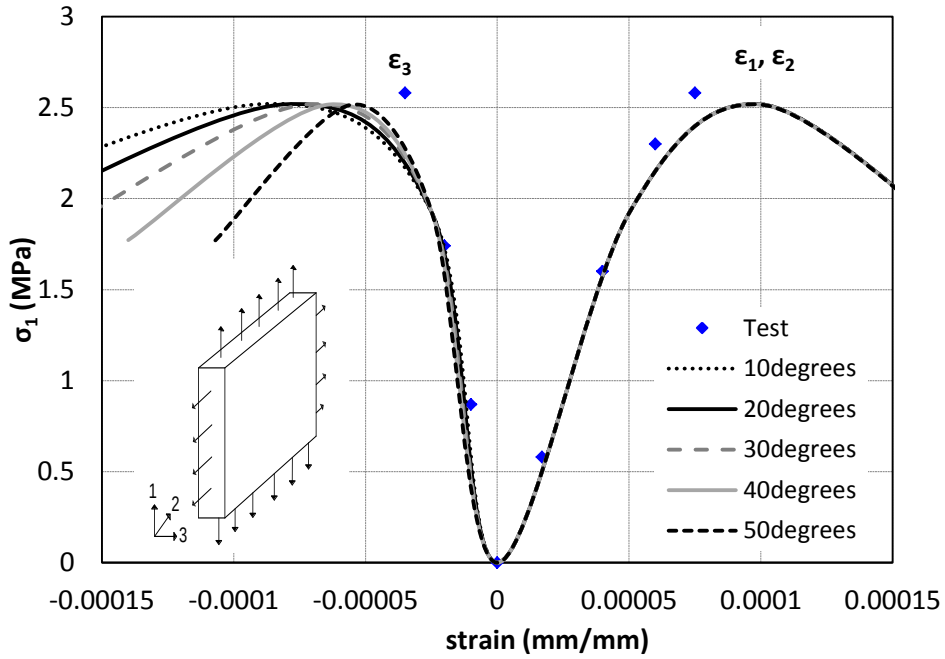

Figure 4.17 Comparison between FEA and tested biaxial tensile stress-strain curves (dilation angle investigation).

Then, the case of tension-compression ($0.103\sigma_1=\sigma_2$) is investigated (see Figure 4.18). Figure 4.19 illustrates the compressive strain ε_1, while Figure 4.20 and Figure 4.21 show the tensile strains, ε_2 and ε_3, respectively. Displacement control analysis is performed in all of the analyses, where the applied displacement is calculated based on the tested strains in directions 1, 2 and 3. In all directions the dilation angle affects the response of the specimen in terms of stress-strain. As the dilation angle is increased the ultimate stress is also increased. Similar to the previous observations, small value for the dilation angle seems to illustrate in a better manner the tested response.

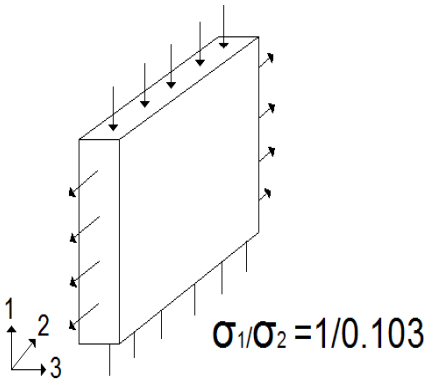

Figure 4.18 Specimen subjected to tension-compression ($0.103\sigma_1=\sigma_2$).

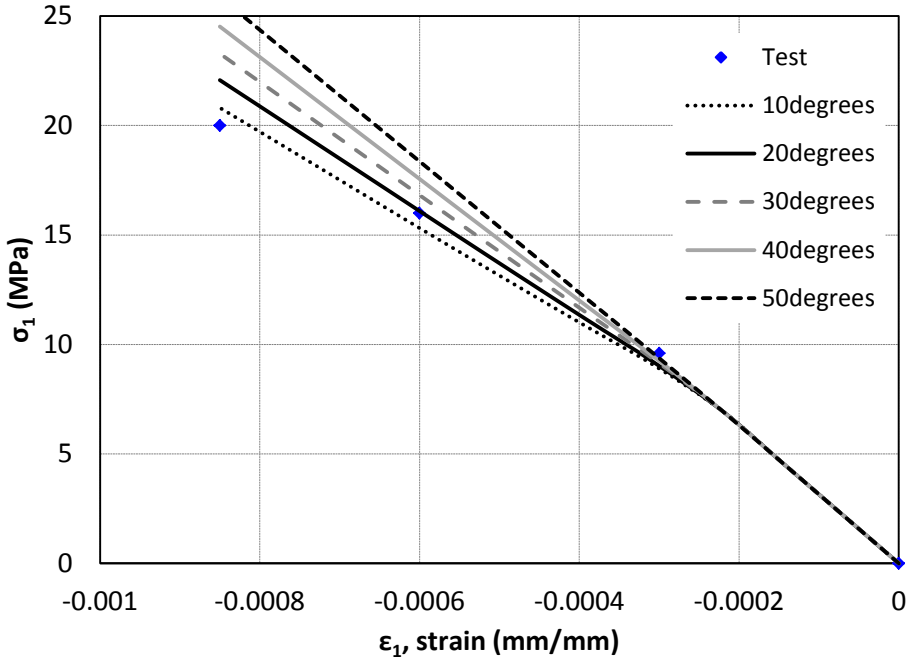

Figure 4.19 Stress-strain curves for tension-compression ($0.103\sigma_1=\sigma_2$) – direction 1.

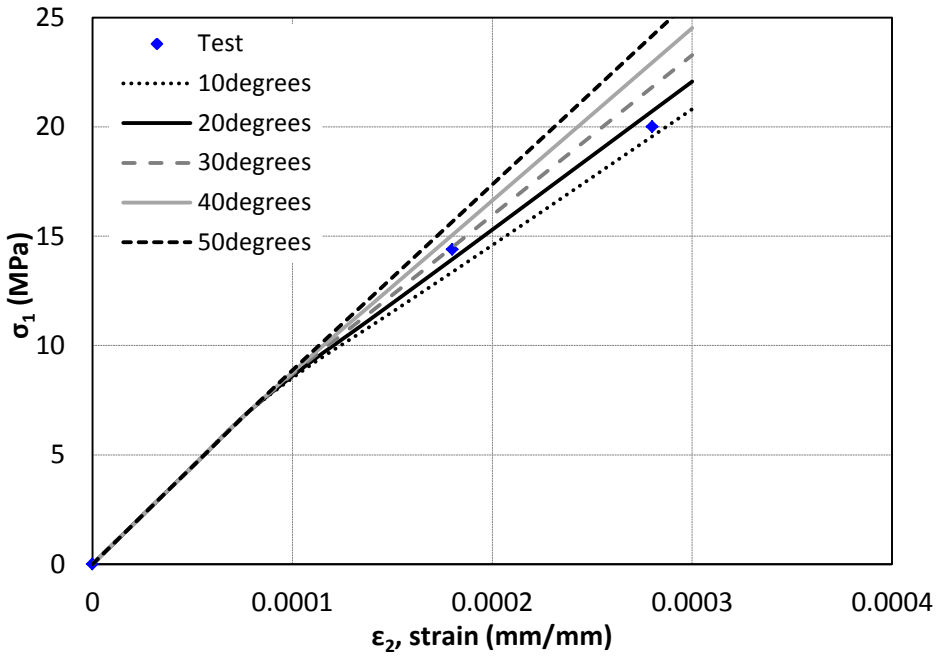

Figure 4.20 Stress-strain curves for tension-compression ($0.103\sigma_1=\sigma_2$) – direction 2.

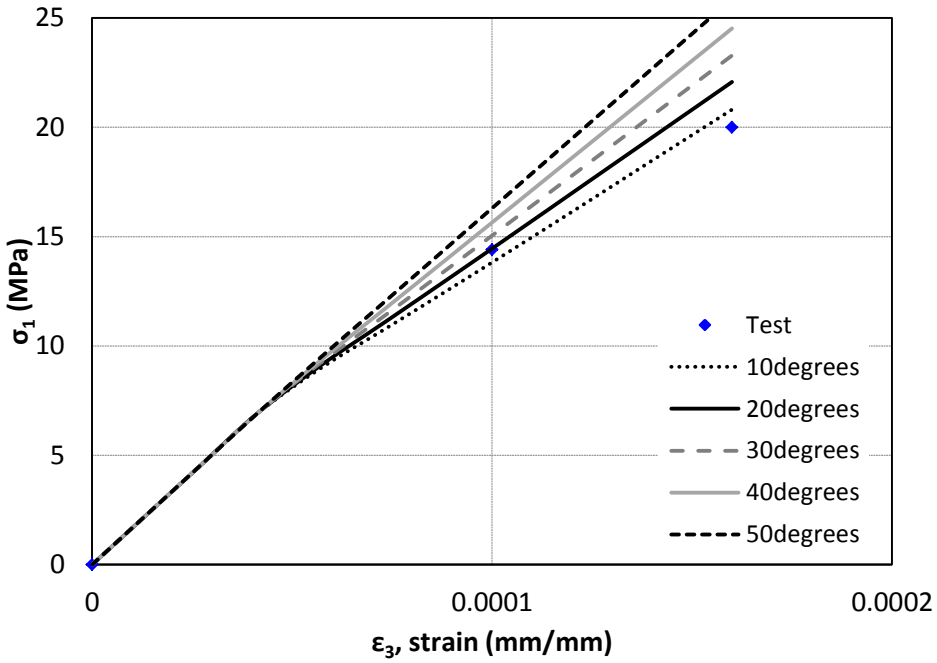

Figure 4.21 Stress-strain curves for tension-compression ($0.103\sigma_1=\sigma_2$) – direction 3.

4.4.2 Shear panel tested by Vecchio (1999)

The shear panel PDV-1 tested by Vecchio (1999) is simulated in ABAQUS using the concrete damaged plasticity model. The dimensions of the tested panel are 890x890x70 mm with reinforcement ratios: 1.82 percent in x-direction (longitudinal) and 0.91 percent in y-direction (transverse). The geometry of the panel and the reinforcements are shown in Figure 4.22 and Figure 4.23, respectively. The compressive strength of concrete is 26.8 MPa corresponding to a strain level of 0.00162 mm/mm and the yield strength of steel is 282 MPa. The nominal diameter of the reinforcement bars is 6 mm. The panel was tested under biaxial compression and shear in proportions of (-0.4:-0.4:1) and was subjected to monotonically increased loading. During the test the panel failed in shear of concrete at the same time with the yielding of the flexural reinforcement in x-direction (longitudinal). The transverse reinforcement had yielded before the failure. This panel is analyzed herein with the concrete damaged plasticity model using the surface tractions in the fixed proportions in order to simulate the shear and the compression, using a force-control procedure in ABAQUS/Standard. The concrete is modeled using C3D8R hexahedral elements and the reinforcement is modelled with (T3D2) 2-noded 3D linear truss elements embedded into the solid concrete elements. The embedded region constraint method in ABAQUS embeds a region of the model within a “host” region of the model or in general within the whole model. As embedded region is considered the reinforcement and as “host” region is considered the concrete member. The dilation angle is considered equal to 30 degrees after investigation. In this example the dilation angle is increased compared to the previous shown plain concrete elements, as the shear panel is a reinforced concrete member. The shear strain is calculated as the displacement at the lower right corner of the specimen. Figure 4.24 shows the tested crack pattern of the panel at failure, while Figure 4.25 illustrates the shear stresses

obtained from the numerical analysis. Finally, Figure 4.26 presents the comparison of the shear stress-strain obtained from the test and FEA. The numerical results are in good agreement with the experimental. The adopted dilation angle is equal to 30 degrees. All other material parameters of the model are considered same as in the previous examples.

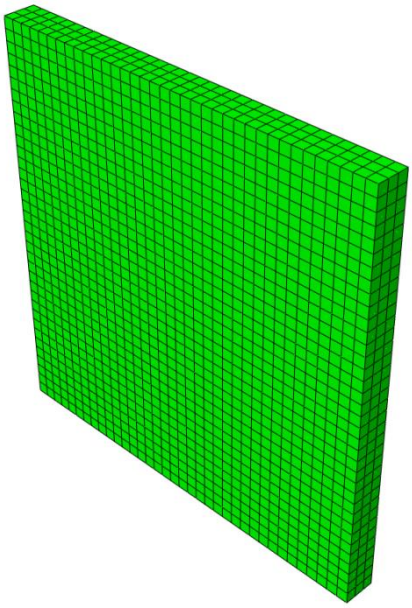

Figure 4.22 Hexahedral mesh elements for concrete.

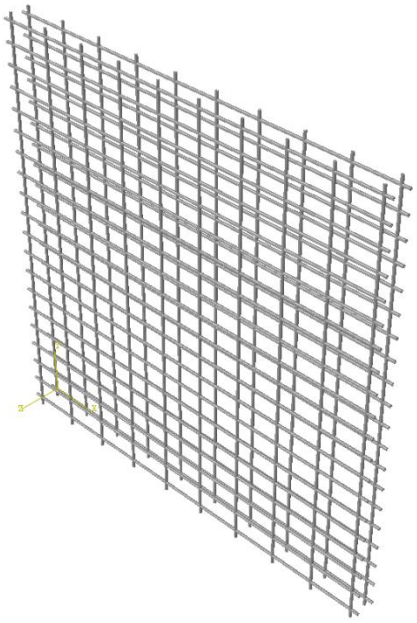

Figure 4.23 Truss elements simulate the reinforcement.

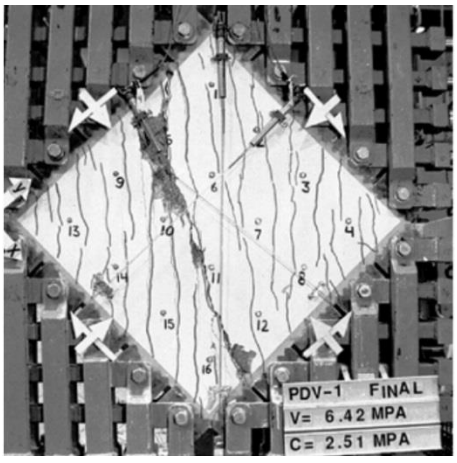

Figure 4.24 Crack pattern Vecchio (1999).

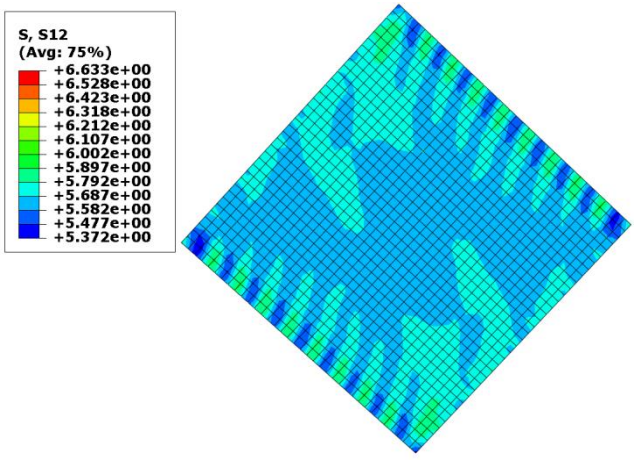

Figure 4.25 Crack pattern from ABAQUS.

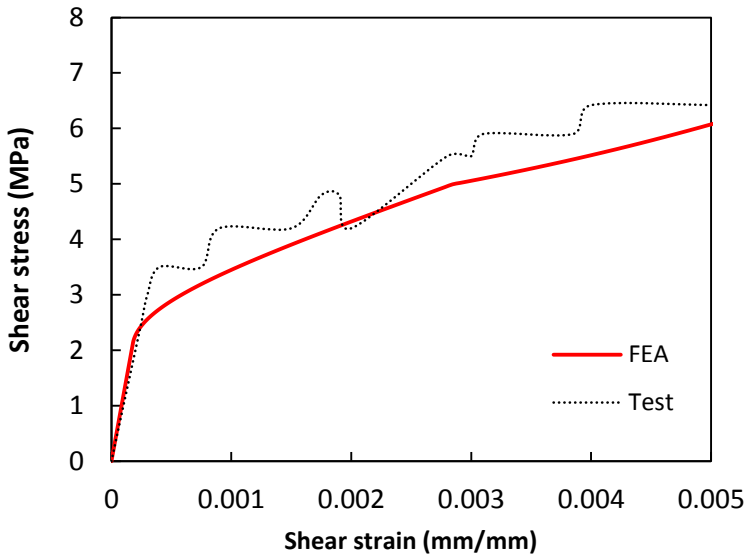

Figure 4.26 Tested and numerical shear stress-strain of panel PDV1.

4.4.3 Beam tested by Leonhardt and Walther (1962)

This example shows a reinforced concrete beam tested by Leonhardt and Walther (1962). The simply supported beam without stirrups failed in shear. The dimensions of the beam are 2550x320x190 mm and that beam is reinforced with two longitudinal bars with diameter 26 mm and total cross-sectional area 1060 mm^2 and cover 37 mm. The loading during the test was applied at two points. In ABAQUS, the beam is modeled using C3D8R elements for concrete and T2D3 elements for the steel. Symmetry is considered and only half of the beam is simulated. Concrete is modeled using different values for the dilation angle in order to investigate the most appropriate value in order the test and numerical response of the specimen to be in good agreement. The dilation angle of 30 degrees is the chosen value that simulates the beam leading to a good agreement between experimental and numerical results (see Figure 4.27). The

comparison between crack patterns observed from test and FEA are in good agreement (see Figure 4.28, Figure 4.29).

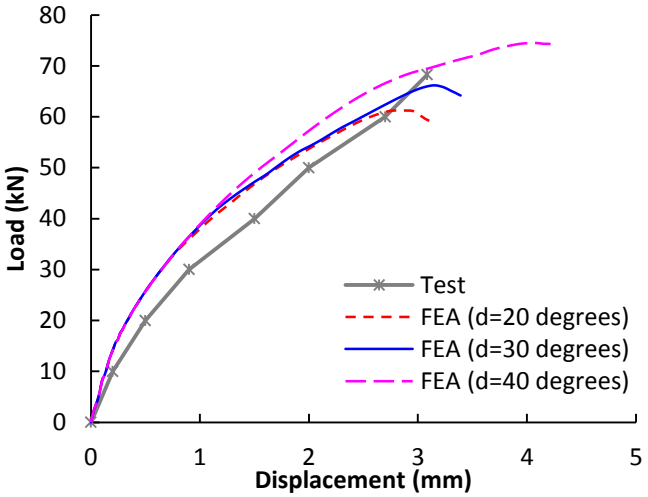

Figure 4.27 Tested and numerical load-displacement response (dilation angle investigation).

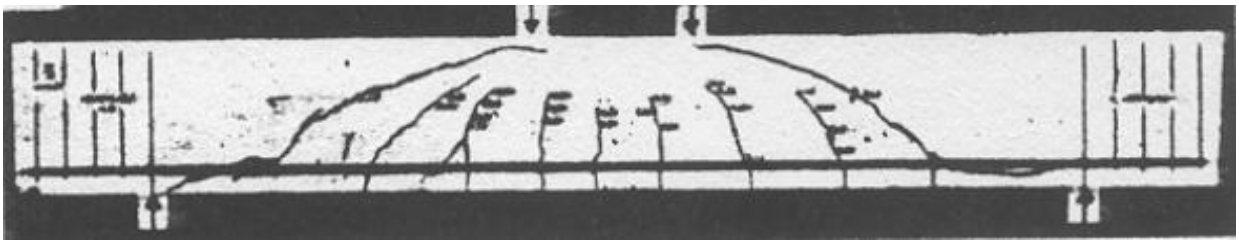

Figure 4.28 Cracking at failure during the test (Leonhardt and Walther, 1962).

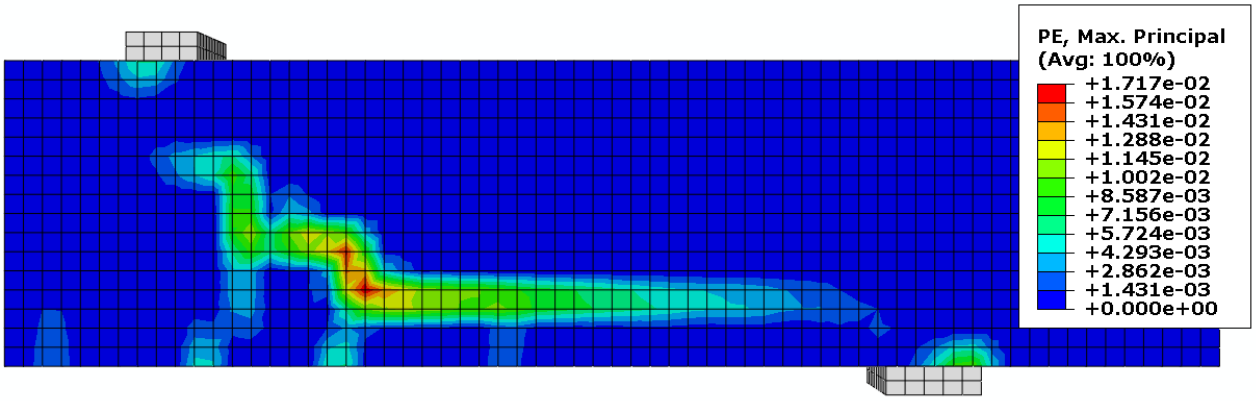

Figure 4.29 Cracking at failure from FEA (half beam).

4.4.4 Beam tested by Aoude at al. (2012)

Two reinforced concrete beams with the same material properties and dimensions tested by Aoude et al. (2012), are analyzed with the concrete damaged plasticity model. The length of the beams is 4400 mm with 300 mm width and 500 mm height. The longitudinal reinforcement consists of four 25M bars for the bottom reinforcement and two 20M bars for the top reinforcement. The compressive strength of concrete is equal to 23.3 MPa and the clear cover of the longitudinal reinforcement is equal to 40 mm. The only difference between the two beams is that the beam B0% is reinforced with only three stirrups of 10M (one in the middle and the other two at the supports), while the specimen BF0% has 10M stirrups at 275 mm. Figure 4.30 shows half of the beams' configuration as it is simulated in ABAQUS. For the beam BF0%, the adoption of higher value for the dilation angle is considered. The dilation angle of beam B0% is adopted equal to 30 degrees while the given value for the beam BF0% is equal to 42 degrees. According to the test results, beam B0% failed at a load of 125.1 kN, while specimen BF0% failed at a load of 245 kN.

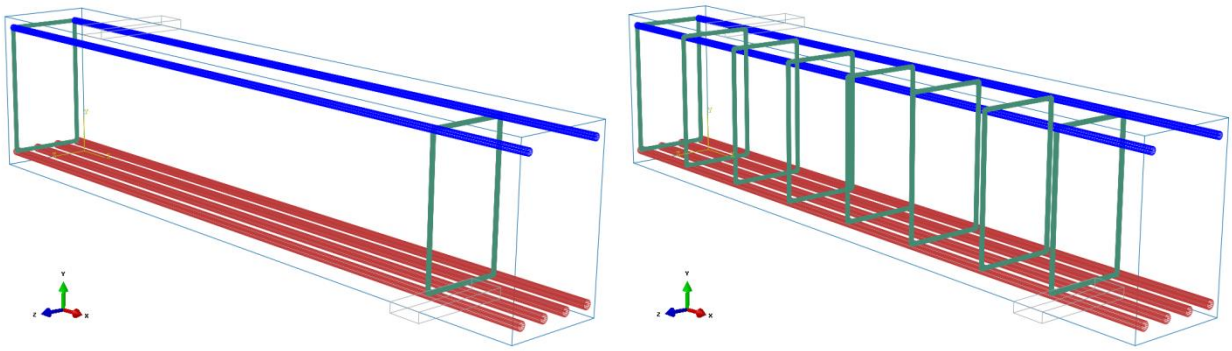

a) b)

Figure 4.30 Modelling of the beams in ABAQUS: a) BO% beam and b) BFO% beam.

Figure 4.31 illustrates the cracking of the beam BO% (beam without stirrups) at the failure load as it is observed after the numerical analysis, while Figure 4.32 shows the cracking of the beam BFO%.

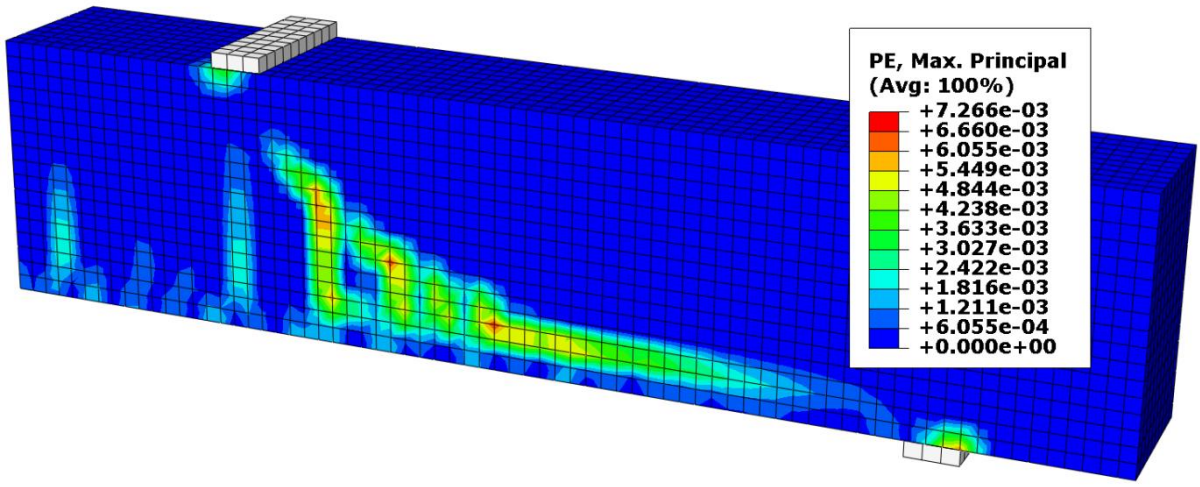

Figure 4.31 Cracking at ultimate load from the numerical analysis of beam BO%.

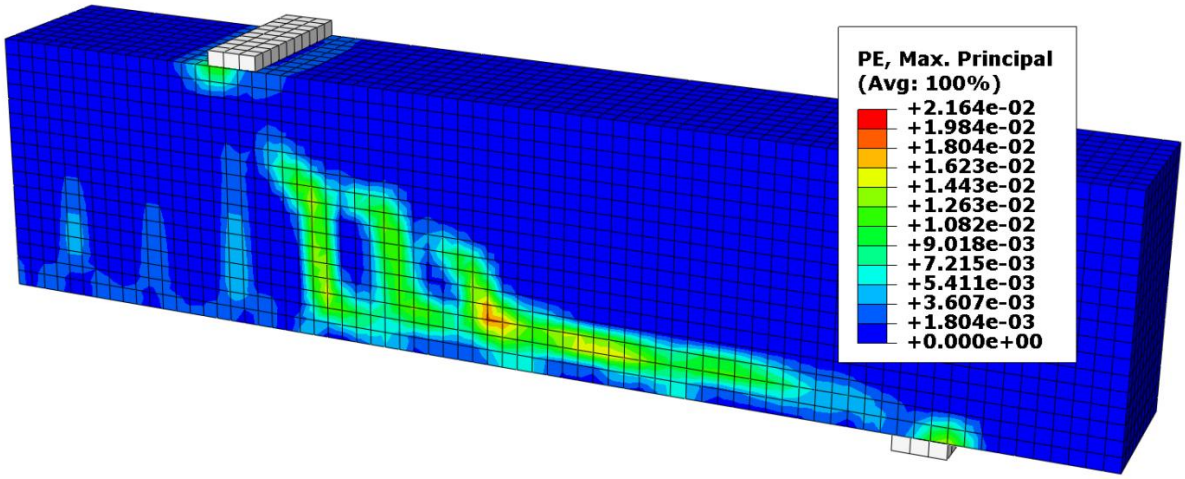

Figure 4.32 Cracking at ultimate load from the numerical analysis of beam BFO%.

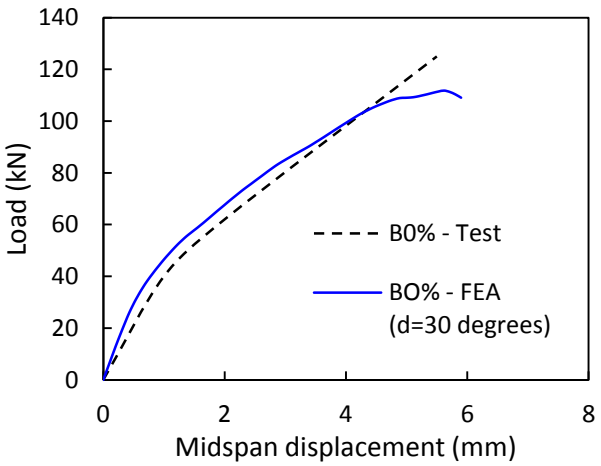

Figure 4.33 Load-deflection response of specimen BO%.

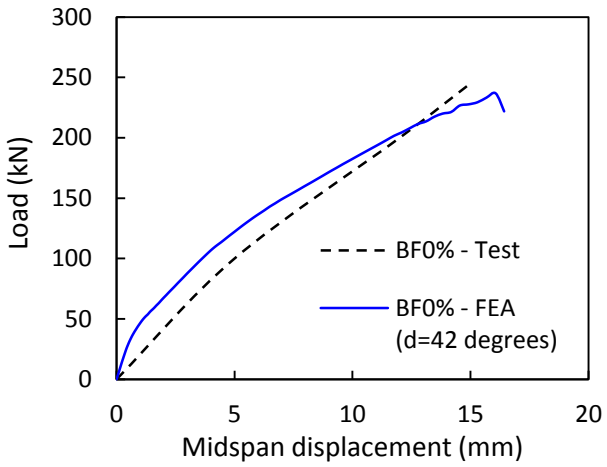

Figure 4.34 Load-deflection response of specimen BFO%.

The comparison between test and FEA results in terms of load versus mid-span deflection response are presented in Figure 4.33 for the specimen BO% and in Figure 4.34 for the specimen BFO%. For the beam without stirrups the proper value for the chosen dilation angle is 30 degrees, while for the beam with stirrups the value of the dilation angle is 42 degrees. Therefore, it becomes herein obvious that the confined concrete and in general members with increased

amount of reinforcement require higher value for the dilation angle in the concrete damaged plasticity model.

4.4.5 Slab tested by Adetifa and Polak (2005)

Specimen SB1 belongs to the test series of reinforced concrete slabs tested by Adetifa and Polak (2005) and in this thesis this slab is considered as the control specimen for all the numerical analyses. In this subsection, a detailed parametric investigation is performed with respect to all appropriate modelling and analysis parameters for the slab SB1. The already described concrete model is adopted and herein the investigation examines the boundary conditions, the type of analysis, the mesh sensitivity, the type of the 3D elements and finally some material parameters of the model. This specimen is an interior slab-column connection without shear reinforcement that was previously tested at the University of Waterloo by Adetifa and Polak (2005). The compressive strength of concrete is 44 MPa and the tensile strength of concrete is 2.2 MPa. The yield strength of the flexural reinforcement is 455 MPa. This specimen was tested under static loading through the column stub. The column is square with dimensions 150x150 mm and is extended 150 mm from the top and the bottom faces of the slab. The height of the slab is 120 mm and the effective depth is 90 mm. The overall dimensions of the slab in plan are 1800x1800 mm with simple supports at 1500x1500 mm. The slab during the test failed in punching shear at a load of 253 kN and at this load the displacement was equal to 11.9 mm. In FEA only one quarter of the slab is simulated due to the double symmetry. For simulating the concrete, 8-node hexahedral elements with reduced integration (C3D8R) are used in order to avoid the hourglassing effect. To model the reinforcement, 2-node linear truss elements (T3D2) are used and the embedded method is adopted to simulate the perfect bond between concrete and

reinforcement. Restraints are introduced at the bottom edges of the specimen in the loading direction. Figure 4.35 shows the geometry and the boundary conditions of the control specimen SB1 in ABAQUS.

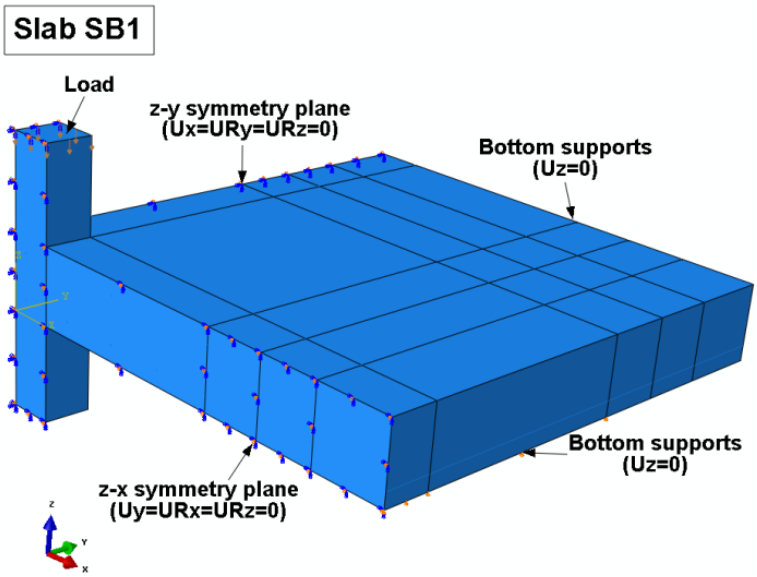

Figure 4.35 Geometry and boundary conditions of specimen SB1.

Two types of analysis are performed: static analysis using the ABAQUS/Standard with viscoplastic regularization and quasi-static analysis in ABAQUS/Explicit. Figure 4.36 illustrates the comparison between the results that are obtained after performing the static and quasi-static analyses. The FEA results are compared with the test results in terms of load-deflection response. Two values for the viscosity parameter in the static analysis are considered: $\mu = 0.00001$ and $\mu = 0.00005$. The chosen value of the viscosity parameter should be around to 15 percent of the time increment step in order for the solution to be improved without causing any changes into the results. Due to the high nonlinearity in FEA solution of slab SB1, the time increment step could not be fixed and it is set as automatic. Thus, the viscosity parameter is found through numerical investigation and the value of 0.00001 is considered as the most appropriate. The viscoplastic

regularization parameter can also be considered as time relaxation parameter. The results obtained from both analyses (static with viscosity parameter equal to 0.00001 and quasi-static), are in good agreement compared to the test results in terms of ultimate load and deflection (see Figure 4.36). Brittle punching shear failures are observed from both analyses with the sharp peak in the load-deflection diagrams. Quasi-static analysis requires less computational time compared to the static analysis. In all subsequent analyses of specimen SB1 and in general in this work, the quasi-static analysis is considered.

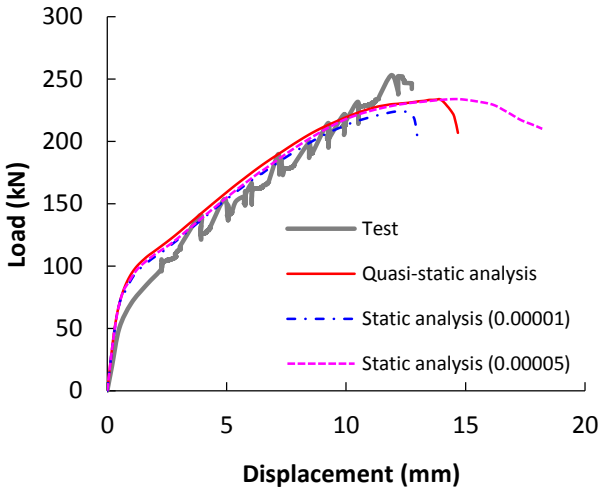

Figure 4.36 Load-displacement response performing static and quasi-static analyses.

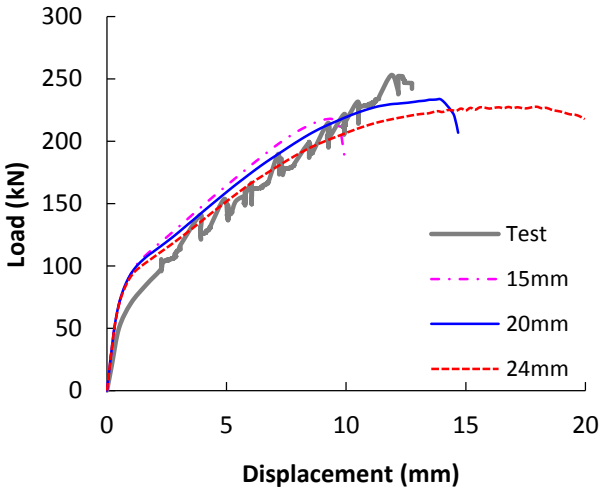

Figure 4.37 Load-displacement response for different mesh sizes.

A mesh convergence study is considered in SB1 specimen. The smeared crack approach used in ABAQUS model appears to lead to strain localization due to strain softening nature of concrete that depends on the dimensions of the elements. The strain localization accumulates within few elements and the rest of the structure starts to unload. Fine mesh gives narrow band of localization and after a while the solution equations fail to converge. This is the reason that the model is mesh size dependent as happens with most plasticity based models. The mesh size dependency can be solved by introducing the characteristic internal crack length and/or by using the viscoplastic regularization. Three different mesh sizes (15 mm, 20 mm and 24 mm) are adopted in the analysis of the specimen SB1 in order to investigate the mesh sensitivity of the FEA model. The mesh chosen values should be larger than the aggregate size (10 mm) however not to too large resulting in a coarse mesh. In macro-mechanics the aggregate size of concrete usually is assumed as the possible minimum mesh size. A finer mesh (less than the aggregate size) can be adopted when the simulation of the concrete is done using micro-mechanics FEA. The mesh size of 15 mm gives 8 elements through the thickness of the slab, while the mesh sizes

of 20 mm and 24 mm, give 6 and 5 elements, respectively. The chosen 24 mm mesh size is considered as the upper limit in the chosen mesh sizes, because less than 5 mesh elements through the slabs' thickness lead to hourglassing numerical effect and distortion of the C3D8R elements. The tensile strains are calculated by dividing the cracking displacements to the characteristic lengths of the elements. However, the results remain mesh size dependent. Figure 4.37 shows the analyses' results that are obtained from each mesh size. The results are mesh size dependent, especially in terms of failure displacements. All of the mesh sizes give similar results in terms of the failure load. The mesh size of 20 mm gives the most accurate results compared to the test data. The mesh size of 24 mm seems to be too coarse and not able to converge giving a ductile and not realistic behaviour to the slab. The mesh size of 15 mm seems to be too small (close the aggregate size) and for that reason it cannot be considered. These observations are made after performing quasi-static analysis. The results with the viscoplastic regularization in ABAQUS/Standard by performing static analysis for the same mesh sizes (15 mm, 20 mm and 24 mm) are still mesh size dependent. The viscous parameter is obtained as a material property for the concrete, introducing rate dependence into the material as relaxation time. The value of the chosen viscous parameter is 0.00001. The consideration of the viscoplastic component in the model does not seem to fully resolve the mesh sensitivity of the problem. However, the mesh size of 20 mm gives the most accurate results compared to the test load-deflection response and this mesh size is chosen in all subsequent simulations of all slabs. This choice has been based not only on the load-deflection responses but also on the comparison with the cracking patterns (Figure 4.38).

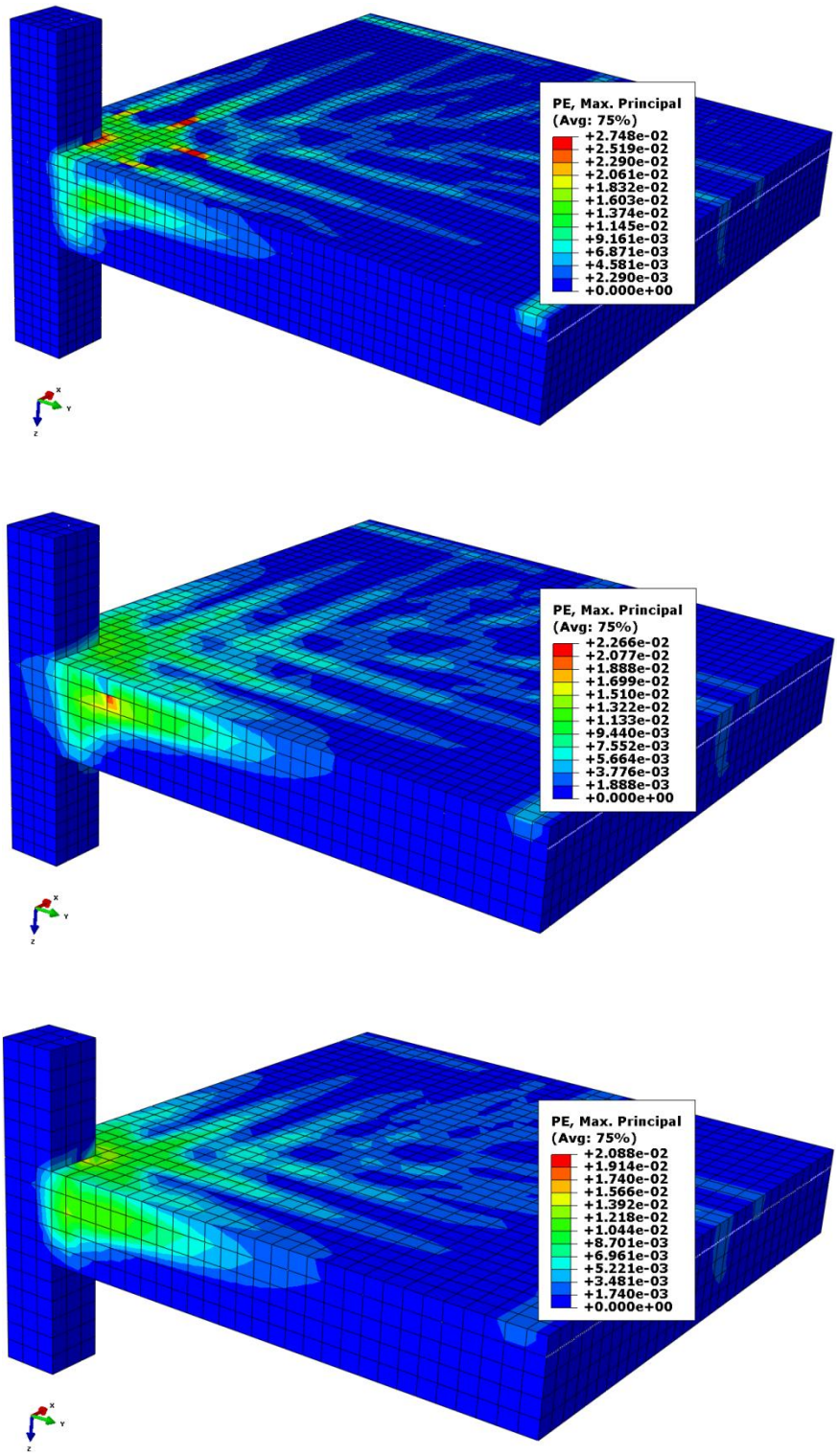

Figure 4.38 Crack patterns at failure for different mesh sizes.

Further investigation is performed to analyze the specimen (SB1) by changing its boundary conditions. After installing simple supports, neoprene is simulated around the bottom of the slab as happened in the real test (neoprene pads 25 mm thick and 50 mm in width were installed along the supporting lines). Neoprene is a hyper-elastic material considered as isotropic and nonlinear. Neoprene exhibits instantaneous elastic response up to large strains and as most elastomers it has low compressive strength compared to its shear flexibility. In finite element analyses when the elastomer materials are modeled with three-dimensional solid elements the numerical solution could be sensitive to the compressive behaviour of the material, therefore special attention is required. The Poisson's ratio for the hyperelastic materials is close to 0.5. Hyperelastic materials are described in terms of a "strain energy potential'' $U(\epsilon)$, which defines the strain energy stored in the material per unit of reference volume as a function of the strain at that point in the material. There are several forms of strain energy potentials available in ABAQUS to model approximately in-compressive isotropic elastomers. Between these models the Mooney-Rivlin model is chosen for the analysis below. However, the mechanical properties of the neoprene are determined by performing uniaxial compressive test on a neoprene specimen. The testing facility consists of a servo-controlled MTS machine equipped with a load cell with a capacity of 100 kN. The grips that are used had 100 mm diameter and the specimen is attached to the upper and lower set of the grips. The lower set is fixed during the test and the upper set is able to move downwards in a displacement control mode with a low speed of movement (Figure 4.39). The specimen's dimensions are 110x50x25 mm in the undeformed configuration. The stress-strain data collected from the experiment until the 80 kN load in which no failure is observed are presented in Figure 4.40. Calculating the load that the neoprene supports carried during the test of the slab SB1, the level of stress that the specific specimen reached was 1.0542

MPa at the strain level of 0.1268 mm/mm, shown in Figure 4.40. At this stress-strain level the response of the tested specimen can be considered as linear and easily the initial modulus of elasticity can be found. However, ABAQUS allows the option of defining the uniaxial compression test data that can be used for the parametric modelling identification of the material coefficients. By using the material evaluation option in ABAQUS we can obtain all needed material coefficients for specifying the Mooney-Rivlin form for the neoprene.

According to ABAQUS (Analysis user's manual 6.12-3, 2012) the strain energy potential in Mooney-Rivlin form is:

$$U = C_{10}(\bar{I}_1 - 3) + C_{01}(\bar{I}_2 - 3) + \frac{1}{D_1}(J^{el} - 1)^2 \tag{4.17}$$

where, C_{10}, C_{01} and D_1 are temperature-dependent material parameters, $\bar{I}_1$ and $\bar{I}_2$ are the first and the second deviatoric strain invariants and J^{el} is the elastic volume ratio. The initial shear modulus and the bulk modulus are given according to Eq. (4.18) and Eq. (4.19), respectively:

$$\mu_o = 2(C_{10} + C_{01}) \tag{4.18}$$

$$k_o = \frac{2}{D_1} \tag{4.19}$$

The ABAQUS material evaluation gives the values for the material parameters C_{10}, C_{01} and D_1 ($C_{10} = 0.2292$, $C_{01} = 1.3203$ and $D_1 = 1.2994e-02$). Therefore, the initial shear modulus is equal to 3.099 MPa and the initial modulus of elasticity that can be considered as three times the shear modulus is equal to $9.297\,MPa$. The Poisson's ratio is equal to $\nu = \left[\left(\frac{3k_o}{\mu_o}\right) - 2\right] / \left[\left(\frac{6k_o}{\mu_o}\right) + 2\right] = 0.49$. The numerical results using the neoprene to simulate the

boundary conditions of the isolated specimen are in good agreement with the test results and they describe better, especially in the initial un-cracked state, the real load-deflection response of the isolated slab (Figure 4.41). The simulation of the boundary conditions using the neoprene overcomes the initial stiffer response obtained from the simulations by considering simple supports (Figure 4.42).

Figure 4.39 Test specimen (neoprene).

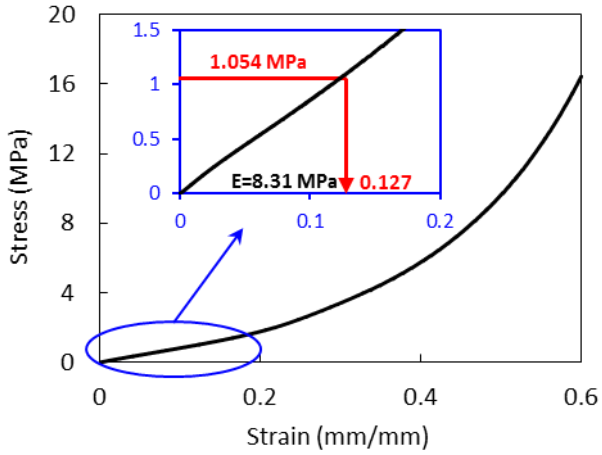

Figure 4.40 Compressive stress-strain behaviour of neoprene.

The numerical results after the material evaluation in ABAQUS ($E = 9.297\ MPa, \nu = 0.49$) are close to the assumption that was discussed earlier by considering the neoprene as elastic material ($E = 8.31\ MPa, \nu = 0.5$).

Investigation using different 3D mesh elements is also performed on the slab SB1. Three different types of elements are adopted in the study: 3D linear hexahedral 8-noded (C3D8R) with reduced integration elements, 3D 4-noded linear tetrahedral elements (C3D4) and 3D 10-noded quadratic tetrahedral elements modified (C3D10M). Only these three types are used due to the ABAQUS/Explicit solution procedure that for example does not allow using (C3D20R) 3D 20-noded quadratic brick elements or C3D10 linear elements. Two different boundary conditions are used during the mesh element investigation: neoprene supports and simple supports around the edges. Figure 4.41 illustrates the load-displacement response of the specimen SB1 supported on neoprene, while the Figure 4.42 shows the response of the simply supported slab SB1. The first important observation comes comparing the two different types of supports: neoprene supports simulate in better manner the initial stiffness of the load-deflection response and the results are in good agreement with the experimental results. However, due to the simplicity of our modelling, the next analyses are performed using only simple supports. The C3D4 elements for both types of supports overestimate the load capacity of the specimen. These elements are poor (fine mesh is needed to get accurate results) and in general they should be placed far from regions where the accuracy is important. Comparing the next two chosen element types, we can conclude that both (C3D8R and C3D10M) elements simulate the slab's response in such way that the obtained results are in good agreement with the experimental results. The modified quadratic tetrahedral elements are robust for large displacement problems. However, the only disadvantage of using this type of elements is the large computational cost. The analysis needs

much longer time to run compared to the hexahedral elements. All numerical analyses are performed using a workstation with 16 GB RAM and an Intel Core i7 Processor running at 3.4 GHz. The ABAQUS version that is used was the 6.12-3 and during all of the analyses parallelization is considered using 7 processors and 7 domains in ABAQUS/Explicit. The computational cost in terms on demand time for each of the next presented analyses using neoprene supports is around; 29 min. for the C3D8R elements, 190 min. for the C3D4 elements and 5,130 min. for the C3D10M elements. Figure 4.43 shows the crack patterns coming from ABAQUS at the failure for each type of element and each type of boundary condition. Neoprene supports seem to present in more realistic way the cracking without to have concentrated strains in the supports as it happens in the simply supported slabs. The crack pattern using neoprene supports and C3D10M elements shows in a better way the cracking compared to the real slab. That actually happens because the C3D10M elements are quadratic elements compared to the linear C3D4 and C3D8R. The tetrahedral elements due to their shape can simulate in better way the radial cracking in the slab, compared to the rectangular hexahedral elements.

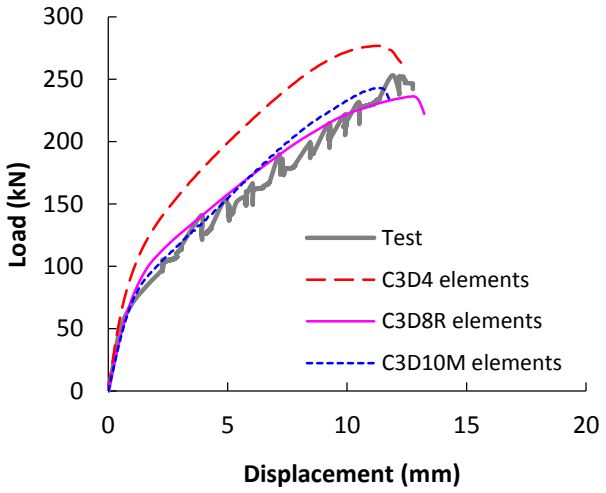

Figure 4.41 Load-deflection response for different mesh elements using neoprene supports.

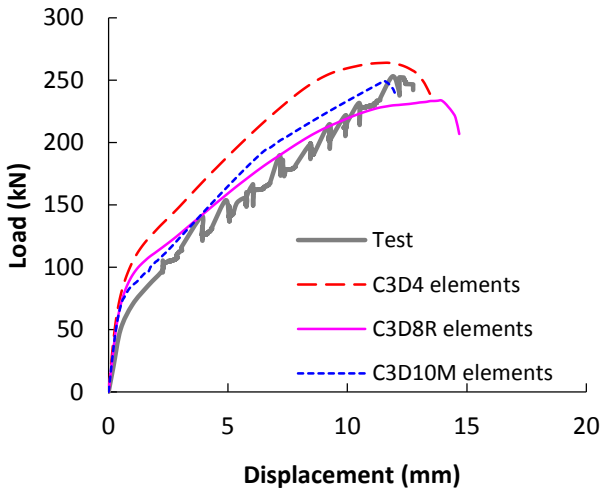

Figure 4.42 Load-deflection response for different mesh elements using simple supports.

Neoprene supports **Simple supports**

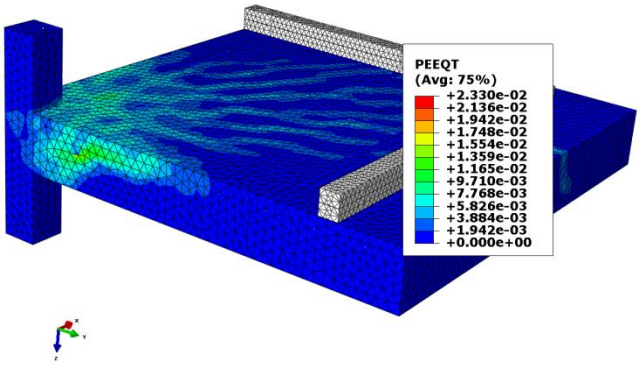

C3D4 elements

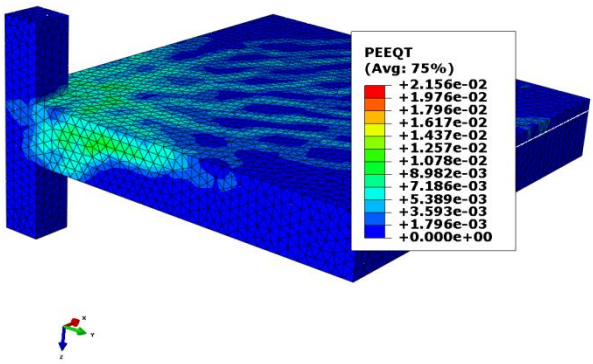

C3D4 elements

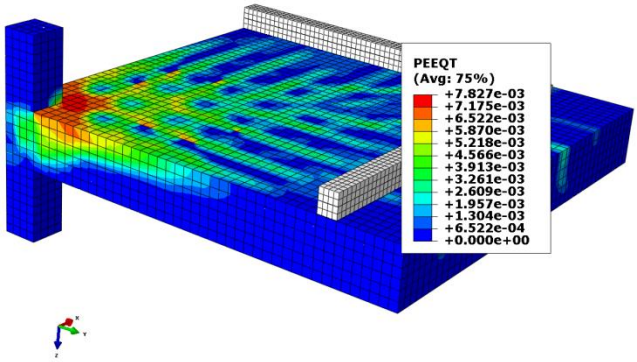

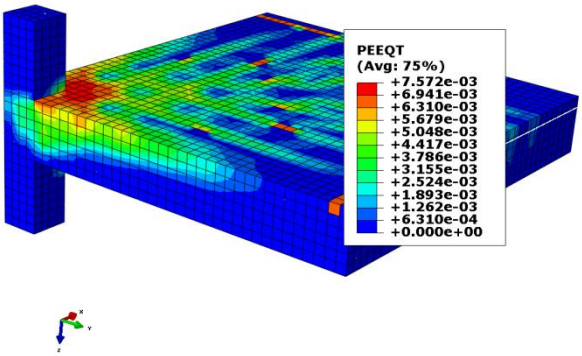

C3D8R elements

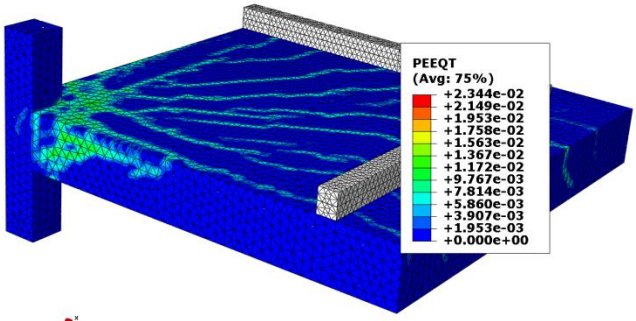

C3D10M elements

C3D8R elements

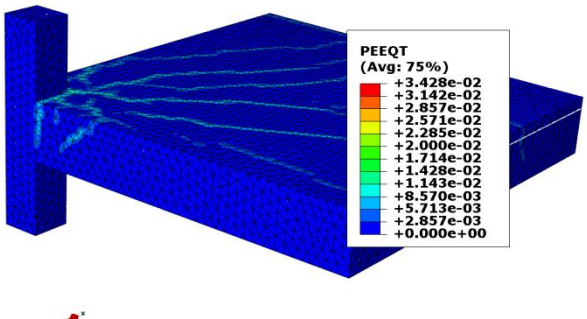

C3D10M elements

Figure 4.43 Cracking at failure for different mesh elements using neoprene and simple supports.

Figure 4.44 illustrates the investigation on the influence of the damage parameters. The damage parameters in the concrete damaged plasticity model take into consideration the degradation of concrete after cracking. The maximum value for the damage parameters in both tension and compression is chosen to be equal to 0.9. The tensile damage parameter at the strain level ε_1 is chosen to be as 0.85. The definition of the compressive damage parameters simplified linear relationship is adopted by given the minimum damage parameter equal to zero at the strain level ε_o and the maximum value 0.9 at the strain level, ε_u. The results obtained from the analysis considering the damage parameters show that the failure of the control specimen SB1 happens earlier compared to the analysis results without considering damage parameters. This becomes clear if one realizes that, the plastic strains are lower compared to the inelastic strains. The latter are considered in the model without the definition of the damage parameters. Without considering the damage parameters, the model behaves with only plasticity, assuming the plastic and inelastic strains to be equal. It could be noted that the damage has no effect at the early stage when the load is 100 kN (see Figure 4.44). This happens because the concrete at this load is almost elastic and no or little damage has occurred. If only tensile damage is considered the

results overestimate the ultimate loading capacity of the slab. When the damaged model is applied to both tension and compression, the model appears to underestimate the ductility of the slab-column connection. Damage in compression seems to have significant effect on the numerical results. Based on the observations of the effect of the damage parameters, it can be said that the damage parameters in the concrete damaged plasticity model in ABAQUS are similar to the hardening parameters used in the classic plasticity theory. For the described problem of punching shear the definition of the damage parameters should not be taken into consideration as it is supposed that the damage parameters are important for cyclic or dynamic loadings where unloading should be defined by plastic strains.

The fracture energy of concrete is related to the strength of concrete and the aggregate size. For the 44 MPa strength of concrete of SB1, the fracture energy is equal to 0.082 N/mm based on the CEB-FIP Model Code 90. The CEB-FIP Model Code 2010 considers a different equation to calculate the fracture energy ($G_f = 73 \cdot {f_{cm}}^{0.18}$). By using this formula the fracture energy for the slab specimen SB1 is equal to 0.148 N/mm. Figure 4.45, illustrates the influence of the fracture energy on the slabs' response. Three different values (0.07 N/mm, 0.082 N/mm and 0.1 N/mm) are studied. The different responses depending on the value of the fracture energy show that the contribution of the tensile behaviour of the concrete to the response of the slab is significant, which is logical since punching shear failure for slabs without shear reinforcement is dependent on the tensile response of concrete. For the following analyses, the fracture energy of 0.082 N/mm is used for the slab specimen SB1. Thus, Eq. (4.16) is used for defining the values of fracture energy for all other specimens.

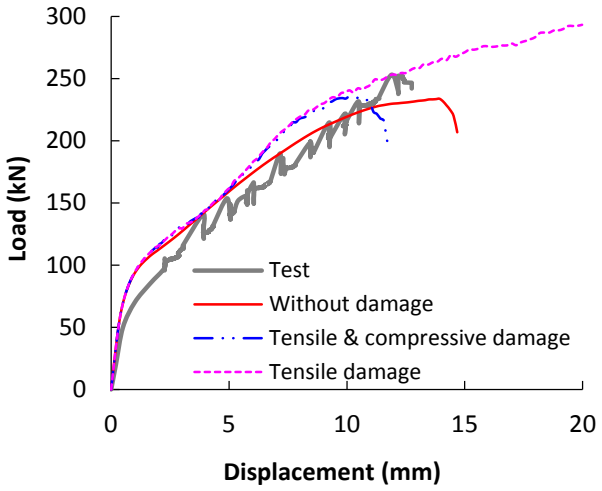

Figure 4.44 Load-displacement response (damage investigation).

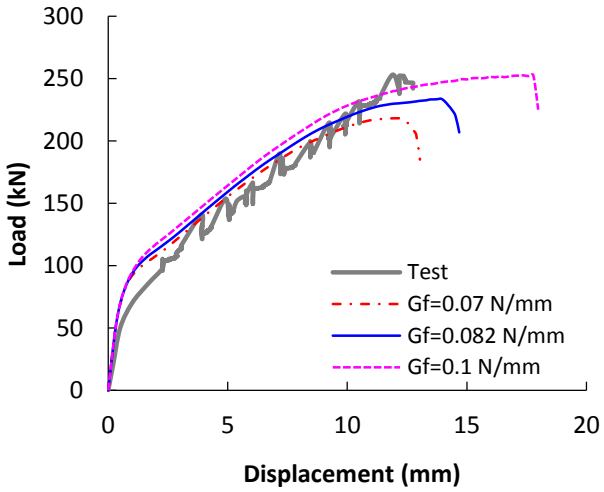

Figure 4.45 Load-displacement response (fracture energy investigation).

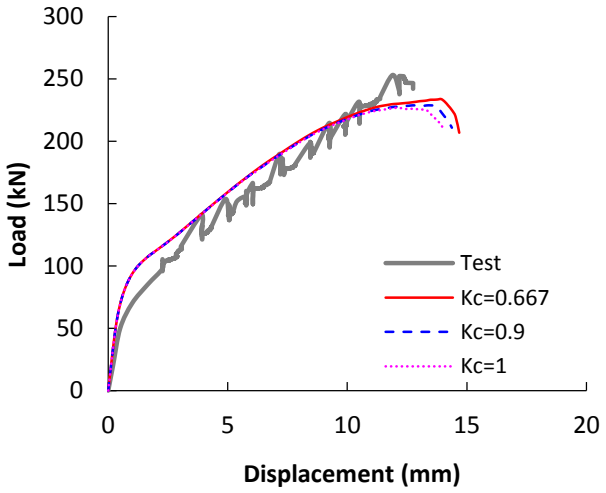

Figure 4.46 Load-displacement response for different shapes of the yield surface.

Figure 4.46 shows the obtained results by performing analyses with different values for the parameter K_c that gives the shape to the yield surface. According to ABAQUS (Analysis user's manual 6.12-3, 2012) the parameter K_c should satisfy the condition: $0.5 < K_c \leq 1$ and the default value that is given for it; is 0.667. Three different values are given for investigation of the parameter, K_c; 0.667, 0.9 and 1. The results indicate that the difference in the load-displacement response of the slab-column connection by giving different shape to the yield surface is not significant. Considering K_c equal to 1, the simulation gives stiffer results and as the parameter K_c is getting less the load and the ultimate displacement are going to be increased. Consequently, for all of the next analyses the parameter K_c is defined with its default value of 0.667.

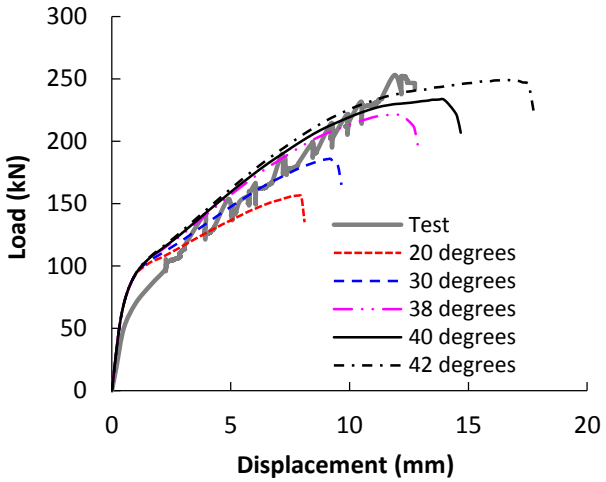

Figure 4.47 Load-displacement response using different values for dilation angle.

The effect of the dilation angle into the model's response is under investigation for the control specimen SB1, as the concrete damaged plasticity model was considered sensitive to the dilatancy in the previous presented examples. Concrete as a brittle material undergoes considerable volume change, which is caused by inelastic strains. This volume change is called dilatancy. In concrete damaged plasticity model the dilatancy can be modeled by defining a value for the dilation angle. According to Chen and Han, 1988, the non-associated flow rule should control the dilatancy, especially for frictional materials such as concrete. Therefore, the dilation angle can be considered as a material parameter for the concrete. Lee and Fenves (1998a) defined the dilatancy parameter α_p equal to 0.2 in the Drucker-Prager plastic potential function (Eq. (4.20)). Other researchers (Wu et al., 2006 and Voyiadjis and Taqieddin, 2009) defined the parameter α_p to range between 0.2 and 0.3.

$$G = \sqrt{2J_2} + \alpha_p I_1 \tag{4.20}$$

Concrete damaged plasticity model uses Eq. (4.21) for the flow potential function, which derives from Eq. (4.20).

$$G(\sigma) = \sqrt{(\varepsilon\sigma_{t0}\,tan\,\psi)^2 + \bar{q}^2} + \frac{1}{3} I_1\,tan\,\psi \tag{4.21}$$

In the analysis of SB1 slab the dilation angle for the model is examined with values varying from 20 degrees to 42 degrees (see Figure 4.47). It can be shown that the difference in ultimate load is small between 38 to 42 degrees. Therefore, the dilation angle is chosen to be set as 40 degrees because it provides a good agreement between the test and numerical results in terms of load-deflection. In order to be accurate for the calculation of the dilation angle let's consider in ABAQUS, the asymptote line for the potential function according to Eq. (4.22).

$$G = q + ptan\psi - c = 0 \tag{4.22}$$

By calculating the derivatives of the function G we can have a relationship between the angle θ and ψ. $dG/dp = \tan\psi$ and $dG/dq = 1$, and by considering the Figure 4.48, $\tan\theta = (dG/dp)/(dG/dq) = tan\psi/1 = tan\psi$.

With the same way we can consider Eq. (4.22), where $q = \sqrt{3J_2}$ and $p = I_1/3$. By calculating the derivatives of the function G, $dG/dp = 3a_p$ and $dG/dq = \sqrt{2/3}$, and then by considering the Figure 4.48, $\tan\theta = (dG/dp)/(dG/dq) = 3a_p/\sqrt{2/3} = 3.67a_p$. Therefore, the relationship between the angle θ and ψ is the following:

$$tan\theta = tan\psi = 3.67a_p \tag{4.23}$$

For a given value of $a_p = 0.2$, $tan\psi = 3.67 \cdot 0.2 = 0.734 \rightarrow \psi = 36.3°$.

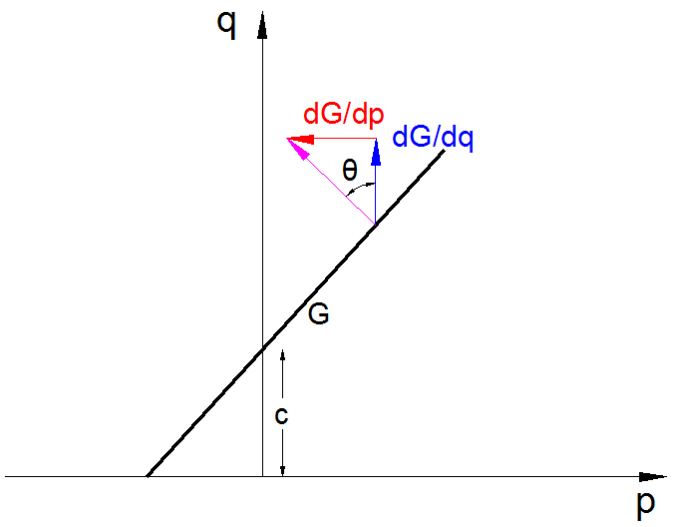

Figure 4.48 Linear yield surface.

4.5 Summary and Conclusions

In this chapter, the concrete damaged plasticity model is presented and used into some examples in order to verify its accuracy. The appropriate calibration of the model is considered by evaluating its parameters. Selected tests by Kupfer et al. (1969) in plain concrete specimens are analyzed using the concrete damaged plasticity model. These specimens were tested under uniaxial/biaxial compression, uniaxial/biaxial tension and tension-compression. Then, a reinforced concrete shear panel tested by Vecchio (1999) is analyzed in order to verify the accuracy of the concrete damaged plasticity model simulating shear stresses-strains. A reinforced concrete beam without stirrups tested by Leonhardt and Walther (1962) is also simulated and analyzed. Two reinforced concrete beams; one with stirrups and the other without stirrups, are analyzed in order to further study the effect of the dilation angle in the concrete damaged plasticity model. The main outcome from the presented examples is that the concrete modelling is very sensitive to the chosen dilation angle value. As the amount of the reinforcement

increases, higher value for the dilatancy is required in order the numerical results to be in good agreement with the experimental. Finally, the model is used for the analysis of a reinforced concrete flat slab (SB1) tested by Adetifa and Polak (2005) that failed in punching shear. This specimen is considered as the control specimen and its parametric investigation in ABAQUS proposes that the calibrated numerical model can be effectively used for the all of the punching shear analyses in this dissertation.

Specimen SB1 is analyzed in both ABAQUS/Standard and ABAQUS/Explicit in order to verify the most appropriate type of analysis for simulating punching shear problems. ABAQUS/Standard is able to provide convergence after the introduction of the viscosity parameter that provides extra relaxation time to the concrete model. However, the chosen relaxation time requires a parametric investigation in order to be a small value without changing the specimen's response. Both types of analysis (static in ABAQUS/Standard and quasi-static in ABAQUS/Explicit) offer similar results and are in good agreement with the experiment. The quasi-static analysis is chosen in this work, herein, due to the less computation time that requires. A mesh convergence study is considered in SB1 specimen. The smeared crack approach used in ABAQUS model appears strain localization due to strain softening nature of concrete that depends on the dimensions of the elements. Three different mesh sizes (15 mm, 20 mm and 24 mm) are used in the analysis of the specimen SB1 in order to investigate the mesh sensitivity of the FEA model. The chosen mesh values should be larger than the aggregate size (10 mm) however not to too large resulting in a coarse mesh. However, the mesh size of 20 mm gives the most accurate results compared to the test load-deflection response. The mesh size of 20 mm is chosen in all subsequent simulations of all slabs. This choice has been based not only on the load-deflection responses but also on the examination of the cracking patterns. In that study,

further investigation is performed analyzing the specimen (SB1) by changing its boundary conditions. After analyzing the SB1 with simple supports, neoprene is also simulated around the bottom edges of the slab as happened in the real test. Neoprene is a hyper-elastic material considered as isotropic and nonlinear. Investigation using different elements is performed on the slab SB1. Three different types of elements are adopted in the study: 3D linear hexahedral 8-noded (C3D8R) with reduced integration elements, 3D 4-noded linear tetrahedral elements (C3D4) and 3D 10-noded quadratic tetrahedral elements modified (C3D10M). A comparison between the numerical results obtained from the different type of elements and boundary conditions and considering also the required computational time, the simple supports with the C3D8R elements are chosen for all subsequent analyses. Damage parameters are also investigated in the material modelling of concrete in specimen SB1. For the described problem of punching shear the definition of the damage parameters should not be taken into consideration. It is supposed that the damage parameters are important for cyclic or dynamic loadings where unloading should be defined by plastic strains. Finally, the dilation angle is further examined in the analysis of the SB1 slab. The 40 degrees seem to describe in an appropriate way the load-deflection response of the slab SB1 compared to the experimental results. This value (40 degrees) is going to be adopted for the next presented numerical simulations of all slabs.

Chapter 5

Reinforced concrete slabs without shear reinforcement

5.1 Introduction

After the investigation and the calibration of the concrete damaged plasticity model presented in the previous chapter; herein, nonlinear finite element analyses of reinforced concrete slab-column connections under static and pseudo-dynamic loadings are conducted to investigate their failures modes in terms of ultimate load and crack patterns. The 3D finite element analyses (FEA) are performed with the appropriate modelling of element size and mesh, and the constitutive modelling of concrete. The material parameters of the damaged plasticity model in ABAQUS are calibrated based on the test results of an interior slab-column connection (SB1) that was presented on the previous chapter. The predictive capability of the calibrated model is demonstrated by simulating different slab-column connections without shear reinforcement. Interior slab-column specimens under static loading, interior specimens under static and reversed cyclic loadings, and edge specimens under static and horizontal loadings are examined. The comparison between experimental and numerical results indicates that the calibrated model properly predicts the punching shear response of the slabs.

Five slab-column specimens (SB1, SW1, SW5, XXX and HXXX) without shear reinforcement are analyzed. The slab, SB1, is an interior slab-column connection that was tested

by Adetifa and Polak (2005) under static loading through the column. The slabs, SW1 and SW5, are interior slab column connections that were tested by Bu and Polak (2009) under gravity static loading through the column and pseudo seismic horizontal loading. Finally, the specimens, XXX and HXXX, are edge slab-column connections that were tested by El-Salakawy (1998) under vertical loading through the column and an unbalanced moment at the columns. The numerical results are compared to the test results in terms of deflections, strength and crack patterns. The aim of this chapter is to present the effectiveness of the proposed calibrated finite element model in describing and analyzing punching shear tests of slabs without shear reinforcement.

5.2 Test specimens

The test specimens used for the finite element analyses have no shear reinforcement and the height of all slab specimens is 120 mm. These specimens are isolated slab-column connections loaded through the column stub and simply supported along the edges that represent the lines of contra flexure in the parent slab-column system. The first analyzed specimen is the interior connection (SB1) that is tested under static loading through the column. The material properties and the dimensions of the slab SB1 are described in the previous chapter. Then, the two interior slab-column connections (SW1, SW5) that were tested under gravity static and pseudo seismic loadings are analyzed. These slabs were loaded in two stages during the test. In the first stage, a vertical load was applied through the top column with a loading rate of 20 kN/min. The slab SW1 was loaded up to 110 kN vertical load, the slab SW5 was loaded up to 160 kN. Then, the vertical loads were kept constant and the two horizontal actuators started to apply horizontal drift to the top and bottom columns at a distance 565 mm from the slab's faces following a specific loading path. The total height of the columns is 700 mm. The gravity shear

ratio, V/V_n, for the slab SW1 is 0.54 and for the slab SW5 0.68, where $V_n = 0.33 \cdot \sqrt{f_c'} \cdot b_o \cdot d$ (MPa), b_o denotes the perimeter length of the critical section and d the effective thickness of the slab equal to 90 mm. All interior connections have overall dimensions in plan 1800x1800 mm with simple supports at 1500x1500 mm. Corners were restrained from lifting during the test. Finally, the two edge slab-column connections (XXX, HXXX) are analyzed. These slabs were tested under a vertical shear force (V) that was applied on the top of the upper column and two horizontal forces (H), leading to the unbalanced moment, that were applied to the columns in three stages at a distance 600 mm from the slab's faces. The total height of the columns is 700 mm. The slabs' in-plane dimensions are 1540x1020 mm. In the first stage of testing, the loads were increased with a rate of 2.5 kN/min. until reaching the service load, $V = 43\ kN$. Then the loads were cycled 10 times between the dead loads and the dead plus the live loads, in order to simulate the repetition of the live loads. At the final stage, the loads were increased at 1.5 kN/min. rate until failure. The ratio between the unbalanced moment (M) produced by the two horizontal forces (H) and the vertical shear force (V) is equal to 0.3 m for the specimen XXX and 0.66 m for the specimen HXXX. These ratios were kept constant during the whole loading process. The dimensions of the specimens and the loading process are presented in Figure 5.1.

The material properties of each tested slab are presented in Table 5.1. The compressive strength of concrete was found from the concrete cylinders, tested at the time of the slabs' tests (over 28 days), and the tensile strength was obtained from the split cylinder tests. The yield strength for the tension and compression longitudinal reinforcement was the same for the slabs SB1, SW1 and SW5. Slabs XXX and HXXX had different yield longitudinal strength for the tension and compression reinforcements. Table 5.2 presents the material properties of the reinforcement. In ABAQUS, the reinforcement is modelled with a uniaxial stress-strain relation

with Young's modulus (E_s) and Poisson's ratio (v) equal to 200000 MPa and 0.3, respectively. Plastic behaviour is defined in a tabular form, including yield stress and corresponding plastic strain. The plastic properties are defined based on the test results with a bilinear strain hardening yield stress - plastic strain curve.

All specimens failed in punching shear. The information regarding their failure loads and comparisons with the simulation results, are presented in Section 5.4 together with the numerical results.

Table 5.1
Material properties of the tested slabs.

Slab specimen	Compressive strength of concrete (MPa)	Tensile strength of concrete (MPa)	Yield strength of flexural reinforcement (MPa)
SB1	44	2.2	455
SW1	35	2	470
SW5	46	2.2	470
XXX	33	1.9	545(tension), 430(compression)
HXXX	36.5	2	545(tension), 430(compression)

Table 5.2
Material properties of the reinforcement.

	Slab specimen	$f_y\ (MPa)$	ε_y	$f_t(MPa)$	ε_t
Interior	SB1	455	0.0023	650	0.25
	SW1, SW5	470	0.0024	650	0.20
Edge	XXX, HXXX (compression)	430	0.0022	600	0.15
	XXX, HXXX (tension)	545	0.0027	900	0.10

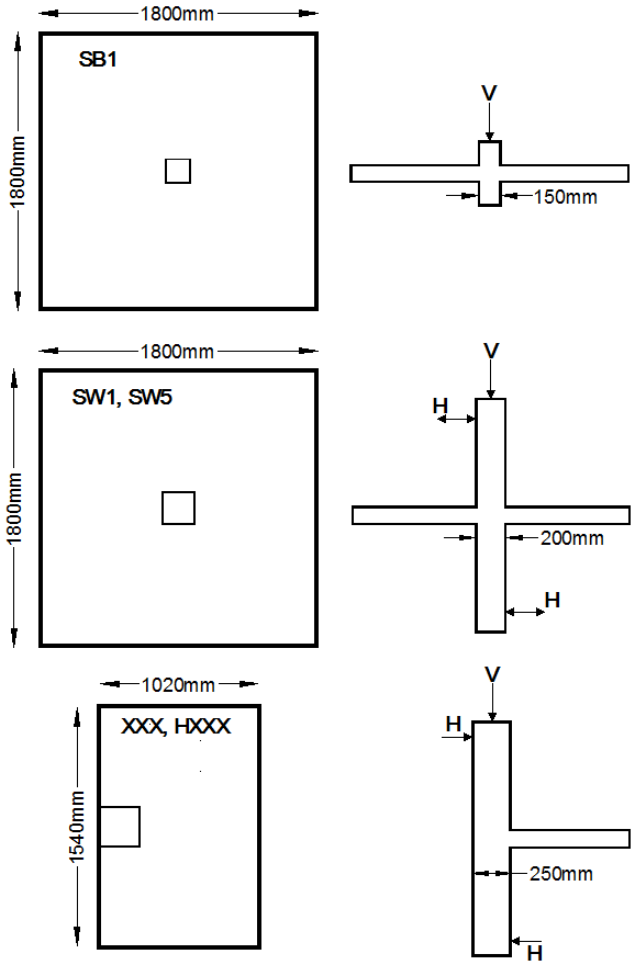

Figure 5.1 Schematic drawings of the specimens - dimensions & loading.

5.3 Finite Element Simulations

By considering specimens' symmetry, one quarter of the control specimen SB1 and half of all of the other slabs (SW1, SW5, XXX and HXXX) are used for the simulations. 8-noded hexahedral (brick) elements are used for concrete with reduced integration (C3D8R) to avoid the shear locking effect. 2-noded linear truss elements (T3D2) are used to model reinforcements. The embedded method is adopted to simulate the bond between the concrete and the reinforcement, assuming perfect bond. 6 brick elements are considered through the thickness of the 120 mm slabs' with all concrete elements having the same size of 20 mm. The specimen SB1

has 9211 elements and 11194 nodes, the specimens SW1 and SW5 had 22028 elements and 26767 nodes and the specimens XXX and HXXX are meshed with 18150 elements and 22123 nodes. Restraints are introduced at the bottom edges of the specimens in the direction of the applied load. The summation of the reactions at the edges, where the boundary conditions are introduced, yields the reactions equal to the punching shear loads. Figure 5.2 shows the geometry and the boundary conditions of the specimens that are used for the simulations. The control specimen SB1 is analyzed using both static analysis in ABAQUS/Standard and quasi-static analysis in ABAQUS/Explicit. In the static analysis, the displacement is applied through the column stub, while in the quasi-static analysis a low velocity is applied. In the quasi-static analysis the load is applied so slowly, that the structure deforms also slowly and the inertia force is ignored. This last type of analysis is used for all specimens. The velocity is increasing with a smooth amplitude curve from 0 (mm/sec) to a different velocity (mm/sec) depending on the specific slab. Slabs SB1, SW1, SW5 and XXX are loaded by applying a velocity that increases from 0 mm/sec to 40 mm/sec, such that the slab displaces at a rate of 20 mm/sec. Slab HXXX is loaded by applying a velocity that increases from 0 mm/sec to 20 mm/sec in order the center of the slab to displace 10 mm/sec.

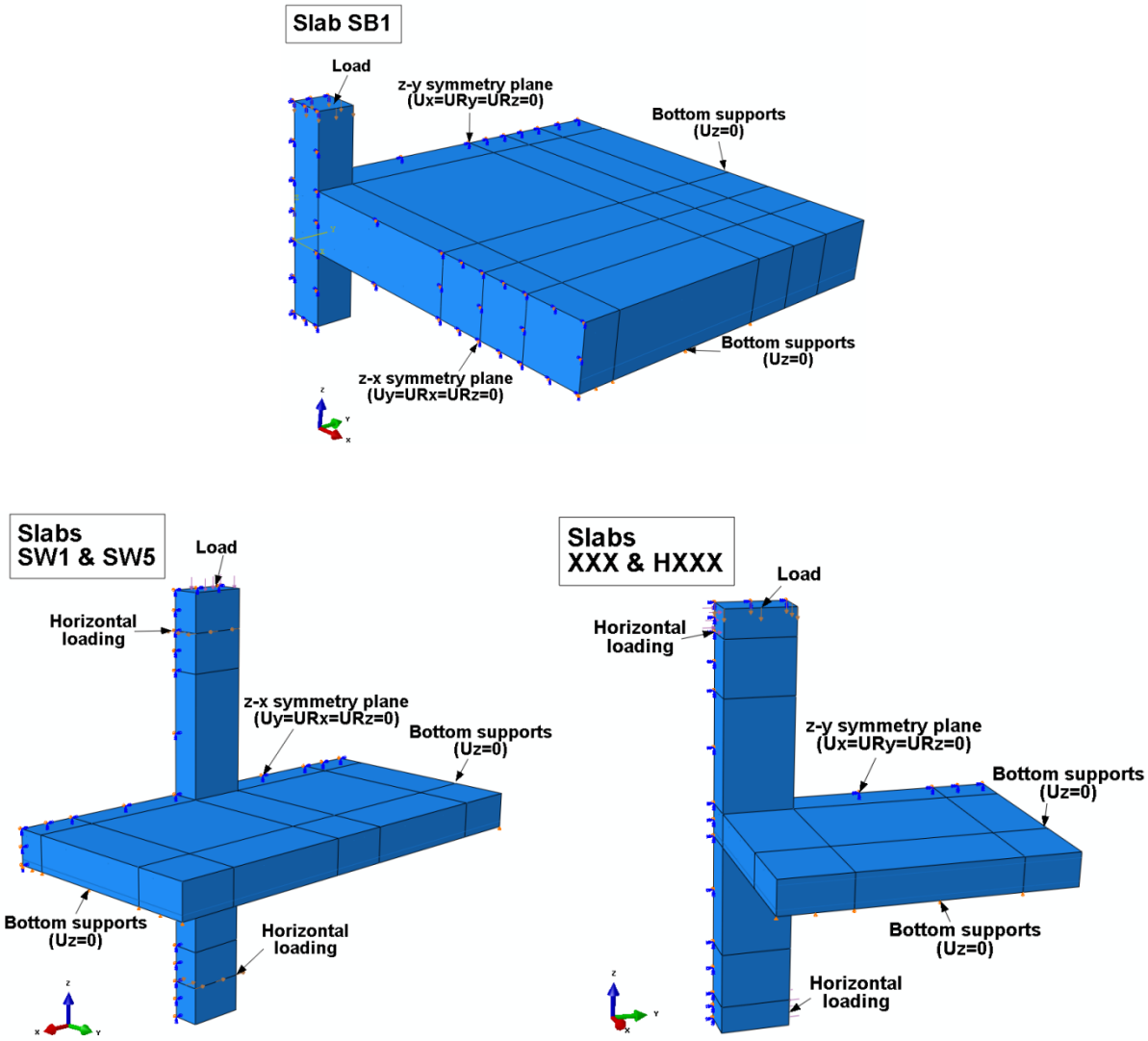

Figure 5.2 Geometry and boundary conditions of the slabs.

At this point, some details about the adopted finite elements and the analysis type are discussed. In discrete finite element modelling, the concrete is modelled by using 3D solid elements and the reinforcement is modelled with truss or beam elements. The truss or beam elements are generally used to simulate the internal reinforcing bars. In some cases where planner reinforcement such as fiber reinforced polymer (FRP) is required in modelling, shell or membrane elements are used. Reinforcement such as steel bolts could also be modelled using

solid 3D elements. The bond between concrete and reinforcement can be modelled with two ways: a) a bond element (usually spring element) is considered at the interface and b) a perfect bond is assumed, where concrete and steel share the same nodes. The perfect bond method (embedded method) is computationally more efficient especially when it is considered for smeared cracking approaches as the ABAQUS does. The finite elements that are adopted and used in this thesis include: continuum, shell, beam and truss elements. The 3D continuum/solid stress-displacement elements are considered herein for modelling the concrete slab and especially the linear (first-order) 8-noded hexahedra/brick (C3D8R) reduced-integration elements. In these elements, each node has three dimensional and translational degrees of freedom. These elements have nodes only at their corners using linear interpolation in each direction and this is why they called linear or first-order elements. The first-order elements can predict the same behaviour with the quadratic (second-order) elements; however a finer mesh it is required. Regarding the formation of the elements, in the absence of an adaptive mesh, all of the stress-displacement elements are using the Lagrangian description of their behaviour, where the material is associated with the element and remains associated with the element during the analysis. The ABAQUS for the integration uses Gaussian quadrature and evaluates the response of the material at each integration point of each element. The reduced integration elements use one integration point less in each direction compared to the fully integrated elements. Fully integrated linear elements appear shear locking causing the elements to be too stiff in bending, thus reduced integration linear elements are preferable. The shear locking in linear fully integrated elements denotes that the shear stress in the elements under pure bending is nonzero. The edges of the linear elements cannot curve in bending. Thus, the horizontal dotted lines that pass through the integration points change in length (Figure 5.3). The vertical dotted lines do not

change in length as it is assumed that the displacements are small. Thus, σ_{22} at all integration points is zero. However, the angle between the vertical and horizontal lines has changed (initially was 90º) indicating that the shear stress σ_{12} at the integration points is not zero. This does not happen under pure bending, where the shear stress is zero. For that reason, reduced integration linear elements are used. The reduced integration linear elements have only one integration point located at the centroid of the element. Considering again one single element subjected to pure bending, this time linear reduced integration element (see Figure 5.4), the dotted lines do not change in length and the angle between them remains 90º showing that all components of stress at the integration point are zero. However, linear reduced-integration elements suffer from their own numerical problem called hourglassing (mesh instability) that results these elements to be too flexible. The bending mode of deformation of the linear reduced integration elements is a zero energy mode as there is no strain by the distortion of the element. That means that the element cannot resist that deformation because it has no stiffness in this mode. In order to avoid or limit that effect, it is required the linear reduced integration elements to have a fine mesh. According to ABAQUS (Analysis user's manual 6.12-3, 2012) reasonable results suggest that at least four elements should be considered through the thickness of a structure carrying bending loads. The fine mesh of the linear reduced integration elements will also help to avoid the distortion of these elements that many times happens. Truss elements that are used for modelling the reinforcement are rods that can carry only tensile or compressive loads, while they do not have resistance in bending. The three dimensional truss elements used in this research have three degrees of freedom.

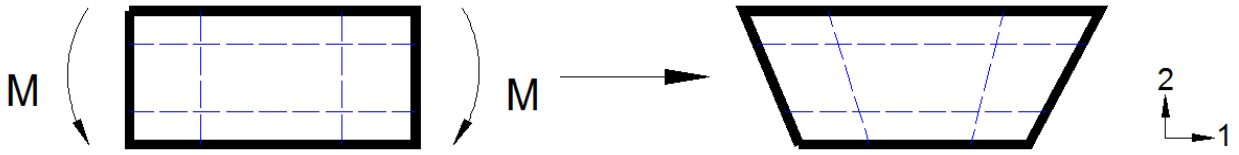

Figure 5.3 Deformation of a linear fully integrated element subjected to bending moment.

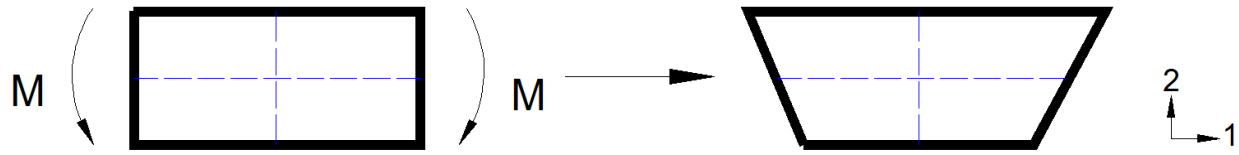

Figure 5.4 Deformation of a linear reduced integration element subjected to bending moment.

ABAQUS has two main analysis products, the ABAQUS/Standard and the ABAQUS/Explicit. ABAQUS/Standard solves the equations of the system implicitly at each solution increment, while ABAQUS/Explicit goes with the solution forward through small time increments without solving the equations of the system at each increment. ABAQUS/Standard uses a stiffness-based solution technique that is always stable, while ABAQUS/Explicit uses an explicit integration solution technique, which is conditionally stable. Thus, the characteristics of each procedure (implicit or explicit) should define which method is the most appropriate for a given structural problem. It can be said herein, that some analysis problems even if they can be effectively solved in ABAQUS/Standard, they appear difficulty converging because of the material complexity, resulting in many iterations. Such analyses become expensive in ABAQUS/Standard because each of the iterations demands many equations that have to be solved. On the other hand, ABAQUS/Explicit determines the solution without iterating by

explicitly taking advantage of the kinematic state of the previous increments, making the analysis more efficient and less time consuming.

Each structural analysis in ABAQUS can be linear or nonlinear. A nonlinear structural problem shows stiffness changes as it deforms. The sources of nonlinearity in structural mechanics are three: a) material nonlinearity, b) boundary nonlinearity and c) geometric nonlinearity. ABAQUS/ Standard uses the Newton-Raphson method in order to get into the solutions of the nonlinear problem. The solution is found by applying the loads gradually and incrementally by having many load increments. Then, it finds the approximate equilibrium at the end of each load increment, where the summation of all of the incremental responses is the approximate solution of the nonlinear analysis. ABAQUS/Explicit defines a solution to the dynamic equilibrium without iterating but by explicitly using the kinematic state of the previous increment. Table 5.3 provides the summary of the concrete material parameters used in concrete damaged plasticity model in ABAQUS for each slab-column connection and details regarding the type of the connection and loading.

Table 5.3
Details of the simulated slabs in ABAQUS.

	Slab specimen	**Type of loading**	f'_c (MPa)	f'_t (MPa)	E_c (MPa)	G_f (N/mm)
Interior	SB1	Static	44	2.2	36483	0.082
	SW1	Static and reversed cyclic	35	2	32538	0.072
	SW5	Static and reversed cyclic	46	2.2	37303	0.085
Edge	XXX	Static and horizontal	33	1.9	31595	0.081
	HXXX	Static and horizontal	36.5	2	33228	0.085

5.4 Finite Element Analysis Results

Figure 5.5 compares the FEA and test results in terms of load-displacement for the control slab SB1. The simulation gives brittle punching shear failure as happened in the experiment. The predicted ultimate load and displacement by the simulation and the test are presented in Table 5.4. The FEA shows a stiffer response compared to the test due to the simple supports that are adopted. The crack pattern on the tension side of the slab at failure is presented in Figure 5.6. The cracking propagates inside the slab adjacent to the column. It starts tangentially near the column and then extends radially as the load increases. At the ultimate load the punching shear cone is visible due to the sudden opening of the cracks. Concrete damaged plasticity model assumes that the cracking initiates when the maximum principal plastic strain is positive. The orientation of the cracks is considered to be perpendicular to the maximum principal plastic strains and thus, the direction of the cracking is visualized through the maximum principal plastic strains. The yielding of the flexural reinforcement occured at the failure in both test and FEA. The tensile longitudinal reinforcement yielded under the column at the failure load.

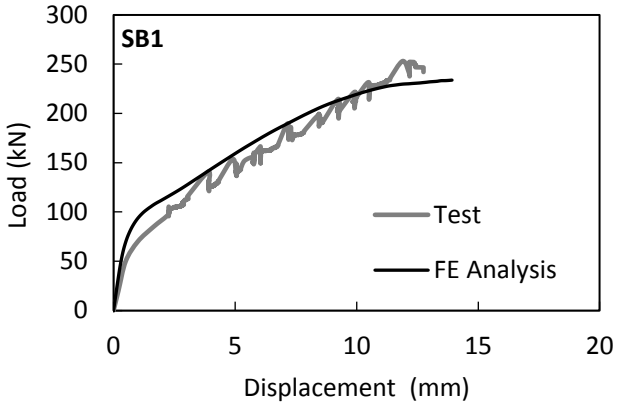

Figure 5.5 Load-displacement curves for slab SB1.

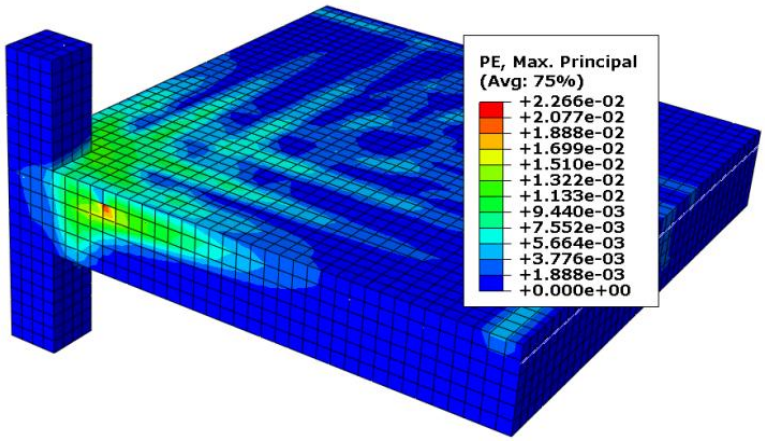

Figure 5.6 Cracking pattern on tension surface at ultimate load for slab SB1 (Load applied upwards on the column) .

Table 5.4
Test and FEA results.

Slab specimen	Test results		FEA results	
	Failure load (kN)	Displacement at failure (mm)	Failure load (kN)	Displacement at failure (mm)
SB1	253	11.9	234	13.9

The maximum tensile principal stresses are shown in Figure 5.7 for the two surfaces of the slab at the failure. The tensile principal stresses can be used in FEA in order to show the crack patterns. However, the maximum plastic equivalent principal strains, as they are presented in Figure 5.6, give a better representation of the cracks. For that reason the strains and not the stresses are going to be used for showing the crack patterns for all of the following analyses.

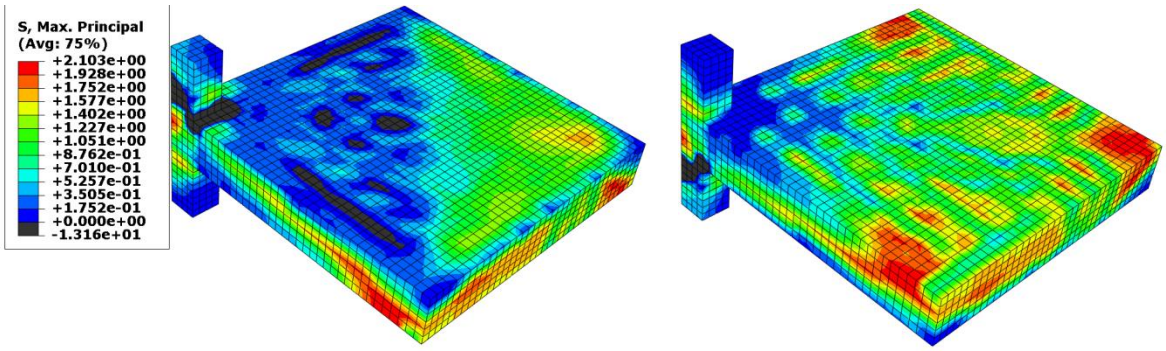

a) Compressive surface (top). b) Tensile surface (bottom).

Figure 5.7 Maximum tensile principal stresses in concrete at the failure.

The calibrated model for specimen SB1 is also applied for the analyses of slabs SW1 and SW5. These slabs were tested under gravity load and horizontal reversed cyclic displacements. The response of the specimens is described by means of horizontal load and drift response. The hysteretic loops in the specimen exhibited pinching, denoting strength and stiffness degradation and subsequently low energy dissipation capacity. In contrast, when the cyclic loading analysis was performed in ABAQUS, the hysteretic loops obtained from the analyses did not exhibit the pinching effect. It must be mentioned that the complexity in constitutive modelling of concrete and the adoption of perfect bond between concrete and reinforcement, created problems in the hysteretic simulations in ABAQUS. Alternatively, in this research, monotonic loading analysis is presented and the results of the finite element simulations show good agreement compared to the experimental results (Figure 5.8 and Figure 5.9). Simulations of specimens show brittle failure after obtaining maximum lateral load similar to the test maximum loads. Figure 5.10 and Figure 5.11 present the crack patterns at failure for slab SW1 and SW5, respectively. Table 5.5 compares the experimental and numerical results in terms of ultimate lateral failure load and drift ratio at the failure load. Yielding of the flexural reinforcement during the test, for the specimen

SW1 appeared first at the tension reinforcement under the column in the direction of the cyclic loading at drift ratio 1.33%, while for the specimen SW5 at the compression reinforcement under the column in the direction of the cyclic loading at drift ratio 1.04%. The FEA results have proved similar yielding of the flexural reinforcement.

Table 5.5
Gravity shear ratio, test and FEA results.

Slab specimen	V/V_n	Test results		FEA results	
		Peak lateral load (kN)	Drift ratio at peak lateral load (%)	Peak lateral load (kN)	Drift ratio at peak lateral load (%)
SW1	0.54	56	2.8	55	2.7
SW5	0.68	60	2.6	61	2.4

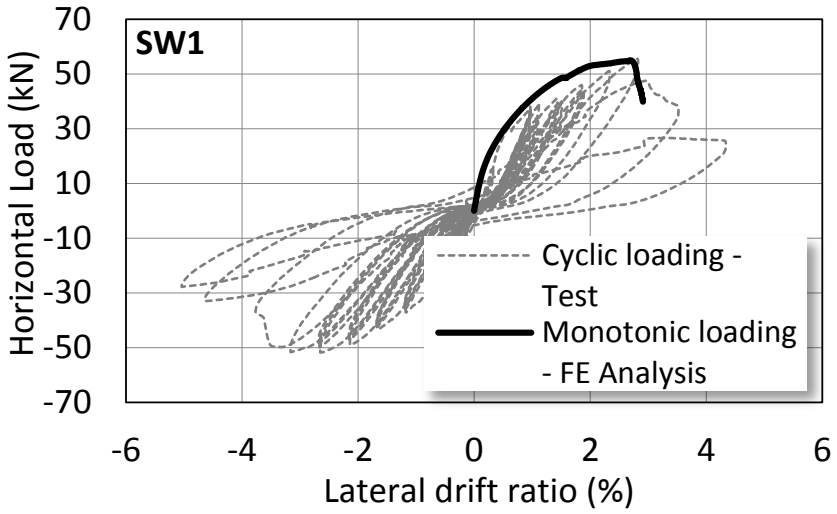

Figure 5.8 Horizontal load versus lateral drift ratio for specimen SW1.

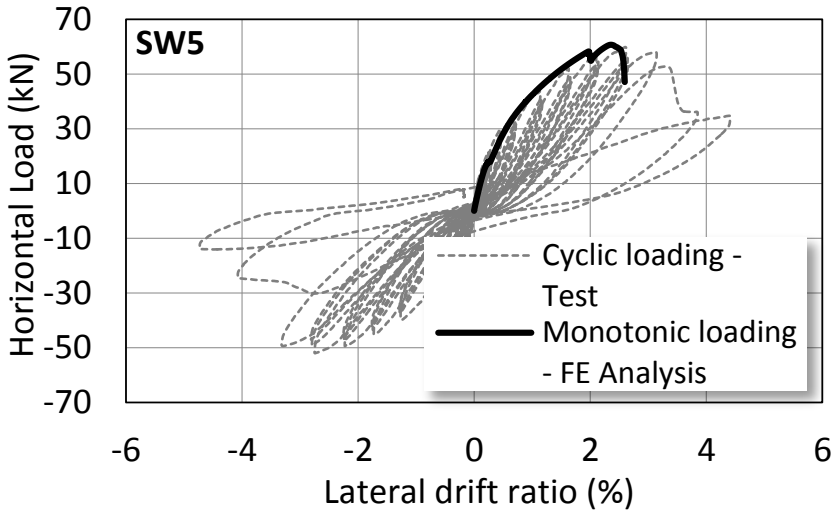

Figure 5.9 Horizontal load versus lateral drift ratio for specimen SW5.

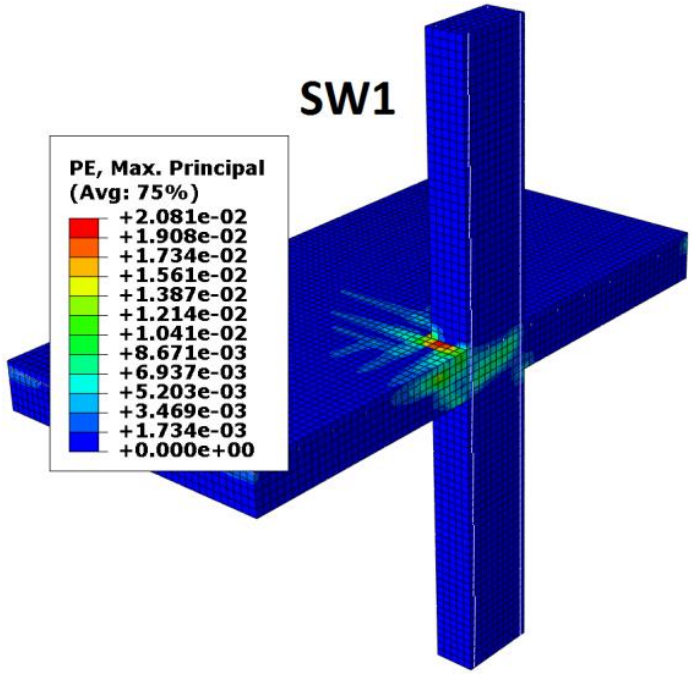

Figure 5.10 Cracking pattern at ultimate load for specimen SW1.

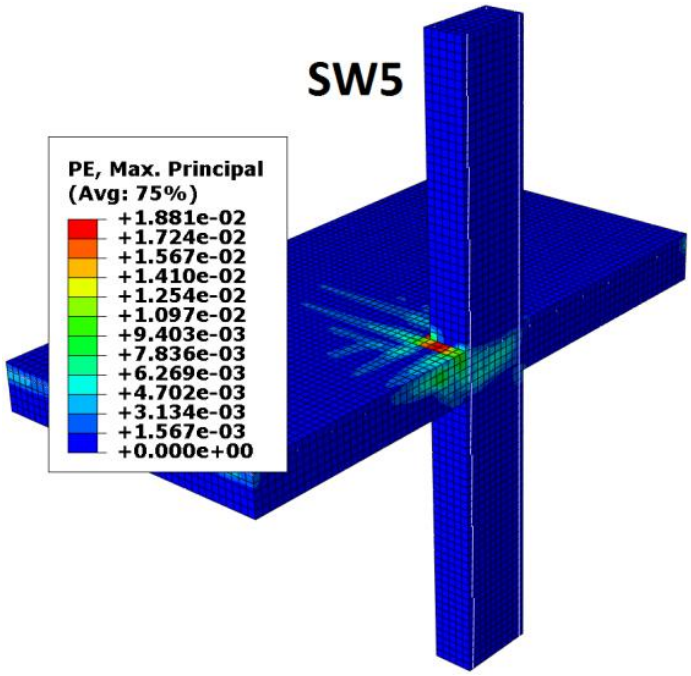

Figure 5.11 Cracking pattern at ultimate load for specimen SW5.

The edge slab-column specimens are examined using the FEA model identical to the one used for SB1. These slabs, tested under constant gravity load to horizontal moment ratios, providing information for the effect of the unbalanced moments on punching shear. Table 5.6 shows the comparison between the slabs XXX and HXXX in terms of failure horizontal load and displacement and subsequently compares the tested and FEA results. Figure 5.12 and Figure 5.13 present the FEA load-displacement results compared to the test results for the slab XXX and HXXX, respectively. All of the simulated responses, in terms of ultimate load and displacement are in good agreement with the results observed from the experiments. For the slab XXX the relative error is within 10% percent, however the relative error for the specimen HXXX is within 20% percent. This difference may be attributed to many reasons. The numerical load-deflection response of the slab HXXX is stiffer compared to the tested response due to possible initial pre-

cracking prior to the test (e.g. shrinkage, handling). It is important to state herein that the numerical results of slab HXXX in terms of failure displacement are in good agreement with the test results. The cracking propagation at the ultimate load for these slabs is presented in Figure 5.14 for the specimen XXX and in Figure 5.15 for the slab HXXX. The FEA cracking of specimen HXXX is concentrated near the column with only some developed radial cracks. The same cracking pattern was observed in the test. The comparison between the predicted crack patterns of slabs XXX and HXXX, show the effect of the higher unbalanced moment at the slab-column connection. The increased unbalanced moment in slab HXXX, reduce the ultimate punching shear load and deflection resulted to a more sudden and brittle punching shear failure. The tensile longitudinal reinforcement under the column has yielded in tests and FEA for both XXX and HXXX slabs. The reinforcement of the slab XXX yielded at 78 kN load and the reinforcement of the slab HXXX yielded at 48 kN load during the tests. The FEA showed almost the same results. The reinforcement of the slab XXX yielded at 73 kN load and the reinforcement of the slab HXXX yielded at 55 kN load for FEA. Good agreement is observed for the activation of the flexural reinforcement in the test and analysis before and after the yielding.

Table 5.6
M/V ratios, test and FEA results.

Slab specimen	M/V (m)	**Test results**		**FEA results**	
		Failure horizontal load (kN)	Displacement at failure load (mm)	Failure horizontal load (kN)	Displacement at failure load (mm)
XXX	0.3	125	15.06	112	17.69
HXXX	0.66	69	5.96	84	6.77

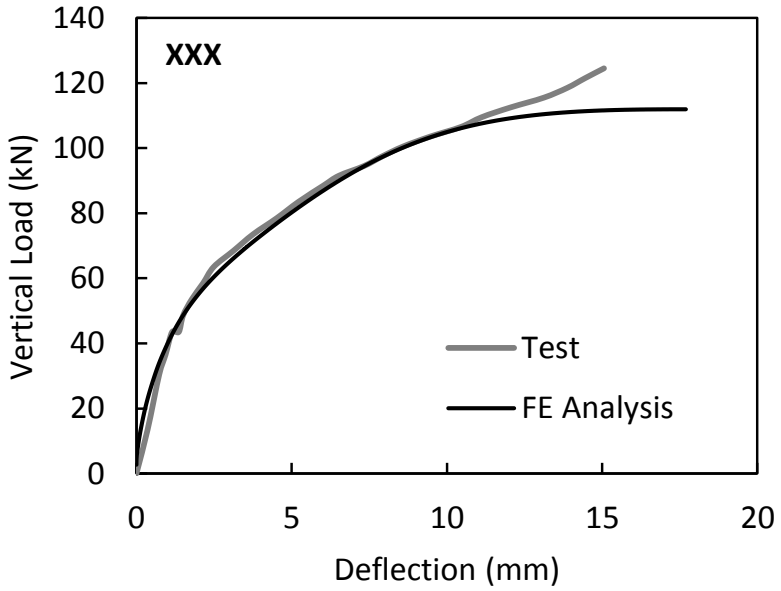

Figure 5.12 Vertical load-deflection for edge slab XXX.

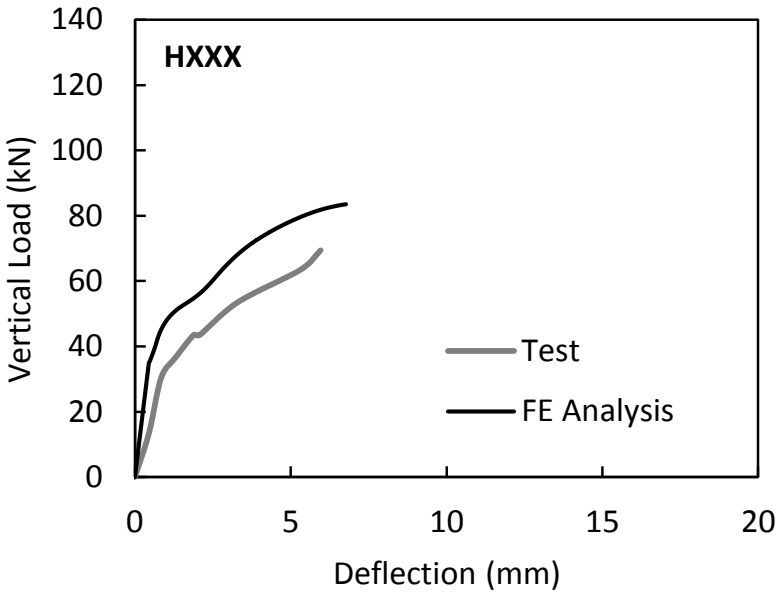

Figure 5.13 Vertical load-deflection for edge slab HXXX.

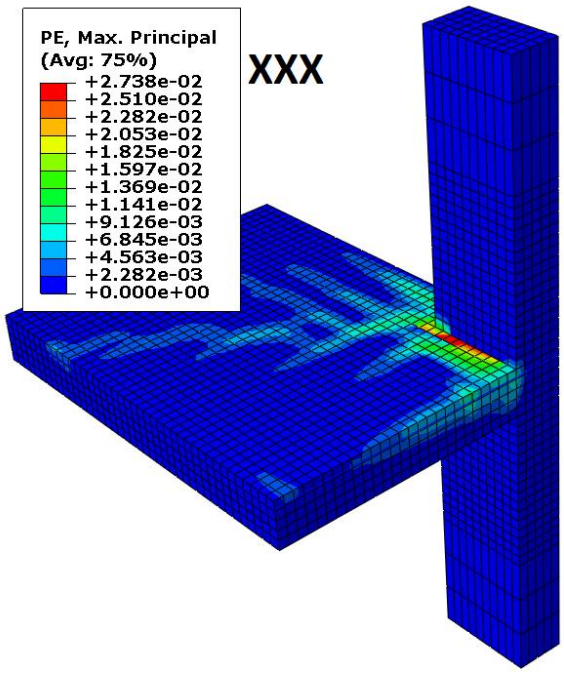

Figure 5.14 Cracking pattern at the ultimate on the tension surface for edge slab XXX.

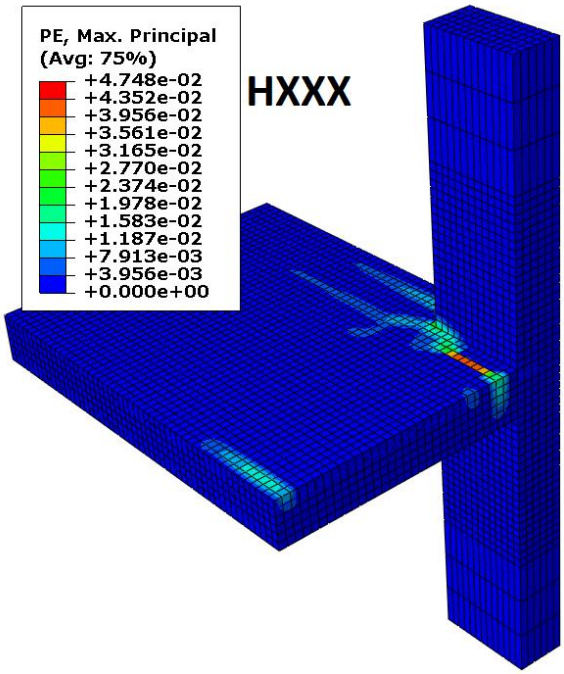

Figure 5.15 Cracking pattern at the ultimate on the tension surface for edge slab HXXX.

5.5 Summary and Conclusions

Finite element analyses with the concrete damaged plasticity model in order to predict the punching shear behaviour of slabs without shear reinforcement, are presented. In particular, five different slab-column connections without shear reinforcement are simulated and analyzed in terms of ultimate load and crack patterns. The constitutive formulation adopted herein is the calibrated damaged plasticity model. The results of the analyses are compared to the test results showing good agreement. That predicts the capability of the calibrated model to simulate the response of reinforced concrete flat slabs without shear reinforcement in terms of ultimate load and cracking pattern. Chapter 6 that follows examines the capability of the calibrated FEA concrete model in reinforced concrete slabs with shear reinforcement. The shear bolt system is modelled in the numerical analyses and a critical review on the code provisions for the shear reinforced slabs is provided.

Chapter 6

Reinforced concrete slabs with shear reinforcement

6.1 Introduction

Nonlinear finite element analyses (FEA) of reinforced concrete slab-column connections with shear reinforcement that failed in punching shear and/or flexure tested under static loading are conducted in order to investigate their failures modes in terms of ultimate load and crack pattern. The damaged plasticity model in ABAQUS previously calibrated based on test results of slabs without shear reinforcement is implemented in all studies. The predictive capability of the calibrated model in slabs without shear reinforcement is demonstrated herein by simulating slab-column connections with shear reinforcement. Four interior specimens are examined and the comparison between experimental and numerical results indicates that the developed model predicts well the punching shear response of these slabs. The proper modelling of the punching shear reinforcement in order to contribute in an increase of punching shear capacity of the slabs is essential in the FEA. Four different modelling approaches for the shear bolts are presented and discussed. The analyses of these approaches are performed on the specimen (SB4) and the comparison between these modelling approaches based on the ultimate load, ductility and crack pattern of the slab SB4 have shown the most appropriate modelling approach that can be used for all other analyses. Discussion and comparison between the design codes (ACI, EC2), the CEB-

FIB Model Code (MC 2010) and the Critical Shear Crack Theory (CSCT) analyzing the slab specimens are presented. Parametric study based on the different shear reinforcement patterns that ACI code and EC2 propose is described.

The research work done using FEA for shear reinforced slabs is limited due to the complexity of the nonlinear finite element models and due to the difficulty in modelling shear reinforcement. In this chapter, the calibrated damaged-plasticity model, is used for the 3D finite element simulations of four interior reinforced concrete flat slabs (SB1, SB2, SB3 and SB4) that were previously tested by Adetifa and Polak (2005). The main objective of this chapter is to provide information and propose advanced methods of modelling shear reinforcement for slabs and in particular the shear bolts. Specimen SB1 (slab without shear reinforcement) has already been simulated using the concrete damaged plasticity model by Genikomsou and Polak (2015). Herein, the calibrated model is applied for the simulation of three other specimens (SB2, SB3, SB4) – specimens with shear reinforcement. It should be noted that the slab SB1 was a control specimen in a test series that included 6 slabs, one slab without shear reinforcement and 5 with shear reinforcement. The concrete in all slabs was from the same batch and the dimensions, the boundary conditions and loading were the same for all tested slabs. Therefore the model calibration that was done for the SB1 is also applicable for the analysis of the slabs SB2, SB3 and SB4.

The numerical results are compared to the test results in terms of deflections, strength and crack patterns. Comparison between ACI 318-11, EC2 (2004), Model Code 2010 and Critical Shear Crack Theory –CSCT (2008,2009) is conducted in terms of ultimate punching shear strength and failure modes of the tested slabs. Differences in design codes and models are

discussed. Parametric study is performed to examine the influence of different shear reinforcement patterns to the punching shear capacity and ductility of the slabs.

6.2 Test specimens

Four interior slab-column connections were tested under static loading through the column by Adetifa and Polak (2005). The schematic drawings of the specimens are presented in Figure 6.1. The dimensions of these square slabs were 1800x1800x120 mm, in which simple supports at 1500x1500 mm were applied. All slabs were reinforced in the same way, using 10M bars at 100 mm and 90 mm for the tension mat and 10M bars at 200 mm for the compression mat. The yield strength of the flexural reinforcement was 455 MPa. The concrete cover was 20 mm and the dimensions of the cross-section of the square columns were 150x150 mm. The columns extended 150mm beyond the top and the bottom surfaces of the slabs and they were reinforced with four 20M bars and 8M ties. The shear reinforcement consisted of shear bolts that were post-installed in the slabs. The shear bolts consist of smooth steel bars having a forged circular head on the one end and the other end threaded (Figure 6.2a). SB1 slab is the control specimen without shear reinforcement. The other slabs; (SB2, SB3 and SB4) were retrofitted with the shear bolts. Prior to the testing, holes with 16 mm diameter were drilled in the slabs to install 9.5 mm diameter shear bolts. The arrangement of the shear bolts was with concentric rows parallel to the perimeter of the column. Each row had two parallel bolts to each face of the column, therefore eight bolts in each row in total. The first row of the shear bolts was placed at distance 45 mm from the column's face and the next rows were spaced at approximately 80 mm (see Figure 6.2b). The yield strength of the shear bolts was 381 MPa. Slab SB2 had two rows of

shear bolts and SB3 and SB4, three and four rows, subsequently. The material properties of the slabs are presented in Table 6.1.

Table 6.1
Material properties of the slabs.

Slab specimen	Concrete				Flexural Reinforcement			Shear Bolt
	f_c' (MPa)	f_t' (MPa)	G_f (N/mm)	E_c (MPa]	f_y (MPa)	f_t (MPa)	E_s (MPa)	f_y (MPa)
SB1	44	2.2	0.082	36483	455	620	200000	-
SB2, SB3, SB4	41	2.1	0.077	35217	455	620	200000	381

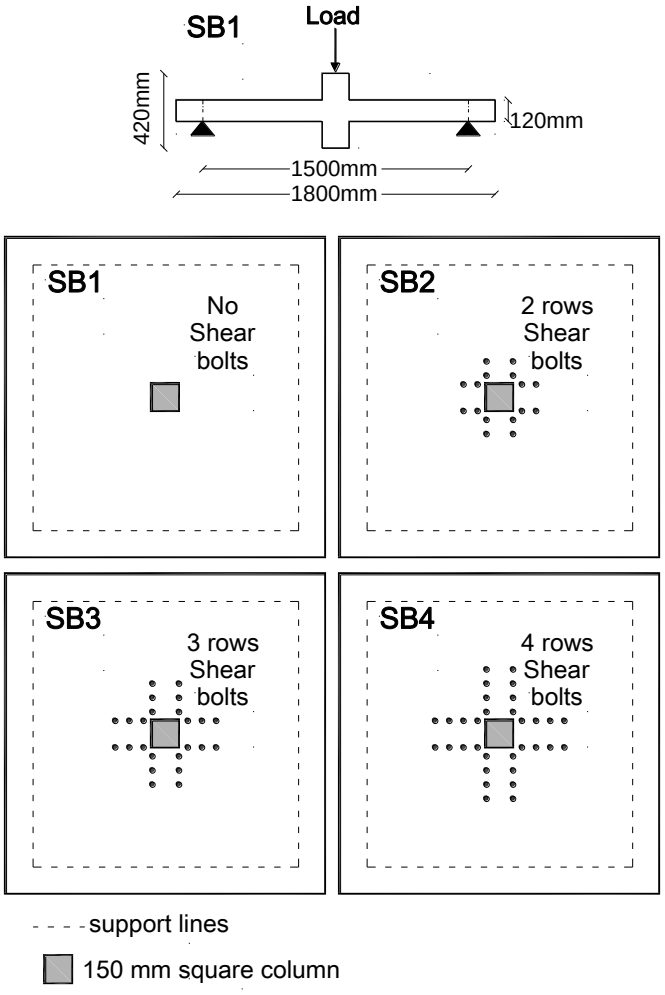

Figure 6.1 Schematic drawings of the specimens.

The yield line theory can be considered in order to estimate the flexural capacity of a reinforced concrete slab. According to Rankin and Long (1987), the theoretical flexural yield line capacity of the slabs (V_{flex}) is equal to 358 kN (Adetifa and Polak, 2005). In slabs without shear reinforcement where the flexural reinforcement ratio is high, the flexural strength of the slab (V_{flex}) is higher than the shear strength provided by the concrete (V_c). In such slabs the failure mode is punching. Slab SB1 (control specimen without shear reinforcement) was designed to fail in punching shear and according to the test observations it failed in a such manner ($V_{test} = 253\ kN$). However, in some cases, it is hard to estimate the failure modes, especially in slabs that failed in flexure, because punching can cause a secondary failure. All of the shear reinforced specimens (SB2, SB3 and SB4), failed outside the shear reinforced area, indicating that punching is critical at the outer critical section. Specimen SB2 (two rows of shear bolts), failed in a punching/flexure mode. The load-displacement curve that drops in a brittle way after reaching the flexural capacity of the tested slab enhances the mixed failure mode. Slab SB3 (three rows of shear bolts) failed in a flexure mode, but after some further deflections the punching cone formed. Finally, the specimen SB4 failed also in flexure, and the graph that presents the load-displacement response of that slab shows the flexure failure mode followed by punching after substantial deformations. The punching shear cone for the specimens SB2, SB3 and SB4 was formed outside the shear bolt zone. Thus, according to the test observations, it was found that the shear bolts increased the ductility of the slabs and provided means for changing the failure modes; from punching to flexure. Figure 6.3 presents the test observations in terms of ultimate load versus displacement for the tested slabs. Table 6.2 shows the yield line flexural capacity, the failure load, the failure displacement and the failure mode for each specimen.

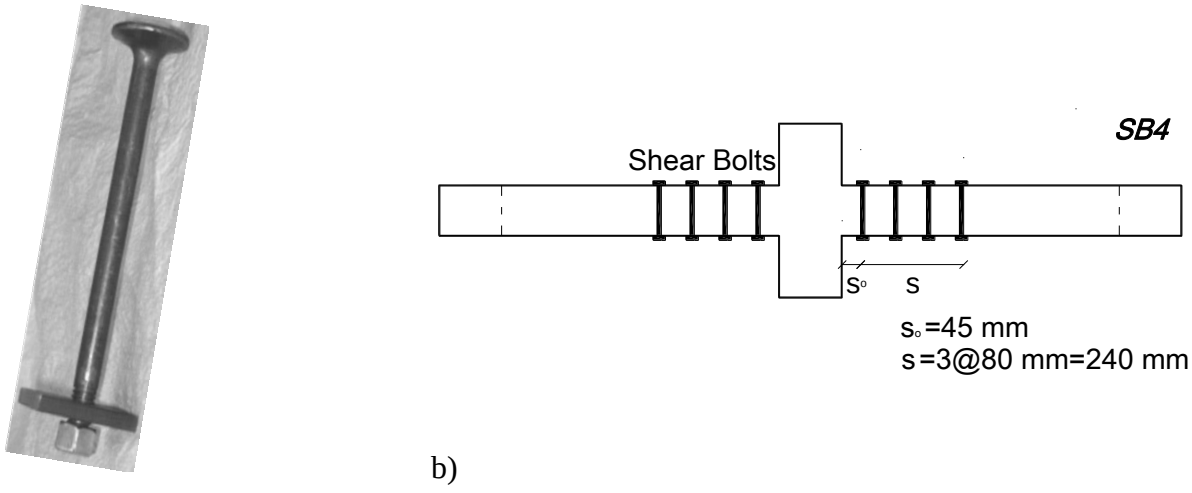

a) b)

Figure 6.2 a) Shear bolt used in the tested slabs; b) Cut section of SB4 slab with the shear bolts.

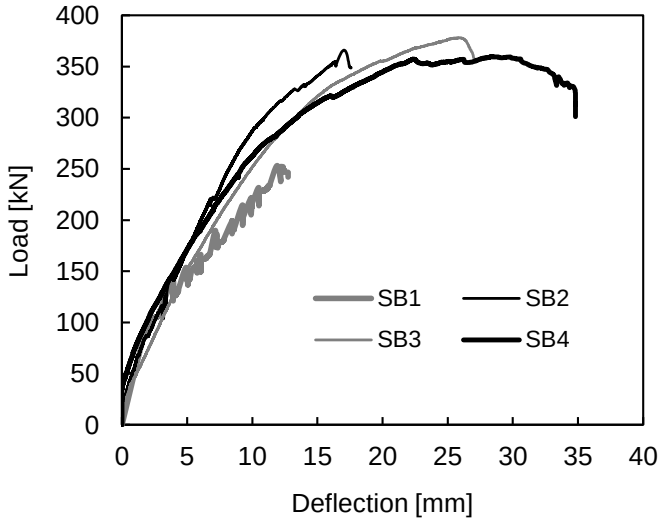

Figure 6.3 Load-deflection response of tested slabs (SB1, SB2, SB3, SB4).

Table 6.2
Test results.

Specimen	No. of rows of shear bolts	Yield line Flexural Capacity (kN)	Failure load (kN)	Displacement at failure (mm)	Failure Mode
SB1	0	358	253	11.9	Punching
SB2	2	358	366	17.1	Punching/Flexure
SB3	3	358	378	25.9	Flexure
SB4	4	358	360	29.8	Flexure

6.3 Methodology of the Finite Element Simulations

Considering the symmetry, one quarter of the slab-column connections is simulated and analyzed in ABAQUS. The concrete is modeled by using 8-noded hexahedral (brick) elements with reduced integration (denoted as C3D8R in ABAQUS) and the longitudinal reinforcement is implemented using 2-noded linear truss elements (denoted as T3D2 in ABAQUS). The concrete and the reinforcement are connected via the embedded method that considers perfect bond. However, the interaction between concrete and reinforcement is enforced through the tension stiffening behaviour of concrete after cracking, that can be considered by the concrete plasticity model. Through the thickness of the slabs (120 mm), 6 mesh elements with 20 mm mesh size are used. This mesh size was considered after a mesh sensitivity analysis that was performed on slab SB1 by Genikomsou and Polak (2015). Quasi-static analysis in ABAQUS/Explicit is implemented and simple supports are applied at the bottom edges of the specimens.

The shear bolt modelling is examined by using different approaches and its investigation is performed on SB4 that is considered as the control specimen for the shear reinforced slabs. The next section presents the modelling approaches and the observations made in each case. In all approaches, the shear bolts were not able to prevent the concrete damage at the column, as happened in the real tests where the heads of the shear bolts contributed to an additional restraint at the compressive zone. For that reason in the following numerical analyses of the shear reinforced slabs, the concrete at the column is simulated as linear elastic. In the tests, and in the real continuous slabs, the volume of the column that is within slab's depth is highly confined and the failure (punching) happens not in the column but in the slab. In the FEA model that confinement has to be addressed in some manner. One way would be to create a complicated

concrete model within the column that includes confinement. However, this is not necessary for this case, as we do not investigate the column's behaviour. Thus, a linear elastic model for the concrete in the column is created, in order to make sure that the failure will not happen in the column. This approach has been also used by other researchers (Liu, Tian and Orton, 2015).

6.4 Shear Bolt modelling investigation on slab SB4

The finite element modelling of the reinforced concrete slabs without shear reinforcement examined by Genikomsou and Polak (2015) was performed using 3D solid elements for the concrete and 3D truss elements for the flexural reinforcement. In the shear reinforced slabs, the main concern is the modelling of the shear bolts. The questions that are raised, are: a) what type of finite elements (trusses/beams/solids) should be used for modelling the shear bolts, b) what type of geometry for the possible truss or beam elements should be adopted, and c) what type of constraint should be applied. The investigation is presented considering four different ways to model the shear bolts: truss elements, beam elements, shell elements and finally solid elements. The obtained numerical results are presented and discussed.

The computational cost in terms of demand time for each of the next presented analyses is approximately; 2 min. for the truss elements, 14 min. for the beam elements, 3 min. for the shell elements and 330 min. for the solid elements.

Truss elements –Beam elements

First, 2-noded 3D linear truss elements (T3D2) are used for the simulation of the shear bolts. The main disadvantage of the truss elements is that they can carry only tensile or compressive loads and they have no resistance to bending due to the only three translational degrees of freedom. This problem, according to Negele et al. (2007), could be solved by distributing the load to the surrounding nodes by connecting additional truss elements to these nodes. Additional truss elements are modeled at the top and bottom of the shear bolts as it is shown in Figure 6.4. These anchorage types of truss elements are considered in order also to prevent from local failures of concrete at the nodes. The T3D2 elements representing the shear bolts are embedded into the solid concrete elements. Configuration of the truss elements representing the shear bolts is shown in Figure 6.4. After performing the appropriate mesh in the model, there were 11,534 nodes and 9,539 elements from which 8,470 are C3D8R and 1,069 T3D2.

Then, as a second option, beam elements are adopted for the shear bolt design. The 3D quadratic beam elements (denoted as B32 in ABAQUS) are shear deformable and account for finite axial strains, having six degrees of freedom. The shear bolt configuration is the same as the previous one by using truss elements (Figure 6.4). Again, perfect bond between concrete and steel is considered through the embedded method. After performing the appropriate mesh in the model, there were 11,838 nodes and 9,539 elements from which 8,470 are C3D8R, 765 T3D2 and 304 B32.

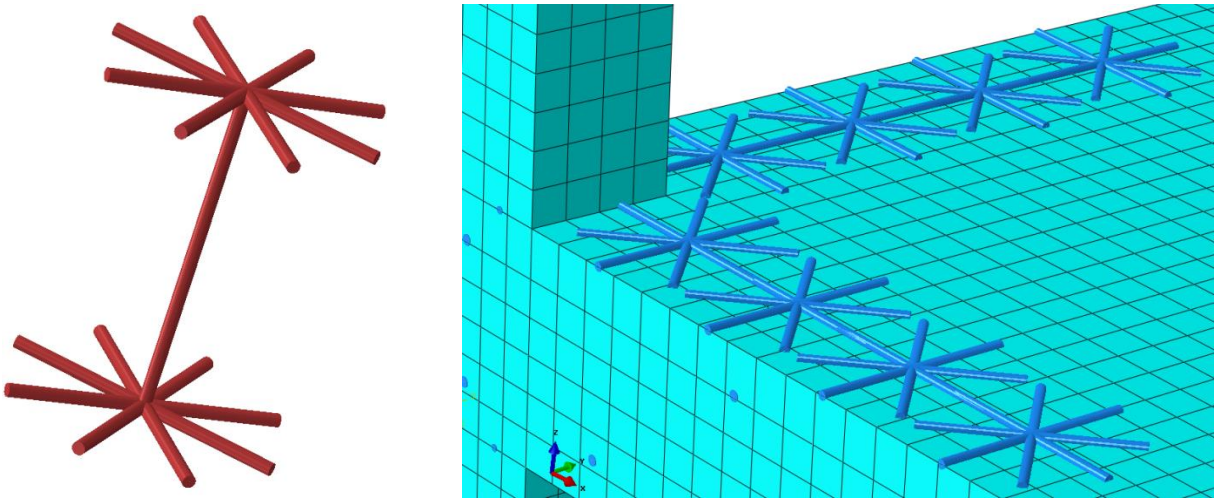

a) Truss/beam elements simulate the shear bolt.

b) Mesh design on SB4 specimen.

Figure 6.4 Truss/beam configuration for shear bolt modelling on SB4 specimen.

Shell elements

3D continuum shell elements with reduced integration (denoted as S4R in ABAQUS) are also considered for modelling the shear bolt system. S4R elements have six degrees of freedom and they are embedded into the concrete-brick elements. The rebar layer definition is used in order to define the amount and position of the shear reinforcement. With this procedure the shear bolts are considered as smeared layer with constant thickness. The thickness can be calculated equal to the area of the cross section of the shear bolt divided by the spacing between the shear bolts. Figure 6.5 illustrates the shear bolt configuration using shell elements. 11,508 nodes and 9,475 elements from which 8,470 are C3D8R, 765 T3D2 and 240 S4R, are used in the model.

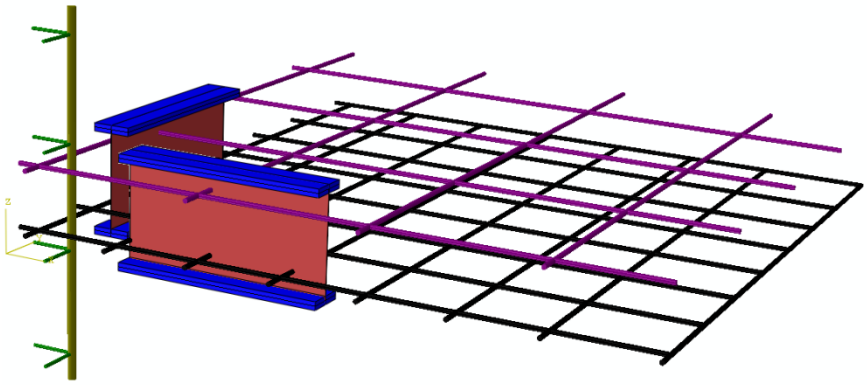

Figure 6.5 Shell elements simulate the shear bolts on SB4 specimen.

Solid elements

The last examined solution to simulate the shear bolts is to use 3D solid elements. 9.5 mm diameter is used for the bolts' stud, 30 mm diameter for the heads and 44 mm diameter for 10 mm thick washers. The bolts are installed into the 16 mm drilled holes of the slab. Tie constraints are adopted to model the interaction between the washers of the bolt and the slab surface and the contact between the different parts of the bolt. Tie constraints tie two separate surfaces together in order no relative motion between them to exist. The advantage of this type of constraint is that allows the two regions to be fused together even if their meshes are not similar. Very important is the proper mesh of the slab due to the present of holes. For that reason the mesh is created after the proper partition of the slab. Figure 6.6 illustrates the shear bolt modelling done by using solid elements and the mesh configuration of the bolt and the surrounding area on the slab. The adopted mesh provides 44,551 nodes and 35,437 elements (34,672 C3D8R and 765 T3D2).

a) Solid elements simulate the shear bolt.

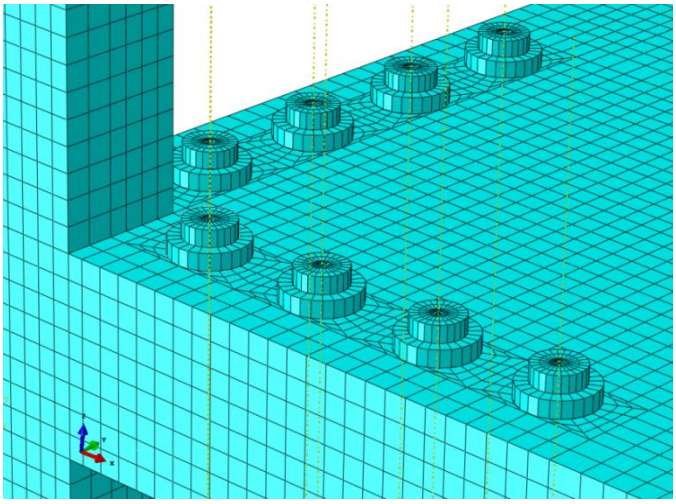

b) Mesh design on SB4 specimen.

Figure 6.6 Solid elements for shear bolt modelling on SB4 specimen.

The comparison between the load-deflection responses obtained from the above modelling approaches is presented in Figure 6.7. Based on the slab's load-deflection response, the approach using beam finite elements for simulating the shear bolts, seems to be better and the response of the slab is reasonable compared to the test results. The truss elements cannot contribute to such an increase of the punching shear capacity of the slab as it was observed from the test; however they improve the ductility of the slab. Shell and solid elements seem to be able to simulate the increase in the load but they do not show the same deflection as happened in the test.

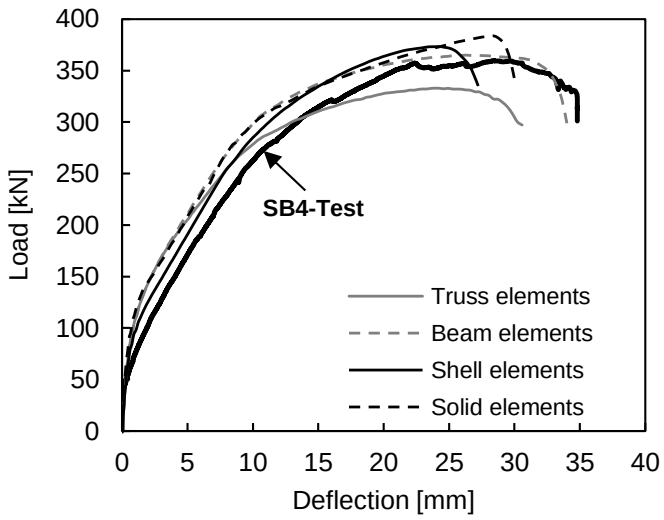

Figure 6.7 Load-deflection response of slab SB4 (shear bolt modelling investigation).

Comparison between the crack patterns from the FEA and real test is presented in Figure 6.8. It should be noted that cracking is perpendicular to the direction of the maximum principal plastic strains due to the smeared crack approach that concrete damaged plasticity model in ABAQUS adopts. Therefore, the crack formation in FEA can be tracked through the maximum principal plastic strains in concrete. The crack propagation starts tangentially at the area of the maximum bending moment near the column and then spreads radially towards the slab edges as the load increases. During the test, SB4 experienced bending cracks near the column on the tension side of the slab. The shear cracks were developed outside the shear reinforcement area causing the secondary failure. Cracks were also observed between the first and second row of the shear bolts leading to a second post-failure shear cracking. Comparing the crack patterns obtained from the FEA and test, the case where the shear bolts are modeled with beam elements (Figure 6.8c), captures best the test cracking.

a) (test)

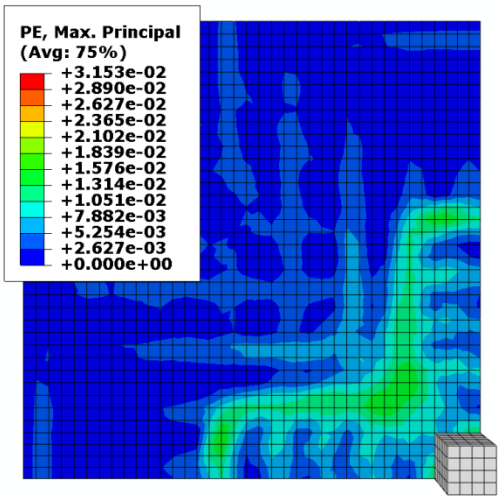

b) (truss elements)

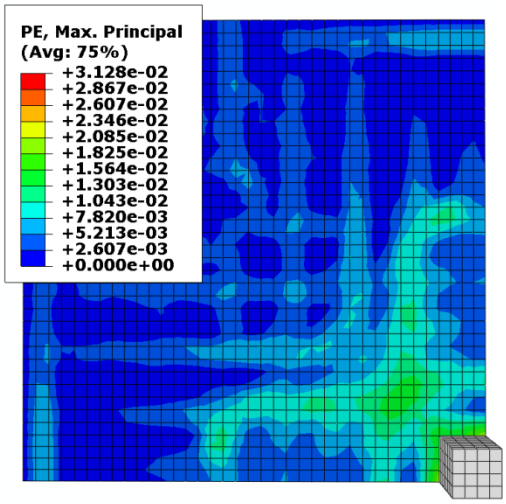

c) (beam elements)

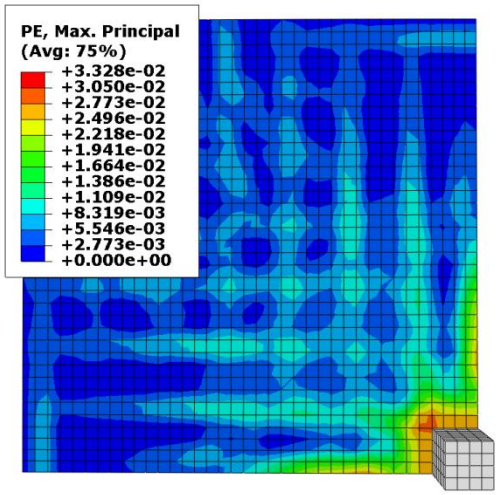

d) (shell elements)

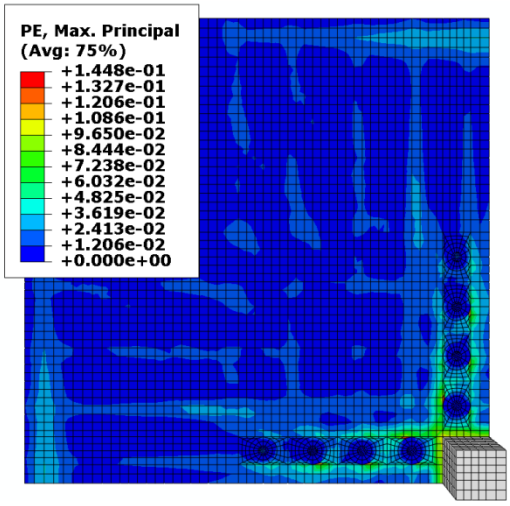

e) (solid elements)

Figure 6.8 Crack patterns of slab SB4 (shear bolt modelling investigation).

6.5 Finite Element Analysis Results

Load-deflection

Figure 6.9 shows the comparison between experimental and analytical results in terms of load-deflection for all specimens. The FEA results for the slabs SB2, SB3 and SB4 that had been retrofitted with the shear bolts are in good agreement with the tested results in terms of ultimate punching shear capacity and displacement. The beam elements that are employed to simulate the shear bolts seem to increase the ductility of the slabs and the punching shear resistance.

Crack pattern

The failure crack development of all slabs from tests and FEA is presented in Figure 6.10. The punching shear cone of specimen SB1 that failed by punching is noticed due to the sudden opening of the shear cracks. All other specimens, failed in flexure first, and they experienced shear cracks outside the shear reinforced area and bending cracks around the column. As the shear reinforcement is increased (SB3, SB4) more cracks can be seen at the column area. The simulated cracks match the experimentally observed cracks well.

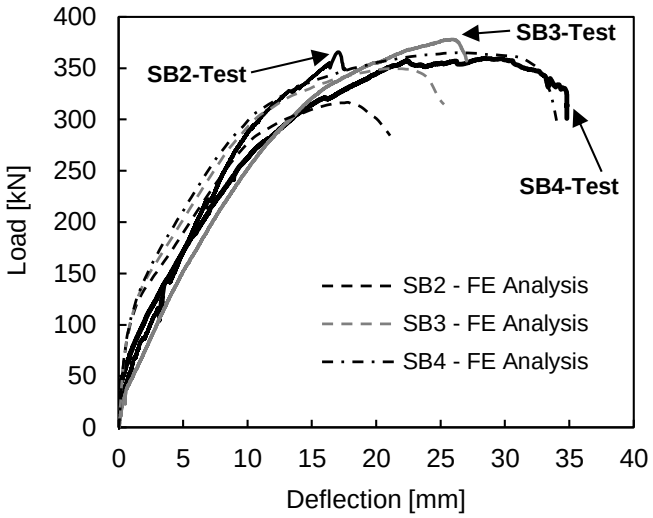

Figure 6.9 Load-deflection response of slabs (SB1, SB2, SB3, SB4).

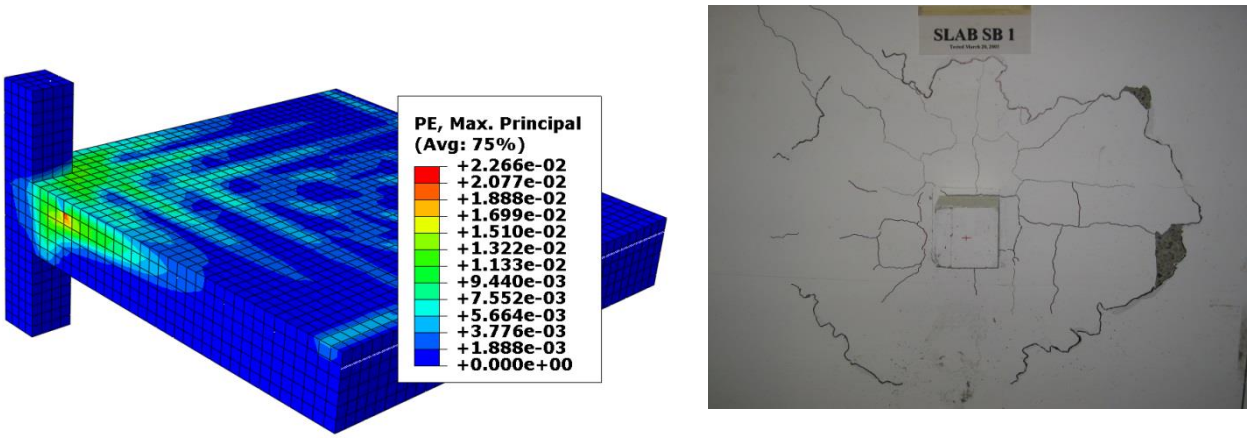

a) SB1 slab (Cracking from FEA and test)

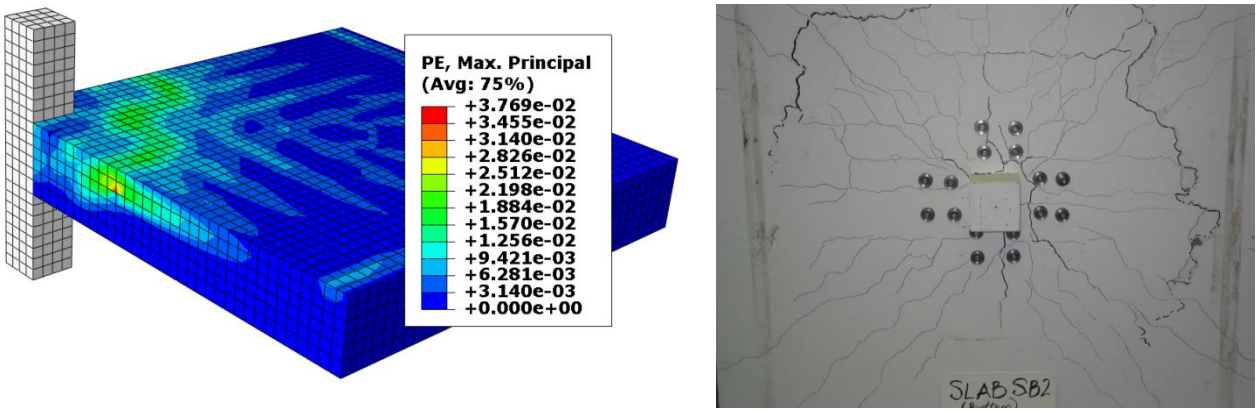

b) SB2 slab (Cracking from FEA and test)

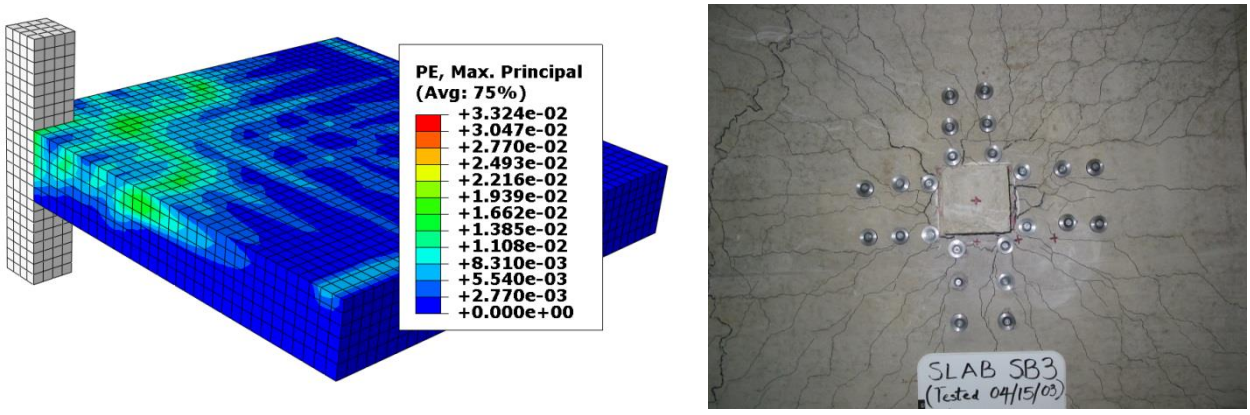

b) SB3 slab (Cracking from FEA and test)

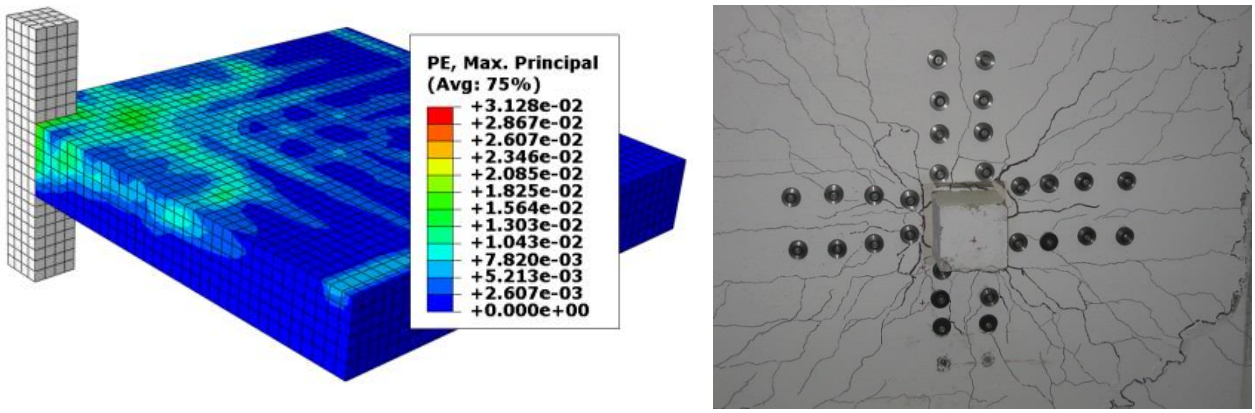

c) SB4 slab (Cracking from FEA and test)

Figure 6.10 Crack pattern at ultimate load.

Strains on longitudinal reinforcement

The strains on the tensile longitudinal reinforcement were measured during the test. The obtained results for the specimen SB1 showed that the first yielding occurred at a load of 240 kN just before the failure. The yielding of the reinforcement of the slab SB2 was observed at load of 224 kN, while for specimens SB3 and SB4 the first yielding occurred at loads 260 kN and 242 kN, respectively. The FEA results show almost the same results for the yielding of the flexural longitudinal reinforcements. The first yielding of the flexural reinforcement of the slab SB4 in

FEA is observed at a load of 285 kN. Yielding of the tension reinforcement is observed for slabs SB1, SB2 and SB3 at loads 228 kN, 275 kN and 297 kN, respectively. Figure 6.11 presents the FEA strains on the flexural reinforcement at the positions that first yielded for the SB1, SB2, SB3, SB4 specimens. During the tests the strain gages were damaged at strains around 0.007 mm/mm. For that reason, the test results for the ultimate loads are not comparable to the FEA results and are not presented herein.

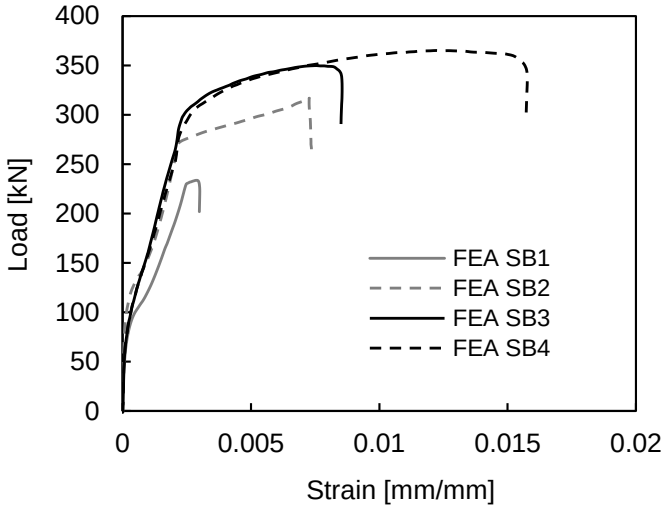

Figure 6.11 Strains on flexural reinforcement in FEA.

Activation of the shear bolts

The strains were measured on the shear bolts stem during testing. Small strains were observed until the ultimate load of the slabs. Only the first bolt started to be activated earlier at a load of 200 kN. In general, the bolts started to be activated at loads higher than the ultimate load of the specimen without shear reinforcement (SB1), because the cracking occurs at similar

loading for the slabs without and with shear reinforcement. However, the bolts limit the opening of the shear cracks. The first row of bolts experiences higher strains compared to the subsequent rows due to the presence of the shear cracks at the area near the column. The outer rows of the bolts were strained suddenly at the ultimate load suggesting that shear cracking reached all of the way to the last row of bolts. After the peak load, approximately 350 kN for all specimens, the bolts showed the highest strains. In the finite element analyses the activation of the shear bolts starts earlier compared to the tests, due to the modelling that is adopted with the assumed perfect bond between the shear reinforcement and concrete. Figure 6.12 presents the strains on the bolts obtained from the test and FEA results for the specimen SB2. Figure 6.13 and Figure 6.14 show the bolt strains for slabs SB3 and SB4, respectively.

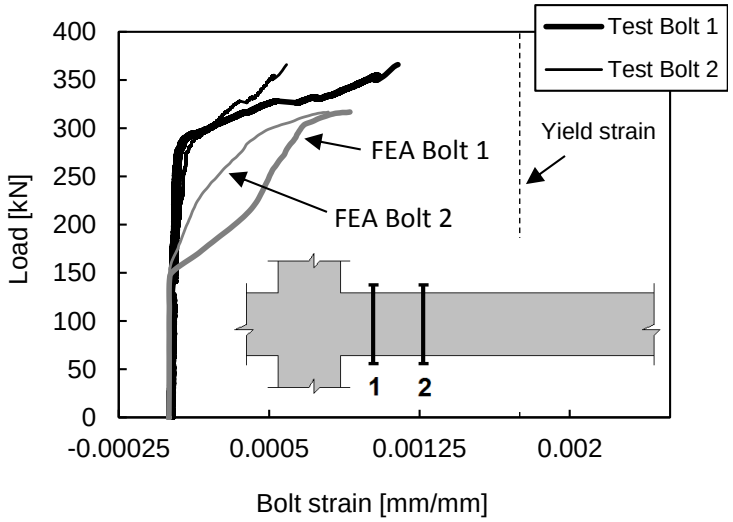

Figure 6.12 Load versus bolt strains for slab SB2 (Comparison between FEA and test).

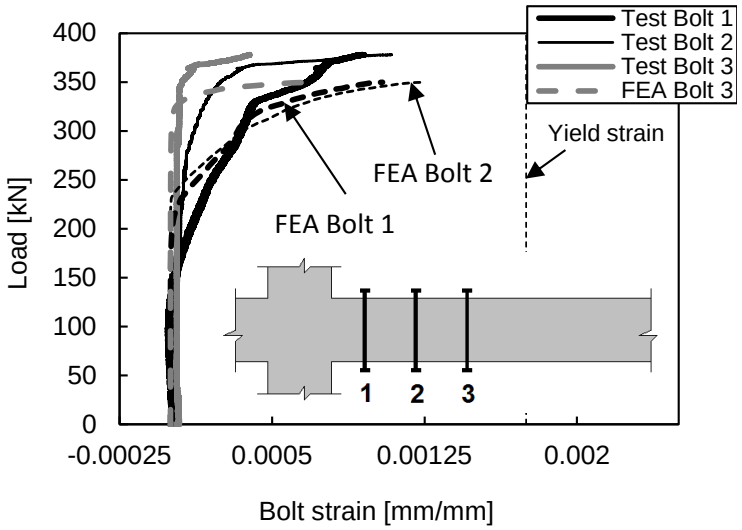

Figure 6.13 Load versus bolt strains for slab SB3 (Comparison between FEA and test).

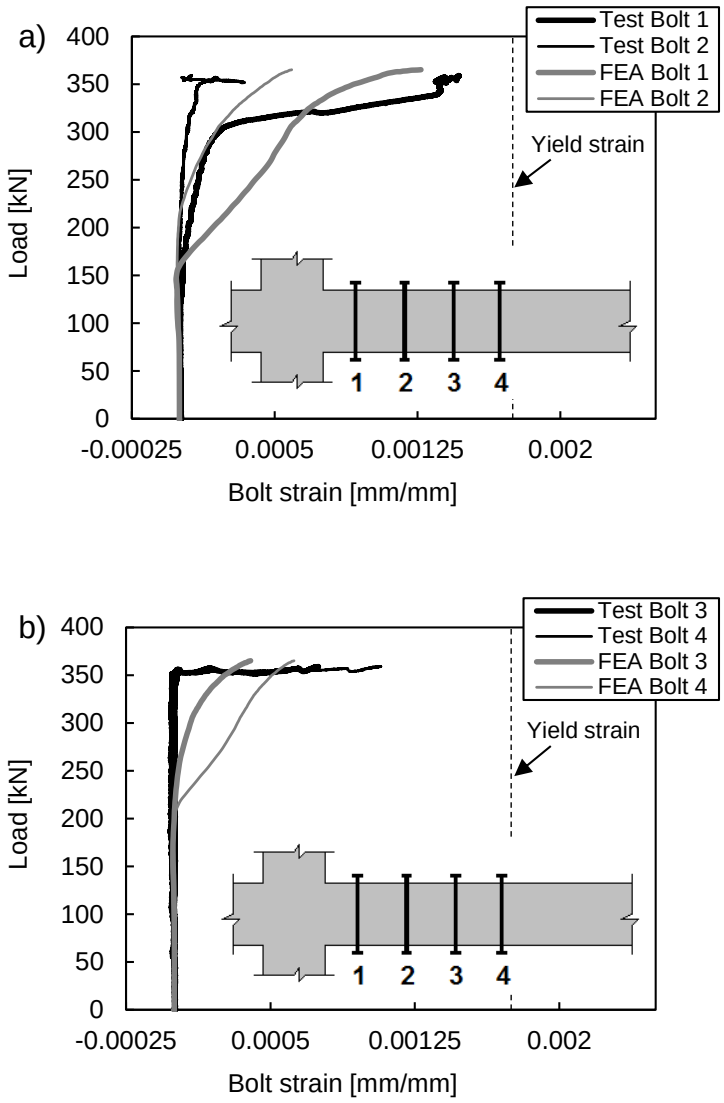

Figure 6.14 Load versus bolt strains for the slab SB4; a) Bolts 1,2 and b) Bolts 3,4.

6.6 Comparison with the codes provisions

Design codes (ACI 318-11 and EC2), Model Code (MC 2010) and Critical Shear Crack Theory (CSCT) adopt an approach involving a critical section at a certain distance from the column perimeter. On this perimeter the shear stress should be less than the shear capacity of the slab. The critical section in EC2 is located at a distance 2d from the column faces, while in

ACI318-1, MC 2010 and CSCT at 0.5d. For the shear reinforced slabs in order to calculate the punching shear resistance outside the shear reinforced area, the control perimeter for the ACI code, Model Code 2010 and CSCT is calculated at distance 0.5d from the outer perimeter of the shear reinforcement, while for EC2 is calculated at distance 1.5d from the outer perimeter of the shear reinforcement. Figure 6.15 shows the critical control perimeters according to all codes.

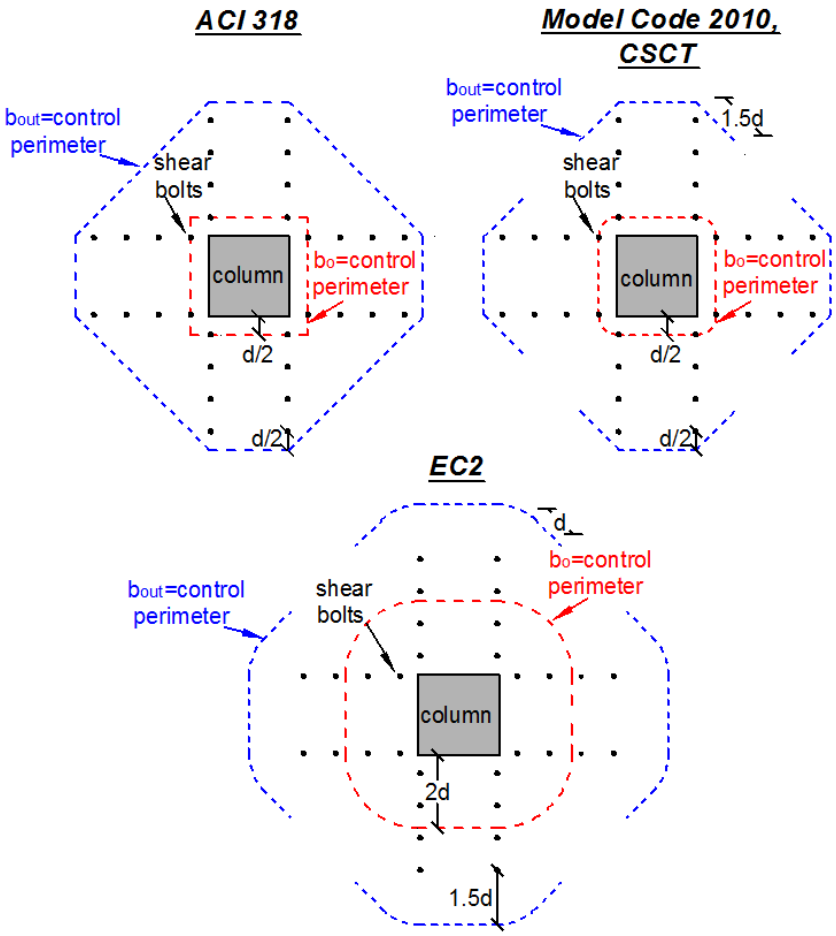

Figure 6.15 Control perimeter according to ACI, EC2, MC 2010 and CSCT.

One other difference between codes and model is that the ACI318-11 code does not account for the effect of the flexural reinforcement ratio and size effects for the calculation of shear resistance direct, while the EC2, MC 2010 and CSCT consider these effects. The ACI318

is based on Moe's research (1961), the EC2 is based on Regan's research (1985), the CSCT is a theory that was proposed from Muttoni (2008, 2009) and MC 2010 is based on the CSCT model. One difference between the design codes (ACI and EC2) compared to the MC 2010 and CSCT, is that both MC 2010 and CSCT examine the failure of the shear reinforced slabs due to the crushing of concrete struts near the column. However, the design codes have already accounted for the failure due to crushing of concrete in the equations by limiting the maximum punching shear strength of slabs without shear reinforcement (ACI) or by reducing the concrete strength (EC2). All basic equations used by each code and model, are described in details in Chapter 2.

Table 6.3 shows the calculations for all slab specimens according to ACI, while Table 6.4 shows all calculations for all slabs according to EC2. Table 6.5 shows the failure loads for all specimens according to the test, FEA, design codes and CSTC model. Figure 6.16 and Figure 6.17 present the load-rotation curves according to the Model Code 2010 and CSCT, respectively.

Table 6.3
Ultimate load (kN) from ACI318-11.

Slab	f'_c [MPa]	b_o [mm]	b_{out} [mm]	d [mm]	A_{vs} [mm^2]	f_{yd} [MPa]	s [mm]	V_c [kN]	V_R [kN]	V_{out} (kN)
SB1	44	960	-	90	-	-	-	***189***	-	-
SB2	41	960	1589	90	566.4	381	80	-	381	***151***
SB3	41	960	2042	90	566.4	381	80	-	381	***194***
SB4	41	960	2495	90	566.4	381	80	-	381	***237***

Table 6.4
Ultimate load (kN) from EC2.

Slab	f_{ck} [MPa]	b_o [mm]	b_{out} [mm]	d [mm]	A_{vs} [mm^2]	f_{ywd} [MPa]	s [mm]	V_c [kN]	V_R [kN]	V_{out} [kN]
SB1	42.4	1730	-	90	-	-	-	***202***	-	-
SB2	39.4	1730	2032	90	566.4	313	80	-	445	***232***
SB3	39.4	1730	2132	90	566.4	313	80	-	445	***243***
SB4	39.4	1730	2204	90	566.4	313	80	-	445	***251***

Table 6.5
Comparison of ultimate load (kN) between test, code provisions and CSCT.

Slab specimen	Test results	FEA results	ACI	EC2	MC 2010	CSCT
SB1	253	234	189	202	198	219
SB2	366	317	151	232	282	237
SB3	378	350	194	243	324	281
SB4	360	365	237	251	339	317

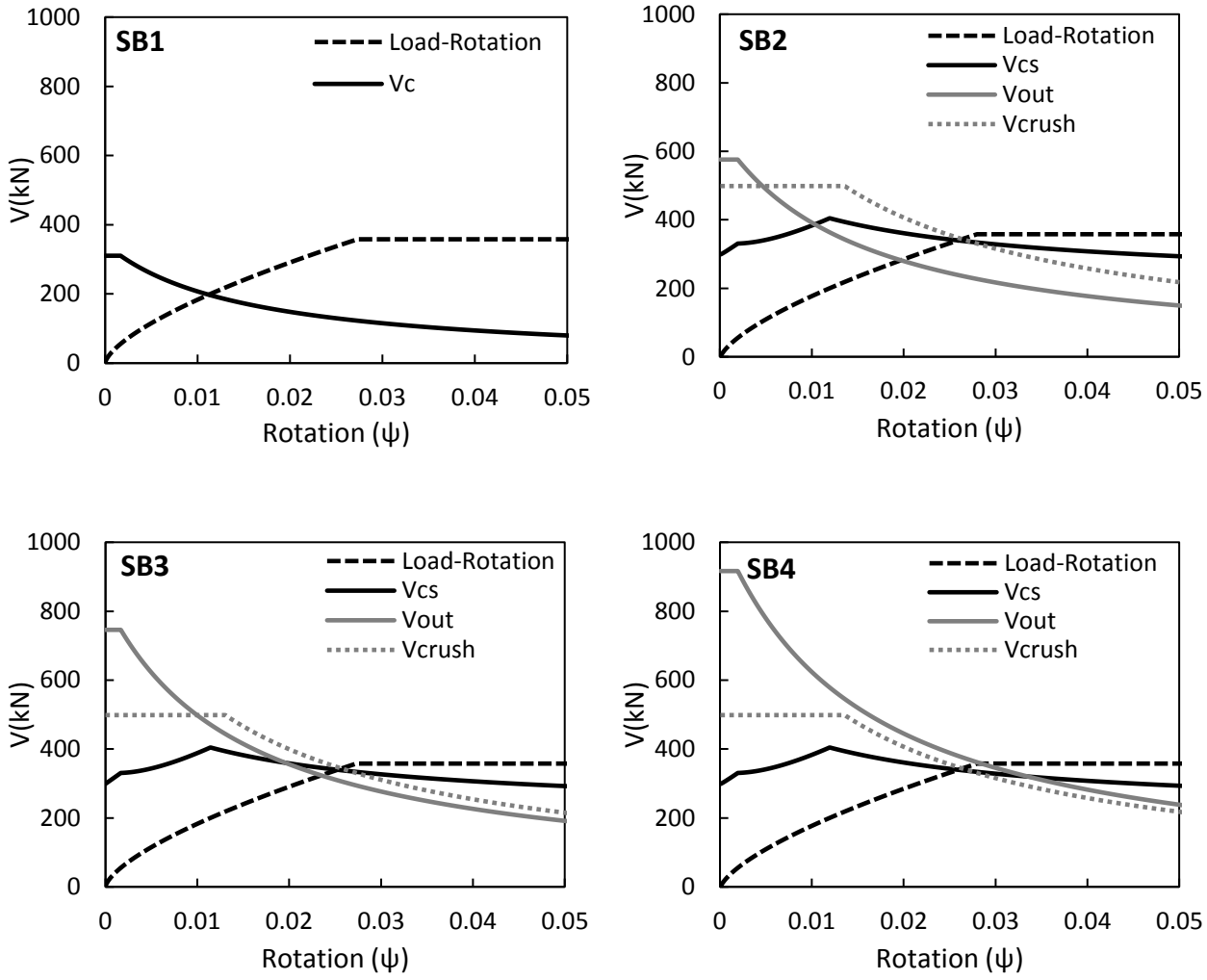

Figure 6.16 Punching shear strength of specimens according to MC 2010.

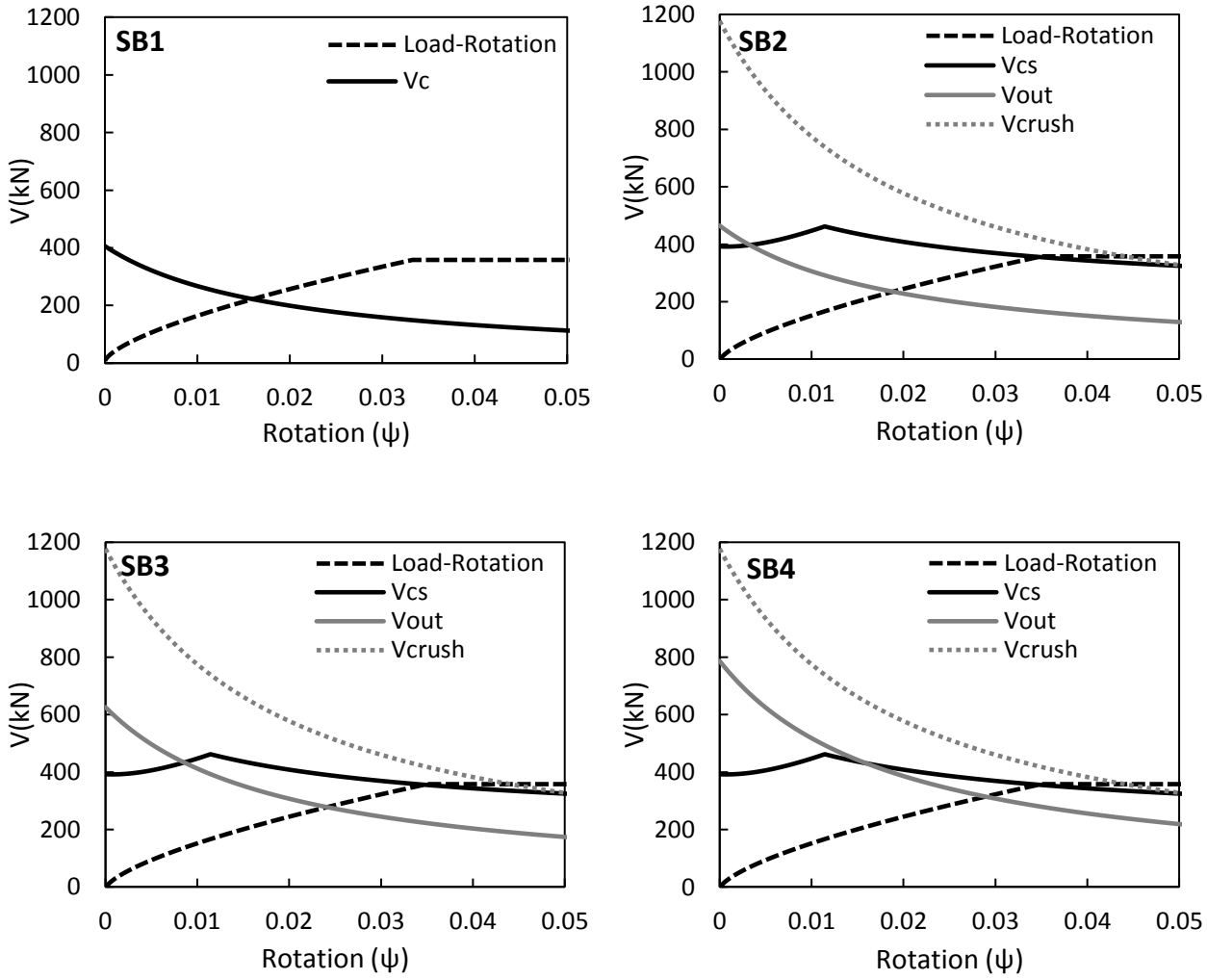

Figure 6.17 Punching shear strength of specimens according to CSCT.

By comparing the observed results, we can conclude that ACI318-11 predicts the most conservative failure loads. This happens because ACI318-11 does not consider the effect of the flexural reinforcement ratio. According to Alexander and Hawkins 2005, the ACI code does not predict accurate the punching shear strength of the slabs, however, provides a lower limit. All of the presented calculation results support the above statement. The disadvantage of EC2 is that it does not account for different shear reinforcement systems.

For the slab without shear reinforcement (SB1), all codes and CSCT give quite similar results. However, the prediction of the punching shear strength for the slabs with shear reinforcement provides significant differences between the codes and the mechanical model. It is remarkable to note that the slab SB2 according to ACI318-11 fails at a load of 151 kN; lower strength than for the specimen SB1. This is unrealistic and happens because of the equation that is used in order to calculate the punching shear resistance for slabs with shear reinforcement outside the shear reinforced area. In contrast, the predicted capacity of SB2 by EC2, Model Code 2010 and CSCT is increased compared to the strength of SB1. Quite interesting is the failure analysis of the slab SB4. Based on ACI318-11 and EC2, SB4 failed outside the shear reinforced area at loads 237 kN and 251 kN, respectively. The MC 2010 predicts that SB4 fails due to flexure failure (339 kN) within the shear reinforced area, while CSCT predicts that SB4 fails due to flexure outside the shear reinforced area, at a load of 317 kN. It can be concluded that both MC 2010 and CSCT are able to take into consideration the effect of the amount of the shear reinforcement, predicting really well the increase in the strength with the increase of the amount of the shear bolts, as the results correspond very well with the test results. Figure 6.18 compares the results in terms of load-rotation between MC 2010 and CSCT for the four slab-column connections.

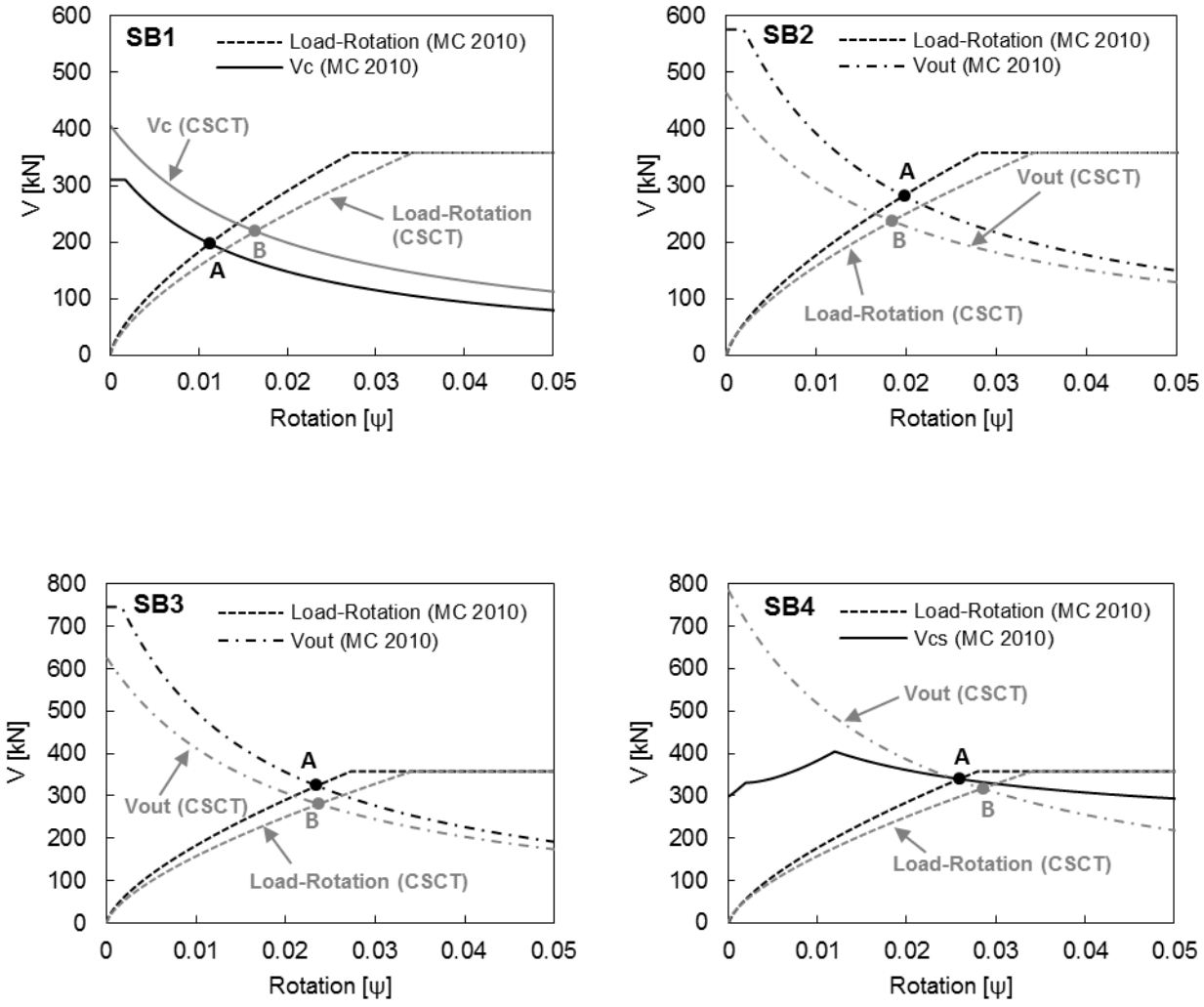

Figure 6.18 Load-rotation curves according to MC 2010 and CSCT.

The effectiveness of the shear reinforcement to increase the punching shear capacity of a slab-column connection depends also on the arrangement of the shear reinforcement around the column. Two different approaches are proposed in the design codes; the rectangular (ACI) and the radial arrangement (EC2). All slabs had the rectangular arrangement for placement the shear bolts as suggested by ACI318-11. In order to investigate the difference between rectangular and

radial arrangement, in terms of failure load, ductility and cracking, the slabs are analyzed with the same amount of shear bolts but this time with the radial placement. Figure 6.19 presents the comparison between the two different types of arrangement of the shear bolts. The failure load in FEA of the SB4 with the rectangular arrangement is 365 kN and the displacement at such load is 29.5 mm. The analysis of the SB4 with the radial arrangement of the shear bolts increases both punching shear capacity and ductility. The slab fails at a load of 380 kN and at a displacement of 47.5 mm. This can be explained by the reduction of the radial cracking provided by the radial arrangement of the shear bolts. The failure load and the deflection are also increased for the slabs SB2 and SB3, when the radial placement of the shear bolts was considered. However, the increase is not as significant as it is for the slab SB4. The numerical results of slab SB2 analyzed with the rectangular placement of the bolts are shown failure at a load of 317 kN and at a displacement of 17.8 mm. The radial arrangement increased the failure load to 321 kN and the displacement to 18.9 mm. Specimen SB3, according to the FEA results using the rectangular arrangement, failed at a load of 349 kN and at a displacement of 21.4 mm. The adoption of the radial arrangement increased the failure to 356 kN and the deflection to 22.9 mm. Figure 6.20 illustrates the cracking at the bottom side of the slab with the radial arrangement at failure and this can be compared with the Figure 6.10 that shows the crack pattern at failure with the rectangular placement of the shear bolts.

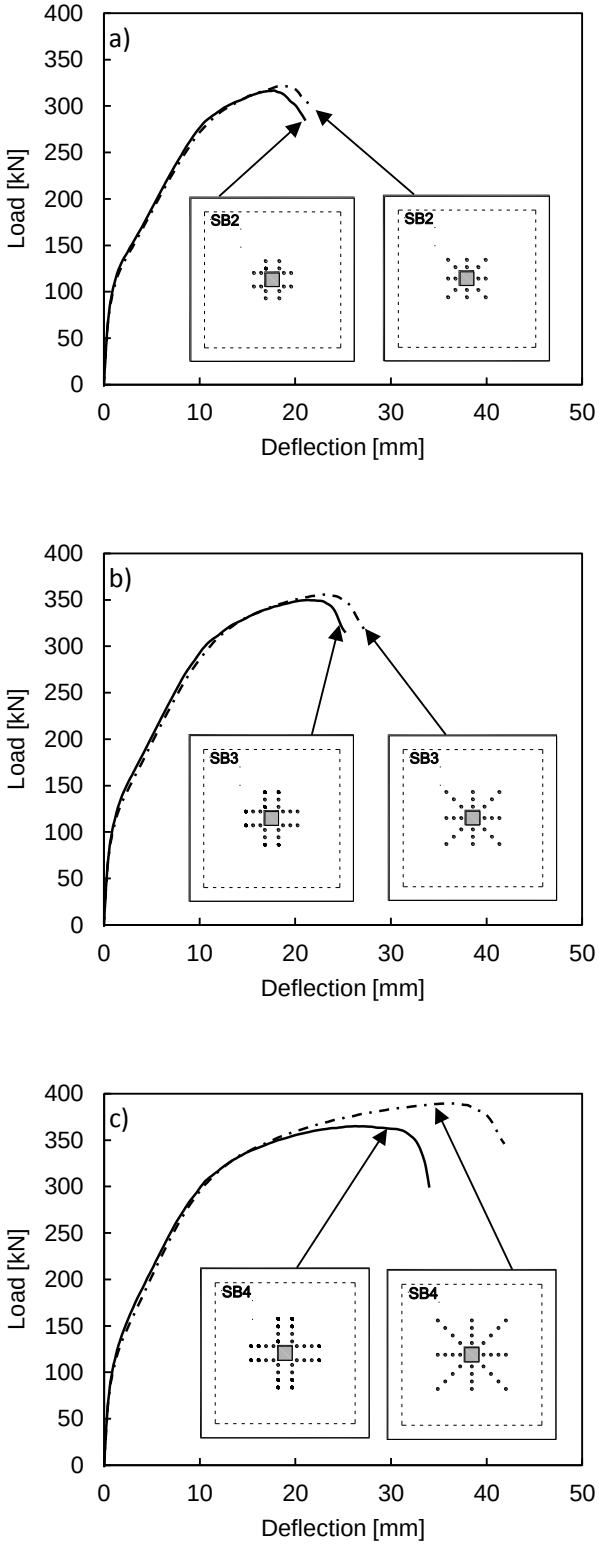

Figure 6.19 Load-deflection response comparing the rectangular and radial placement of the shear reinforcement: a) SB2, b) SB3 and c) SB4.

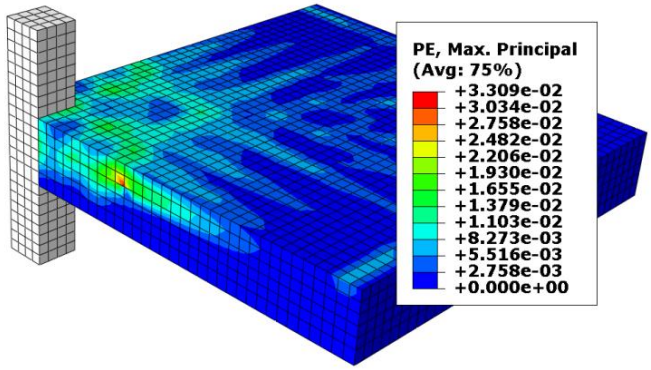

a)

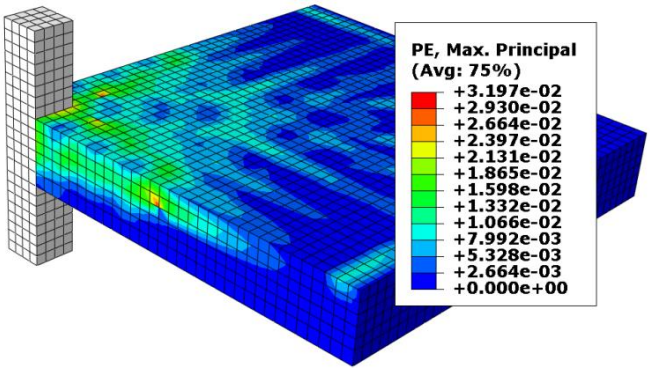

b)

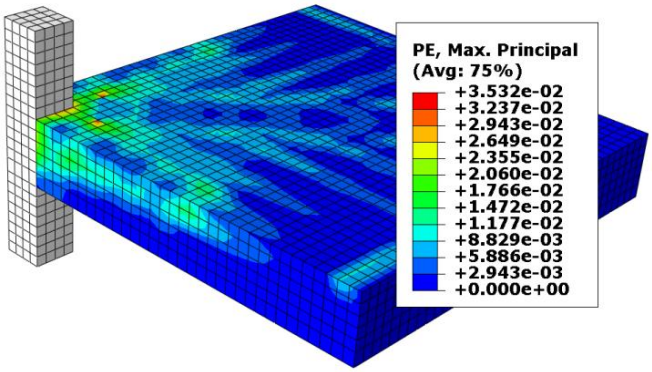

c)

Figure 6.20 Crack pattern using the radial arrangement of shear reinforcement: a) SB2, b) SB3 and c) SB4.

6.7 Summary and Conclusions

The finite element simulations of shear reinforced concrete slabs using the concrete damage plasticity model are undertaken and analyzed. Four interior slab-column connections are analyzed in terms of ultimate load, displacement and cracking propagation. The outcomes of these analyses assess the capability of the proposed model in analyzing punching shear of shear reinforced concrete slabs. The proposed calibrated concrete model, which was used for the analysis of slabs without shear reinforcement is also effective for simulating shear reinforced slabs.

The most reliable modelling approach of the shear reinforcement (shear bolts) is carried out with beam elements, while three other different modelling approaches for the shear bolts are presented. The proposed modelling approach could be applicable for modelling also other types of shear reinforcement. Cracking propagation of all slabs provided by the FEA is in good agreement with the experimental crack patterns. All of the shear reinforced specimens fail outside the shear reinforced area as happened in the real tests. Yielding of the longitudinal reinforcement is also verified by FEA. The first yielding of all specimens appears on the tensile reinforcement near the column. This is in a good agreement with the test observations. The FEA of the shear reinforced slabs are in good agreement with the experimental results in terms of ultimate load-ductility and cracking development. That shows and verifies that the calibrated concrete damaged plasticity model could accurately predict the punching shear response of concrete slabs with shear reinforcement.

Code provisions and models are assessed in terms of ultimate load. ACI code presents the most conservative results. Both design codes (ACI and EC2) seem to underestimate the

contribution of the amount of the shear reinforcement. In contrast, MC 2010 and CSCT account for the contribution of the increased shear reinforcement. The results that MC 2010 and CSCT give for all slabs are closer to the test results. MC 2010 predicts that the SB4 fails inside the shear reinforced area, while all others show that the SB4 slab fails outside the shear reinforcement area. The two shear reinforcement arrangements proposed by the design codes are simulated and compared. The rectangular arrangement suggested by ACI code is compared to the radial placement recommended by EC2, in terms of failure load and displacement. Radial arrangement seems to increase both failure load and deflection.

Chapter 7

Parametric studies: Opening effect on punching shear resistance

7.1 Introduction

The opening effect investigation is presented for edge and interior slabs, in order to show the capability of the proposed model in such simulations and compare the obtained results with the code provisions. The effect of the location, the distance from the column and the size of the opening on the punching shear resistance, are investigated. The results, confirm that the punching shear resistance is decreased with the increase in opening size and with the decrease in opening distance from the column.

Punching shear failure can happen in reinforced concrete flat slabs due to the development of high shear stresses in the slab-column connection area. These shear stresses become higher when openings and unbalanced moments exist. Unbalanced moments are present due to the geometry and location of the slab, the loading conditions and due to openings in slabs. These openings are often created for reasons such as ventilation, air conditioning, heating, or electrical ducts. Due to architectural reasons openings are usually needed next to the columns, leading to a reduction of the volume of concrete that can resist the punching shear. While, flat slabs started to be tested in the 1950s by Elstner and Hognestad (1956) and later by Moe (1961), the phenomenon of opening in flat slabs started to be examined only nowadays by recent

researchers, such as, El-Salakawy et al. (1999), Teng et al. (2004), Bu and Polak (2009), Borges et al. (2013) and Anil et al. (2014).

To supplement testing, FE analyses can be a method to examine flat slabs with openings and to reinforce the test conclusions. In the study presented herein, 3D finite element analysis (FEA) is adopted simulating the edge slabs tested by El-Salakawy et al. (1999). The analyses are conducted using the calibrated concrete damaged plasticity model. The slabs are without shear reinforcement and with different sizes and locations of openings. Nine edge slab-column connections previously tested are simulated under gravity and lateral loadings. The numerical results are compared to the test results in terms of deflections, strength and crack patterns.

The code provisions are based on the limited available empirical data. Herein, the punching shear capacity of all test specimens is going to be assessed using the ACI 318-11 code. ACI 318-11 adopts the critical shear perimeter at a distance d/2 from the loaded area (column), while the EC-2 2004 considers the critical or basic control perimeter, at a distance 2d from the column face. EC-2 2004 considers the critical shear perimeter with circular ends, while the ACI 318-11 adopts the critical shear perimeter to be rectangular. Both codes adopt a reduction of the critical perimeter depending on the size and the location of the opening. A part of the controlled perimeter contained between two tangents drawn to the outline of the opening from the center of the loaded area (top surface of column) is considered to be ineffective. The EC-2 adopts the previous reduction in the controlled perimeter if the shortest distance between the perimeter of the loaded area (column) and the edge of the opening is smaller or equal to 6d, where d is the effective slab's depth. The ACI 318 code considers this distance as 10h, with h to be the thickness of the slab (see Figure 7.1).

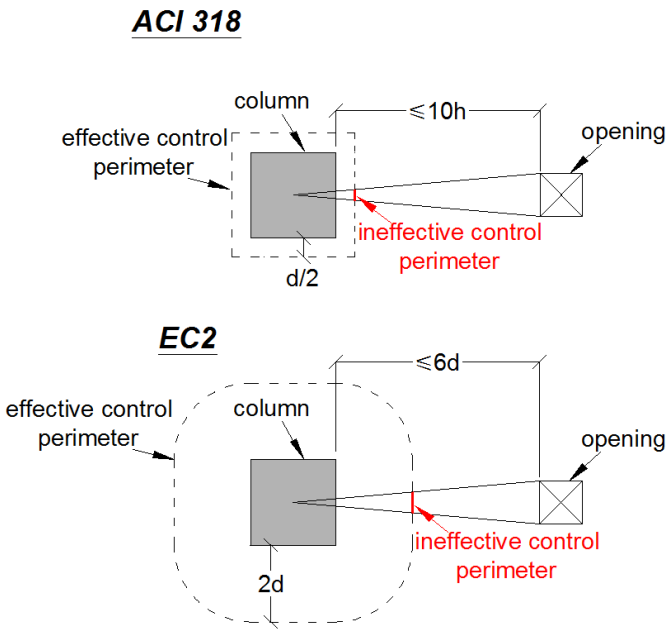

Figure 7.1 Control perimeter near an opening according to ACI 318 and EC2.

7.2 Test specimens

Nine edge slab-column connections (XXX, SF0, SE0, SF1, SF2, CF0, HXXX, HSF0, HSE0) were tested under a vertical shear force P that was applied on the top of the upper column and two lateral forces F that were applied to the column ends in three stages. Seven of them had openings in the slabs (SF0, SE0, SF1, SF2, CF0, HSF0, HSE0). In the first stage of loading, the loads were increasing with a loading rate of 2.5 kN/min. until reaching the service load of P=43 kN. Then the load was cycled 10 times between the dead and the dead plus the live loads in order to simulate the fluctuations of the live loads. At the final stage, the load was increased with 1.5 kN/min. loading rate until each specimen failed. The ratio between the unbalanced moment M produced by the two horizontal forces F and the vertical shear force P was equal to 0.3 m for the specimens XXX, SF0, SE0, SF1, SF2, CF0 and 0.66 m for the specimens HXXX, HSF0, HSE0 to account the additional moment, which may affect the slab-column connection due to the horizontal loads. These ratios were kept constant in the whole loading process. All of the

specimens had the same dimensions (1540x1020x120 mm) with top and bottom column stubs (250x250 mm) extending out 700 mm. The column was reinforced with 6-25M bars and with 8M@115 mm ties. The effective depth of all slabs was 90 mm with clear cover of concrete 20 mm. The horizontal loads were applied at distance 600 mm from the top and bottom faces of the slab. The size of the openings was 150x150 mm for all slabs, except the slab CF0 which had an opening 250x250 mm, same size as the column. Information about the compressive strength of concrete and the test results of all slabs are given in Table 7.1. Additional reinforcement was placed around the openings in specimens SF0, SF1, SF2, CF0, SE0, HSF0 and HSE0 equivalent to that interrupted by the openings. The properties for the reinforcements are shown in Table 7.2. The average tension reinforcement ratio of the slabs in both directions was equal to 0.75% and the compression reinforcement ratio in both directions was 0.45%. The loading process, the dimensions of the specimens and the location of the openings are presented in Figure 7.2. These slabs failed in punching shear and in the next sections are presented their failure loads together with the simulations' results.

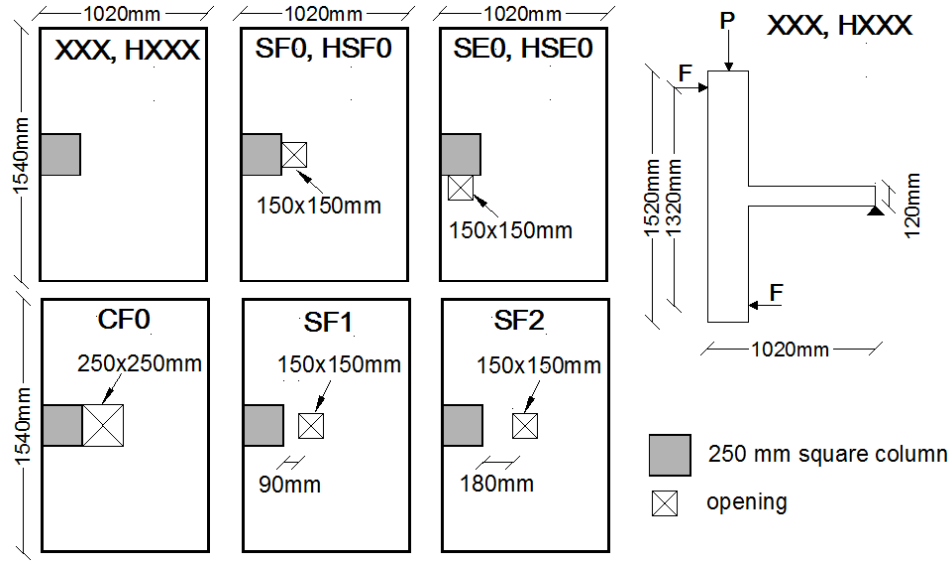

Figure 7.2 Schematic drawings of the nine edge specimens.

Table 7.1
Material properties of concrete and test results.

Slab	f'_c (MPa)	M/P (m)	Failure load (kN)	Maximum displacement (mm)
XXX	33	0.3	125	15.06
SF0	31.5	0.3	110	15.95
SE0	32.5	0.3	120	15.55
SF1	33	0.3	115	15.02
SF2	30	0.3	114	13.44
CF0	30.5	0.3	86	11.01
HXXX	36.5	0.66	69	5.96
HSF0	36	0.66	58	6.95
HSE0	36.5	0.66	65	5.26

Table 7.2
Material properties of flexural reinforcement.

Steel layer	Bar size	f_y (MPa)	ε_y	f_t (MPa)	ε_t	E_s (MPa)
Compressive	5M	430	0.0022	600	0.15	195000
Tensile	10M	545	0.0027	900	0.10	180000

7.3 Finite element simulations

One half, of the slab-column connections, is used for the simulations in ABAQUS. The symmetry is not effective for the specimens SE0 and HSE0, and for that reason the whole slabs are analyzed. Six 20 mm mesh elements are used through the depth of the slabs. Concrete is modelled with 8-noded hexahedral with reduced integration elements (C3D8R) and the reinforcement is modeled using 2-noded 3D truss elements (T3D2) that can transmit only axial loads. In ABAQUS, the C3D8R finite elements are continuum stress/displacement 3D solid elements of first order with reduced integration. Perfect bond between concrete and reinforcement is assumed through the embedded method. This means that the interaction between concrete and reinforcement is indirectly considered through the concrete material modelling by using the tension stiffening response for the tensile behaviour. Simple supports are

introduced at the bottom of the slabs. Quasi-static analysis in ABAQUS/Explicit solver is performed for all specimens. For accuracy in quasi-static analyses a smooth amplitude curve should be adopted simulating the increasing velocity. In our analyses, the velocity is applied through the column stub simulating the displacement control analysis that is performed in tests. Mass scaling is not considered for reducing the computational solution time in the analyses and the energy balance equation is evaluated at the end of each analysis in order to estimate whether or not each simulation produces a proper quasi-static response.

7.4 Finite element analysis results

The nine edge slab-column connection specimens failed in punching shear. The response of the specimens is described in terms of ultimate vertical load and deflection. The results obtained from the nonlinear finite element analyses describe accurately the response of the tested slabs. In all specimens the FEA results predicted the punching shear capacity almost 10% lower compared to the test results. The test and the FEA results for each specimen are described in Table 7.3. In both test and numerical results the tensile reinforcement yielded first under the column. The cracking propagation in both test and the FEA started on the tension side of the slabs. For specimens with ratio M/P=0.3 m, the cracking started at an approximately vertical load of 40-50 kN while for the specimens with ratio M/P=0.66 m, the cracks are initiated at an approximately vertical load of 30-40 kN. The cracks started from the inner corners of the columns and developed towards the edges of the slabs. Cracks on the compressive side of the slabs are developed at approximately 75% of the ultimate load for the specimens with ratio M/P=0.3 m, compared to the specimens with ratio M/P=0.66 m which did not develop cracks on the compressive side of the slabs. It should be noted that the first cracks for the specimens SF0

and CF0 started from the inner corners of the openings and developed in a similar way to those that started from the columns' corners.

The effect of the location of the opening size of 150x150 mm, in terms of the distance from the front column face, on the punching shear capacity is small. The comparison between the slabs SF0, SF1 and SF2, in terms of vertical load versus deflection, shows that the slab SF0 with the opening in front of the front column face has the lower punching capacity compared to the two other slabs. However, the differences between these three specimens were not significant. The opening is located at a distance 90 mm and 180 mm from the front column face for the slab SF1 and SF2, respectively. It is observed from both test and analytical results that both slabs (SF1 and SF2) have almost the same response in terms of ultimate vertical load and displacement (Figure 7.3a).

As illustrated in Figure 7.3b, the slab with the side face opening (SE0) has stiffer response compared to the slab SF0 that has a face front opening. In terms of ultimate load the slab SE0 has about 10% higher ultimate load compared to the slab SF0. Test and numerical results in terms of load-deflection response are in good agreement for the specimen SE0.

Figure 7.3c presents the effect of the opening size. Three slabs are compared in terms of ultimate load and displacement. Slab XXX is the control specimen without opening, slabs SF0 and CF0 have the opening located at the front column face, with size 150x150 mm and 250x250 mm, respectively. Both experimental and analytical results show that as the opening is larger, both stiffness and strength are reduced.

The effect of the unbalanced moments to the ultimate load is presented in Figure 7.3d. The slabs HXXX and HSF0 with unbalanced moment to shear force ratio 0.66 m are compared

to the slabs XXX and SF0 with unbalanced moment to shear force ratio 0.3 m, for both tested and analytical results. The slab HXXX had lower tested punching shear capacity (about 50% less) compared to the slab XXX. The finite element simulations showed that the punching shear capacity of the slab HXXX was 25% lower compared to the slab XXX. The tested slab HSF0 had lower punching shear capacity (about 47%) compared to the tested slab SF0. The finite element simulations showed that the punching shear capacity of the slab HSF0 was 38% lower compared to the slab SF0.

Table 7.3
Comparison between test and FEA results.

	Test results		**FEA results**	
Slab specimen	Failure load (kN)	Maximum displacement (mm)	Failure load (kN)	Maximum displacement (mm)
XXX	125	15.06	112	17.69
SF0	110	15.95	97	14.94
SE0	120	15.55	109	17.75
SF1	115	15.02	102	14.57
SF2	114	13.44	106	13.74
CF0	86	11.01	86	12.75
HXXX	69	5.96	84	6.77
HSF0	58	6.95	60	6.93
HSE0	65	5.26	76	6.23

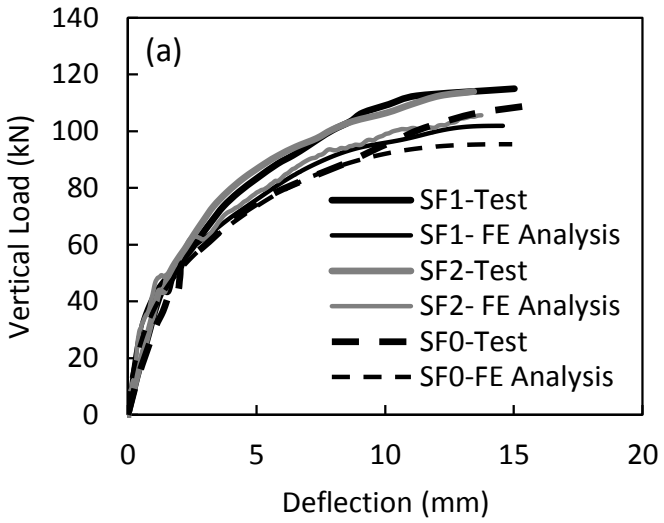
(a)
Vertical Load (kN)
Deflection (mm)
SF1-Test
SF1- FE Analysis
SF2-Test
SF2- FE Analysis
SF0-Test
SF0-FE Analysis

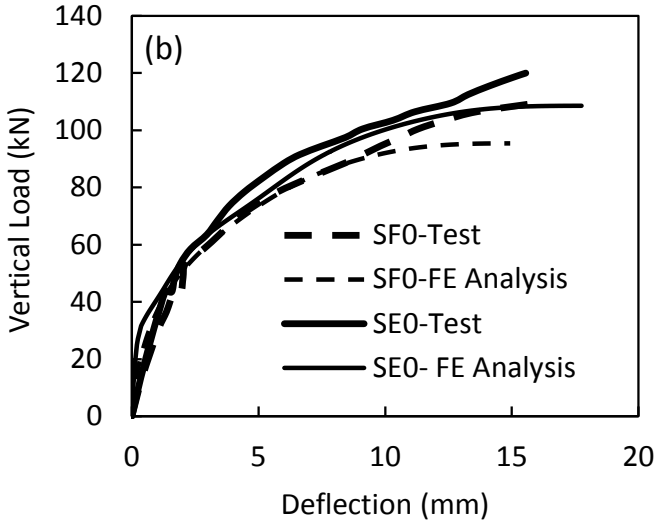
(b)
Vertical Load (kN)
Deflection (mm)
SF0-Test
SF0-FE Analysis
SE0-Test
SE0- FE Analysis

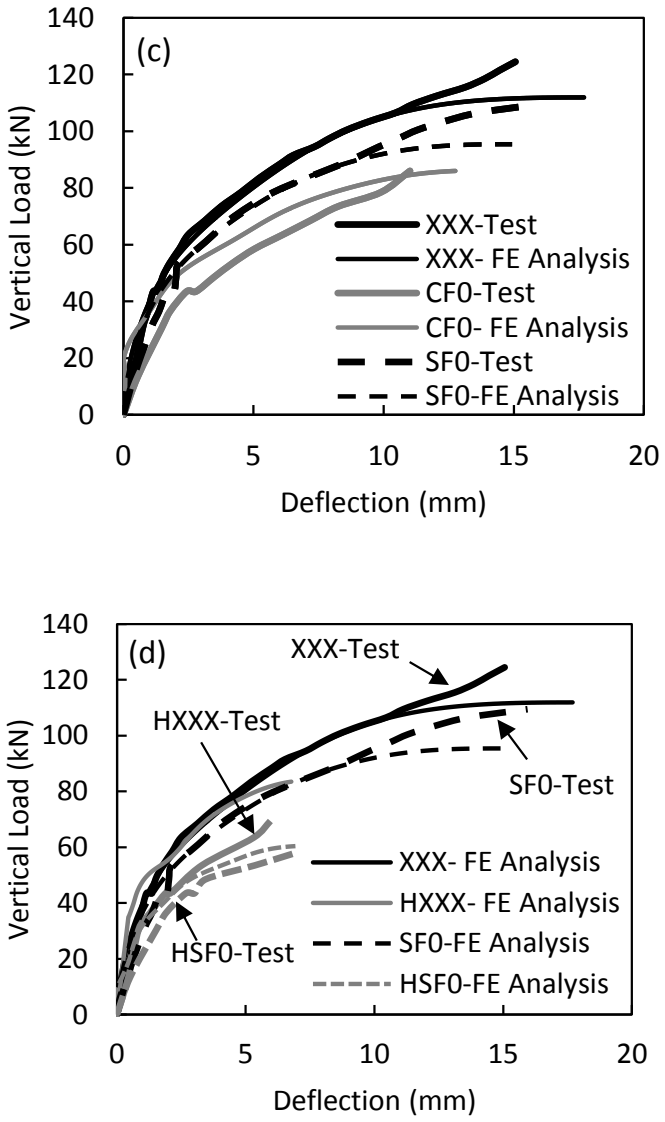

Figure 7.3 Vertical load-deflection responses of the slabs.

Figure 7.4 illustrates the cracking patterns on the tension side of the slab at failure, as it was observed from the tests and FEA. Crack patterns at failure of three slabs were chosen for comparison. The cracking in concrete damaged plasticity model can be illustrated through the positive maximum principal plastic strains. It is clear that all cracking patterns obtained from the finite element simulations are in good agreement with the cracking propagation observed from

the tests. The adopted perfect bond between concrete and reinforcement shows a more continuous cracking and not so discrete compared to the real cracking from the tests and the cracking that can be provided from the FEA by considering a not perfect bond. However, the bond-slip effect is considered in the concrete damaged plasticity model through the tension-stiffening model.

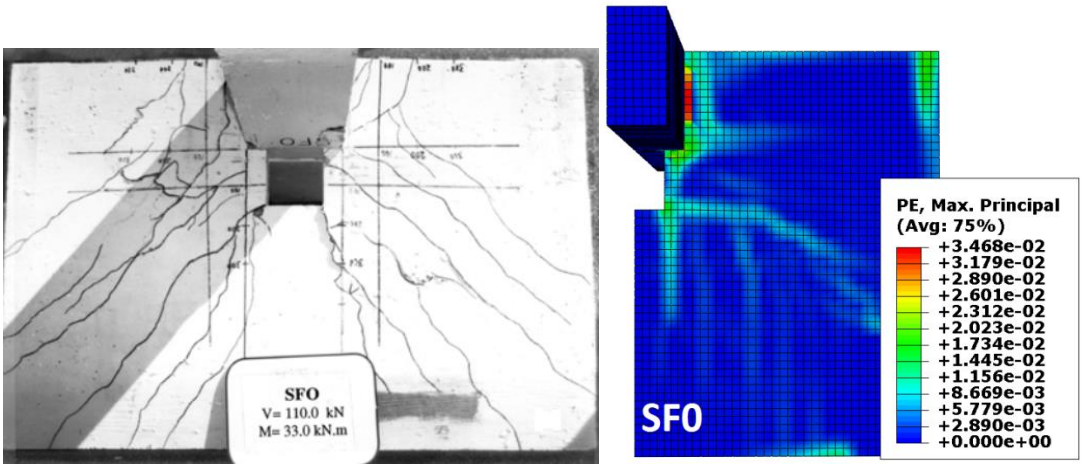

a)

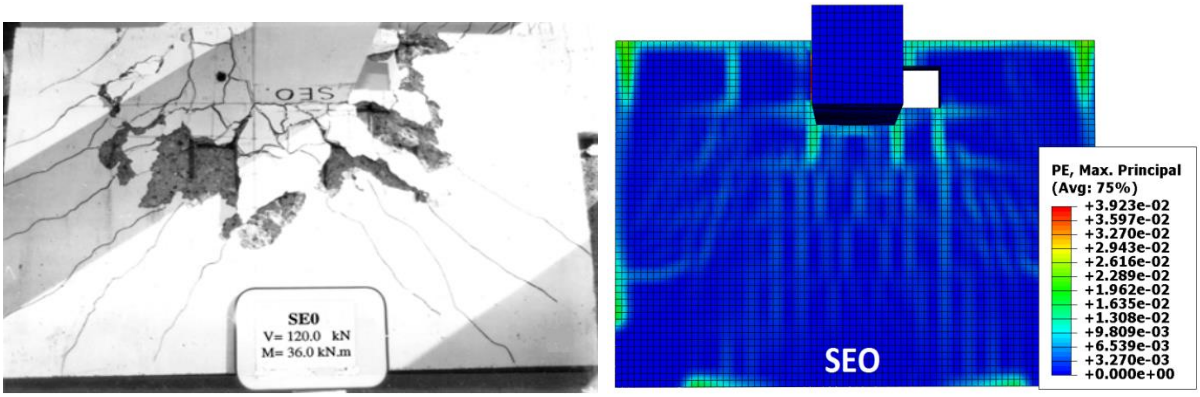

b)

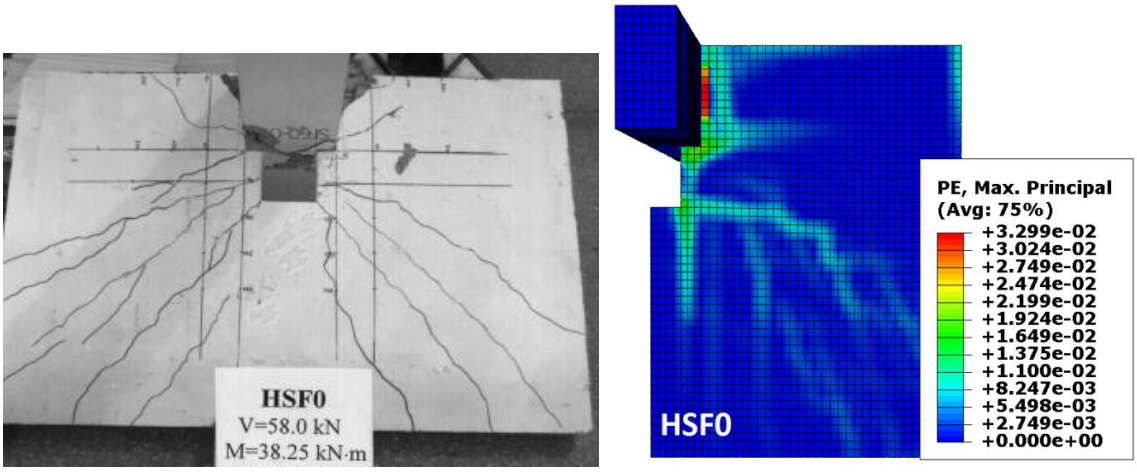

c)

Figure 7.4 Comparison between tested and FEA cracks at the failure: a) slab SF0, b) slab SE0 and c) slab HSF0.

The cracks on the tension surface of the slabs SF0, SF1 and SF2 are presented in Figure 7.5. These three slabs have the same size of opening (150x150 mm) located in front of the column in the direction of the unbalanced moments but at different distances from the column's face. Specimen SF0 has the opening adjacent to the column, while specimens SF1 and SF2 have the opening located at a distance of 90 mm and 180 mm from the column's face, respectively. It is noticed from both experimental and analytical results, that these three slabs have almost similar ultimate loads and deflections. However, the cracking patterns are different due to the location of the opening. The cracking propagation from the numerical analyses could be presented into three loading stages. Up to 40% of the ultimate load the cracking is concentrated for all specimens around the column with some radial cracks on the tension side of the slab on the diagonal (Figure 7.5a). It is quite interesting to notice that this diagonal cracks in the case of specimens SF0 and SF1 start to develop at the corner of the opening, while for specimen SF2 start to develop at the corner of the column. At the 80% of the ultimate load the shear cracks

have already developed and extended further, and tangential cracks have developed and continued to the diagonal of the slab (Figure 7.5b). At this load stage more radial cracks have occurred and become visible. At the ultimate load, the shear cracks open suddenly. As it is obvious from Figure 7.5c, the shear cracks of the specimen SF1 form next to the column with secondary developed cracks starting from corner of the opening. However, the cracks at failure of the specimen SF2 do not develop past the opening.

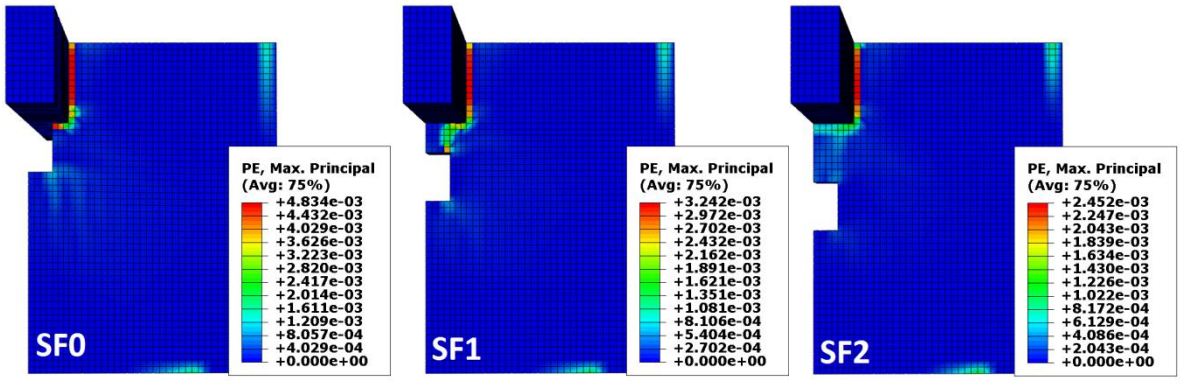

a)

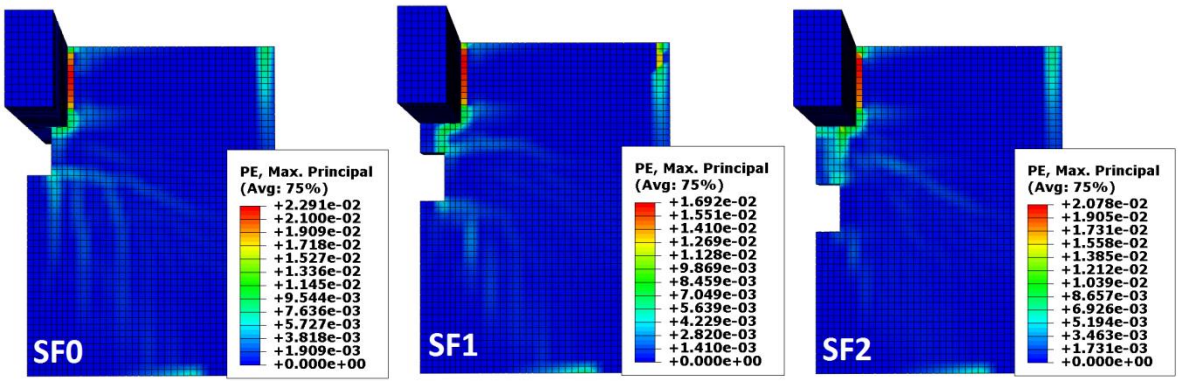

b)

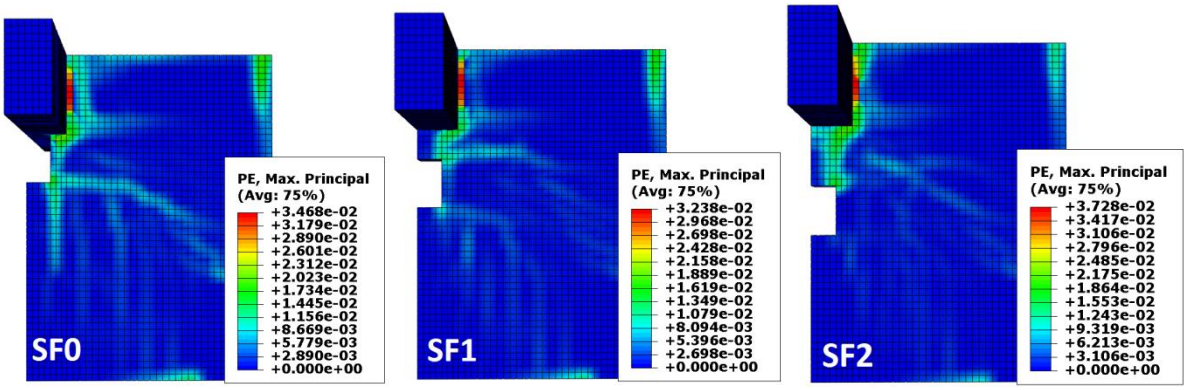

c)

Figure 7.5 Cracking process at the tension surface of the slabs SF0, SF1, SF2: a) 40% of ultimate load, b) 80% of ultimate load and c) ultimate load.

7.5 Unbalanced moments according to ACI318-11

The tested edge slab-column connections consist of slabs without shear reinforcement. The loading in all specimens was vertical and lateral, at the same time. In this section, the test and numerical results are compared with the punching shear loads that ACI 318-11 provides. Herein, a detailed description on how ACI calculates the punching shear loads is given. Two slab-column connections, one without opening (XXX) and one with opening (SF0), are considered.

ACI 318-11

For slabs under gravity load and connection moment (M), the moment in ACI318-11 can be derived from the following equation:

$$v_f = \frac{V_f}{b_o d} + \frac{\gamma_v M_f c}{J_c} \tag{7.1}$$

where, v_f is the factored shear stress, V_f is the vertical factored shear force, b_o is the control perimeter, d is the effective depth of the slab, J_c is the property of assumed critical section analogous to the polar moment of inertia, $\gamma_v = 1 - \frac{1}{1+\frac{2}{3}\sqrt{\frac{b_1}{b_2}}}$ is the fraction unbalanced moment transferred by shear eccentricity, where b_1 is the width of the critical section perpendicular to the moment vector and b_2 is the other side length and c is the centroid of the shear perimeter.

According to ACI318-11 the punching shear resistance of the slabs without shear reinforcement (V_c) is:

$$V_c = min\begin{cases} 0.33\lambda b_o d\sqrt{f'_c} \\ 0.17\lambda b_o d\sqrt{f'_c}\left(1+\frac{2}{\beta_c}\right) \\ 0.083\lambda b_o d\sqrt{f'_c}\left(2+\frac{\alpha_s d}{b_o}\right) \end{cases} \quad (f'_c \; in \; MPa) \tag{7.2}$$

Slab-column connection XXX (slab without opening)

The compressive strength of slab XXX is $f'_c = 33\,MPa$ and the effective depth $d = 90\,mm$. Figure 7.6 shows the control perimeter measured at distance $d/2 = 45\,mm$ from the face of the column and the eccentricity.

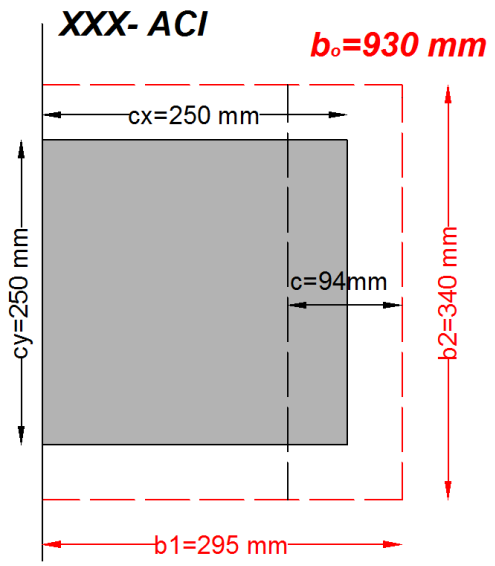

Figure 7.6 Control perimeter and eccentricity for slab XXX.

The control perimeter for the slab XXX is $b_o = 2 \cdot c_x + b_2 = 2 \cdot 295 + 340 = 930\ mm$.

The eccentricity is equal to $c = \frac{\left(c_x + \frac{d}{2}\right)^2}{b_o} = \frac{\left(250 + \frac{90}{2}\right)^2}{930} = 93.6\ mm$.

The fraction of the unbalanced moment transferred by the eccentricity is equal to $\gamma_v = 1 - \frac{1}{1 + \frac{2}{3}\sqrt{\frac{b_1}{b_2}}} = 1 - \frac{1}{1 + \frac{2}{3}\sqrt{\frac{295}{340}}} = 0.383$. The polar moment of inertia is equal to $J_c = 2b_1\frac{d^3}{12} + 2d\frac{b_1^3}{12} + 2b_1 d\left(\frac{b_1}{2} - c\right)^2 + b_2 dc^2 = 2 \cdot 295 \cdot \frac{90^3}{12} + 2 \cdot 90 \cdot \frac{295^3}{12} + 2 \cdot 295 \cdot 90\left(\frac{295}{2} - 93.6\right)^2 + 340 \cdot 90 \cdot 93.6^2 = 8.43 \cdot 10^8\ mm^4$.

The punching shear resistance of the slab XXX (V_c) is calculated using Eq. 7.2:

$$V_c = min\begin{cases} 0.33\lambda b_o d\sqrt{f'_c} = 0.33 \cdot 1 \cdot 930 \cdot 90 \cdot \sqrt{33} = 159\ kN \\ 0.17\lambda b_o d\sqrt{f'_c}\left(1 + \frac{2}{\beta_c}\right) = 0.17 \cdot 1 \cdot 930 \cdot 90 \cdot \sqrt{33} \cdot \left(1 + \frac{2}{\frac{250}{250}}\right) = 245\ kN \\ 0.083\lambda b_o d\sqrt{f'_c}\left(2 + \frac{\alpha_s d}{b_o}\right) = 0.083 \cdot 1 \cdot 930 \cdot 90 \cdot \sqrt{33} \cdot \left(2 + \frac{30 \cdot 90}{930}\right) = 196\ kN \end{cases}$$

The ratio of the moment (M) to the vertical force (V) is equal to $M/V = 0.3$. Thus, Eq. 7.1 can be used in order to calculate the value of the vertical force (V). We consider that $v_f = v_c$.

$$v_f = \frac{V_f}{b_o d} + \frac{\gamma_v M_f c}{J_c} \rightarrow 0.083 \cdot 1\sqrt{33} \cdot \left(2 + \frac{30 \cdot 0.09}{0.93}\right) =$$

$$= \frac{V_f}{0.93 \cdot 0.09} + \frac{0.383 \cdot (0.3V_f - V_f(0.125 - 0.0486)) \cdot 0.0936}{0.000843} \rightarrow V_f = 88\ kN$$

Slab-column connection SF0 (slab with opening)

The compressive strength of slab SF0 is $f'_c = 31.5\ MPa$ and the effective depth $d = 90\ mm$. Figure 7.7 shows the control perimeter considering the opening measured at a distance $d/2 = 45\ mm$ from the face of the column and the eccentricity.

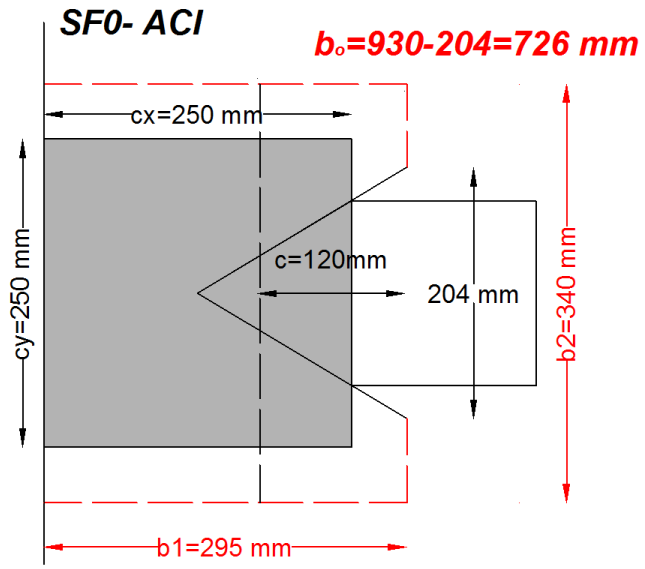

Figure 7.7 Control perimeter and eccentricity for slab SF0.

The control perimeter for the slab SF0 is $b_o = 930 - 204 = 726\,mm$. The eccentricity is equal to $c = \frac{\left(c_x + \frac{d}{2}\right)^2}{b_o} = \frac{\left(250 + \frac{90}{2}\right)^2}{726} = 119.9\,mm$.

The fraction of the unbalanced moment transferred by the eccentricity is equal to $\gamma_v = 0.383$. The polar moment of inertia is equal to $J_c = 2b_1\frac{d^3}{12} + 2d\frac{b_1^3}{12} + 2b_1 d\left(\frac{b_1}{2} - c\right)^2 + (b_2 - 204)dc^2 = 2 \cdot 295 \cdot \frac{90^3}{12} + 2 \cdot 90 \cdot \frac{295^3}{12} + 2 \cdot 295 \cdot 90\left(\frac{295}{2} - 119.9\right)^2 + (340 - 204) \cdot 90 \cdot 119.9^2 = 6.37 \cdot 10^8\,mm^4$.

The punching shear resistance of the slab SF0 (V_c) is calculated using Eq. 7.2:

$$V_c = min\begin{cases} 0.33\lambda b_o d\sqrt{f'_c} = 0.33 \cdot 1 \cdot 726 \cdot 90 \cdot \sqrt{31.5} = 121\,kN \\ 0.17\lambda b_o d\sqrt{f'_c}\left(1 + \frac{2}{\beta_c}\right) = 0.17 \cdot 1 \cdot 726 \cdot 90 \cdot \sqrt{31.5} \cdot \left(1 + \frac{2}{\frac{250}{250}}\right) = 187\,kN \\ 0.083\lambda b_o d\sqrt{f'_c}\left(2 + \frac{\alpha_s d}{b_o}\right) = 0.083 \cdot 1 \cdot 726 \cdot 90\sqrt{31.5}\left(2 + \frac{30 \cdot 90}{726}\right) = 174\,kN \end{cases}$$

The ratio of the moment (M) to the vertical force (V) is equal to $M/V = 0.3$. Thus, Eq. 7.1 can be used in order to calculate the value of the vertical force (V).

$$v_f = \frac{V_f}{b_o d} + \frac{\gamma_v M_f c}{J_c} \rightarrow 0.083 \cdot 1\sqrt{31.5} \cdot \left(2 + \frac{30 \cdot 0.09}{0.726}\right) =$$

$$= \frac{V_f}{0.726 \cdot 0.09} + \frac{0.383 \cdot (0.3V_f - V_f(0.125 - 0.0486)) \cdot 0.1199}{0.000637} \rightarrow V_f = 56\ kN$$

Based on the design equations and the material properties of each slab, Table 7.4 compares the failure punching shear loads according to tests, FE analyses and ACI318-11. The results from the finite element analyses are close to the experimental results. However, ACI318-11 appears conservative predictions. Especially, for the slabs with openings, ACI predicts much lower punching shear loads compared to the results from the tests and FEA.

Table 7.4
Ultimate load for edge specimens according to test, FEA and ACI results.

Slab specimen	Failure load (kN)		
	Test results	**FEA results**	**ACI 318-11**
XXX	125	112	88
SF0	110	97	56
SE0	120	109	78
SF1	115	102	70
SF2	114	106	72
CF0	86	86	33
HXXX	69	84	54
HSF0	58	60	33
HSE0	65	76	53

7.6 Parametric investigation on the effect of opening location and size

Parametric analyses to investigate the effect of the opening location and size are conducted. Figure 7.8 presents the edge specimens considered for the numerical analyses. The slabs SF0, SF1, SF2 and CF0, are the tested slabs that were presented earlier and the others are the specimens that are created for the parametric investigations. Two opening sizes are considered: 150x150 mm and 250x250 mm. The distance of these openings from the column ranges from 0 mm to 450 mm depending on the d (effective depth of the slab), (450 mm=5d, where d=90 mm). Figure 7.9 presents the effect of the opening location and size for the slabs. All FEA show that as the opening is located further to the column the punching shear capacity of the slab increases; if the opening is located at distance 5d (450 mm), the strength of the slab becomes almost the same with the strength of the specimen that has no opening (XXX). At distance 450 mm the punching strength of the specimen SF5 and CF5 is 110 kN and 109 kN, respectively. The FEA ultimate load of the slab XXX is 112 kN. Therefore, the punching shear load of the slab SF5 is 1.8% less and the punching shear load of the slab CF5 is 2.7% less, both compared with the ultimate load of the slab without opening (XXX). Also, the difference in the ultimate loads between the slabs with the smaller and larger openings seems to be not significant after the distance 4d. Therefore, the reduction of slab's strength, due to openings should be considered when the opening is located in distance less than 5d from the column.

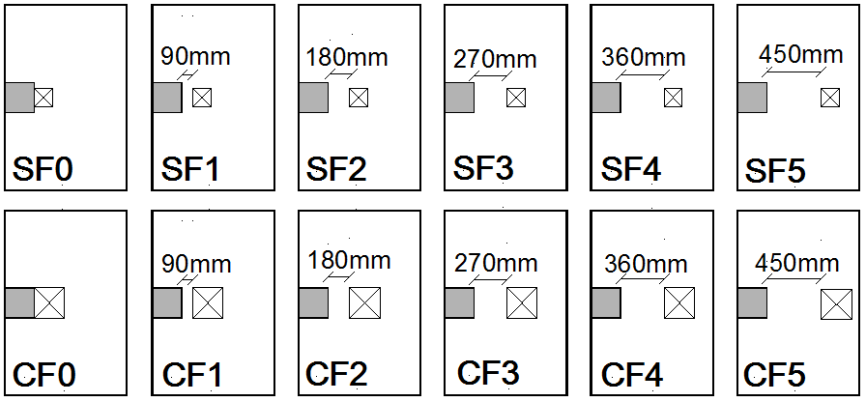

Figure 7.8 Schematic drawing of the edge slabs with different openings and at different location.

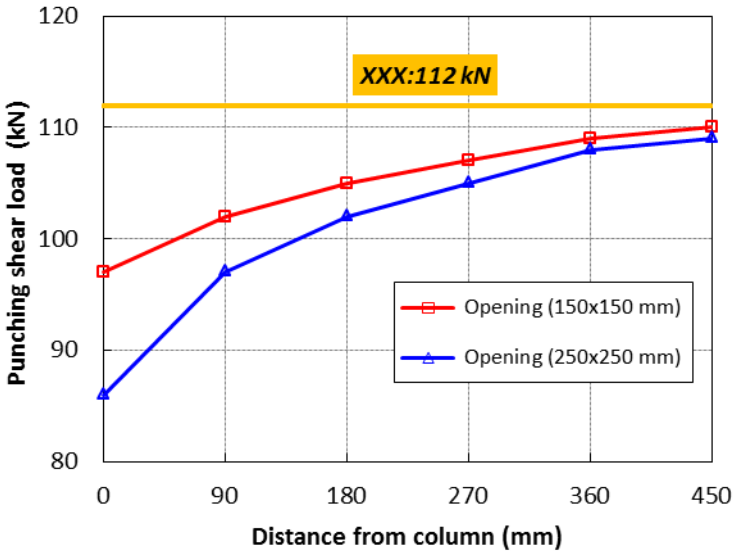

Figure 7.9 Distance effect of the opening on the punching shear resistance of the edge slabs.

Then, interior slab-column connections are considered for parametric investigation on the effect of opening size and location on the slabs' capacity. The parametric analyses for the interior slabs are chosen based on the specimen SB1 that was tested under gravity load through the column. During the test, specimen SB1 failed in punching shear at a load of 253 kN. The FEA results showed the punching shear failure at a load of 234 kN. Figure 7.10 shows the interior specimens considered for the numerical analyses. Two opening sizes are considered for the parametric studies: 70x70 mm and 150x150 mm. Analyzing one quarter of the slab SB1 due to

the symmetry, two openings are adopted in each case. The distance of these openings from the column ranges from 0 mm to 450 mm (450 mm=5d, where d is the effective depth of the slab equal to 90 mm).

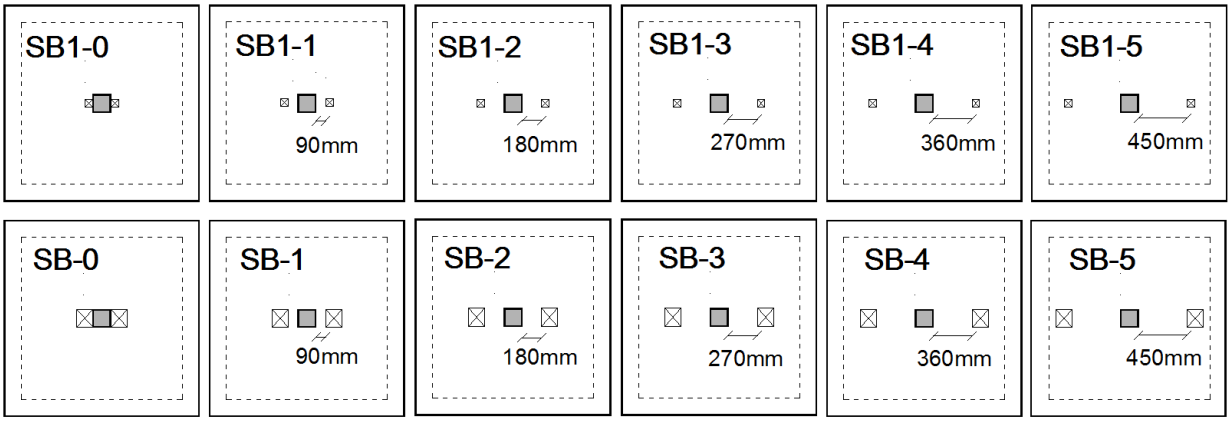

Figure 7.10 Schematic drawing of the interior slabs with different size and location of the openings.

Figure 7.11 shows the effect of the opening location and size for the interior slabs. All of the numerical results show that as the opening is located further to the column, the punching shear capacity of the slab is increased; when the openings are located at a distance more than 4d from the column, the ultimate loads are almost the same for all specimens. At opening distance of 5d (450 mm), the strengths of the specimens SB1-5 and SB-5 are 223 kN and 219 kN, respectively. The ultimate load of the SB1 (slab without openings) was found equal to 234 kN. Therefore, the ultimate loads of the slabs SB1-5 and SB-5 compared to the punching shear load of specimen SB1, are 4.7% and 6.4% lower. The higher difference on the ultimate loads compared to the previous shown edge slabs, can be explained due to the existence of two openings in the interior slabs.

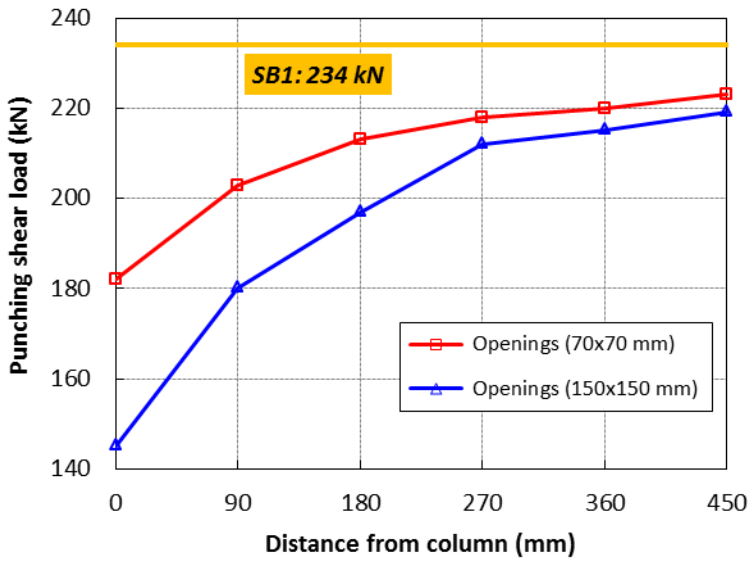

Figure 7.11 Distance effect of the opening on the punching shear resistance of the interior slabs.

The cracking at the tension surface of six chosen interior slabs SB1-0, SB-0, SB1-1, SB-1, SB1-5 and SB-5 is presented in Figure 7.12. The slabs SB1-0, SB1-1 and SB1-5 have the same size of openings (70x70 mm) located at different distances from the column's face. Specimen SB1-1 has the openings adjacent to the column, while specimens SB1-1 and SB1-5 have the openings located at a distance of 90 mm and 450 mm from the column's face, respectively. For comparison, the cracking pattern of the slabs SB-0, SB-1 and SB-5 that have larger openings (150x150 mm) is presented. The cracking patterns are different due to the location and size of the opening.

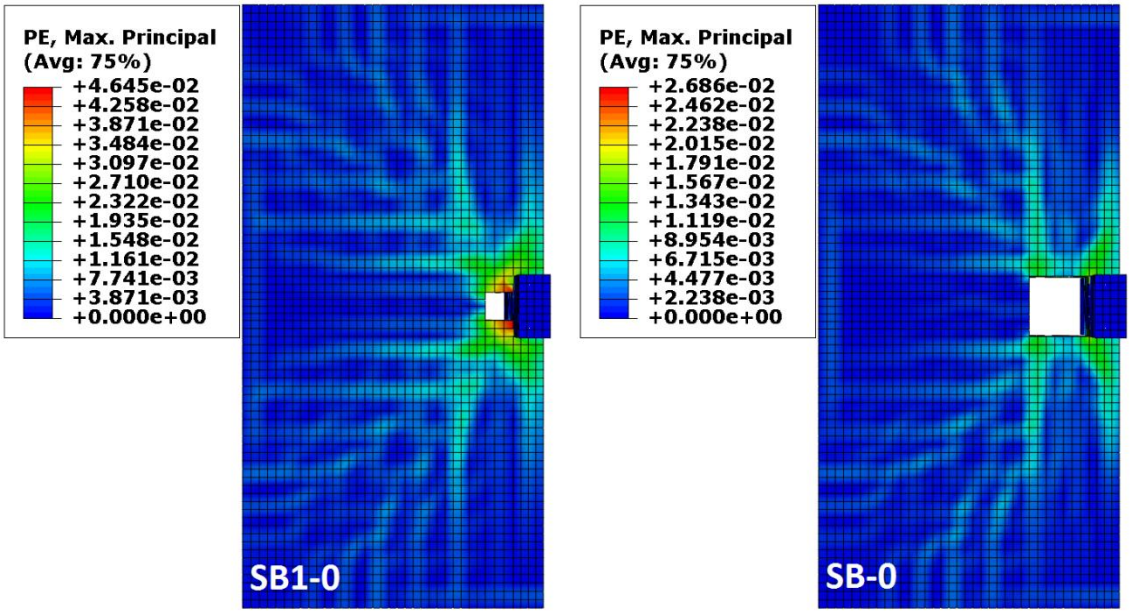
PE, Max. Principal
(Avg: 75%)
+4.645e-02
+4.258e-02
+3.871e-02
+3.484e-02
+3.097e-02
+2.710e-02
+2.322e-02
+1.935e-02
+1.548e-02
+1.161e-02
+7.741e-03
+3.871e-03
+0.000e+00
SB1-0
PE, Max. Principal
(Avg: 75%)
+2.686e-02
+2.462e-02
+2.238e-02
+2.015e-02
+1.791e-02
+1.567e-02
+1.343e-02
+1.119e-02
+8.954e-03
+6.715e-03
+4.477e-03
+2.238e-03
+0.000e+00
SB-0

a)

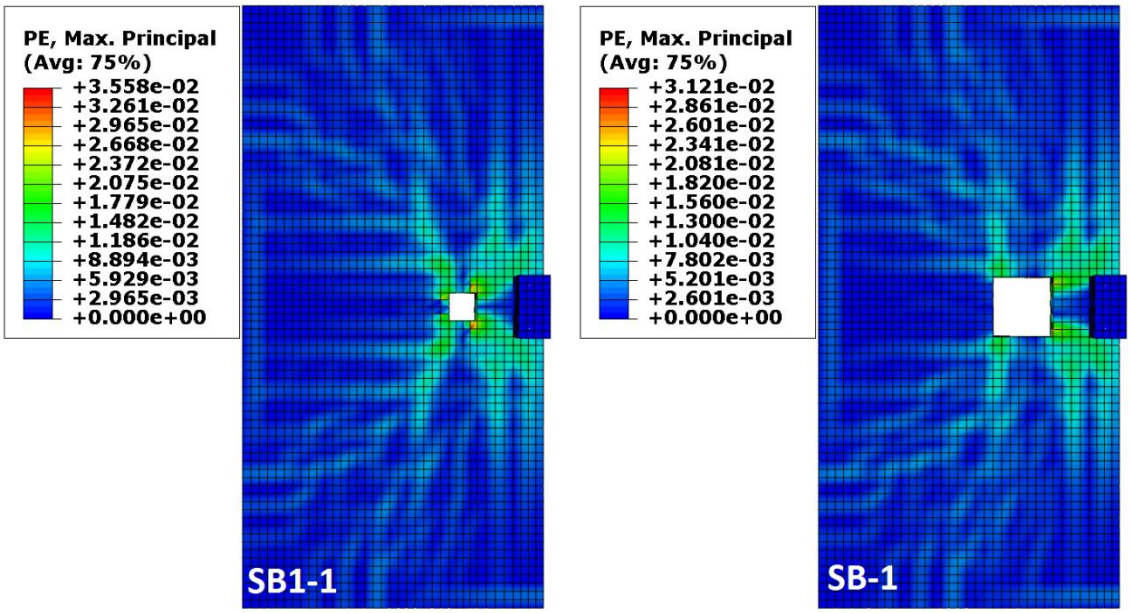
PE, Max. Principal
(Avg: 75%)
+3.558e-02
+3.261e-02
+2.965e-02
+2.668e-02
+2.372e-02
+2.075e-02
+1.779e-02
+1.482e-02
+1.186e-02
+8.894e-03
+5.929e-03
+2.965e-03
+0.000e+00
SB1-1
PE, Max. Principal
(Avg: 75%)
+3.121e-02
+2.861e-02
+2.601e-02
+2.341e-02
+2.081e-02
+1.820e-02
+1.560e-02
+1.300e-02
+1.040e-02
+7.802e-03
+5.201e-03
+2.601e-03
+0.000e+00
SB-1

b)

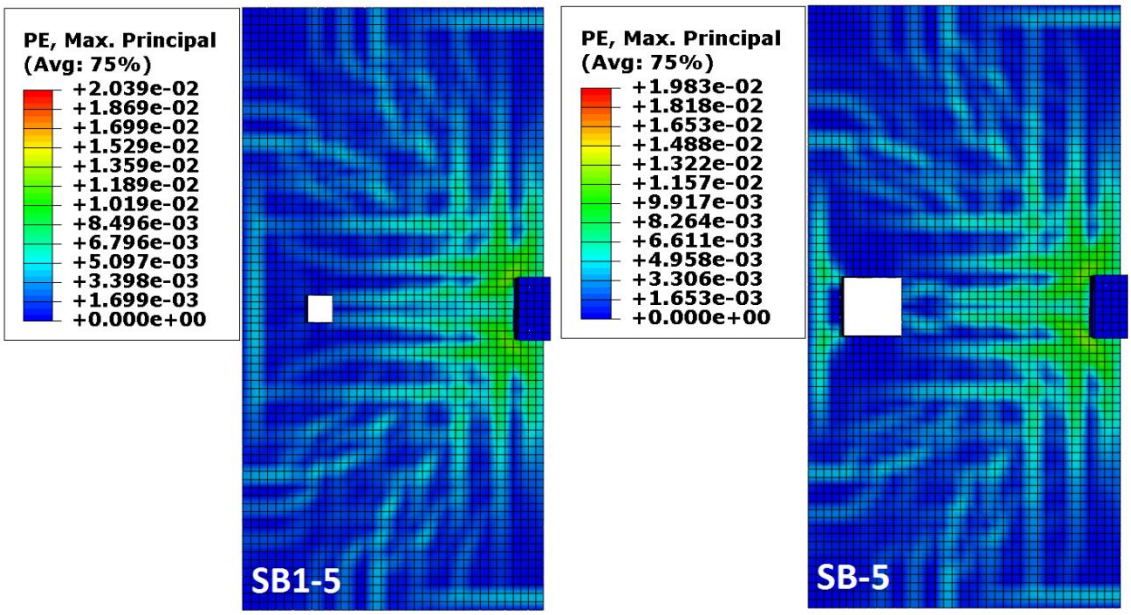

c)

Figure 7.12 Crack pattern of interior slabs: a) openings at distance 0d, b) openings at distance 1d and c) openings at distance 5d.

With respect to the code predictions (ACI and EC2), Table 7.5 presents the ultimate loads of the interior slab-column connections from the FEA and the design codes. In all the cases, the design codes appear safe results; while ACI gives the most conservative. Figure 7.13 illustrates the comparison of the punching shear loads between FEA and design codes for the specimens with openings of 70x70 mm. When the openings are located direct next to the column, both design codes give almost the same predictions, however, when the openings are further located, the design codes give different results. In case of the slab SB1-0 the difference in the design codes is 2 kN but in case of the slab SB1-5 the difference is 11 kN. Therefore, as the opening is located further from the column, the difference in the design codes becomes higher and if we examine the slab SB1 that has no openings, ACI predicts a punching shear load of 189 kN and EC2 a resistance of 202 kN, leading to a difference of 13 kN. Considering now the slabs with

openings of 150x150 mm (see Figure 7.14) again the highest difference (9 kN) between the two design codes appears when the opening is located at the distance of 450 mm. It can be concluded that both design codes for the most worst scenario, when the openings are located next to the column, even if they adopt different formulae for calculating the punching shear resistance with different control perimeter, they predict similar failure loads. When the openings exist further from the column and in the case that no openings exist, the difference in the predicted results becomes higher.

Table 7.5
Comparison of ultimate load between FEA and codes for interior specimens.

Specimen	Distance from the column (mm)	Size of openings(mm)	FEA Punching load (kN)	ACI Punching load (kN)	EC2 Punching load (kN)
SB1-0	0	70x70	182	145	147
SB-0	0	150x150	145	95	101
SB1-1	90	70x70	198	169	177
SB-1	90	150x150	180	146	149
SB1-2	180	70x70	213	176	185
SB-2	180	150x150	197	161	167
SB1-3	270	70x70	218	180	190
SB-3	270	150x150	212	169	176
SB1-4	360	70x70	220	182	192
SB-4	360	150x150	215	173	181
SB1-5	450	70x70	223	183	194
SB-5	450	150x150	219	176	185

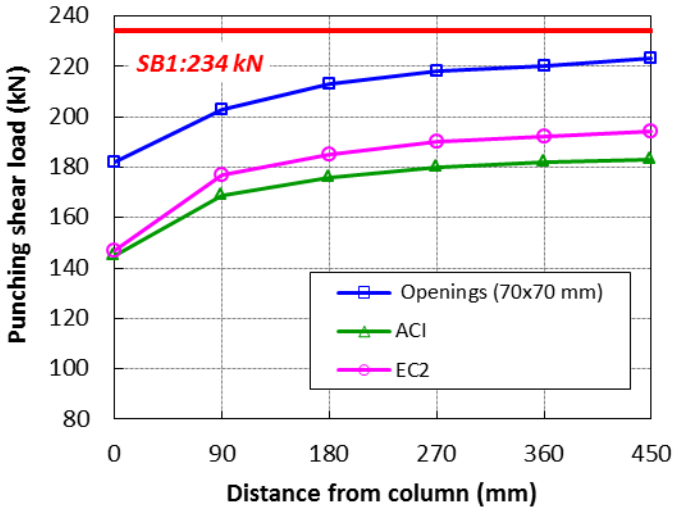

Figure 7.13 Distance effect of the opening on the punching shear resistance of the interior slabs with openings (70x70 mm) – Comparison with the design codes.

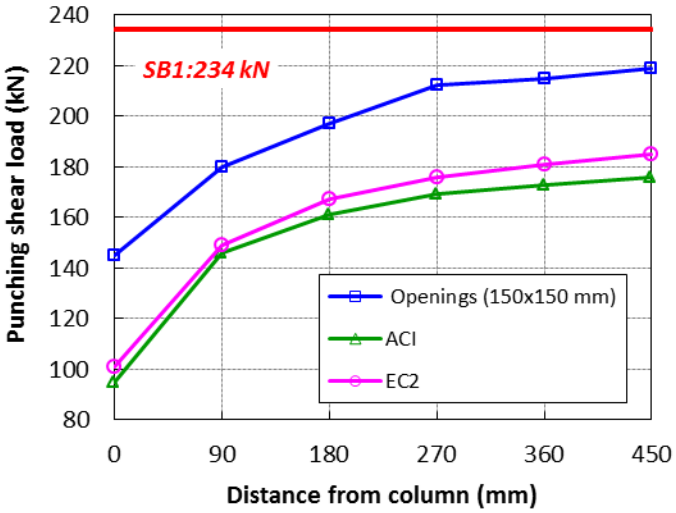

Figure 7.14 Distance effect of the opening on the punching shear resistance of the interior slabs with openings (150x150 mm) – Comparison with the design codes.

Figure 7.15 compares the punching loads of the two design codes for the two sizes of openings. The punching shear loads are calculated for openings located from 0d until 9d from the face of the column. EC2 after the distance 6d considers the punching strength of the slab same as the capacity of the slab without any opening. ACI will predict the same load with the specimens

that have no openings, only if the opening is located at a distance 10h=1200 mm from the column.

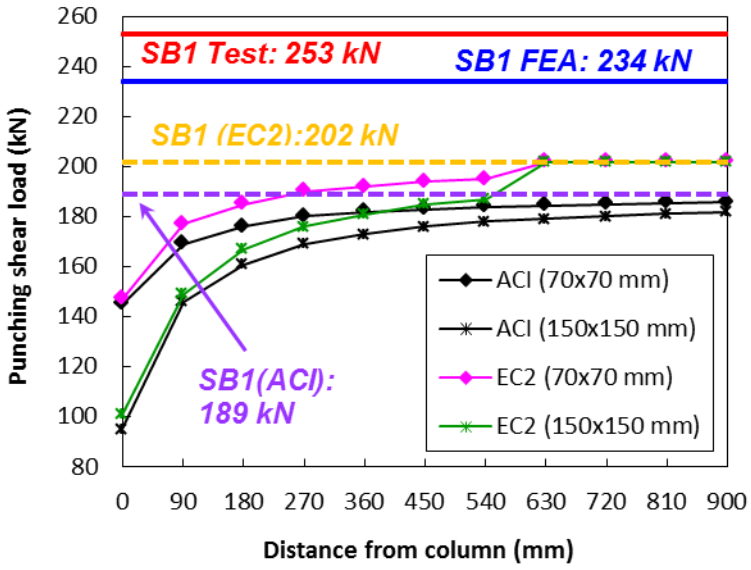

Figure 7.15 Distance effect of the opening on the punching shear resistance of the interior slabs.

7.7 Summary and Conclusions

The opening effect is studied on edge specimens and parametric investigation is performed on edge and interior slab-column connections. The openings in existing slabs reduce the punching shear strength. This reduction is dependent on the distance from the opening to the face of the column. However, when the opening is located at distance d (SF1 slab) and 2d (SF2 slab) from the column, the punching shear capacity of the slabs remained almost the same during the tests. The finite element analysis can give an insight into slabs' behaviour by showing the cracking propagation. The propagation of cracking shows that the shear cracks are observed around the column and also at the corners of the openings and in the cases that the openings are located at a distance from the column (SF1 and SF2) and not next to it (SF0); secondary cracks

are illustrated beginning from the corners of the openings. The results obtained from the parametric investigation regarding the influence of the size and location of the opening have shown that when the opening is located at a distance larger than 4d from the column the punching shear capacity of the slab remains almost the same as for the slab without openings. The code provisions of ACI 318-11 and EC-2 2004 give safe results compared to the test and numerical observations. All presented analyses of that chapter show that the concrete damaged plasticity model correctly predicts the punching shear response of the analyzed slabs. The good agreement between test and numerical results for all the slab-column connections indicate that the calibrated model in ABAQUS could be considered for future parametric investigation in reinforced concrete slabs with openings. The FEA can supplement the experimental data for slabs with openings. These verified and calibrated finite element models can be used to calibrate the code provisions for the punching shear capacity of the slabs with openings.

Chapter 8

Parametric studies: Continuity effect on punching shear capacity

8.1 Introduction

Design codes for punching shear resistance of flat slabs are based on test results from isolated slab-column connections. However, by testing isolated slabs, the compressive membrane action of the continuous slab-column system is ignored. This can result in lower punching shear strength compared to the actual strength of the real slab systems. Testing continuous slab system is very uneconomical and in most cases not possible. In this chapter, finite element analyses (FEA) are performed in order to investigate the effect of the compressive membrane action in flat concrete slabs by comparing results from isolated specimens and continuous floor systems. The adopted FE formulation and the material parameters were previously calibrated on the isolated test specimen (SB1) under gravity loading. In this study, this calibrated model is considered for analyzing the slab SB1 as continuous, where its boundary conditions are modified, and also the slab is considered to have larger in-plane dimensions in order to examine slab's continuity. Finally, numerical analyses of existing punching shear tests that examine the compressive membrane action effect are conducted to show the accuracy of the FEA model. All numerical analyses indicate that the shear capacity of a continuous slab is higher compared to the capacity of the conventional isolated slab specimen. The predictive capability of the FEA models

can allow future investigations on the effect of membrane action in order to supplement the limited testing background on this area, and for future recommendations for the code provisions.

8.2 Compressive membrane action effect

Punching shear failure in reinforced concrete flat slabs occurs due to the development of a three-dimensional state of stresses that is created by the high transverse stresses around the column and the in-plane stresses. Inclined cracks are created inside the slab, which then propagate and form a major inclined crack. When this crack reaches the compressive zone, a punching shear cone around the column is formed leading to the punching shear failure. Punching failure is brittle and sometimes can lead to a progressive collapse of the building. Many researchers performed studies in order to examine the punching shear failure in concrete slabs and on the methods to prevent it. Several tests have been done starting in 1950s and then several theories and models have been proposed. In these experiments, isolated slabs were considered, representing a slab-column connection limited by the line of contra-flexure for radial moments, which become zero at a distance approximately 0.22L, where L is the center-to-center span between the columns. All of these isolated tested slabs had no restraint for lateral in-plane movement and they were simply supported around the edges. These test results were the basis of design codes' design methods for punching shear resistance of flat slabs. However, the in-plane restraining forces creating the compressive membrane action in the concrete slabs were ignored.

In continuous reinforced concrete slabs, the tensile strains at the mid-depth of a slab lead to an expansion of the slab, creating horizontal displacements. These mid-depth tensile strains are the result of concrete material nonlinearity. However, the lateral stiffness of the columns opposes this expansion by imposing compressive membrane forces (in-plane restraining forces)

(see Figure 8.1). The result of this phenomenon, that is called compressive membrane action, is the increase of the flexural and the shear capacity of a slab.

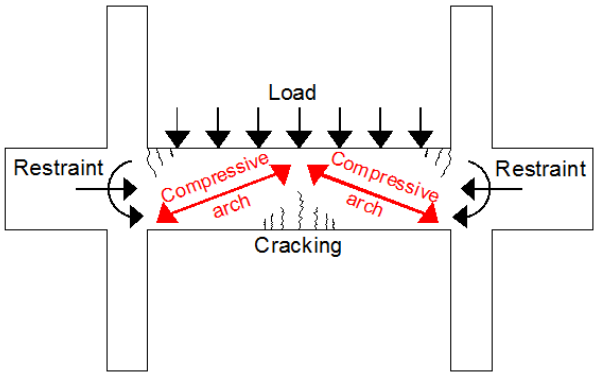

Figure 8.1 Membrane action.

The first investigations on the effect of the membrane action in concrete slabs can be found in the observations done by Westergaard and Slater (1921). Later, other researchers performed tests in order to explain and examine the effect of the membrane action connected with the boundary conditions on the concrete slab's capacity. These include work done by Ockelston (1955), Elstner and Hognestad (1956), Christiansen (1963), Park (1964), Long and Bond (1967), Hopkins and Park (1971), Lander et al. (1977), Long et al. (1978), Rankin and Long (1987), Guice and Rhomberg (1988), Vecchio and Collins (1990), Vecchio and Tang (1990), Chana and Desai (1992), Alexander and Simmonds (1992), Sherif (1996), Choi and Kim (2012).

Elstner and Hognestad (1956) conducted tests by changing the boundary conditions of the slabs. They considered: a) all edges to be simply supported; b) only two opposite edges to be simply supported and c) only the corners to be simply supported. The test results indicated a significant strength reduction in such cases where the edges were not continuously supported.

Long and Bond (1967) performed full panel tests showing an increase in the capacity of the slabs compared to the isolated test specimens. Rankin and Long (1987) tested 17 specimens that ranged from the isolated specimens having their edges at the line of contra-flexure (0.22L) to the full panel specimens. All specimens were simply supported at the line of the contra-flexure. The test results show an increased ultimate load with an increase of the slabs' size. The lowest increase was noticed to be around 30% for full panels with reinforcement ratio 1.1% and around 50% for full panels with reinforcement ratio 0.5%. Other researchers tested slab subsystems in order to investigate the membrane action effect on slab's capacity. Vecchio and Collins (1990) examined the collapse of a four-story warehouse building with flat slabs that happened in 1978. When the collapse took place, Vecchio and Collins found that the total load of the third floor of the building was about 4.5 times higher compared to the design load. The investigation's results showed that high strength was created due to the effect of the membrane action. Vecchio and Tang (1990) tested two slab strip specimens to isolate the influence of the membrane action. The two specimens were different only in the support conditions; in the first specimen the end supports were allowed to move only horizontally, in the second specimen the edge supports were fixed. The second specimen (fixed supports) failed at a higher load compared to the first specimen. Alexander and Simmonds (1992) examined three different types of boundary conditions for the slabs: a) rotations at the edges and restrained corners, b) rotations and restrained edges and c) restrained rotations at the corners. The obtained test results showed that the rotational restraint increased the punching shear capacity of the slabs. Chana and Desai (1992) tested isolated and continuous slabs. The side lengths of the slabs were equal to 0.4L and 1.5L for the isolated and continuous slab, respectively. The test results indicated a significant

increase in the ultimate load of the continuous slab, around 52%, compared to the strength of the conventional specimen.

In addition to the test programs described herein, Einpaul et al. (2015) presented a numerical method to calculate the capacity of continuous slabs. Comparing the results coming from their model to specific test results, they concluded that the membrane action effect increases the strength capacity of a slab. Numerical analyses of two-way slabs using finite element methods examining the membrane action effects are limited. Finite element analysis using shell elements to simulate the concrete in order to investigate the compressive membrane action against the progressive collapse of the flat slabs can be found in the work done by Dat and Hai (2013), Keyvani et al. (2014) and Liu et al. (2015). In these works, the compressive membrane action was found to be important source of enhancement for the punching shear strength of the slabs preventing a progressive collapse of the slab structures.

Three dimensional nonlinear finite element analyses (FEA) are presented and applied to simulate continuous slabs and then to compare their behaviour with the isolated slab test results. FEA can be used effectively, after appropriate modelling and material calibration, to supplement the existing test background. Parametric investigations can be performed via FEA modelling, exploring a variety of issues related to punching shear. In this work, the ABAQUS software is used with the simulation of the concrete material done using the concrete damaged plasticity model. The concrete damaged plasticity model has been previously calibrated on the interior concrete slab (SB1) in order to examine its punching shear failure. Herein, the calibrated model is used to analyze the isolated specimen SB1 as continuous; using different boundary conditions and also different dimensions. The analysis of the whole floor system, from which the SB1 specimen has been taken, is also simulated and analyzed. Following this, two test specimens

from literature, in which the membrane action effect was examined, are presented and analyzed to show and prove the effectiveness and the accuracy of the FEA model in continuous slabs modelling. FEA results of all of these slabs are compared to the test results, and the discussion is provided. Finally, discussion based on the code provisions for punching shear and comparison with the numerical results of the continuous slabs is presented.

8.3 Finite element simulation of the system continuity

The increased punching shear capacity of a reinforced concrete flat slab due to the membrane action effects can be evaluated by examining the restraining in-plane forces acting in the slab. The magnitude of these restraining forces is hard to find, because it depends on the stiffness of the flat slab structure provided by the supports and the slab itself. Also, it is difficult to test continuous slabs and for that reason, a common empirical approach is to test slabs simply supported at the outer edge. Non-linear finite element analysis can be performed to examine all possible sources of restraint for the continuous slab specimens. In this section, the previously shown slab SB1 is examined considering the membrane action effect, and then, two slabs tested by Chana and Desai (1992), where the membrane action effect was evaluated, are modeled and analyzed. In both cases the modelling and the analysis of the slab supported at the outer edges, as it is explained earlier, show the enhancement in the punching shear due to the membrane action. However, taking the advantage of the FEA, the aim of this study is to analyze also different support conditions that have not been examined in the experiments, and to simulate and analyze a real floor system. All of these studies are presented in the subsection 8.3.1 where SB1 and varietions of its boundary conditions are shown. Then, subsection 8.3.2 shows the comparison between numerical and experimental results for the slabs tested by Chana and Desai (1992), who

tested both isolated and continuous slabs, in order to verify the accuracy of the proposed FEA model for analyzing continuous slabs.

8.3.1 Slab-column connection SB1 tested by Adetifa and Polak (2005)

The previously shown isolated specimen SB1 is now examined as continuous. Figure 8.2 illustates the two continuous models:

Continuous Model 1: Restrained supports with both horizontal and vertical restraints (pinned supports) at the locations of the lines of the contraflexure in order to provide lateral restraints and simulate the continuous scenario (Figure 8.2a). The lateral restraints are applied not only at the bottom of the slab but also at the whole height of the slab.

Continuous Model 2: The slab is modeled with dimensions (1.6L=6000 mm) and simple supports are introduced at distance 0.4L=1,500 mm and at 1.5L=5,625 mm (Figure 8.2b), where L denotes the center-to-center span of the slabs (L=3,750 mm). That model is based on the bending moment diagram of a floor system simulating the zero moments with the support conditions.

The FEA results are presented in Figure 8.3 in terms of load-deflection response and are compared to the numerical and experimental results of the isolated simply supported slab. The adopted methods that represent the continuity (Figure 8.2a, Figure 8.2b), show an increase in the failure load but decreased ductility, compared to the test and the FEA results of the conventional slab. In particular, Table 8.1 shows the analysis results in terms of failure load and displacement for all of the specimens. The load-deflection responses of the two continuous models are shown in Figure 8.3. The ultimate load of the continuous model 1 is increased by around 68% and the

ultimate load of the continuous model 2 is increased by around 50%, both compared to the numerical results of the isolated simply supported slab.

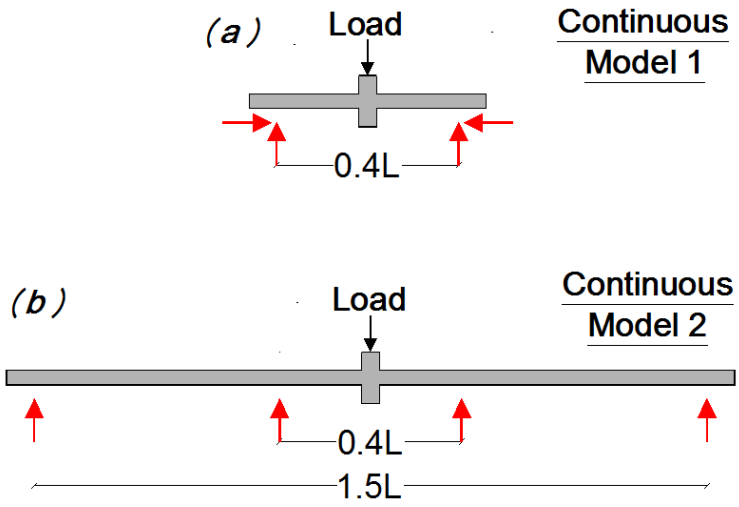

Figure 8.2 Adopted continuous models for the slab SB1.

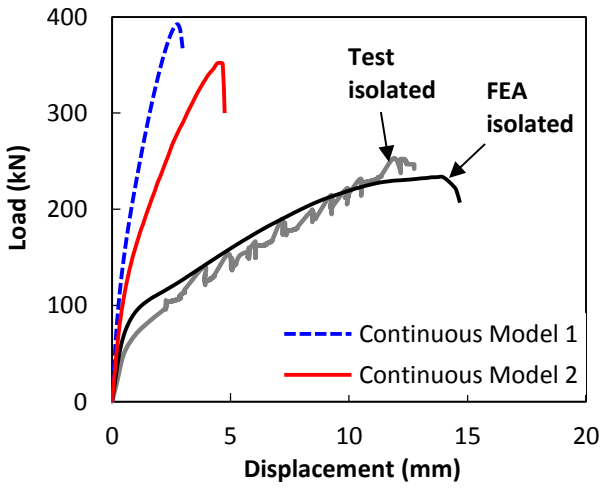

Figure 8.3 Load-deflection curves of the continuous slabs (comparison with the simply supported isolated).

Table 8.1
FEA Results.

Specimen	Failure load (kN)	Displacement at failure (mm)
Isolated	234	13.9
Continuous Model 1	392	2.7
Continuous Model 2	352	4.5

The developed crack patterns of the analyzed continuous slabs at failure, are presented below (Figure 8.4). The continuous slabs concentrate the crack propagation around the column and it does not spread to the edges, as it happens on the isolated slab (Figure 8.5). This can be explained by considering the smaller deflection that the continuous slabs have, compared to the deflection of the simply supported slab. Smaller deflection leads to lower crack widths and thus to larger punching shear capacity.

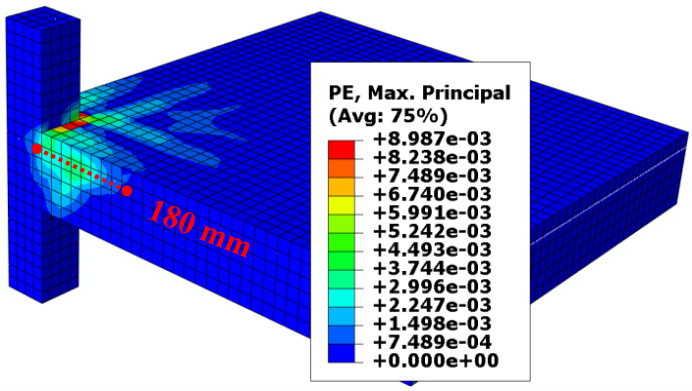

(a)

(b)

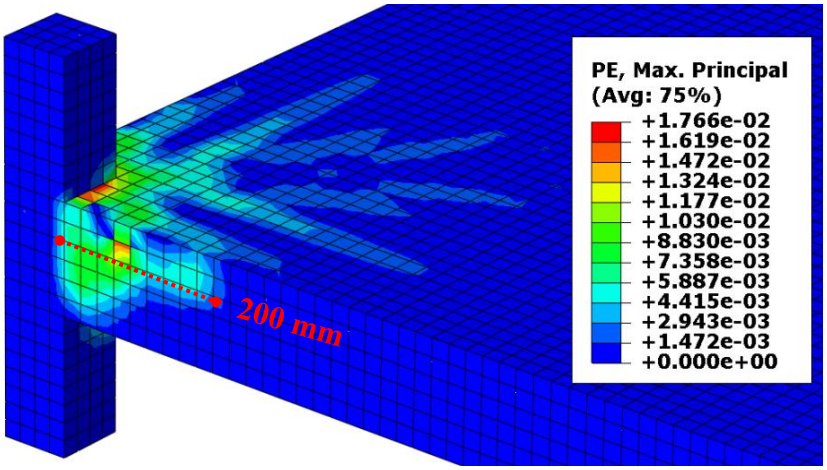

Figure 8.4 Crack patterns: a) Continuous Model 1, b) Continuous Model 2.

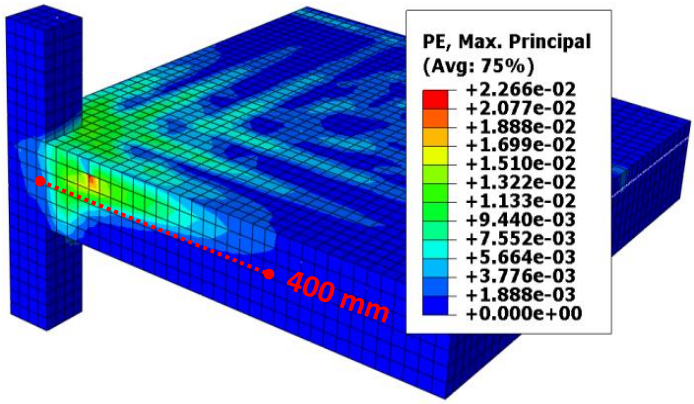

Figure 8.5 Crack pattern of the isolated simply supported slab SB1.

Considering now that the punching shear capacity of a real slab is not the same as the capacity of the simply supported isolated slab and not such increased as this one of the isolated lateral restrained slab, the isolated slab is modeled with simple supports and axial spring elements in order to evaluate the effect of lateral restraint. Figure 8.6 shows the spring elements that are installed at the edges of the isolated simply supported slab at each element node. Different stiffness is given to each spring element and the results in terms of load-deflection response are shown in Figure 8.7. The given stiffness to the springs varies depending on the support conditions; low stiffness displays similar results to the simply supported slab and high

stiffness shows the fully restrained case. The spring stiffness of 30,000 N/mm gives almost the same load-deflection response to the continuous model 2.

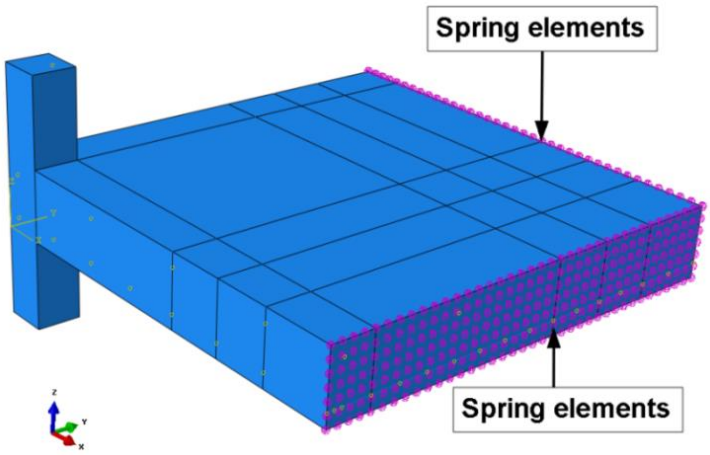

Figure 8.6 Spring elements simulate the later restraint.

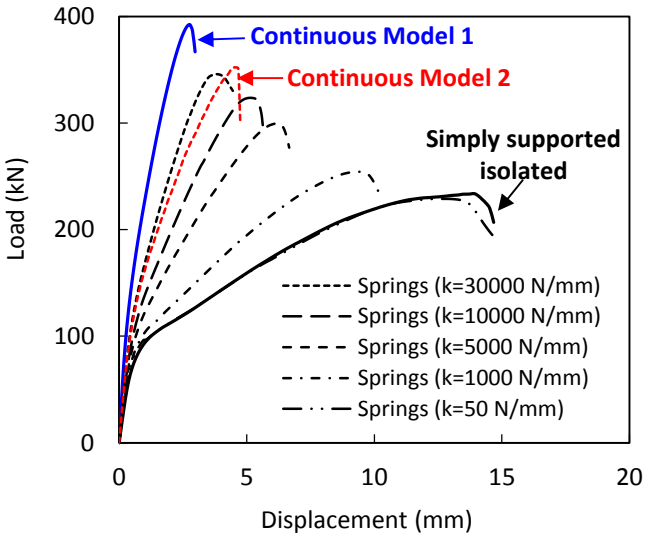

Figure 8.7 Load-deflection responses of the slabs with different stiffness of the spring elements (comparison with the isolated and two continuous slabs).

Then, the whole floor system, from which the SB1 slab was taken, is simulated and analyzed using the finite element methods. Due to symmetry, one quarter of the floor flat system is considered and the adopted boundary conditions are presented in Figure 8.8. A high uniformly distributed factored load of 18.5 kPa due to the high percentage of flexural reinforcement is applied to the floor system and the columns are restrained at the bottom. The punching shear load of the slab is measured as the reaction at the bottom of the column where the boundary conditions are introduced and the displacement is monitored at two points: at distance 0.2L from the column and at the middle of the slab. Figure 8.9 shows the numerical results in terms of load-deflection of the slab SB1 after the analysis of the flat floor system. For comparison, in the same graph are shown the numerical responses of the isolated simply supported and continuous slabs. The ultimate punching shear load of the slab by analyzing the whole floor system is equal to 291 kN, 24% higher than the load of the simply supported isolated slab, while the analysis of the continuous model predicts an ultimate load 50-68% higher than the isolated slab. Similar results presented by Keyvani et al. (2014) where the compressive membrane action was examined in the progressive collapse of flat concrete slabs. Keyvani et al. showed that the punching shear strength of a laterally restrained slab was increased 34% compared to the strength of the isolated slab and the punching shear strength of an actual flat slab system was around 17% higher compared to the strength of the isolated slab.

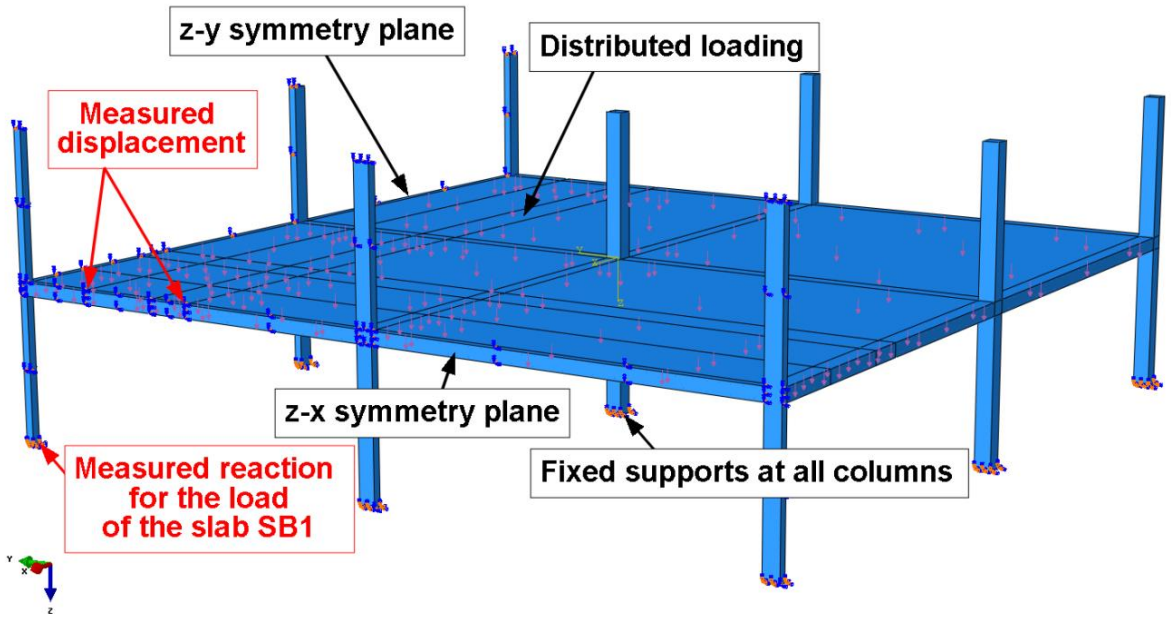

Figure 8.8 Boundary condition of one quarter of the whole floor system.

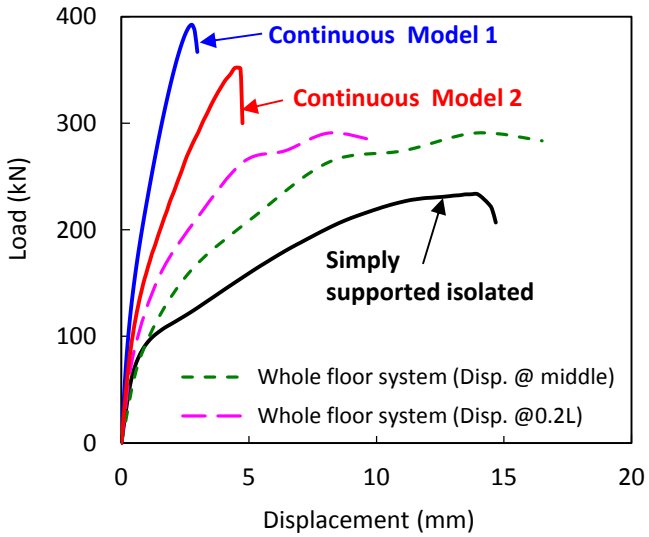

Figure 8.9 Load-deflection responses of the floor slab system.

The crack pattern at failure of the interior slab-column connection SB1 after analyzing the floor system is shown in Figure 8.10. The cracking is concentrated around the column and

spreads at a distance of 300 mm from the face of the column. This development length of the cracks is smaller compared to this from the isolated simply supported slab (400 mm) and larger than the cracking development length of the continuous models (180-200 mm).

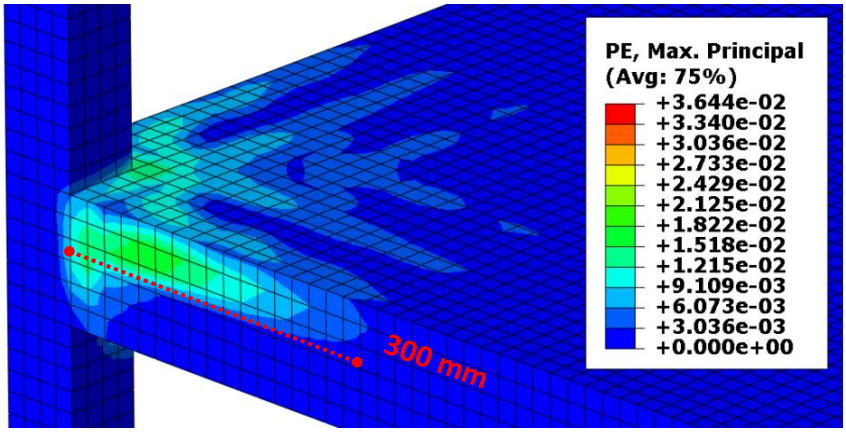

Figure 8.10 Crack pattern of SB1 on the floor slab system.

8.3.2 Slabs tested by Chana and Desai (1992)

In order to validate the accuracy of the concrete damaged plasticity model in punching shear simulations of continuous slabs, the numerical model herein is applied to analyze punching shear tests reported in literature. Two tested interior slab-column connections, are simulated and analyzed. The purpose of these tests was to examine the effect of the membrane action on the punching shear capacity of the slabs. Both tested slabs had no shear reinforcement and were taken from a prototype structure, where the flat slab spans between the columns were equal to 6000 mm. One slab was considered as continuous and its dimensions were equal to 9000x9000 mm, while the second tested specimen was the isolated slab with dimensions 2400x2400 mm on plan. Both slabs were simply supported at the column foot. The thickness of the isolated slab was 240 mm with effective depth 200 mm and the dimensions of its square column were 300x300

mm. The continuous specimen was 250 mm thick with effective depth 210 mm and the dimensions of its column were 400x400 mm. The load was applied for both slabs through eight points placed at a radius of 1.2 m from the center.

Table 8.2
Material properties, reinforcement and test results of slabs tested by Chana and Desai (1992).

Specimen	$f'_c(MPa)$	$f'_t(MPa)$	$f_y(MPa)$	$A_s(mm^2)$	**Tensile** $\rho_s(\%)$	**Failure load (kN)**	**Displacement at failure (mm)**
Isolated	40.3	2.7	500	314	0.79	850	18
Continuous	26.8	2.31	500	314	0.86	1225	2.49

Table 8.2 shows the material properties, reinforcement and test results for the continuous and isolated slab. In the numerical analyses only one quarter of both slabs is simulated due to symmetry. Figure 8.11 illustrates the continuous and isolated specimen with the boundary conditions and applied load.

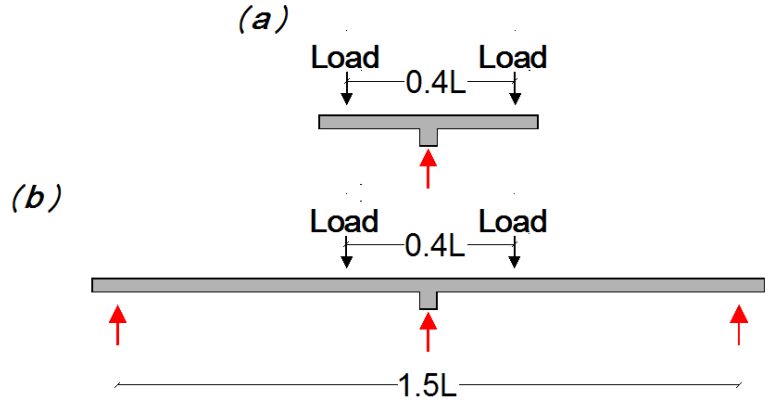

Figure 8.11 Boundary conditions and loads of the slabs tested by Chana and Desai: a) isolated and b) continuous.

Parametric investigation is performed in order to calibrate the FEA model because these slabs were tested in a different way compared to the slab SB1 and also they were thick (250 mm-the isolated and 240 mm-the continuous) compared to the thickness of the SB1 that was 120 mm. The parametric investigation is done on the isolated specimen, where only the mesh size is examined. The model in ABAQUS is mesh size dependent because it is a plasticity based model, therefore, a mesh convergence study should always be performed. Figure 8.12 shows the numerical results in terms of load-deflection response for the isolated specimen by using three different mesh sizes: 20 mm, 30 mm and 40 mm. The obtained results of all different mesh sizes are in good agreement, however the mesh size of 40 mm is chosen for the analyses of both isolated and continuous slab due to less computational cost. All other material parameters are considered same in slab SB1.

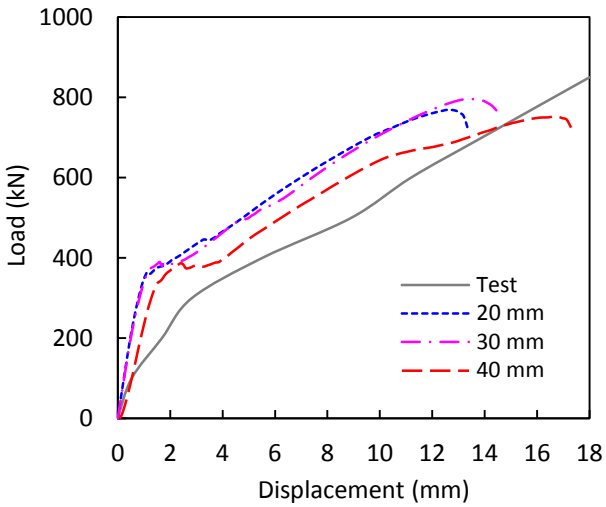

Figure 8.12 Load-deflection response of the isolated slab for different mesh sizes.

Figure 8.13 illustrates the comparison between the isolated and continuous slab in terms of tested and numerical failure load and deflection. The results from the FEA models are in good

agreement with the test results. The numerical analyses show an ultimate load of 752 kN and 1248 kN for the isolated and continuous slab, respectively. The deflections at the loading points at failure are 16.7 mm for the isolated slab and 2.4 mm for the continuous slab. Both numerical load-deflection responses of the slabs appear stiffer compared to the tested responses. This seems to happen because of the adopted support conditions that are simplified compared to the test support conditions.

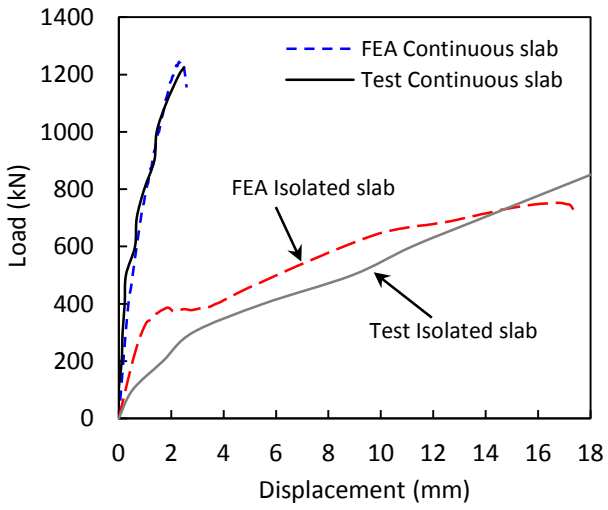

Figure 8.13 Comparison between tested and FEA load-deflection curves of the isolated and continuous slab.

According to the test observations, both specimens failed in a brittle punching. Radial cracking was developed on the tension side of both slabs; starting from the loading column and then propagating to the edges. Isolated specimen appeared the maximum crack width (0.3 mm) before failure, while the maximum crack width before failure for the continuous slab was equal to 0.15 mm. However, the radial cracks of the continuous slab stopped before the loading points, compared to the cracks of the conventional isolated slab that continued until the edges. This can be explained due to the membrane action effect that controls the crack width and its

development. Both tested crack patterns are effectively predicted by the FEA crack patterns (see Figure 8.14). The continuous slab failed in a significantly increased load compared to the isolated specimen. In the tests the ultimate load of the continuous slab is increased 52% compared to the ultimate load of the isolated slab. The FEA results show that the continuous specimen has 60% higher punching shear strength compared to the isolated slab. This increase of the ultimate load (60%) is higher compared to the numerical results presented earlier for the Continuous Model 2 of the slab SB1 (50%). That can be explained by considering that the specimens tested by Chana and Desai had lower both: the reinforcement ratio and the span to thickness ratio, compared to the slab SB1. According to tests done on one-way slabs by Gruice and Rhomberg (1988) with different flexural reinforcement ratio and span to thickness ratio, it was found that the compressive forces can enhance the strength of the slabs by 30-100%. Higher increase in the ultimate load was observed for slabs with lower reinforcement ratio and lower span to thickness ratio. Similar observations for the effect of the span-depth ratio to the punching shear strength of the slabs, were made by Lovrovich and McLean (1990). They concluded after performing a test series that as the span-depth ratio decresed the punching shear strength of a slab increases due to the development of compression struts between the loading point and the supports. In this arch mechanism, the in-plane compressive forces have also concurred to the increase of the punching shear strengths.

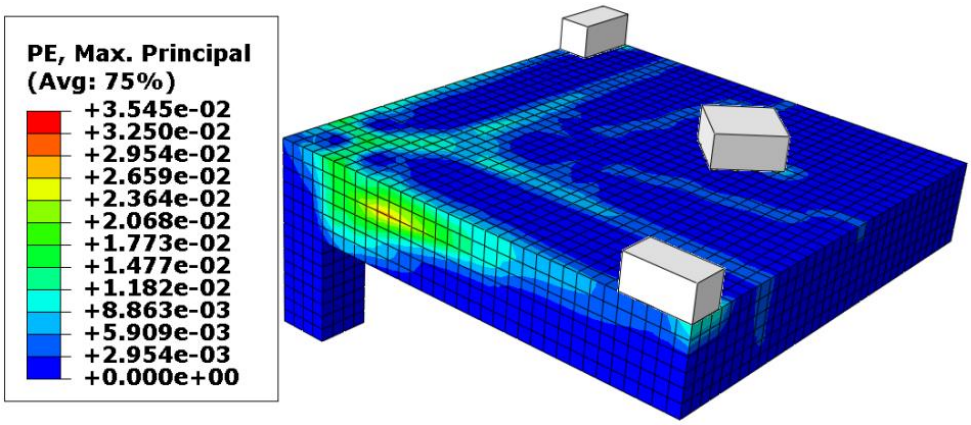

a)

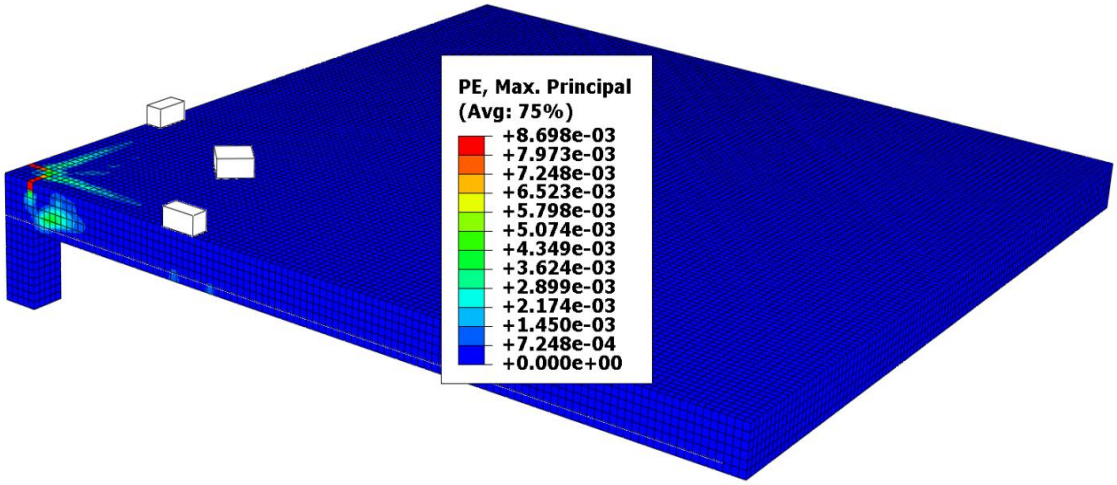

b)

Figure 8.14 Crack patterns on tension side of the slabs: a) isolated and b) continuous.

Table 8.3
Comparison of ultimate FEA load (kN) between isolated and continuous slabs.

Slab specimen	FEA load V_I (kN) Isolated slab	FEA load V_C (kN) Continuous slab	V_C / V_I
SB1 (Continuous Model 1)	234	392	1.675
SB1 (Continuous Model 2)	234	352	1.504
SB1 (whole floor)	234	291	1.244
Slab tested by Chana and Desai	752	1248	1.660

Table 8.3 summarizes and compares the FEA results of all specimens. The analysis of the slab SB1 (Continuous Model 1) shows that the ultimate load is increased 67.5% compared to the ultimate load of the isolated slab SB1. The SB1 (Continuous Model 2) slab has an ultimate load 50.4% higher than the ultimate load of the isolated slab SB1. At this point, if we consider the numerical results of the slabs tested by Chana and Desai [17], we can see that the ultimate load of the continuous slab is 66% higher compared to the load of the isolated slab. The continuous slab tested by Chana and Desai has the same boundary conditions with the slab SB1 (Continuous Model 2). Based on these results we can conclude that the contunuous models presented in this research increase the ultimate load of the isolated slabs between 50.4-67.5%. However, the numerical results of the slab SB1 considered in the whole floor system shows that the ultimate load of a real flat slab is about 24.4% higher than the the observed load of the isolated slab.

8.4 Comparison with the design approaches

The compressive membrane action effect is ignored in the design provisions. Comparing the results of the isolated slabs (test and FEA) with the recommendations of the design provisions (ACI318-11, EC2 2004), we can conclude that the design codes underestimate the punching shear capacity of the slabs (see Table 8.4) introducing of course safety margins. Only

for the isolated specimen tested by Chana and Desai [17] the code predictions are really close to the test results. We can state also herein that the formulae of both design codes are considered without the safety factors. However, if we compare now the numerical results of the continuous slab SB1 and the test and numerical results of the continuous slab [17] with the code predictions, we can actually conclude that the design codes are very conservative. If we compare only the SB1 (Continuous Model 2) slab with the design codes, we can observe that EC2 predicts an ultimate punching shear load about 150 kN less than the FEA load and ACI underestimates the FEA load about 163 kN. Now, if we compare the continuous slab [17] (same continuous model with slab SB1 (Continuous Model 2)) with the design codes, we can see that EC2 predicts a punching shear load 347 kN less that the FEA load and ACI predicts an ultimate punching shear load 373 kN less than the FEA load. Thus, the punching shear design provisions that are based on test results of isolated slabs are conservative and modifications accounting the membrane action effect can be taken into consideration. These modifications could be done after analyzing many and different continuous slabs. Slabs with shear reinforcement should be also considered. The calibrated FEA models can be used in this direction in order to future provide parametric studies

Comparing now the results between the design codes, it can be said that EC2 gives higher punching shear resistance for all slabs, compared to the predictions that ACI provides. EC2 shows 13 kN higher punching shear resistance compared to ACI for the slab SB1. However, for the isolated slab [17] the punching shear resistance from EC2 is around 9 kN higher compared to the load that ACI predicts. EC2 predicts an ultimate punching shear load about 26 kN higher than the ACI for the continuous slab [17]. Thus, the predictions from EC2 are closer to the punching shear resistance of the tested and FEA isolated slabs compared to ACI.

Table 8.4
Comparison of ultimate load (kN) between test, FEA and design codes for slab SB1 and slabs tested by Chana and Desai.

Slab specimen	Test results	FEA results	ACI	EC2
SB1 isolated	253	234	189	202
SB1 continuous 1	*Not tested*	392	189	202
SB1 continuous 2	*Not tested*	352	189	202
SB1 whole floor	*Not tested*	291	189	202
Chana and Desai isolated	850	752	838	847
Chana and Desai continuous	1225	1248	875	901

8.5 Summary and Conclusions

3D nonlinear finite element methods can be effectively used in punching shear simulations to examine the continuity of reinforced concrete slabs. The existing test database of isolated slabs can be examined using FEA, considering a variety of boundary conditions in order for the continuity to be adopted in the simulations. The calibrated concrete damaged plasticity model in ABAQUS predicts accurately the responses of the continuous and isolated slabs. The lateral restraints combined with the simple supports at the edges of the isolated specimen SB1 (Continuous Model 1) increase the punching strength 68%, while the simple supports in the SB1 slab with dimensions 1.5L (Continuous Model 2), increase the punching strength by about 50%. Thus, the obtained numerical results of the two continuous models show quite similar increase of the punching shear load. Due to the membrane action effect, the deflections of all simulated continuous specimens are smaller compared to the isolated simply supported slab. For that reason the continuous specimens show smaller crack widths and the crack patterns are concentrated around the area of the column and they are not spread to the edges of the slabs. Subsequently, the continuous slabs have higher punching shear strength.

The whole floor system analysis shows that the actual slab has 24% higher punching shear resistance compared to the strength of the isolated simply supported slabs. This punching shear strength is less than the one found for the continuous slabs. Therefore, the continuous models overestimate the compressive membrane action effect and its contribution to the punching shear strength.

The current design provisions of punching shear do not consider the membrane action effect. Design provisions, tests and FEA of isolated slabs give safe predictions compared to the actual flat slabs. However, the design code accuracy could be enhanced if membrane action is considered. Finite element analyses done of isolated specimens can be extended using the appropriate dimensions and boundary conditions in order to simulate and analyze the same slabs as continuous. These results can be helpful in future code developments. The aforementioned conclusions suggest further studies, both numerical and experimental, to better examine and understand the membrane action effect in reinforced concrete slabs in order to apply it for code calibration.

Chapter 9

Conclusions and Future Research

9.1 Summary and Conclusions

Although, the testing database for punching shear is huge; it does not always provide consistency of results and the code provisions that are based on empirical formulations arising from these tests, raise critical questions and issues. At this point, the finite element analysis (FEA) can be used in order to supplement the testing database and to investigate different aspects in the punching shear failure of the concrete slabs. However, the FEA models should be calibrated and only then can be properly used in the numerical simulations.

The work presented in this dissertation investigates the capability of the proposed calibrated concrete damaged plasticity model for punching shear simulations of reinforced concrete slabs. The chosen concrete damaged plasticity model is calibrated based on selected tests from literature. Then, a further calibration of the model is done by analyzing a previously tested interior slab-column connection (SB1) which is considered as the control specimen for this research. Many material parameters are studied, among them, the dilation angle, the fracture energy and the damage variables. The mesh size sensitivity issue of the model is addressed. Mesh-dependence remedies even if the characteristic length and the viscoplastic regularization were considered. However, it is observed that the cracking propagation together with the load-deflection response of the slab should be taken into consideration for the adoption of the proper mesh size. The accurate modelling of the support conditions according to the real test is also

performed. Neoprene supports are modelled in slab SB1 and solve the stiffer response issue that the simple supports show in the load-deflection response. Also, a detailed study using different types of 3D elements for modelling the concrete slab is presented. The C3D10M and C3D8R elements using neoprene supports provide the most accurate prediction for the crack pattern of the slab SB1. Accurate prediction is also given for the load-displacement response.

Then, the calibrated concrete damaged plasticity model is validated for predicting the punching shear response of different types of slab-column connections without shear reinforcement. In particular, five different slab-column connections without shear reinforcement are simulated and analyzed in terms of ultimate load and crack patterns. The results of the analyses are compared to the test results and show good agreement. The presented analyses indicate that the proposed model could be used in future parametric studies on different aspects influencing punching shear in concrete slabs. Some limitations are observed in the case of the cyclic loading, due to the simplicity of the adoption of the perfect bond between concrete and reinforcement, where the hysteretic simulations in ABAQUS are not successful. The tests have shown pinching, denoting strength and stiffness degradation and low energy dissipation capacity. However, the FEA do not exhibit the pinching effect. In that case, monotonic analysis is performed and the numerical backbone curves are found to be in good agreement with the experimental punching shear load.

The effectiveness of using the calibrated model in shear-reinforced slabs is also examined. Four interior slab-column connections are simulated and analyzed in terms of ultimate load, displacement and cracking propagation. The FEA results confirm beyond reasonable doubt the accuracy of the proposed model predicting the punching shear failure in concrete slabs with shear reinforcement. The modelling of the shear reinforcement (shear bolts) in ABAQUS is done

with beam elements, which are found to be appropriate to simulate the increase in the ultimate load and displacement of the tested slabs. A detailed novel modelling description of the punching shear reinforcement is offered. Investigation on using different modelling approaches for the shear bolt modelling is performed. These different proposed modelling approaches could be adopted and used in the analysis of any reinforced concrete slab. The activation of the shear bolts seems to be effective in FEA even if it starts earlier due to the perfect bond that is assumed in the numerical analyses. Code provisions and models are assessed in terms of ultimate load for the shear reinforced slabs and compared to the test and FEA results. ACI code presents the most conservative punching shear loads. However, both design codes (ACI and EC2) seem to underestimate the contribution of the amount of the shear reinforcement. In contrast, MC 2010 and CSCT account for the contribution of the increased shear reinforcement. The two proposed shear reinforcement arrangements by the design codes are simulated and compared. The rectangular arrangement used by the ACI code is compared in terms of failure load and displacement with the radial arrangement used by the EC2. Radial arrangement in the FEA increases both failure load and deflection.

The calibrated concrete damage plasticity model is also considered in simulations of slabs with openings. The results obtained from the parametric investigation regarding the influence of the size and location of the opening show that when the opening is located at a distance larger than 5d from the column the punching shear capacity of the slab remains almost the same as for the slab without openings. Regarding the effect of the size of the openings, the numerical studies show that after the distance 4d the size of the opening does not affect the response of the slab. The numerical results are compared with the code provisions and show that ACI gives conservative results.

The compressive membrane action effect in reinforced concrete slabs is also investigated. The calibrated concrete damaged plasticity model in ABAQUS predicts accurately the responses of continuous slabs. The lateral restraints combined with the simple supports at the edges of the isolated specimen SB1 (Continuous Model 1) increase the punching strength by 68%, while the simple supports in the SB1 slab with dimensions 1.5L (Continuous Model 2), increase the punching strength by about 50%. Due to the membrane action effect, the deflections of all simulated continuous specimens are smaller compared to the isolated simply supported slab. For that reason the continuous specimens show smaller crack widths and the crack patterns are concentrated around the column. Subsequently, the continuous slabs have higher punching shear strength. The whole floor system analysis show that the actual slab has 24% higher punching shear resistance compared to the strength of the isolated simply supported slabs. This punching shear strength is less than the one found for the continuous slabs. That conclusion indicates that the design codes are really conservative as they are based on isolated slabs. The real slab-column system has a punching shear resistance about 24% higher than this one that the isolated simply supported slab shows.

In conclusion, it can be said that the calibrated concrete damaged plasticity model accurately predicts the punching shear strength of concrete slabs. All of the numerical analyses in this research are performed with the same calibrated concrete model and the results that they show are in good agreement with the experimental findings. Thus, the concrete damaged plasticity model can be used for parametric studies in order to provide useful information for future code modifications.

9.2 Directions for future research

The calibrated concrete damaged plasticity model can be used in various parametric studies. Further investigation on the effect of the unbalanced moments on interior and edge slab-column connections can be conducted. From the analyses presented in this thesis, the unbalanced moments were studied for the edge slab-column connections showing the decrease in punching shear capacity of the specimens. However, a parametric investigation can be performed in accordance with studies in the distribution and magnitude of the internal forces, which cannot be measured directly from the tests. The rigorous nonlinear finite element methods can account for cracking, crushing of concrete and yielding of reinforcement. Therefore, the internal forces at the critical section can be calculated and then the fraction of unbalanced moment transferred by shear eccentricity can be estimated.

The opening effect can be studied on continuous slabs in order to evaluate the punching shear strength of slabs having openings after the lines of the contra-flexure. The numerical results will be compared with the code predictions. Code recommendations for the compressive membrane action effect and opening effect will be offered.

The calibrated concrete damaged plasticity model can be used for simulations where the post-punching behaviour of the slabs will be examined. Reinforced concrete slabs without shear reinforcement and with different flexural reinforcement ratios and also flat slabs with shear reinforcement will be simulated and analyzed. Useful and important outcomes can be offered for the effectiveness of using different shear reinforcements and theirs influence in the post-punching response of the slabs. Extended finite element analyses and studies can be considered for analyzing reinforced concrete slabs with different types of shear reinforcement. In this work

the simulation of the shear bolt system was presented. Stirrups, shear studs and shear heads can also be modeled in future nonlinear finite element analyses, in order to provide recommendations and guidelines for the numerical simulations of shear reinforced concrete slabs. Parametric studies should be performed examining the effect of the reinforcement ratio, the thickness of the slab, the shear reinforcement layout/amount and the column rectangularity. All of these parametric studies will propose verifications to the code provisions.

Future work can explore the effectiveness of the proposed calibrated model in cyclic loading simulations of reinforced concrete slabs. The adoption of the appropriate damage parameters should be examined to simulate the stiffness recovery and the opening-closing effect of concrete. As it was noticed from the cyclic loading analyses in the interior slab-column specimens, the pinching effect was not captured in the load-deflection response. That problem could be solved with further investigation that will take into consideration the proper modelling of the bond between concrete and reinforcement.

Special cases regarding non-typical slab-column connections, where the concentrated load or/and the column is located near a linear support, can be analyzed in FEA using the calibrated concrete model. The simulation slabs supported on long walls will also be analyzed in order to gain information about the cracking and the strains in both concrete and reinforcement.

References

ABAQUS Analysis user's manual 6.12-3, *Dassault Systems Simulia Corp.*, Providence, RI, USA.

ACI Committee 318. (2011). "Building Code Requirements for Structural Concrete (ACI 318-11) and Commentary." *American Concrete Institute*, Farmington Hills, MI.

Addessi, D., Marfia, S., and Sacco, E. (2002). "A plastic nonlocal damage model." *Comput. Methods Appl. Eng.* 191:1291-1310.

Adetifa, B., and Polak, M.A. (2005). "Retrofit of interior slab-column connections for punching using shear bolts." *ACI Struct. J.*, 102(2), 268–274.

Alexander, S.D.B., and Simmonds, S.H. (1992). "Tests of column-flat plate connections." *ACI Structural Journal* 1; 89:495-502.

Alexander, S.D.B., and Hawkins, N.M. (2005). "A design prospective on punching shear." *Punching Shear in Reinforced Concrete Slabs, ACI SP232-06*, 97-108.

Anil, O., Kina, T., and Salmani, V. (2014). "Effect of opening size and location on punching shear behaviour of two-way RC slabs." *Magazine of Concrete Research*, 66(18): 955-966.

Argyris, J. (1960). "Energy theorems and structural analysis." Aircraft Engineering, 1954 and 1955, re-printed by Butterworth's Scientific Publications, London.

Babazadeh, A., Burgueno, R., and Silva, P.F. (2015). "Use of 3D Finite-Element Models for Predicting Intermediate Damage Limit States in RC Bridge Columns." *ASCE Structural Engineering, 2015 DOI: 10.1061/(ASCE)ST.1943-541X.00001253.*

Balomenos, G.P., Genikomsou, A.S., Polak, M.A., and Pandey, M.D. (2015). "Efficient method for probabilistic finite element analysis with application to reinforced concrete slabs", *Engineering Structures, Elsevier,* 103(8):85-101.

Bazant, Z.P., and Planas, J. (1998). Fracture and size effect in concrete and other quasibrittle materials. *CRC Press*.

Borges, L.L.J., Melo, G. S., and Gomes, R.B. (2013). "Punching shear of reinforced concrete flat plates with openings." *ACI Structural Journal*; 110(4):547-556.

Braestrup, M.W., Nielsen, M.P., Jensen, B.C. and Bach, F. (1976). "Axisymmetric punching of plain and reinforced concrete." Report R75, Struct. Research Laboratory, Technical Univ. of Denmark, Copenhagen.

Birkle, G., and Dilger, W. (2008). "Influence of Slab Thickness on Punching Shear Strength." *ACI Structural Journal*, 105(2):180-188.

Broms, C. E. (2000). "Elimination of flat plate punching failure mode." *ACI Struct. J.*, 97(1), 94-101.

Broms, C. E. (2007). "Flat plates in seismic areas: Comparison of shear reinforcement systems." *ACI Struct. J.*, 104(6), 712-721.

Bu, W., and Polak, M.A. (2009). "Seismic Retrofit of Reinforced Concrete Slab - Column Connections using Shear Bolts." *ACI Structural Journal*; 106(4):514-522.

Chana, P.S, and Desai, S.B. (1992). "Membrane action, and design against punching shear." *Struct Eng*; 70(19):339-43.

Chen, W.F. (1982). Plasticity in reinforced concrete, McGraw-Hill Book Company, New York.

Chen, W.F., and Han, D.J. (1988). Plasticity for Structural Engineers, Springer, New York.

Choi, J.W., and Kim, J-H. (2012). "Experimental investigations on moment redistribution and punching shear of flat plates." *ACI Struct J*; 109(3):329-38.

Clough, R.W. (1960). "The finite element method in plane stress analysis." *Proceedings 2nd ASCE Conference Electronic Computation*, Pittsburg.

Cook, R. (1995). Finite element modelling for stress analysis. John Wiley and Sons, Inc.

Cornelissen, H., Hordijk, D., Reinhardt, H. (1986). "Experimental determination of crack softening characteristics of normal weight and lightweight concrete." *Heron*; 31(2):45-56.

Christiansen, K.P. (1963). "The effect of membrane stresses on the ultimate strength of interior panel in a reinforced concrete slab." *Struct Eng*; 41(8):261-65.

Comi, C. (2001). "A non-local model with tension and compression damage mechanisms." *Eur. J. Mech. A/Solids* 20:1-22.

Comi, C., and Perego, U. (2001). "Fracture energy based bi-dissipative damage model for concrete." *Int. J. Solids Struct.* 38:6427-6454.

Comité Euro-International du Béton, CEB-FIP-model Code 1990: Design code, Thomas Telford, London, 1993.

Comité Euro-International du Béton, CEB-FIP-model Code 2010. Lausanne, Switzerland, 2010.

Corley, W.G., and Hawkins, N.M. (1968). "Shearhead reinforcement for slabs." *ACI J.*, 65(10), 811-824.

Dat, P.X., and Hai, T.K. (2013). "Membrane actions of RC slabs in mitigating progressive collapse of building structures." *Eng Struct*, 55(13):107-15.

De Borst, R., and Van der Giessen, E. (1998). Materials instabilities in solids. John Wiley and Sons.

De Borst, R., Crisfield, M.A., Remmers, J.J.C., and Verhoosel, C.V. (2012). Non-linear Finite Element Analysis of Solids and Structures. Wiley, United Kingdom.

Dilger, W. H., and Ghali, A. (1981). "Shear Reinforcement for Concrete Slabs." *J. of Struct. Division*, 107(12): 2403-2420.

Eder, M.A., Vollum, R.L., ELghazouli, A.Y., and Abdel-Fattah, T. (2010). "Modelling and experimental assessment of punching shear in flat slabs with shearheads." *Eng. Structures*, 32 (12):3911-3924.

Einpaul, J., Fernandez Ruiz, M., and Muttoni, A. (2015). "Influence of moment redistribution and compressive membrane action on punching shear strength of flat slabs." *Engineering Structures*, 86(4):33-42.

El-Salakawy, E.F., Polak, M.A., and Soliman, M.H. (1998). "Reinforced Concrete Slab-Column Edge Connections subjected to High moments." *Can. J. of Civil Eng.*, 25(3):526-538.

El-Salakawy, E.F., Polak, M.A. and Soliman, M.H. (2000). "Reinforced Concrete Slab-Column Edge Connections with Shear Studs." *Can. J. of Civil Eng.*, 27(2):338-348.

El-Salakawy, E.F., Polak, M.A., and Soudki, K.A. (2002). "Rehabilitation and Strengthening of Reinforced Concrete Slab-Column Connections." *Can. J. of Civil Eng.*, 29(4):602-611.

Elgabry, A. A., and Ghali, A. (1990) "Design of Stud-Shear Reinforcement for Slabs." *ACI Struct. J.*, 87(3):350-361.

Elstner, R.C. and Hognestad, E. (1956). "Shearing strength of reinforced concrete slabs." *J. ACI*, 53(2):29–58.

European Committee for Standardization. (2004). "Design of concrete structures – Part 1-1: General rules and rules for buildings." *Eurocode 2*, Brussels, Belgium.

Faria, R., Oliver, J., and Ceverra, M. (1998). "A strain-based plastic viscous-damage model for massive concrete structures." *Int. J. Solids Structures*, 35(14):1533-1558.

Federation Internationale du Béton (fib) - Model Code for concrete structures 2010, Ernst & Sohn, Germany, 2013.

Feenstra, P.H., and de Borst, R. (1996). "A composite plasticity model for concrete.", *International Journal of Solids and Structures*, 33(5):707-730.

Fernandez, Ruiz M., and Muttoni, A. (2009). "Applications of the critical shear crack theory to punching of R/C slabs with transverse reinforcement." *ACI Struct. J.*, 106(4):485-494.

Genikomsou, A.S., and Polak, M.A. (2015a). "Finite element analysis of punching shear of concrete slabs using damaged plasticity model in ABAQUS." *Engineering Structures,* 98(4):38-48.

Genikomsou, A.S., and Polak, M.A. (2015b). " Finite element analysis of reinforced concrete slabs with punching shear reinforcement." under preparation.

Genikomsou, A.S., and Polak, M.A. (2015c). "3D Finite element investigation of the compressive membrane action effect in reinforced concrete flat slabs." under preparation.

Genikomsou, A.S., and Polak, M.A. (2015d). "Finite element investigation on the effect of openings in flat concrete slabs." under preparation.

Genikomsou, A.S., and Polak, M.A. (2014) "Finite Element Analysis of Punching Shear in Flat Slabs using ABAQUS", Structures Congress 2014, SEI of ASCE, April 3-5, 2014, Boston, Massachusetts, USA.

Genikomsou, A.S., and Polak, M.A. (2014) "FEA of RC Slabs under static and cyclic loading based on damage plasticity model", 8th International Conference, AMCM 2014 (16-18 June), Wroclaw, Poland.

Graf, O. (1933). "Versuche über die Widerstandsfähigkeit von Eisenbetonplatten unter konsentrierten Last nahe einem Auflager." *Deutscher Ausschuss fürEisenbeton,*73, 1-16.

Grassl, P., Lundgren, K., and Gylltoft, K. (2002) "Concrete in compression: a plasticity theory with a novel hardening law." *International Journal of Solids and Structures*, 39(20):5205-5223.

Grassl, P., and Jirásek, M. (2006). "Damage-plastic model for concrete failure." *Int J Solids Stuct*, 43(22-23):7166-96.

Guan, H., and Polak, M.A. (2007). "Finite element studies of reinforced concrete slab-edge column connections with opening." *Canadian J. of Civil Engineering*, 34(8), 952-965.

Guice, L.K., and Rhomberg, E.J. (1988). "Membrane action in partially restrained slabs." *ACI Struct J*, 85(4):365-73.

Hanna, S.N., Mitchell, D., and Hawkins, N.M. (1975). "Slab-Column Connections Containing Shear Reinforcement and Transferring High-Intensity Reversed Moments." SM 75-1, Division of Structures and Mechanics, Department of Civil Engineering, University of Washington, Seattle, Washington.

Hansen, N.R., and Schreyer, H.L. (1994). "A thermodynamically consistent framework for theories of elastoplasticity coupled with damage." *Int J Solids and Struct*; 31(3): 359-89.

Hanson, N.W., and Hanson, J.M. (1968). "Shear and Moment Transfer Between Concrete Slabs and Columns." *Journal of the PCA Research and Development Laboratory*, 2-16.

Harajli, M.H., Maalouf, D., and Khatib, H. (1995). "Effect of Fibers on the Punching Shear Strength of SlabColumn Connections." *Cement & Concrete Composites*, 17(2):161-170.

Hawkins, N.M. (1974). "Shear Strength of Slabs with Shear Reinforcement." *ACI SP-42*, 785-816.

Hillerborg, A. (1985). "The theoretical basis of a method to determine the fracture energy G_F of concrete." *Materials and Struct.*, 18(4):291-296.

Hopkins, D.C., and Park, R. (1971). "Test on a reinforced concrete slab and beam floor designed with allowance for membrane action." *ACI Publ SP-30-10*: 223-34.

Imran, I., and Pantazopoulou, S.J., (2001). "Plasticity model for concrete under triaxial compression", *Journal of Engineering Mechanics*; 127(3):281-290.

Islam, S., and Park, R. (1976). "Tests on slab-column connections with shear and unbalanced flexure." *J. of Struct. Division*, 102(3):549-568.

Jefferson, A.D. (2003). "Craft – a plastic-damage-contact model for concrete. I. Model theory and thermodynamic considerations." *Int. J. Solids Struct.* 40: 5973-5999.

Jirasek, M., and Bazant, Z.P. (2002). Inelastic Analysis of Structures. Wiley, England.

Jirásek, M., and Patzák, B. (2002). "Consistent tangent stiffness for nonlocal damage models." *Computers and Structures*, 80:1279-1293.

Jirásek, M., Rolshoven, S., and Grassl, P. (2004). " Size effect on fracture energy induced by non-locality." *Int. J. Numer. Anal. Meth. Geomech.* 28:653-670

Kachanov, L.M. (1986). Introduction to continuum damage mechanics, Martinus Nijhoff Publishers, Dordrecht, The Netherlands.

Kang, T.H.-K., and Wallace, J.W. (2005). "Dynamic responses of flat plate systems with shear reinforcement." *ACI Struct. J.*, 102(5):763-773.

Keyvani, L., Sasani. M., and Mirzaei, Y. (2014). "Compressive membrane action in progressive collapse resistance of RC flat plates." *Eng. Struct.*, 59:554-64.

Kinnunen, S., and Nylander, H. (1960) “Punching of concrete slabs without shear reinforcement.” Transactions 158, Royal Institute of Technology, Stockholm.

Krajcinovic, D. (1996). Damage Mechanics. North-Holland.

Kupfer, H., Hilsdorf, H.K., and Rusch, H. (1969). “Behahior or concrete under biaxial stresses.” *ACI J*, 66(8):656-666.

Ladeveze, P. (1983). Sur une theorie de l’endommagement anisotrope, Rapport interne No. 34, LMT Cachan, France.

Lander, M., Schaeidt, W., and Gut, S. (1977). Experimentelle Untersuchungen an Stahlbeton-Flachdecke. EMPA Bericht no. 205, Switzerland.

Langohr, P.H., Ghali, A., and Dilger, W.H. (1976). “Special shear reinforcement for concrete flat plates.” *ACI J.*, 73(3), 141-146.

Lee, J., and Fenves, G.L. (1998). “Plastic-Damage Model for Cyclic Loading of Concrete Structures.”*J. of Engin. Mechan.*, 124(8):892-900.

Lee, J., and Fenves, G.L. (1998). “A plastic-damage concrete model for earthquake analysis of dams.” *Earthquake eng and struct dyn* ,27(9):937-56.

Lemaitre, J., and Chaboche, J.L. (1990). Mechanics of solid materials, Cambridge University Press, New York.

Leonhardt, F., and Walther, R. (1962). “Beiträge zur Behanbung der Schubprobleme in Stalbetonbau.” Beton und Stahlbetonbau (Berlin), 54-64 and 141-149.

Liu, J., Tian, Y., and Orton, S.L. (2015). "Resistance of Flat-Plate Buildings against Progressive Collapse. II: System Response." *Struct Eng J,* 10.1061/(ASCE)ST.1943-541X.0001295 , 04015054.

Logan, D. (2007). A first course in the finite element method. Thomson.

Long, A.E., and Bond D. (1967). "Punching shear of reinforced concrete slabs." *Proc Inst of Civ Eng.*, 37:109-135.

Long, A.E., Cleland, D.J., and Kirk, D.W. (1978). "Moment transfer and the ultimate capacity of slab column structures." *Struct Eng*, 56A(4):95-102.

Lovrovich, J.S., and McLean, D.I. (1990). "Punching Shear Behaviour of Slabs with Varying Span-Depth Ratios." *ACI Struct J*, 87(5):507-511.

Luccioni, B., Oller, S., and Danesi, R. (1996). "Coupled plastic-damaged model." *Comput. Methods Appl. Mech. Eng.*, 129: 81-89.

Lubliner, J., Oliver, J., Oller, S., and Oñate, E. (1989). "A plastic-damage model for concrete." *International J. Solids Struct.*, 25(3):299-326.

MacGregor, G.J., and Bartlett, M.F. (2000). Reinforced Concrete: Mechanics and Design, Pearson Canada.

Maekawa, K., Pimanmas, A., and Okamura, H. (2003). Nonlinear Mechanics of Reinforced Concrete. Taylor and Francis Group.

Mazars, J. and Bazant Z.P. (1988). Cracking and damage: Strain localization and size effect. Elsevier Applied Science.

Mazars, J., and Pijaudier-Cabot, G., "Continuum damage theory - Application to concrete." *Journal of Engineering Mechanics,* 115(2):345-365.

Masterson, D.M., and Long, A.E. (1974). "The punching strength of slabs, a flexural approach using finite elements." *ACI Spec Publ S-42*, 2(4):747-68.

Megally, S., and Ghali, A. (2000). "Seismic Behaviour of Edge Slab-Column Connections with Stud Shear Reinforcement." *ACI Struct. J.*, 97(1):53-60.

Mercan, B., Schultz, A.E., and Stolarski, H.K. (2010). "Finite element modeling of prestressed concrete spandrel beams." *Engineering Structures, Elsevier,* 32:2804-2813.

Moe, J. (1961). "Shearing strength of reinforced concrete slabs and footings under concentrated loads." Development Department Bulletin D47, Portland Cement Association, Skokie, Illinois.

Moehle, J.P. (1988). "Strength of slab-column edge connections." *ACI Struct J*, 85(1):89-98.

Muttoni, A., and Schwartz, J. (1991). "Behaviour of Beams and Punching in Slabs without Shear Reinforcement." *IABSE Colloquium*, Zurich, Switzerland, 62:703-708.

Muttoni, A. (2003). "Shear and Punching Strength of Slabs without Shear Reinforcement." *Beton-und Stahlbetonbau*, Berlin, Germany, 98(2):74-84 (in German).

Muttoni, A. (2008). "Punching shear strength of reinforced concrete slabs without transverse reinforcement." *ACI Struct. J.*, 105(4):440-450.

Naaman, A.E., Likhitruangsilo, V., and Parra-Montesinos, G. (2007). "Punching Shear Response of HighPerformance Fiber-Reinforced Cementitious Composite Slabs." *ACI Structural Journal*, 104(2):170-179.

Negele, A., Eligehausen, R., Ožbolt, J., and Polak, M.A. (2007). "Finite-element simulations on punching tests of shear retrofitted slab-column connections." Proc., IA-FraMCoS-6: International Association of Fracture Mechanics for Concrete and Concrete Structures, Catania, Italy, 911–918.

Nguyen, G.D. (2002). Constitutive modelling of concrete, First year report, Department of Engineering Science, Oxford University.

Nguyen, G.D., and Houlsby, G.T. (2004). "A thermodynamic approach to constitutive modelling of concrete." Proceedings of the 12th conference, Association for Computational Mechanics in Engineering (ACME-UK), Cardiff, U.K.

Ockelston, A.J. (1955). "Load tests on a three-storey reinforced concrete building in Johannesburg." *Struct. Eng.*, 33(10).

Omidi, O., and Lotfi, V. (2010). "Numerical Analysis of Cyclically Loaded Concrete under large tensile strains by the plastic-damage model." *Scientia Iranica*, 17(3):194-208.

Ortiz, M. (1985). "A constitutive theory for the inelastic behaviour of concrete." *Mechanics of Materials* 4:67-93.

Park, R. (1964). "Ultimate strength of rectangular concrete slabs under term uniform loading with edges restrained against lateral movement." *Proc Inst Civ Eng*, 28:125-50.

Peerlings, R.H.J. (1999). Enhanced damage modelling for fracture and fatigue, PhD dissertation, Eindhoven University of Technology, Eindhoven, The Netherlands.

Pillai, S.U., Kirk, W., and Scavuzzo, L. (1982). "Shear Reinforcement at Slab-Column Connections in a Reinforced Concrete Flat Plate Structure." *ACI Journal*, 79(1):36-42.

Polak, M. A. (2005). "Shell finite element analysis of RC plates supported on columns for punching shear and flexure." *International J. for Comp.-Aided Eng. and Software*, 22(4):409-428.

Polak, M.A., El-Salakawy, E. and Hammill, N.L. (2005). "Shear reinforcement for concrete flat slabs." *ACI Special Publ* SP-232-05:75-96.

Rankin, G.I.B, and Long, A.E. (1987). "Predicting the enhanced punching shear strength of interior slab-column connections." *Proc Inst of Civ Eng*; 82(1):1165-86.

Regan, P.E. (1974). "Design for Punching Shear." *Struct Eng J.*, 52(6):197-207.

Regan, P.E., and Braestrup, M.W. (1985). Punching shear in reinforced concrete - A state-of-the-art report, Bulletin d'Information No. 168, Comité Euro-International du Béton, Lausanne.

Richart, F.E. (1948). Reinforced concrete walls and column footings, part 1 and 2." *ACI J*, 20(2): 97-127, 20(3):237-260.

Robertson, I.N., Kawai, T., Lee, J., and Johnson, G. (2002). "Cyclic Testing of Slab-Column Connections with shear reinforcement." *ACI Struct. J.*, 99(5):605-613.

Rombach, G. (2004). Finite element design of concrete structures. Thomas Telford.

Salari, M. R., Saeb, S., Willam, K. J., Patchet, S. J., and Carrasco, R. C. (2004). "A coupled elastoplastic damage model for geomaterials." *Comput. Methods Appl. Mech. Eng* 193(27-29):2625-2643.

Seible, F., Ghali, A., and Dilger, H.W. (1980). "Preassembled shear reinforcing units for flat plates." *ACI J.*, 77(1):28-35.

Sherif, A.G. (1996). Behaviour of reinforced concrete flat slabs. PhD thesis, Dept. Civ. Eng., Univ. Calgary, Canada.

Simo, J.C., and Ju, J.W. (1987). "Strain- and stress-based continuum damage model-I. Formulation." *International Journal of Solids and Structures*, 23(7):821-840.

Sozen, M.A., and Siess, C.P. (1963). "Investigation of multiple-panel reinforced concrete floor slabs, design methods-their evolution and comparison." *ACI J.* , 999-1025.

Swamy, R., and Ali, S. (1982). "Punching shear behaviour of reinforced slab-column connections made with steel fiber concrete." *ACI J.*, 79:392-406.

Talbot, A.N. (1913). Reinforced concrete wall footings and column footings. University of Illinois Engineering Experiment Station, Bulletin No 67, 114.

Tan, Y., and Teng, S. (2005). "Interior Slab-Rectangular Column Connections Under Biaxial Lateral Loadings." *Punching Shear in Reinforced Concrete Slabs, ACI SP232-09*, 147-174.

Teng, S., Cheong, H.K., Kuang, K.L., and Geng, J.Z. (2004). "Punching shear strength of slabs with openings and supported on rectangular columns." *ACI Structural Journal*, 101(5):678-687.

Turner, M., Clough R.W., Martin, H.C. and Topp, L.J. (1956). "Stiffness and deflection analysis of complex structures." *J. Aeronaut. Sci.* 23(9):805-823.

Ung-Quoc, H. (2003). Theorie de degradation du beton et developpement d'un nouveau modele d'endommagement en formulation incrementale tangente – Calcul a la rupture appliqué au cas des chevilles de fixation ancrees dans le beton, PhD dissertation, L'ecole nationale des ponts et chausses, France.

Vecchio, F.J., and Collins, M.P. (1990). "Investigating the collapse of a warehouse." *Concrete Int.*, 2(3):72-8.

Vecchio, F.J., and Tang, K. (1990). "Membrane action in reinforced concrete slabs." *Can. J. Civil Eng.*, 17:686-97.

Vecchio, F.J. (1999). " Towards cyclic load modelling of reinforced concrete." *ACI Struct. J.*, 96(2):193-202.

Voyiadjis, G.Z., and Taqieddin, Z.N. (2009). "Elastic Plastic and Damage Model for Concrete Materials: Part I-Theoretical Formulation." *Int. J. Struct. Changes Solids-Mech. Applications*, 1(1):31-59.

Westergaard, H.M., and Slater, W.A. (1921). "Moments and stresses in slabs." *ACI J.*, 17:415-538.

Willam, K.J., and Warnke, E.P. (1974). Constitutive model for the triaxial behaviour of concrete, International association of bridge and structural engineers, Seminar on concrete structure subjected to triaxial stresses, paper III-1, Bergamo, Italy, IABSE Proc. 19.

Wu, J.Y., Li, J., Faria, R. (2006). "An energy release rate-based plastic-damage model for concrete." *Int. J. Solids Struct.,* 43(3):583-612.

Yazdani, S., and Schreyer, H.L. (1990). "Combined plasticity and damage mechanics model for plain concrete." *ASCE Journal of Engineering Mechanics* 116(7):1435-1450.

Zienkiewicz, O.C. (1971). The finite element method in engineering science. 2nd edition McGraw-Hill, New York.